Design and structural optimization of a high entropy alloy (HEA) of the CoCrFeMnNi family with high mechanical resistance.

Michal Mroz

N°d'ordre NNT : 2018 LYSE M003

THESE de DOCTORAT DE L'UNIVERSITE DE LYON
opérée au sein de
l'Ecole des Mines de Saint-Etienne

Ecole Doctorale N° 488
Sciences, Ingénierie, Santé

Spécialité de doctorat : Sciences et Génie des Matériaux

Soutenue publiquement le 15/02/2018, par :
Michal Mroz

Design et optimisation structurale d'un alliage à forte entropie (HEA) de la famille CoCrFeMnNi à haute résistance mécanique.

Design and structural optimization of a high entropy alloy (HEA) of the CoCrFeMnNi family with high mechanical resistance.

Devant le jury composé de :

Legros, Marc	Directeur de recherche	CEMES Toulouse	Président
Jacques, Pascal	Professeur	Université de Louvain	Rapporteur
Tancret, Franck	Professeur	Université de Nantes	Rapporteur
Cordier, Catherine	Maître de conférences	Université Lille	Examinatrice
Van Landeghem, Hugo	Chargé de recherche	CNRS, SIMAP	Examinateur
Favre, Julien	Maître-assistant	EMSE	Examinateur
Fraczkiewicz, Anna	Directrice de recherche	EMSE	Directrice de thèse
Borbely, Andras	Directeur de recherche	EMSE	Co-directeur de thèse
Mithieux, Jean-Denis	Docteur	APERAM Isbergues	Invité

Spécialités doctorales	Responsables :	Spécialités doctorales	Responsables
			O. Roustant, Maître-assistant
SCIENCES ET GENIE DES MATERIAUX	K. Wolski Directeur de recherche	MATHEMATIQUES APPLIQUEES	
MECANIQUE ET INGENIERIE	S. Drapier, professeur	INFORMATIQUE	O. Boissier, Professeur
GENIE DES PROCEDES	F. Gruy, Maître de recherche	SCIENCES DES IMAGES ET DES FORMES	JC. Pinoli, Professeur
			X. Delorme, Maître assistant
SCIENCES DE LA TERRE	B. Guy, Directeur de recherche	GENIE INDUSTRIEL	
SCIENCES ET GENIE DE L'ENVIRONNEMENT	D. Graillot, Directeur de recherche	MICROELECTRONIQUE	Ph. Lalevée, Professeur

EMSE : Enseignants-chercheurs et chercheurs autorisés à diriger des thèses de doctorat (titulaires d'un doctorat d'État ou d'une HDR)

ABSI	Nabil	CR	Génie industriel	CMP
AUGUSTO	Vincent	CR	Image, Vision, Signal	CIS
AVRIL	Stéphane	PR2	Mécanique et ingénierie	CIS
BADEL	Pierre	MA(MDC)	Mécanique et ingénierie	CIS
BALBO	Flavien	PR2	Informatique	FAYOL
BASSEREAU	Jean-François	PR	Sciences et génie des matériaux	SMS
BATTON-HUBERT	Mireille	PR2	Sciences et génie de l'environnement	FAYOL
BEIGBEDER	Michel	MA(MDC)	Informatique	FAYOL
BLAYAC	Sylvain	MA(MDC)	Microélectronique	CMP
BOISSIER	Olivier	PR1	Informatique	FAYOL
BONNEFOY	Olivier	MA(MDC)	Génie des Procédés	SPIN
BORBELY	Andras	MR(DR2)	Sciences et génie des matériaux	SMS
BOUCHER	Xavier	PR2	Génie Industriel	FAYOL
BRODHAG	Christian	DR	Sciences et génie de l'environnement	FAYOL
BRUCHON	Julien	MA(MDC)	Mécanique et ingénierie	SMS
CAMEIRAO	Ana	MA(MDC)	Génie des Procédés	SPIN
CHRISTIEN	Frédéric	PR	Science et génie des matériaux	SMS
DAUZERE-PERES	Stéphane	PR1	Génie Industriel	CMP
DEBAYLE	Johan	MR	Sciences des Images et des Formes	SPIN
DEGEORGE	Jean-Michel	MA(MDC)	Génie industriel	Fayol
DELAFOSSE	David	PR0	Sciences et génie des matériaux	SMS
DELORME	Xavier	MA(MDC)	Génie industriel	FAYOL
DESRAYAUD	Christophe	PR1	Mécanique et ingénierie	SMS
DJENIZIAN	Thierry	PR	Science et génie des matériaux	CMP
DOUCE	Sandrine	PR2	Sciences de gestion	FAYOL
DRAPIER	Sylvain	PR1	Mécanique et ingénierie	SMS
FAUCHEU	Jenny	MA(MDC)	Sciences et génie des matériaux	SMS
FAVERGEON	Loïc	CR	Génie des Procédés	SPIN
FEILLET	Dominique	PR1	Génie Industriel	CMP
FOREST	Valérie	MA(MDC)	Génie des Procédés	CIS
FRACZKIEWICZ	Anna	DR	Sciences et génie des matériaux	SMS
GARCIA	Daniel	MR(DR2)	Sciences de la Terre	SPIN
GAVET	Yann	MA(MDC)	Sciences des Images et des Formes	SPIN
GERINGER	Jean	MA(MDC)	Sciences et génie des matériaux	CIS
GOEURIOT	Dominique	DR	Sciences et génie des matériaux	SMS
GONDRAN	Natacha	MA(MDC)	Sciences et génie de l'environnement	FAYOL
GONZALEZ FELIU	Jesus	MA(MDC)	Sciences économiques	FAYOL
GRAILLOT	Didier	DR	Sciences et génie de l'environnement	SPIN
GROSSEAU	Philippe	DR	Génie des Procédés	SPIN
GRUY	Frédéric	PR1	Génie des Procédés	SPIN
GUY	Bernard	DR	Sciences de la Terre	SPIN
HAN	Woo-Suck	MR	Mécanique et ingénierie	SMS
HERRI	Jean Michel	PR1	Génie des Procédés	SPIN
KERMOUCHE	Guillaume	PR2	Mécanique et Ingénierie	SMS
KLOCKER	Helmut	DR	Sciences et génie des matériaux	SMS
LAFOREST	Valérie	MR(DR2)	Sciences et génie de l'environnement	FAYOL
LERICHE	Rodolphe	CR	Mécanique et ingénierie	FAYOL
MALLIARAS	Georges	PR1	Microélectronique	CMP
MOLIMARD	Jérôme	PR2	Mécanique et ingénierie	CIS
MOUTTE	Jacques	CR	Génie des Procédés	SPIN
NEUBERT	Gilles			FAYOL
NIKOLOVSKI	Jean-Pierre	Ingénieur de recherche	Mécanique et ingénierie	CMP
NORTIER	Patrice	PR1	Génie des Procédés	SPIN
O CONNOR	Rodney Philip	MA(MDC)	Microélectronique	CMP
OWENS	Rosin	MA(MDC)	Microélectronique	CMP
PERES	Véronique	MR	Génie des Procédés	SPIN
PICARD	Gauthier	MA(MDC)	Informatique	FAYOL
PIJOLAT	Christophe	PR0	Génie des Procédés	SPIN
PINOLI	Jean Charles	PR0	Sciences des Images et des Formes	SPIN
POURCHEZ	Jérémy	MR	Génie des Procédés	CIS
ROUSSY	Agnès	MA(MDC)	Microélectronique	CMP
ROUSTANT	Olivier	MA(MDC)	Mathématiques appliquées	FAYOL
SANAUR	Sébastien	MA(MDC)	Microélectronique	CMP
STOLARZ	Jacques	CR	Sciences et génie des matériaux	SMS
TRIA	Assia	Ingénieur de recherche	Microélectronique	CMP
VALDIVIESO	François	PR2	Sciences et génie des matériaux	SMS
VIRICELLE	Jean Paul	DR	Génie des Procédés	SPIN
WOLSKI	Krzystof	DR	Sciences et génie des matériaux	SMS
XIE	Xiaolan	PR0	Génie industriel	CIS
YUGMA	Gallian	CR	Génie industriel	CMP

Acknowledgements

Table of contents

Introduction

Speaking of metal alloys one thinks mostly of those in which one component is dominant and other components are a small supplement (e.g. steels or aluminium alloys). However, since the 1970s the research of new materials, later called "high entropy alloys" [1], has been conducted [2]. Their composition, with all the elements (not less than five) in approximately equal proportions, differs significantly from conventional alloys and so traditional physical metallurgy rules implemented here. It may result in a number of enhanced properties (mechanical, magnetic, corrosion) that can be applied in many fields, hence the increasing interest of researchers and materials scientists. The main motivation is to explore a central region of multicomponent alloy phase diagrams which has not been examined so far. This gives a large number of possibilities and can conceivably result in finding new materials to potentially replace at least some of traditional alloys in specific conditions.

High entropy alloys have been studied at the Ecole des Mines de Saint-Etienne (MINES) since September 2013, when together with another Master of Science student, Clement Gayton, we have started working on the Master research project under supervision of Prof. Anna Fraczkiewicz, concerning microstructure and mechanical properties of the reference equiatomic CoCrFeMnNi high entropy alloy. After this first project, many other compositions were studied, not always with great success. However, a very novel and original high entropy alloy called A3S® (for Austenitic Super Stainless Steel) was developed in the laboratory. This alloy was patented in France in 2014 [3]. It possesses a stable face-centered cubic structure and is easily formable at room and high temperatures, maintaining high resistance and ductility (even at cryogenic temperatures). The new composition was based on the reference equiatomic CoCrFeMnNi alloy taken from the literature.

The main objectives of this thesis were to analyze the physical mechanisms which are at the origin of the mechanical properties of the two high entropy alloys with a view

of their optimization. Chosen materials were the reference X1 (equiatomic "Cantor alloy" CoCrFeMnNi) and the novel A3S® (Co20Cr15Fe26Mn17Ni22). A deviation from the equiatomic composition of only a few percent results in a significant increase of the mechanical resistance. For precise explanations, the research program combines thermodynamic modeling (Thermo-Calc software) with diverse and high level experimental techniques (scanning electron microscopy + EBSD, transmission electron microscopy, atom probe tomography, X-ray diffraction, mechanical tests).

At the beginning of this work, a bibliographic introduction is presented, concerning all the basic concepts, definitions and fundamental formation criteria as well as most recent results, which number is increasing rapidly each year. The second chapter is devoted to the types of applied methods and techniques. Then, the whole path of material design is described, dedicated essentially to Thermo-Calc simulations and to basic thermodynamic parameters calculations. Following, the evaluation of microstructures and mechanical properties of both the X1 and A3S are investigated, focusing on the differences between these two materials. This chapter is finally followed by a more complex analysis of the origins of the mechanical properties, regarding phenomena of recovery, recrystallization, thermal stability and characterization of dislocations.

High entropy alloys, with their exceptional properties and frequently unexpected behavior, could possibly replace some of traditional materials in particular conditions (e.g. very high or low temperatures). Still, many phenomena are not well understood and further studies are needed. In our work we succeeded in obtaining, developing and optimizing a novel original A3S® high entropy alloy, with superior properties compared to the reference material. What is more, this study allowed the MINES St-Etienne to launch several different projects on high entropy alloys with the industrial support (APERAM, Aubert & Duval, EDF).

1. State of the art of High Entropy Alloys

The history of metals and alloys is directly connected with our civilization progress. Starting with the Copper Age, through the Bronze Age and the Iron Age until our modern society, different materials have been developed and mastered. To start with, only pure metals were used (copper, gold, silver), but their strength was too low to make weapons or tools and their usage was mostly decorative. Even though at this time there was no knowledge about crystal defects, people realized that materials after deformation (for example by hammering) are stronger. In the Bronze Age, a completely new approach appeared: mixing two (or more) metals was giving much better mechanical properties than that of either of metals taken individually. After that, with progressing discovery of new elements in periodic table, different materials were studied and used for industrial applications. Until the nineteenth century, only 34 elements had been known [4]. Industrial and scientific revolution in 1800 - 1849 allowed identifying another 25 elements, and next 24 came with development of spectroscopy techniques. In total 118 elements are known to exist today [4].

1.1. Definition of high entropy alloys

Yet, all these traditional materials have been based on only one or two principal elements with additions of different minor elements to improve the properties. This impasse in metallurgy has been recently broken by a discovery of high entropy alloys [5], considered along with bulk metallic glasses as "multicomponent materials" (in fact, this term is not strictly defined). They are based on more than two main elements and regularly possess unique properties. Mackay [6] was the first to propose that the number of phases decreases for four and more components, even though the Gibbs phase rule permits it to increase. It means that obtaining materials with complicated compositions and simple structures should be possible. That leads to a concept of high entropy alloys (HEAs), consisting of five or more elements in similar ratios with a simple single-solid solution structure. Importance of the topic is reflected by the

number of publications increasing greatly every year. This bibliographic review is based on papers published until September 2017.

One of the main motivations of working on high entropy alloys was to explore the central region of phase diagrams in multicomponent alloys [2]. Hence, the content of different elements in HEAs is approximately equal and should be between 5% and 35%. Further, the number of elements should be more than five to facilitate solid solution forming. Since there is neither "solute" nor "solvent" in HEAs, these terms apply simply to "elements". This unique approach opens a new field in metallurgy, with an unlimited number of possible compositions of new materials.

The link between solid solutions and entropy can be explained by thermodynamics principles. Let's consider a binary model alloy in a solid state with the phase stability of type A + B. A contribution of the entropy of mixing to the Gibbs free energy can be found in the equation:

$$\Delta G_{mix} = \Delta H_{mix} - T\Delta S_{mix}$$

where: ΔG_{mix} – the Gibbs free energy of mixing; ΔH_{mix} – the enthalpy of mixing; T – absolute temperature; ΔS_{mix} – the entropy of mixing.
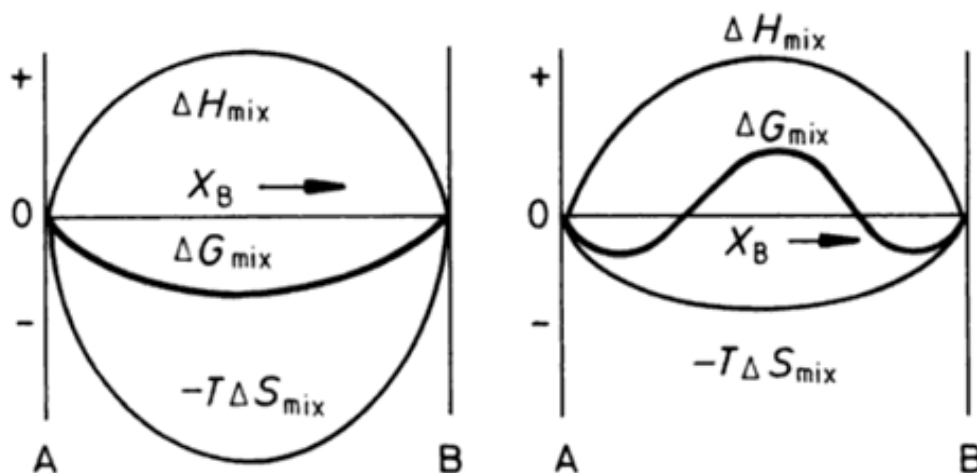
Figure 1. Free energy curves for various conditions [7], where X$_B$ is amount of solute.

If the enthalpy is constant, increasing the entropy makes the single-phase system more stable (lower Gibbs free energy), Figure 1 a. For a positive enthalpy of mixing, the entropy of mixing (or temperature) must be high and then only one phase is present. In other case, phase separation occurs (Figure 1 b).

For equiatomic or equimolar ratio alloys, the configurational entropy of mixing (which is one of the contributions to the total entropy of mixing S_{mix}) attains its maximum:

$$\Delta S_{conf} = Rln(N)$$

where: R – gas constant; N – number of components.
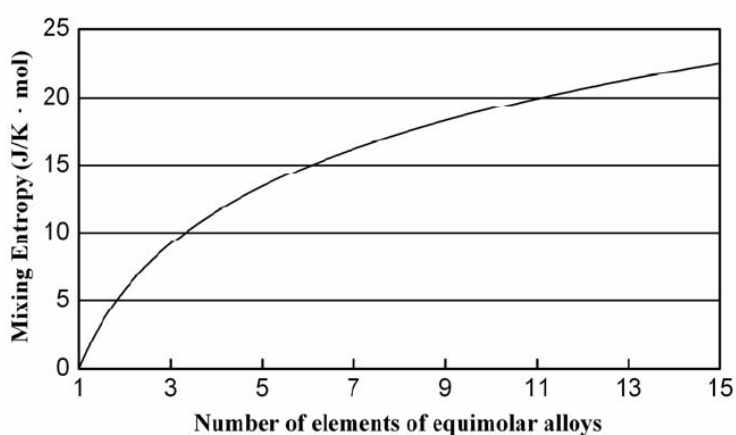
Figure 2. The configurational entropy of mixing as a function of the number of elements of equimolar alloys [8].

If the configurational entropy is higher than 1.5R (which corresponds to five elements), it may be high enough to overcome the effect of the mixing enthalpy in alloy systems for a solid solution formation and an alloy can be considered as a high entropy alloy. However, for more than 5 elements the relative increase of configurational entropy of mixing is less important [8] (Figure 2) and the risk of obtaining complex structure is high. According to this definition, traditional alloys with one or two major elements can be considered as "low entropy alloys". Materials with three or four major elements are grouped as "medium entropy alloys".

This new concept promises a great number of materials, increased even more if we consider that small additions of elements can modify the microstructure and properties significantly. Nevertheless, there is no clear definition of a high entropy alloy and above explanations should be only a guideline for future research. Some alloys which fall outside this box can still be considered as HEAs.

1.2. Core effects in HEAs

Yeh et al. [8], [9] distinguished four basic effects influencing the properties, microstructure, thermodynamics and kinetics of HEAs: high entropy, severe lattice distortion, sluggish diffusion and cocktail effect. Since HEAs are not classical materials with one principal element but contain many elements in similar proportions, these effects can differ from conventional alloys.

<u>High entropy effect</u>

First and probably the most important effect from which these novel materials took their name is the high entropy effect, allowing formation of simple solid solution structures. According to the classical physical metallurgy, increasing the number of elements increases also the possibility of forming more complicated microstructures, since more reactions between elements are probable. Gibbs phase rule ($P = C + 2 - F$, where: P is the number of phases, C is the number of components and F is the number of degrees of freedom) indicates that at a given pressure alloy may form up to 6 equilibrium phases for a 5-component system (since there are at least 5 elements in HEAs). A microstructure containing many phases is usually very brittle and not desirable in the industry. However, many experiments showed that it is not always true and in HEAs usually only few (could be one) simple solid solution phases of face-centered cubic (FCC) and body-centered cubic (BCC) structure are dominant.

A solid material can form different states: solid solutions, intermetallic compounds or amorphous phases. Solid solutions can be disordered simple structures (FCC, BCC, Hexagonal Close-Packed) with randomly distributed atoms or more complex ordered structures ($L1_2$, B2). Intermetallic compounds have a given stoichiometry with a crystal structure not necessarily the same as of its forming elements and they may display a long-range ordering. Amorphous phase has no crystal structure. All these states are characterized by different entropies and enthalpies of mixing [10].
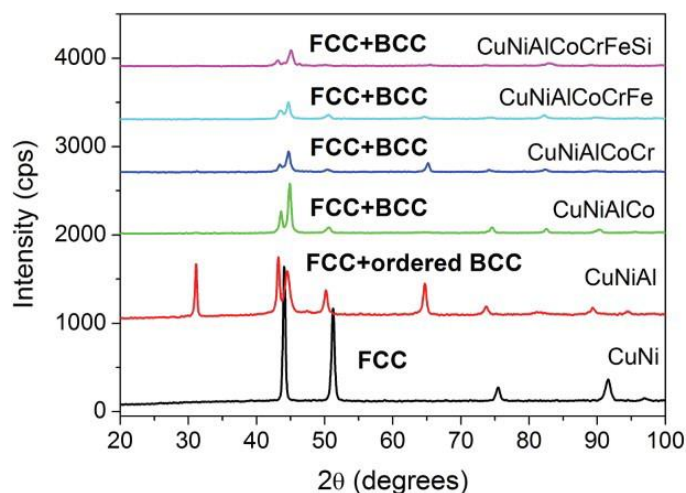
Figure 3. The XRD patterns of a series of alloys designed by the addition of one new element to the previous composition [11].

High entropy of mixing stabilizes solid solutions (which are high entropy phases) instead of i.e. intermetallic compounds that are ordered phases with lower entropy. This effect is stronger at higher temperatures. Commonly used alloying elements are FCC-type (Al, Cu, Ni), BCC-type (Fe, Cr, Mo) and HCP-type (Co, Ti), but for most of the studied alloys either FCC or BCC or BCC+FCC structures (Figure 3) are obtained [11].

This means that for high entropy materials the contribution of the entropy of mixing should be high enough to minimize the Gibbs free energy and form a solid solution. On the other hand, if the enthalpy of mixing is positive and high, it will overcome the effect of entropy and intermetallic compounds will be formed [12]. High positive enthalpy of mixing means that there is a tendency to separate and certain elements will segregate. Further, other factors have to be taken into account, for example the atomic size or electronegativity of elements. As one can see the entropy of mixing has an important influence on the formation of solid solution in HEAs but many different factors should be also considered. This question will be further discussed in Chapter 1.3.

Sluggish diffusion

Diffusion in high entropy alloys was first supposed to be sluggish [13]. In HEAs, each site is surrounded by different atoms (with different parameters such as atomic size or electronegativity) and hence differences in lattice energies are high. This may lead to

lower diffusion kinetics of vacancy formation and migration. The first and most noteworthy work on this subject was done by Tsai et al. [13], who used the diffusion couple method in Co-Cr-Fe-Mn-Ni alloys to study diffusion parameters and compare them with different FCC materials. The diffusion rate in HEAs turned out smaller than in pure metals and stainless steels. On the other hand, the normalized activation energies (Figure 4) were higher in HEAs than in other investigated materials. The sluggish diffusion in HEAs was attributed to larger value of the LPE (lattice potential energy), which influences vacancy formation and migration enthalpies [14]. By applying quasi-chemical model it was proved that in $CoCrFeMn_{0.5}Ni$ HEA the LPE fluctuation is elevated compared to FCC metals. For nickel atom the potential energy is about 1.5 time higher than in Fe-Cr-Ni (Figure 5).

Figure 4. Normalized activation energies of diffusion for Cr, Mn, Fe, Co and Ni in different matrices [13].

In the work of Divinsky et al. [15], however, it was noted that the diffusion is not necessarily considered as sluggish in CoCrFeNi and CoCrFeMnNi and can be faster in the quinary alloy. Pickering and Jones proved experimentally that this effect is of lower significance than initially expected [16].
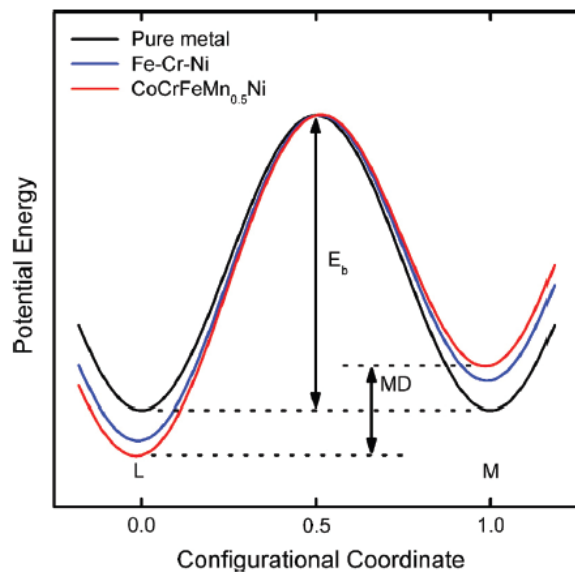
Figure 5. Variation of lattice potential energy for different materials during the migration of nickel [13].

The sluggish diffusion effect would set high entropy alloys apart from standard materials. It would be responsible for high temperature strength and structural stability in HEAs [17]–[19]. Moreover, formation of nanostructures would become easier since long-distance diffusion is more difficult and lower mobility of dislocations occurs [20], [21]. Some of HEAs were already examined in applications where slow diffusion kinetics plays a main role and they show important capability, for example as diffusion barriers [22].

Severe lattice distortion

The size of elements in HEAs varies and may lead to a severe lattice distortion. This hypothesis was confirmed by different diffraction techniques. Owen et al. [23] studied the lattice strain using neutron diffraction. By comparing CoCrFeMnNi HEA with other materials (pure nickel, Ni-Cr alloys, Ni - 37.5 Co - 25 Cr) they observed the greatest peak broadening in the HEA, suggesting the highest lattice strain. In the work of Yeh et al. [24], the XRD intensities of studied HEAs decreased with increasing number of elements, again indicating higher lattice strain.

Since each atom is surrounded by a different type of atoms with different size (Figure 6), the whole lattice is exposed to strains and stresses. Moreover, different bonding energies and crystal structures between adjacent elements cause lattice distortion, too [24]. These effects can explain high strength, tensile brittleness and slower kinetics of phase transformations of these alloys. For example values of hardness are few times higher in refractory HEAs than it is expected from the mixture rule [25].
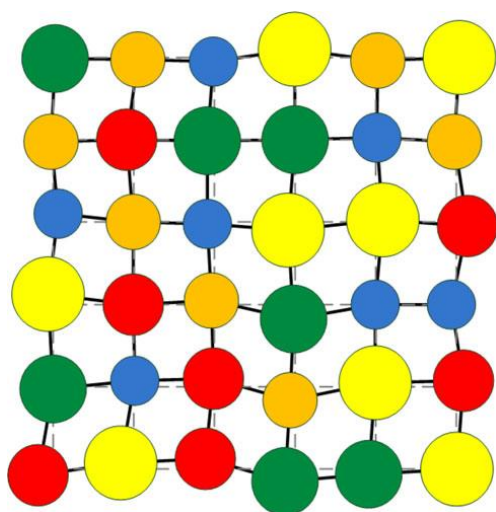
Figure 6. Severely distorted lattice in a multielement crystal structure [9].

As a consequence, thermal and electric conductivity are reduced as a result of electron and phonon scattering [26]. Since the

lattice distortion caused by thermal vibration of atoms is small compared to the severe lattice distortion, there is a very small effect of temperature on properties of HEAs [27]. Lu et al. [28] studied influence of temperature on thermal diffusivity in pure aluminum and different HEAs containing this element (Figure 7). In Al, thermal diffusivity is strongly decreasing with temperature, while in all the investigated HEAs this parameter is slightly positive and almost not sensitive to temperature.
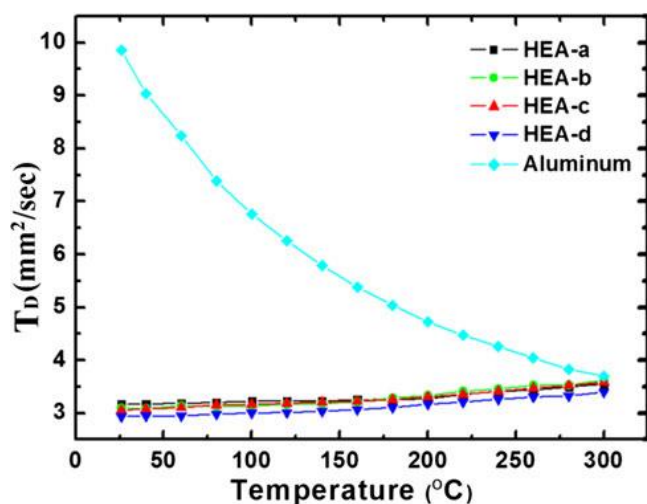
Figure 7. Thermal diffusivities as a function of temperature for pure aluminum and different HEAs [28].

Some of values of thermal conductivity and electrical resistivity, in comparison with different metals and alloys, are presented in Table 1. For example, electrical resistivity of CoCrFeNi and AlCoCrFeNi is of 142 and 221 μΩ·cm respectively and is higher than for conventional materials [29].

Table 1. Electrical resistivity and thermal conductivity of some HEAs and representative conventional metals [29]–[33].

Material	Thermal conductivity (W/m·K)	Electrical resistivity (μΩ·cm)
CoCrFeNi	12	142
AlCoCrFeNi	11	221
304 stainless steel	15	69
Inconel 718	11	125
Fe	80	10
Al	237	3
Cu	401	1.7
Ni	91	7

Cocktail effect
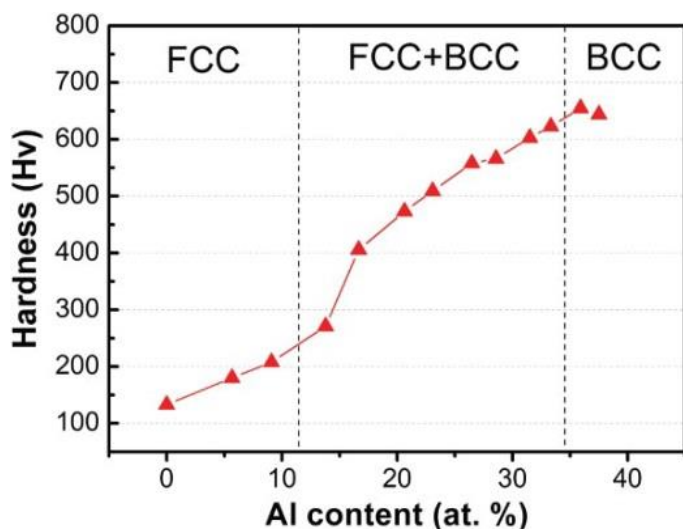
Figure 8. Strengthening effect of aluminum addition on the cast hardness of Al$_x$CoCrCuFeNi alloy [34]**.**

The properties of an alloy with many elements are different from that containing only one principal element. In HEAs, next to the properties of all the elements, interactions between elements must be given due consideration as well. It means that a given result of mixing few metals is different than expected from a simple sum of their properties. For example the hardness of Al$_x$CoCrCuFeNi (Figure 8) [34] can change depending on the content of aluminium. The increasing amount of Al causes a phase change from FCC to FCC + BCC and then to BCC; BCC phase is harder but more brittle.

Unusual phenomena may be expected in HEAs, coming from their complicated compositions and interactions between elements. Other effects of these interactions, having synergetic character, are expected.

All these four effects are indispensable for understanding any possible unusual phenomena occurring in high entropy alloys.

1.3. Fundamental criteria for HEAs formation and phase stability

As it was mentioned earlier, formation criteria for high entropy alloys are not obvious and a single correct approach for classifying these new materials does not exist yet. For example, the range of thermodynamic parameters for bulk metallic glasses, single-phased solid solution alloys or intermetallic phases is still not fully established. Many calculations and experiments still have to be done to facilitate matching the elements. In various articles the investigations show that even in alloys calculated as single-phased, intermetallic phases are also frequently present [35], [36]. Strict methodology has not been developed yet. By reason of lack of well-established phase diagrams for most HEAs, different physical factors and rules controlling phase stability have been proposed.

In the majority of publications only one or two phases are searched for, preferably solid solutions. Even though at the beginning HEAs were considered only as single-phased, this approach has changed and now not only single-phased alloys are in the center of interest (e.g. strengthening by intermetallic compounds of $L1_2$ type). Due to high complexity of HEAs their optimization is not straightforward and different rules must be applied, starting with Hume-Rothery rules. Then, various parameters such as entropy and enthalpy of mixing, atomic size or electronegativity are correlated with obtained microstructures. Phase stability is an essential issue and understanding it can facilitate obtaining desired structures and properties.

The first factors that should be taken into account when looking for new compositions of high entropy alloys are the four well-known criteria for forming solid solutions in binary alloys, known as Hume-Rothery rules [37]. These rules can be used in a first approach for choosing the elements in HEAs. For an A-B alloy:

- The difference between the atomic diameter of A and B should be smaller than 15%;
- A and B should have identical crystal structure for complete solubility;

- A and B should have the same valency;

- A and B should have similar electronegativity.

All these apply to HEAs except a necessity of having the same crystal structure of all elements. Following Hume-Rothery rules, great importance of the atomic size mismatch δ is evident. Guo et al. [12] made an attempt to distinguish the formation of a solid solution and an amorphous phase in HEAs using this parameter and enthalpy of mixing ΔH_{mix}. Atomic size mismatch δ is defined as:
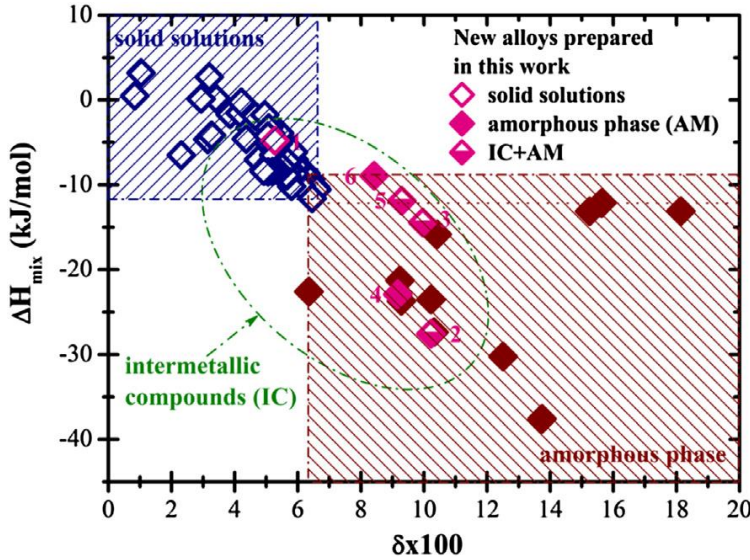
$$\delta = \sqrt{\sum_{i=1}^{n} c_i(1 - r_i/\bar{r})^2}$$

where: $\bar{r} = \sum_{i=1}^{n} c_i r_i$; c_i − atomic percentage of the i-th element; r_i −atomic radius of the i-th element; n – number of alloying elements.

Figure 9. A δ - ΔH_{mix} plot [12].

Enthalpy of mixing ΔH_{mix} is defined as:

$$\Delta H_{mix} = \sum_{i=1,i\neq j}^{n} c_i c_j \Gamma_{ij}$$

where: $\Gamma_{ij} = 4\Delta_{mix}^{AB}$ and Δ_{mix}^{AB} is the mixing enthalpy of binary liquid equiatomic AB alloys. The coefficient "4" is introduced intentionally in the Miedema's model [38].

According to the confusion principle when the number of the elements with different atomic radii in the system increases, then the possibility of forming a crystal structure gets lower. As can be seen in Figure 9, solid solutions can form when δ is small (δ < 0.06) and ΔH_{mix} has a little positive or a little negative value (-11.6 < ΔH_{mix} < 3.2 kJ/mol). Amorphous phase forms in the opposite conditions: when δ is large and ΔH_{mix} is very negative. In the ellipse region (on the graph) intermetallic compounds are found as well (however not as a dominant phase). Proper values of δ and ΔH_{mix} are then

necessary, but not sufficient for the solid phase forming in HEAs. They can only show efficiently the conditions to avoid intermetallic compounds.
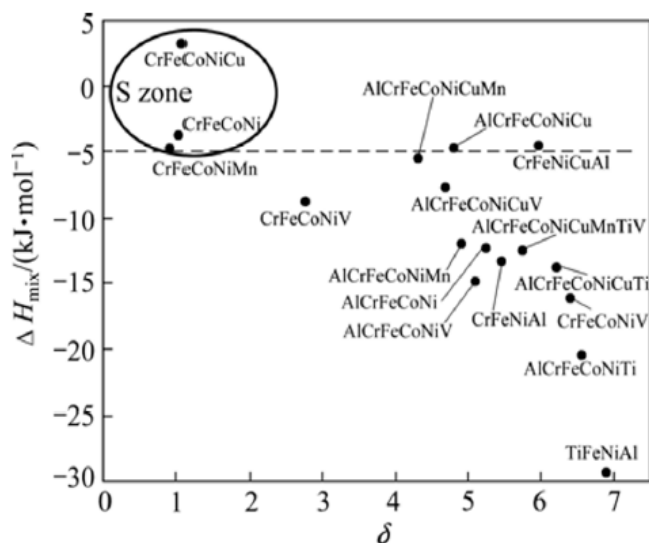
Figure 10. Location of alloy by comprehensive atomic radius and mixing enthalpy [39].

Similar results were obtained by Ren et al. [39] after investigating seventeen different high entropy alloys with various components. Single-phased HEAs were formed only for exact values of mixing enthalpy and atomic radius mismatch δ (Figure 10). These results confirm that if the alloy consists of late (i.e. V, Nb) and first transition elements (i.e. Fe, Co, Ni, Cu) with similar electron configuration, its mixing enthalpy is very negative and the effect of mixing entropy is small so the structure is more complex than single-phased. Still, CoCrFeMnNi and CoCrFeNi HEAs which contain only late transition elements, easily forms a solid-solution structure. If a first transition element, i.e. vanadium, is added to 4-elements CoCrFeNi in equiatomic proportion, the structure becomes more complex.

Next parameter that has to be considered in search of HEAs is evidently the entropy of mixing that affects the phase formation in multicomponent alloys systems. In case of the multicomponent alloys, unlike in the traditional materials, the microstructure and properties are determined by entropy which contribution to the free energy is higher than that of enthalpy. This competition between entropy and enthalpy of mixing has been defined in a new Ω parameter defined as $\Omega = \frac{Tm\Delta Smix}{\Delta Hmix}$ [40]. The value of $T_m\Delta S_{mix}$ can indicate the driving force for forming solid solutions; if it is high, the forming process is easier.

In Figure 11, the relation between Ω and δ is presented. For $1.1\% < \delta < 6.6\%$ and $\Omega > 1$, only solid solutions were formed. In the zone S+I (solid solutions + intermetallics), where Ω and δ decrease, the ordered phases (intermetallics) can precipitate as well. For δ above ~6.5% intermetallics are a dominant phase. Bulk metallic glasses are located in zone B, where a difference in atomic size of elements is significant.
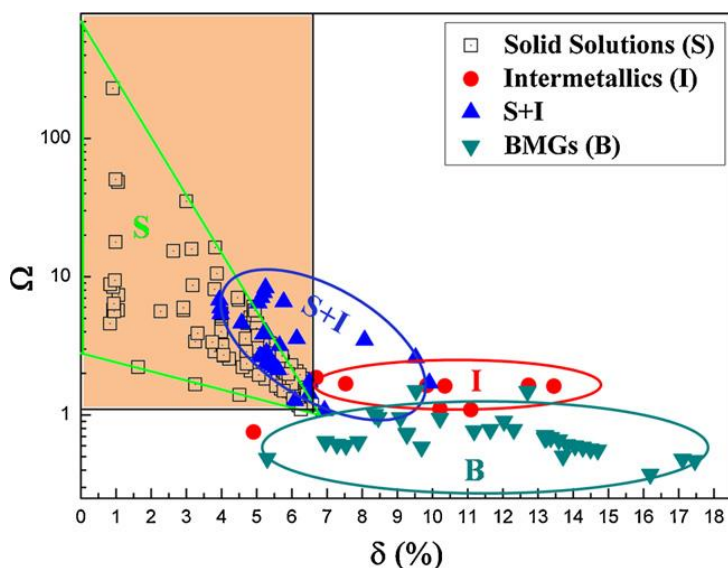
Figure 11. The relationship between parameters δ and Ω for multi-component alloys [40]**.**

Further parameters, such as valence electron concentration (defined as $VEC = \sum_{i=1}^{n} c_i (VEC)_i$), were applied to search stability of FCC and BCC phases in HEAs [41]. The electron concentration was defined here as a number of total electrons including d-electrons accommodated in the valence band. More classical definition – average number of itinerant electrons per atom (e/a) – was considered as not correct for HEAs which are made of transition metals; in this case a value of e/a depends on the environment.

Values of VEC and other parameters (the atomic size difference, the mixing enthalpy ΔH_{mix} and the electronegativity difference) were calculated for the $Al_xCoCrCuFeNi$ and $Al_xCrCuFeNi_2$ systems. The results are presented in Figure 12. For VEC > 8, only one FCC phase exists. Mixed FCC and BCC phases occur for 6.87 < VEC < 8, and for VEC < 6.87 only a BCC phase is present. It means that VEC can be a useful parameter for predicting phase stability in HEAs. To make their conclusions even more reliable, more data from the literature was collected by the authors (Figure 13). There are many more results and not all of them are strictly compatible with the values of 6.87 < VEC

< 8, but the whole tendency is correct. All the BCC alloys present VEC < 6.67 and all the FCC alloys have VEC > 8; only several FCC+BCC alloys are out of the range of 6.67-8 VEC.
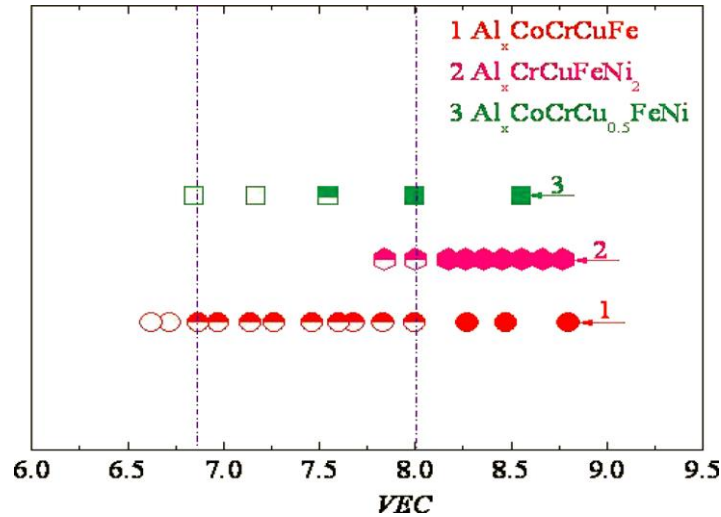
Figure 12. Relationship between VEC and the FCC, BCC phase stability for three HEA systems. Fully closed symbols: single FCC phase; fully open symbols: single BCC phase; top-half closed symbols: mixed FCC and BCC phases [41]**.**
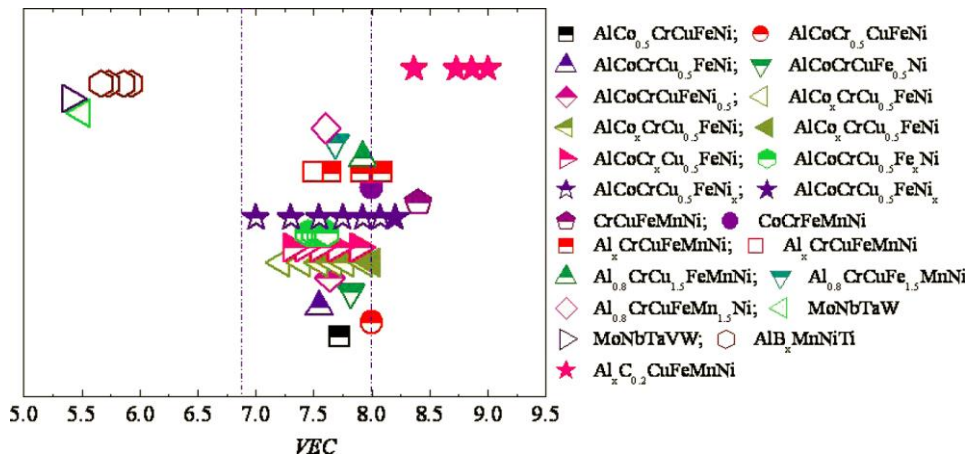
Figure 13. Relationship between VEC and the FCC, BCC phase stability for different HEAs. Note on the legend: fully closed symbols: single FCC phases; fully open symbols: single BCC phase; top-half closed symbols: mixed FCC and BCC phases [41]**.**

The electronegativity mismatch is another parameter adapted from Hume-Rothery rules ($\triangle\chi = \sum_{i=1}^{n} c_i \cdot (1 - \frac{\chi_i}{\chi_a})$), where χ_i is an electronegativity of i-th element and χ_a is an average electronegativity) that influences phase formation in multicomponent systems [42]. Instead of Pauling scale, Allen scale was used with different definition of electronegativity. It is based on the average ionization energy of the valence electrons

for free atoms in their ground state and for the transition metals it differs from Pauling's values.

Three categories were distinguished (Figure 14): FCC or BCC for single solid solutions, SS (BCC+FCC) for two solid solutions and the others with intermetallic phases (IM). In the plot there are clear differences between these groups. For 1% < δ < 6% and the electronegativity mismatch between 3 and 6, intermetallic compounds are not formed (in agreement with earlier results). FCC solid solutions occur for a lower radius mismatch and higher electronegativity mismatch than BCC solid solutions. With growing electronegativity differences, the formation of sigma phase starts to dominate and then intermetallic compounds appear. It was pointed that for non-equiatomic HEAs with a minority element, it is more probable to stabilize intermetallic compounds.
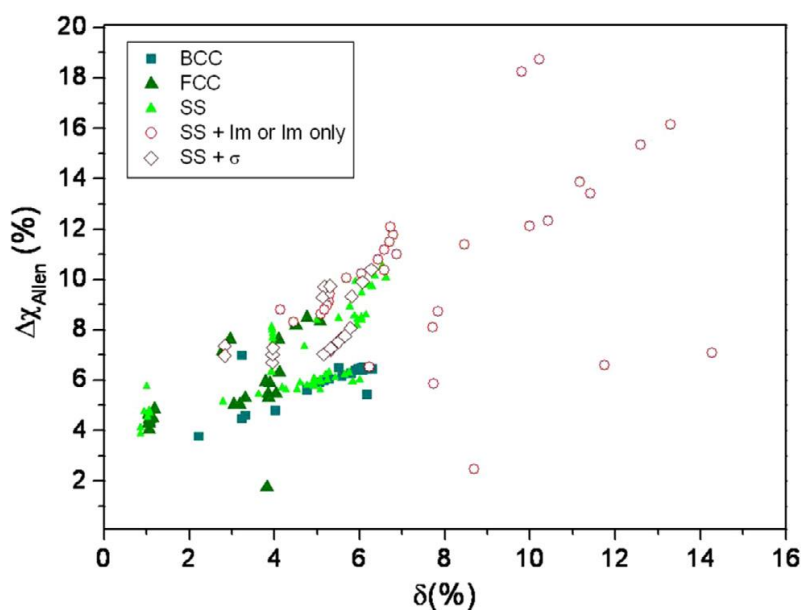
Figure 14. Radius vs. electronegativity mismatch for the multicomponent systems [42]**.**

Overall, it was proved that the standard rules of forming a solution between two elements are not sufficient for much more complex high entropy alloy systems. Few important parameters have to be considered while searching for new high entropy alloys: atomic radius, entropy and enthalpy of mixing, valence electron concentration and electronegativity. These should be a very first indicator in choosing HEAs

compositions, but not the only ones. Normally, these parameters must be combined with more advanced thermodynamic simulations such as CALPHAD (CALculation of PHAse Diagrams) or *ab initio* methods.

Finite-temperature *ab initio* methods were used to investigate thermodynamic properties of the CoCrFeMnNi [43]. Here, the study focused on contributions to entropy other than the configurational one, such as vibrational, electronic and magnetic entropy. Even though modeling of HEAs is difficult due to their high complexity, large number of elements and chemical disorder, first obtained results were interesting. The authors showed that the configurational entropy is not a dominant factor in HEA formation and to correctly predict phase formation other types of entropy must be taken into account. Vibrational, electronic and magnetic entropies can contribute up to 50% of the total entropy and must be included in determining phase stability (Figure 15).
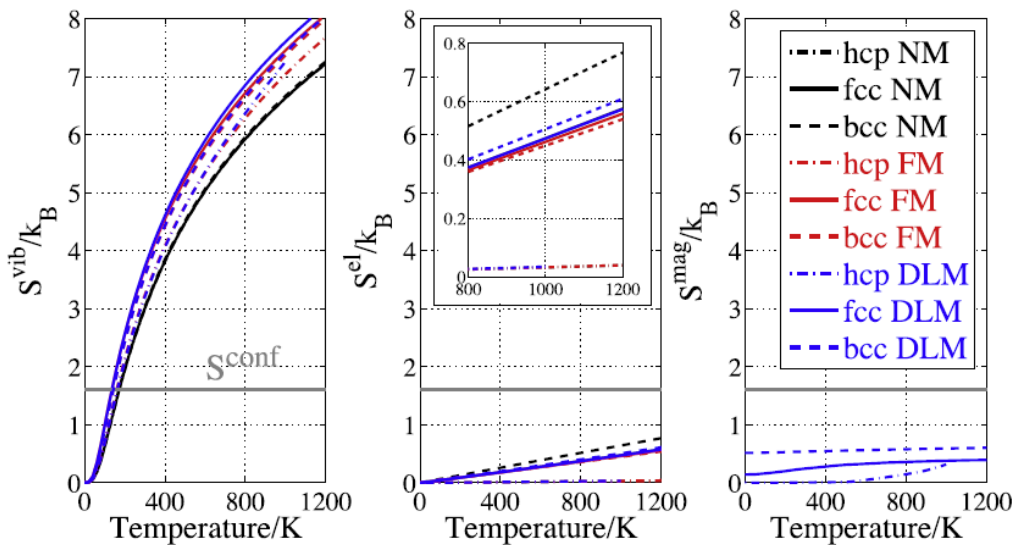
Figure 15. Temperature dependence of the vibrational entropy S^{vib} (left), the electronic entropy S^{el} (middle), and the magnetic entropy S^{mag} (right) in the hcp (dash-dotted lines), fcc (solid lines), and bcc (dashed lines) structure for the NM (non-magnetic; black), FM (ferromagnetic; red), and DLM (disordered local moments; blue) state [43].

Another approach to design single solid solution HEAs was proposed by Tancret et al. [44] using a Gaussian process statistical analysis and combining physical parameters

with computational thermodynamics. Here, a risk of finding a non-single phased HEA was minimized by applying nine physical criteria and four thermodynamic databases in Thermo-Calc. This method was verified on 322 alloys from the literature and the results were satisfying: several tens of equimolar HEAs with a stable single solid solution were proposed (Figure 16).
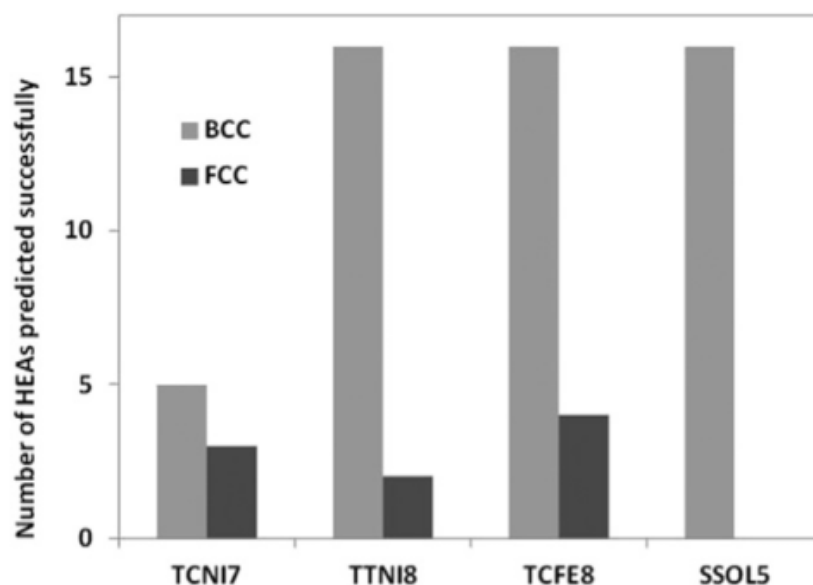
Figure 16. Single-phases HEAs successfully predicted by the combined approach using different databases [44]**.**

These examples prove that making assumptions about phase formation in HEAs based only on fundamental parameters may not be successful and more advanced simulation techniques are probably necessary to obtain satisfying results.

1.4. High entropy alloys as future industrial materials

Materials with improved properties that can be adapted for new applications are constantly desired. For this reason HEAs, with their rich variety of compositions, microstructures and properties, have attracted attention of the research and industry. Thus, important improvement of materials behavior is expected, in the hope of replacing traditional materials in more demanding environments and operating conditions. Nevertheless one should keep in mind that HEAs are not a one specific type of materials with similar properties, but depending on composition and even proportions between elements can give completely different values of strength, high temperature and corrosion resistance, magnetism, conductivity, etc.

Among several fields where higher performance of materials is always demanded, and therefore HEAs could be applied, the most important are [8]: aerospace industry (where high elevated-temperature strength and corrosion resistance is needed), nuclear industry (for high elevated-temperature strength and low irradiation damage) but also steel development (by improving mechanical properties, especially at extreme temperatures).
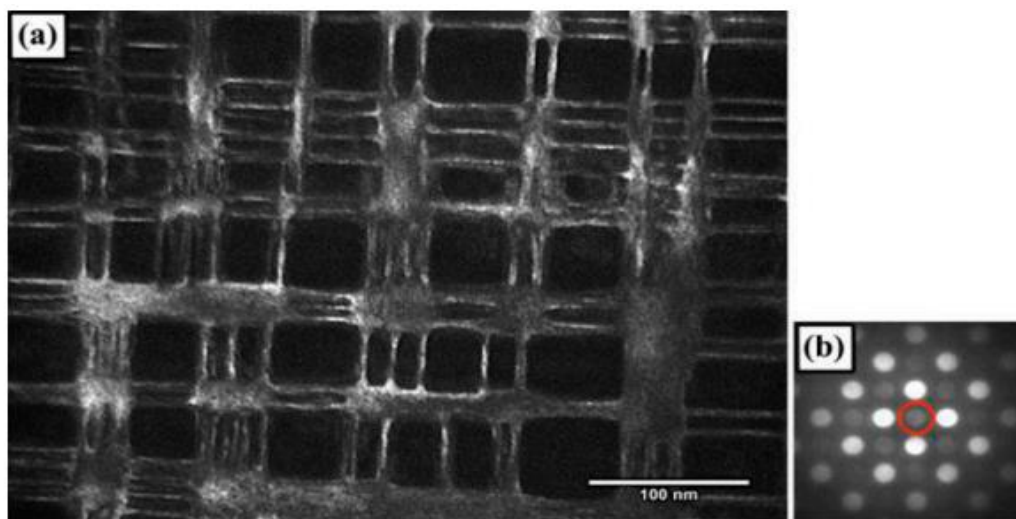
Figure 17. a) Dark field (DF) TEM image and b) a diffraction pattern obtained with a (001) superlattice reflection of AlMo0.5NbTa0.5TiZr. Bright channels correspond to ordered B2 phase [45]**.**

For future applications in the aerospace industry, materials suited to high temperatures are investigated, among them HEAs. Conventional materials used in this field, such as Ni and Co superalloys, have certain disadvantages (high weight, at some point weak oxidation and corrosion resistance, microstructural instability at high temperatures). Hence, HEAs compositions based on late transition metals and refractory elements (W, Zr, Ta, Nb, etc.) are intensively studied because of their mechanical resistance to creep. Different compositions were investigated, for example WNbMoTa and WNbMoTaV [25], both with a single BCC phase and the microhardness (500 g load) of respectively 4455 MPa and 5250 MPa at room temperature. Melting temperature of both materials was high (respectively 3177 and 2946 K). Another HE superalloy, AlMo0.5NbTa0.5TiZr [45], possesses a BCC structure with very fine nano-scaled precipitations, forming a microstructure similar to this of superalloys (Figure 17), but with BCC as a strengthening phase and B2 structure as a matrix phase. Formation of tertiary precipitates was not observed. Yield strength remains very high at temperatures even at 1000°C (745 MPa) and is higher than in some of conventional Ni-based superalloys (i.e. 560 MPa for Inconel MA758 at 760°C [46]).
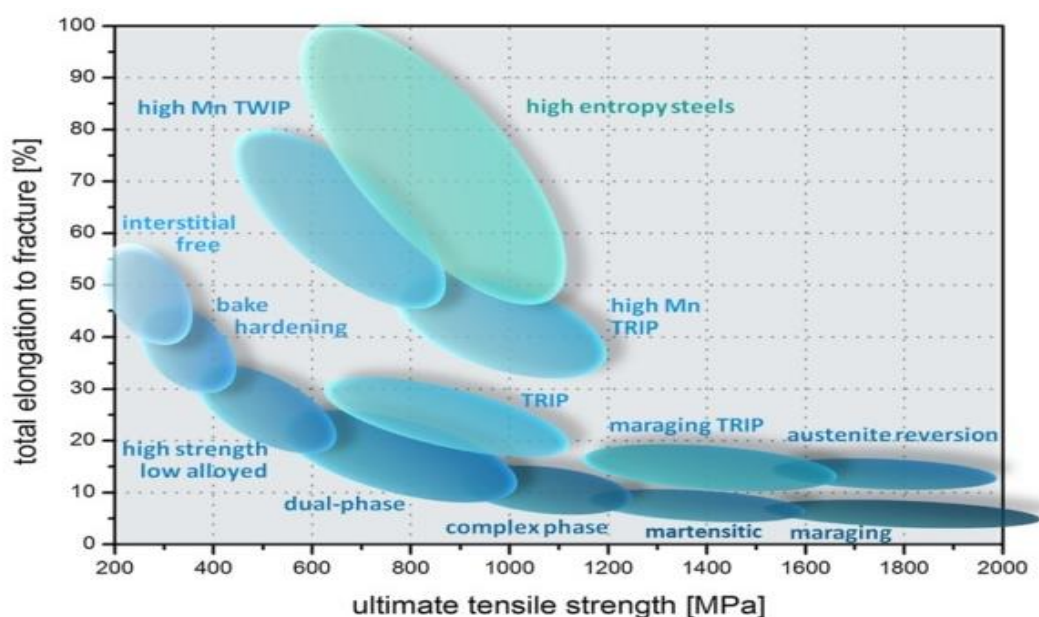
Figure 18. Total elongation to fracture vs UTS for different types of steels [47].

Nuclear power is providing about 10% of world's electricity [48]. Reactors used in nuclear plants last about 50 years and are made up mostly of stainless steel, which weakens with time. Thus, new materials that could work at even higher temperatures and last longer are searched. For selected equiatomic compositions, first results of irradiation tests compared to austenitic steels are very promising, with much less defects after bombarding with heavy ions [49]. In CuNiFeCo, irradiation (studied by means of molecular dynamic simulations) causes much lower defects mobility than in pure metals and thus the defects tend to isolate than to create agglomerations [50]. A steady state of defect creation and annihilation is reached here much faster than in conventional materials. This high resistance to irradiation can be explained by high stresses in the crystal structure and chemical disorder, both affecting heat dissipation and defect motion kinetics.

In the steel industry, improving mechanical properties is a permanent challenge, especially when both high resistance and ductility must be provided equally. Research on combining these two properties has been already successful in the case of a dual-phase CoCrFeMn by Li et al. [51], where transformation-induced plasticity of steels (TRIP) and solid-solution strengthening of HEAs were coupled. It is a valuable example that not always only one phase is desirable in HEAs and new strategies of their design are still needed. Raabe et al. proposed a strategy in developing what they called "high entropy steels" [47]. It was pointed out that a very little attention is concerned to interstitial elements in Fe-based HEAs, like Fe-Mn-Al-Si-C. In this approach, a single-phased material with excellent strength, ductility and toughness was successfully processed (Figure 18). These properties increase even more at low temperatures. Cryogenic steels could be replaced as well by the equiatomic CoCrFeMnNi, since its mechanical properties are preserved and improved at even 77K [52] (see more: Chapter 1.5.2). Comparing to other materials (Figure 19), this alloy has high fracture toughness (200MPa·m$^{0.5}$) with relatively high yield strength (~750MPa at 77K). Moreover, many HEAs possess much better corrosion properties than for

example 304 stainless steel (Al$_{0.5}$FeCoCrNiCu [53], CrFeNiCuMoCo, Al$_x$FeCoNiCrTi [54]).
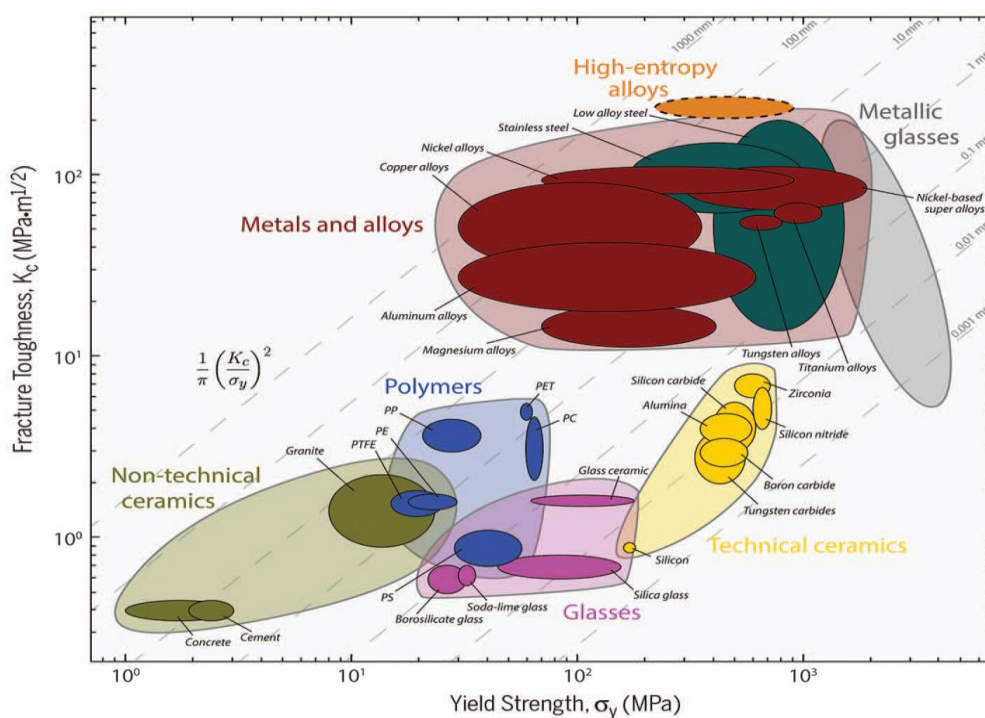
Figure 19. Ashby map of fracture toughness as a function of yield strength [52]**.**

Next to these three main areas of HEAs application, there are still many other possibilities of using these novel materials. For example, easier formation of nanostructures and thus high density of grain boundaries, together with severe lattice distortion and sluggish diffusion reduce thermal conductivity. This may be applied in casting mold production, where low thermal conduction is needed to slow down solidification and produce thin castings with large area, made of Al or Mg alloys. Because of good mechanical (high hardness and wear resistance) and corrosion properties, HEAs can be applied in hardfacing technology as protection layers on the surface of machine components. The wear resistance can be further increased by suitable heat treatment, oxidizing or nitriding. HEAs could also be used as thermal barrier coatings [55]. As can be seen, HEAs can be designed and developed for different applications, and further research is needed to reveal their potential for industrial usage.

1.5. The CoCrFeMnNi family of high entropy alloys

The idea of mixing many elements in equal proportions came up initially in the 1970s from Cantor [56], who suggested that this new approach may result in opening a completely new and unknown field of metallurgy dominated by one-component alloys. Indeed, first results had shown high mechanical resistance and phase stability, notably for an equiatomic CoCrFeMnNi HEA. Unfortunately, this new concept has been abandoned for many years and had to wait until the next century to be developed, due to lack of interest, funding and conservative thinking of many researchers.

In 2004, after more than 25 years since the concept was invented, Cantor et al. [2] wrote one of the first and most influential publications based on a long-term research on high entropy alloys, in which they examined a five component equiatomic $Co_{20}Cr_{20}Fe_{20}Mn_{20}Ni_{20}$ alloy. Its microstructure and properties were studied using standard techniques: optical microscopy, scanning electron microscopy, electron probe microanalysis, X-ray diffraction and microhardness measurements. Although they have focused on the 5-element equiatomic composition, in the same work they checked as well alloys based on CoCrFeMnNi with addition of other transition metals (Nb, Ti, V) and alloys consisting of 20 (Mn, Cr, Fe, Co, Ni, Cu, Ag, W, Mo, Nb, Al, Cd, Sn, Pb, Bi, Zn, Ge, Si, Sb, Mg) and 16 (Mn, Cr, Fe, Co, Ni, Cu, Ag, W, Mo, Nb, Al, Cd, Sn, Pb, Zn, Mg) elements in equimolar proportions. This 16- and 20-elements alloys were multiphase and brittle so they were rejected, but surprisingly even if they consisted of so many elements, only one FCC phase was dominant. Still, only CoCrFeMnNi remained single-phased.

Since 2004, the equiatomic CoCrFeMnNi became one of the most studied HEAs, with rapidly growing number of publications each year. Interest from widely known universities and research centers (especially Oak Ridge National Laboratory) is remarkable. There, mostly exceptional mechanical properties of the material have been

investigated, as well as new models predicting formation and optimization of other high entropy alloys. The interest of the various researchers is certainly proof of the uniqueness and great hopes placed in this new group of alloys.

Table 2. Binary mixing enthalpies in Co-Cr-Fe-Mn-Ni alloys [56]**.**

	Cr	Mn	Fe	Co	Ni
Cr	-	-3.8	5.9	6.8	6.4
Mn		-	-4.7	2.2	-14
Fe			-	-1.3	-4.6
Co				-	-0.2
Ni					-

Equiatomic CoCrFeMnNi alloy [2] contains only one FCC phase and it solidifies dendritically [57], [58]. Presence of a single phase can be explained by low positive or negative heats of mixing for all unlike atomic pairs (Table 2). In this case the mixing entropy effect is sufficient to overcome the enthalpy effect. EDX maps showed the differences in composition (primary segregation), with dendritic areas richer in Fe, Co, Cr and interdendritic ones richer in Mn and Ni (Figure 20). Obtained hardness was approximately 300HV and it increased with addition of Nb, Ti and V. In other 6-elements (FeCrNiMnCo + V, Nb, Ti, Cu or Ge) equiatomic alloys, dominant dendritic FCC phase was present with other phases. XRD analysis showed that lattice parameters for all alloys were in the range 0.358-0.364 nm. None of examined alloys forms metallic glass even if it is common for multicomponent systems where the solidification process is more difficult.
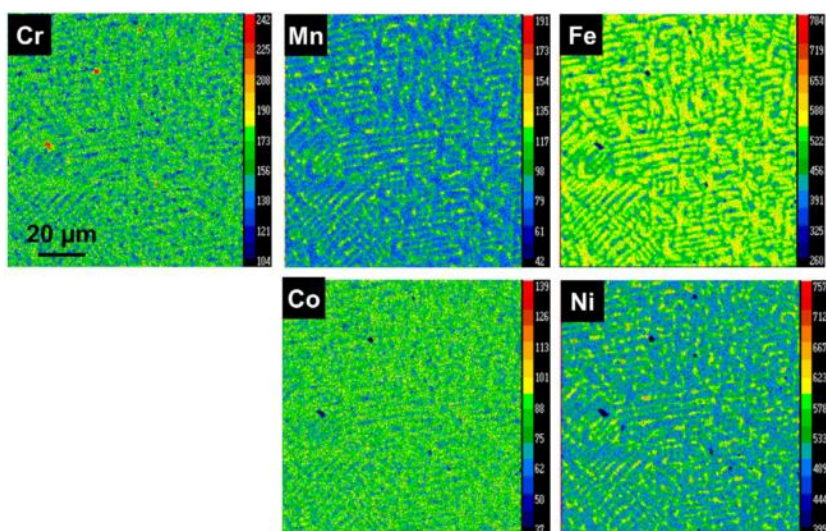
Figure 20. Electron Probe MicroAnalysis maps of the CoCrFeMnNi after induction melting and suction casting [57]**.**

1.5.1. Thermal stability

Because this equiatomic alloy (CoCrFeMnNi) was single-phased and seemed to fulfill all the criteria to create a high entropy alloy, it became a reference alloy for many further investigations. However, an important number of recent articles have shown that its microstructure is unstable after different heat treatments, when the formation of a BCC and/or σ phase becomes possible. Presence of new phases depend on the initial conditions of the material (i.e. if it is severely deformed) and its purity. All the observations of new phases in this alloy are summarized in Figure 21, including as well the state of material before annealing (recrystallized or severe plastic deformed).
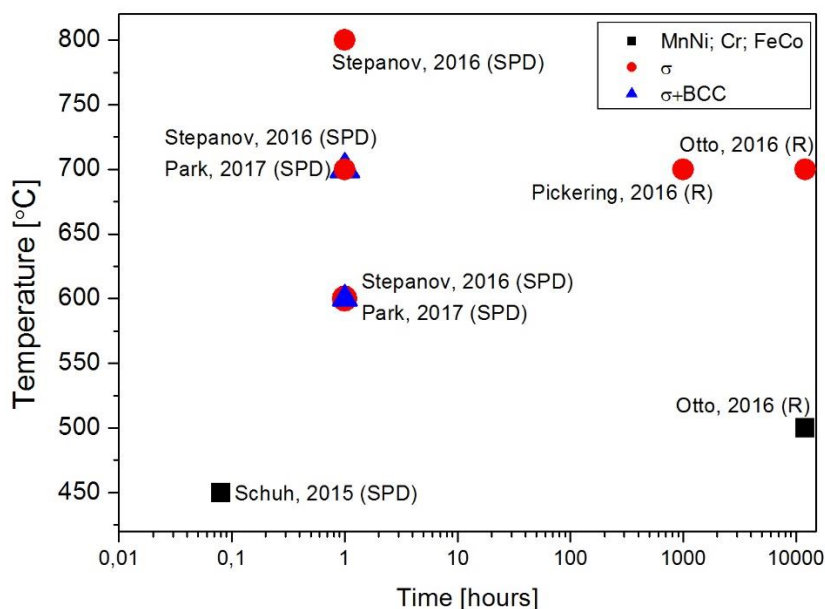
Figure 21. Summarized observations of the secondary phases in the CoCrFeMnNi (based on the literature). State of material before annealing: R – recrystallized; SPD – severe plastic deformed.

Schuh et al. [59] produced the CoCrFeMnNi by arc melting and drop casting and subjected it to severe plastic deformation using high pressure torsion. The material was then heat treated at 450°C for different times. After time as short as 5 minutes, phase decomposition was initialized, with three new phases in high entropy matrix: Mn-Ni-rich phase, Fe-Co-rich phase and Cr-rich phase. Here the decomposition may

be facilitated by high deformation of the material and thus more possible nucleation sites.

Then, Pickering et al. [60] observed Cr-rich precipitations in grain boundaries in the CoCrFeMnNi, identified as σ and $Cr_{23}C_6$ (having its origins in surface contamination) phases. The precipitations formed after heat treatment at 700°C for 500 and 1000 hours.

To verify the influence of a very long heat treatment, Otto et al. [61] studied microstructural evolution of the equiatomic CoCrFeMnNi alloy after 500-day annealing at 500, 700 and 900°C. After 500 days at 900°C the alloy remains single-phased because most likely at this temperature a single solid solution is stable. However, after 500 days at 700°C, Cr-rich precipitates of σ type are detected, essentially at grain boundaries. After 500 days at 500°C the microstructure is even more complex, with three phases in the matrix: a BCC phase rich in Cr, a tetragonal phase rich in Ni and Mn (Figure 22) and a B2 phase rich in Fe and Co (in agreement with [59]).
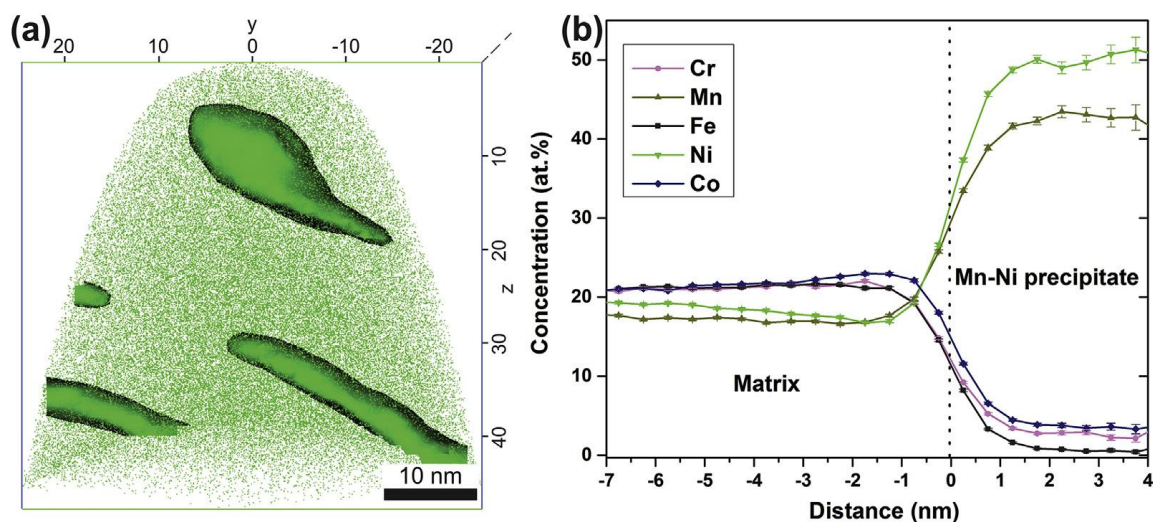
Figure 22. APT Ni map with the distribution of the NiMn precipitates in the CrMnFeCoNi HEA after a 500-day anneal at 500°C and (b) concentration of elements in the matrix and Mn-Ni precipitate [61]**.**

Additionally, Stepanov et al. [62] observed formation of second phases rich in Cr (of BCC and σ type) after annealing at 600°C for 1 hour. Samples were cold rolled before heat treatment, indicating high deformation rate. Severe plastic deformation may

explain faster phase transformations due to a big number of grain boundaries and high density of defects (dislocations, vacancies) which are the fastest diffusion paths [59]. On the other hand, no difference in size and volume fraction of the second phases after different rolling processes was found. Even though the cold rolling produces more deformed structure with a higher density of grain boundaries and vacancies, apparently grain size is not a decisive factor for phase transformation kinetics.
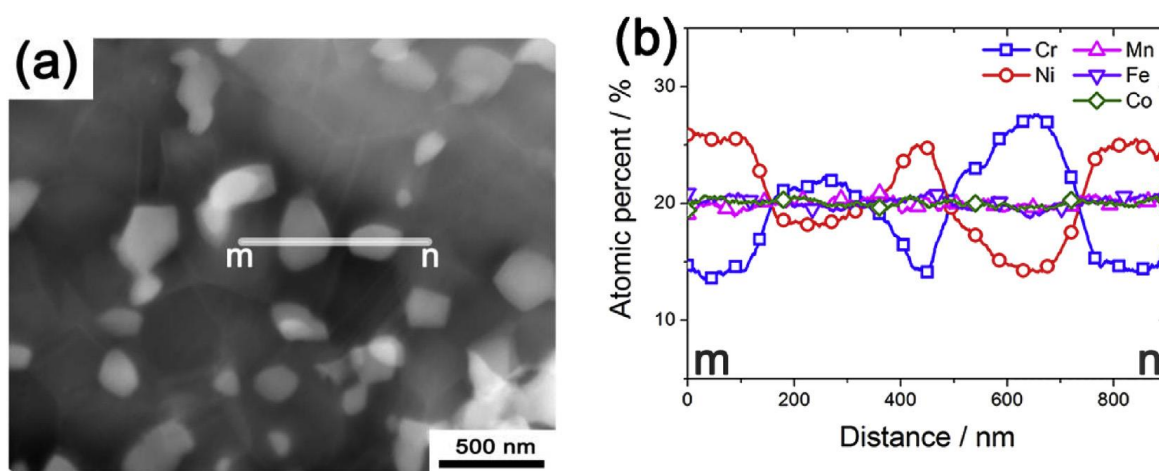
Figure 23. High angle annular dark field scanning TEM image (a) and chemical composition profile (b) of the CoCrFeMnNi annealed at 700ºC for 3.6 ks after HPT process [63].

Formation of Cr-rich σ phase was confirmed by Park et al. [63] in their study on the alloy processed in high pressure torsion, another severe plastic deformation technique, and annealed at temperatures between 600 and 900ºC. XRD analysis confirmed only one FCC phase for heat treatments above 800ºC. Below this temperature, in specimens annealed at 600 and 700ºC for 10s – 1h, a second phase appeared. Its density increased with decreasing temperature. The size of this second phase was of nanometric scale (Figure 23 a). While the second phase is enriched in Cr (Figure 23 b), its amount is depleted in the matrix. The opposite effect is observed for Ni. For other elements, the difference of concentration is smaller than 2%. This phase is analogous to the sigma phase existing in steels. Besides, the formation of Cr-rich phase was confirmed by thermodynamic calculations with Thermo-Calc software.

1.5.2. Mechanical properties

Mechanical properties of the CoCrFeMnNi were intensively studied through hardness, compression and tensile tests.

George et al. [64] investigated tensile properties of the equiatomic CoCrFeMnNi and, for comparison, a medium-entropy alloy – CoCrFeNi (medium-entropy alloys are alloys based on three or four principal elements [65]). Both of them are FCC single-phased. Before tensile tests, alloys were hot-rolled to obtain a recrystallized microstructure.
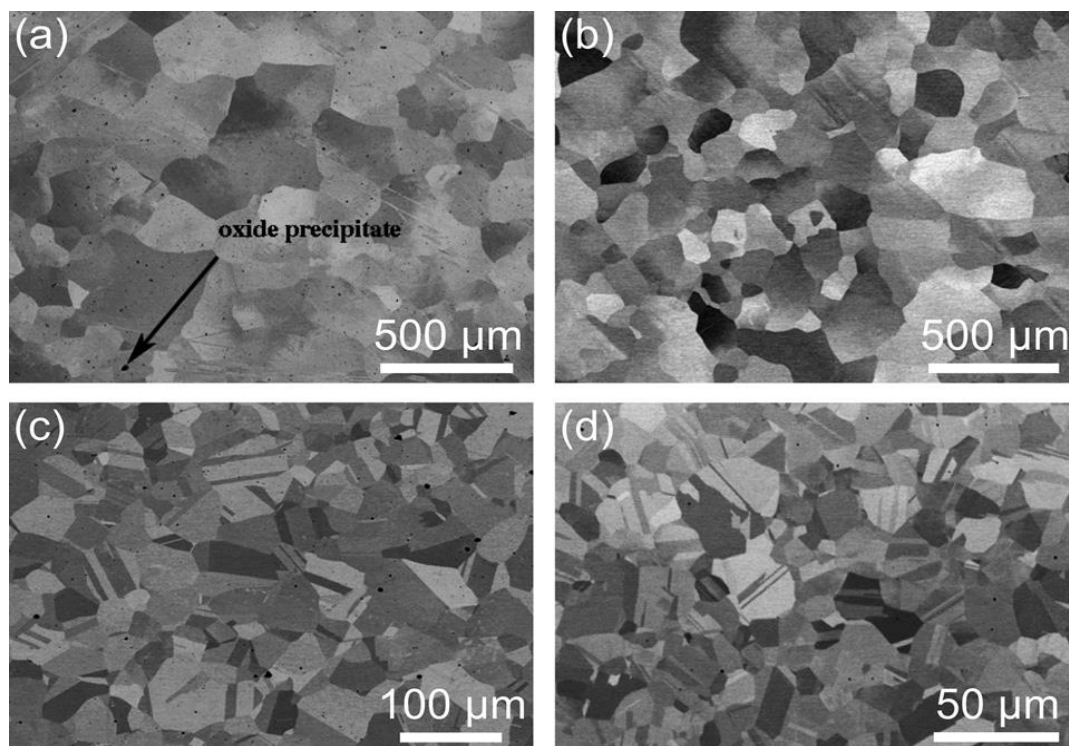
Figure 24. Backscattered electron images of (a) CrMnFeCoNi, (b) CrFeCoNi after casting and homogenization, and (c) CrMnFeCoNi, (d) CrFeCoNi after hot rolling [64].

Using SEM+EDX, in CoCrFeMnNi small oxide particles were detected, which were not present in CoCrFeNi (Figure 24 a, b). This type of oxidation is frequently reported on the surface of high manganese steels. However, X-ray diffraction did not show any peaks corresponding to these particles; their total volume was too small. Grain size after hot-rolling was of about 32 and 11 µm for quinary and quaternary alloy,

respectively (Figure 24 c, d). After annealing for 1 hour at the range of temperatures between 600 and 1000°C, only at 900°C and higher grain growth was observed. Many annealing twins were found, typical for FCC metals and alloys with low stacking fault energies.
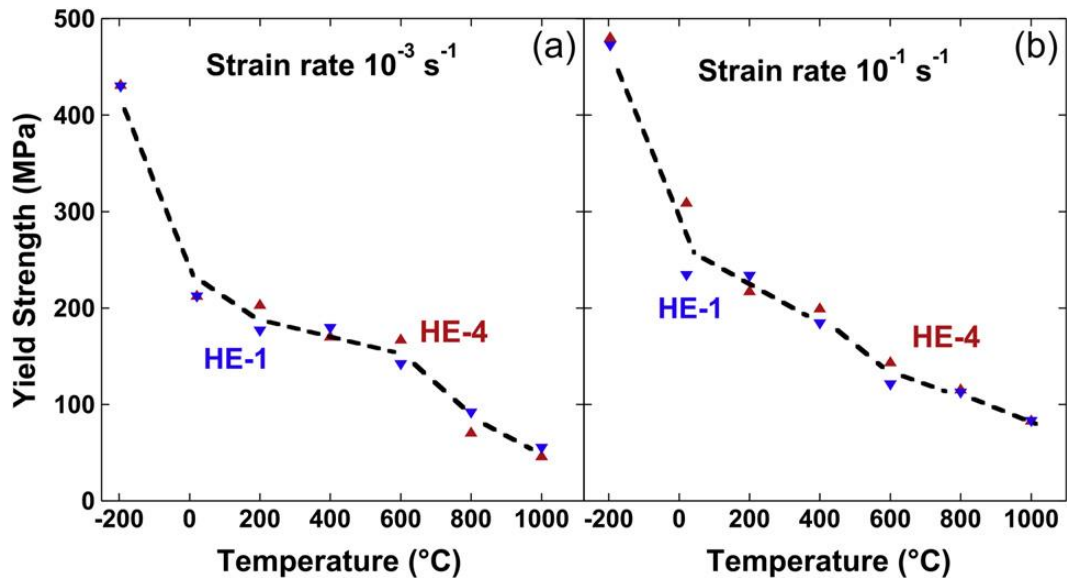
Figure 25. Temperature dependencies of the 0.2% offset yield strengths of the CrMnFeCoNi (HE-1) and CrFeCoNi (HE-4) alloys tensile tested at engineering strain rates of 10^{-3} s^{-1} (a) and 10^{-1} s^{-1} (b) [64].

The temperature dependence of the yield strength at two different strain rates is presented in Figure 25. Slope of the lines is bigger for very low and very high temperatures; these are regions of strong temperature dependence. This strong dependence at low temperatures is atypical for FCC metals, indicating stronger barriers to dislocation motion. The results for both strain rates are similar, indicating weak strain rate dependence (for higher strain rate, both alloys have lightly higher strengths). The ultimate tensile strengths and yield strengths of both alloys were compared; the difference of these two values shows the work hardening (for similar elongation). At low temperatures it is high (the difference between UTS and YS is the biggest) and it decreases with the temperature. Both values show strong temperature dependence. The ductility is not increasing with decreasing yield strength, but

inversely – it decreases from 60% at liquid nitrogen temperature to 35% at 600°C. High work hardening and ductility at low temperatures are suggested to be caused by a deformation-induced nanoscale twinning [64].

Otto et al. [66] have investigated the influence of temperature and microstructure on tensile properties of the CoCrFeMnNi. The ingots were cold-rolled and then annealed for one hour at three different temperatures (1073, 1273 and 1423K) to obtain recrystallized structures with different grain sizes (4.4, 50 and 155 μm, respectively). After annealing, high density of twins was found. Before tensile tests, all the samples were analyzed with TEM and the grains were found to be largely dislocation-free.
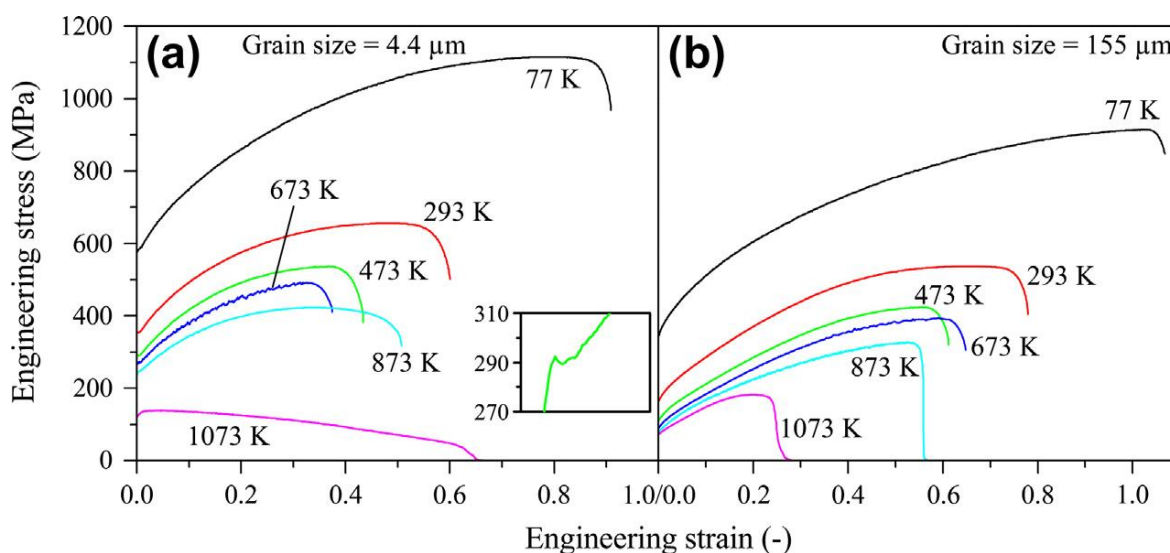
Figure 26. Representative engineering stress–strain curves of the CoCrFeMnNi with different grain size: a) 4.4 μm and b) 155 μm [66].

In Figure 26 the stress-strain curves after tensile tests at different temperatures for two different grain sizes are presented. For the samples with the finest grains and for temperatures higher then 473K a small load drop after a yield point is observed (the inset in Figure 26 a). For bigger grains this phenomenon does not occur. The highest strength and elongation to fracture are obtained at the lowest temperature. Increasing temperature results in decline of these properties.
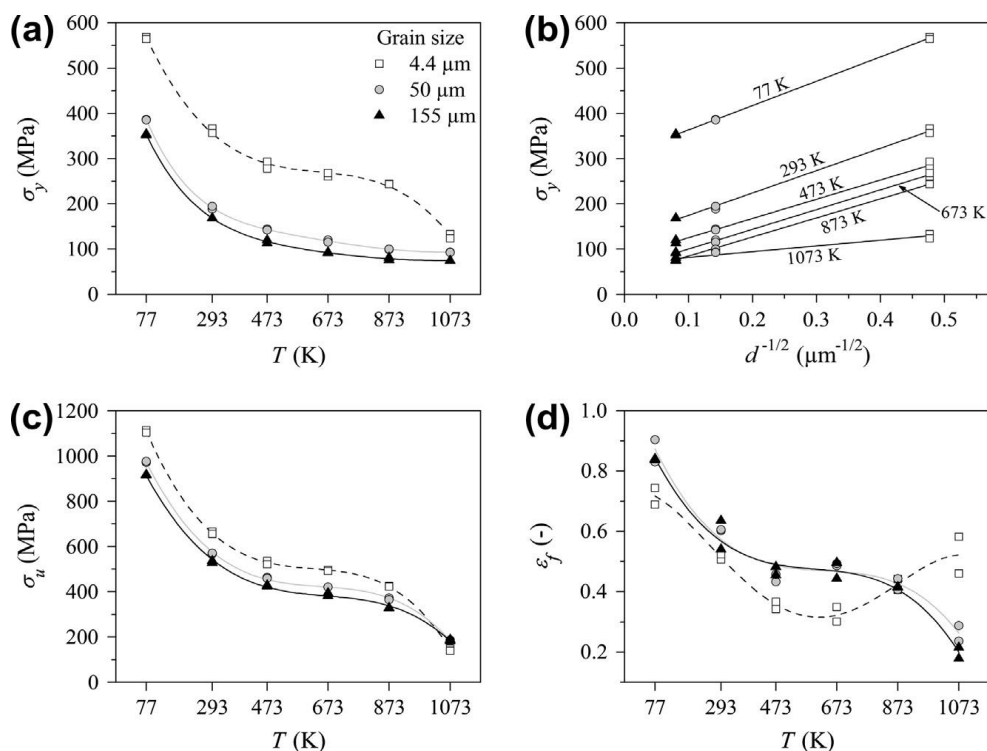
Figure 27. Temperature and grain size dependence of (a, b) 0.2% offset yield stress, (c) ultimate tensile strength and (d) elongation to fracture for the CoCrFeMnNi alloy [66].

In Figure 27 effects of grain size on different properties are shown. For the smallest grain size, the yield strength is the highest and the elongation is the lowest (except 1073K temperature). Both yield strength and elongation increase with decreasing temperature. In the graph (b) the Hall-Petch law was applied and the dynamic Hall-Petch effect was observed, involving extra interfaces in grains introduced by twinning during deformation. The authors presented also that the work hardening for fine-grained material is lower than for two others, for which it is identical. The temperature dependence of work hardening was similar for all the samples.

Different deformation modes at room and cryogenic temperatures were confirmed by Gludovatz et al. [52]. Here again the CoCrFeMnNi reveals higher yield strength and ductility at 77K than at 200K and 293K (Figure 28), in contrary to many other conventional materials. At 77K deformation induced nanotwinning was observed in addition to planar slip, contributing to high ductility, work hardening and damage resistance. Fracture toughness at room temperature shows value of 217 MPa/m² and,

surprisingly and in contrary to austenitic stainless steels, remains constant with decreasing temperature (221 and 219 MPa/m² at 200K and 77K, respectively). These values were associated with observed fracture surfaces (not shown here), where fully ductile fractured structure was found. During deformation at low temperature no martensitic transformation was observed.
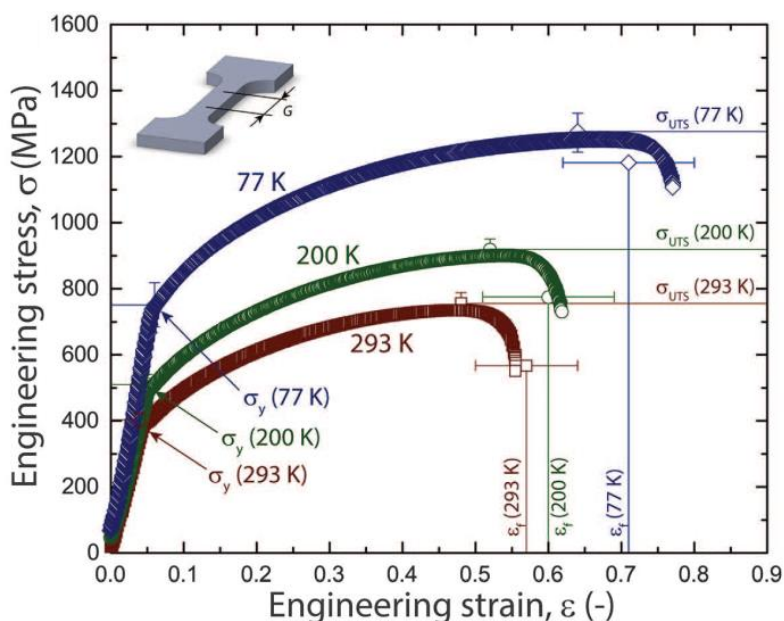
Figure 28. Tensile stress-strain curves at different temperatures [52]**.**

In a different work Otto et al. [67] were working on the cold-rolled CoCrFeMnNi and its microstructural evolution after heat treatment. Recrystallization, grain growth and twins in annealed specimens were studied, in function of different parameters. In Figure 29, hardness values for different rolling reductions and annealing temperatures are shown. These values are increasing with deformation due to higher dislocation density and grain size reduction; for a thickness reduction of 21% the hardness is about half of that of 96% (from 222 to 418 HV). What is significant, the hardness increases for annealing in 400-500°C (about 10-18%); the reason was not clarified. For 600°C and higher temperatures, hardness decreases rapidly and reaches the lowest value at final temperature (1000°C) due to recrystallization and grain growth. For 96, 92 and 84% reductions, full recrystallization was obtained after 1 hour annealing at 800°C. For 61

and 41% it was 900°C, and for 21% - 1000°C. The grains were equiaxed and many annealing twins were observed. The grain size was of about 4 – 5 µm after recrystallization for reductions between 61 and 96%. For lower reductions and temperature above 800°C, grains were larger. EBSD results showed that after one hour annealing at 800-900°C, the number of twins increased with thickness reduction. For 84% and higher reduction, more than 50% of all boundaries are twin boundaries. The twin density is proportional to the grain size, what is explained by a connection between formation of new twins and microstructural length scales. In fact, twin boundary fraction depends only on the grain size (and not on annealing parameters such as time and temperature).
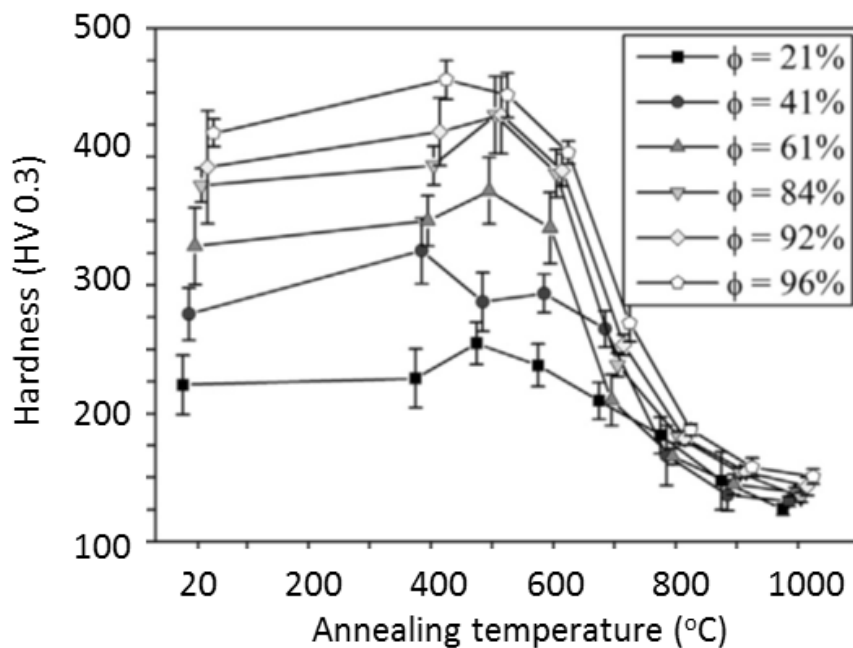
Figure 29. Vickers hardness after 1-h anneals at various temperatures for samples subjected to different thickness reductions by cold rolling [67]**.**

Dynamic recrystallization and high temperature deformation behavior of the CoCrFeMnNi were studied by Stepanov et al. [68], who performed compression tests at 600-1100°C with a true strain of about 1.4. Discontinuous dynamic transformation, with necklace formation of new grains, was observed (Figure 30 a). Corresponding BF

TEM images (Figure 30 b) revealed grains and subgrains of ~200nm, many of them dislocation-free or with only few dislocations.
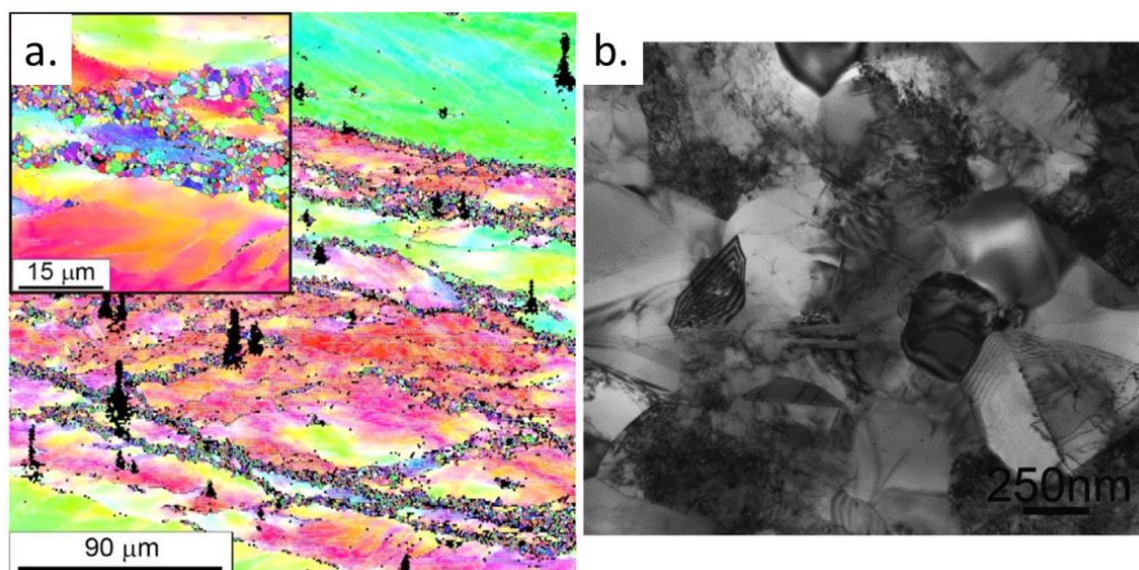
Figure 30. a) EBSD IPF map of CoCrFeMnNi after hot compression at 700°C and b) corresponding BF TEM image [68].

The alloy showed different mechanical behavior and the activation energy below and above 800°C, which is a transition temperature between high and low strength due do evolution of the structure. Obtained microstructures are typical for materials where discontinuous dynamic recrystallization (dDRX) occurs [69]–[71] and agrees with low stacking fault energy of the CoCrFeMnNi. The dDRX occurs commonly in materials with low to medium SFE values [72].

With its remarkable mechanical properties, the CoCrFeMnNi HEA may replace many other conventional materials. These properties must be studied in particular at low and high temperatures, where the stacking fault energy and thus the mechanisms of deformation change. The phenomena of plastic deformation and solid solution strengthening have not been fully understood yet and need to be characterized more accurately.

1.5.3. The influence of crystal defects on the mechanical properties

1. <u>Stacking fault energy</u>

Understanding crystalline defect behavior in HEAs is crucial for explaining their unusual mechanical properties. One of the factors influencing this behavior is stacking fault energy (SFE), a material parameter which affects its mechanism of deformation and depends on temperature and chemical composition. Materials with low SFE are keener to deform by twinning because dissociation of dislocations is easier. Wide stacking fault results in more difficult climb and cross-slip of dislocations - the work hardening rate will be increased. SFE is an important parameter for ultra-fine grained (UFG) and nanomaterials. These materials attract attention of engineers due to their high strength, but usually low ductility may be a problem. However, Zhu et al. [73] proved in their work that it is possible to optimize both mechanical properties by activating different mechanisms of deformation. For certain structure of nano-grained (NG) copper (orange points in Figure 31) both high ductility and yield strength were obtained.
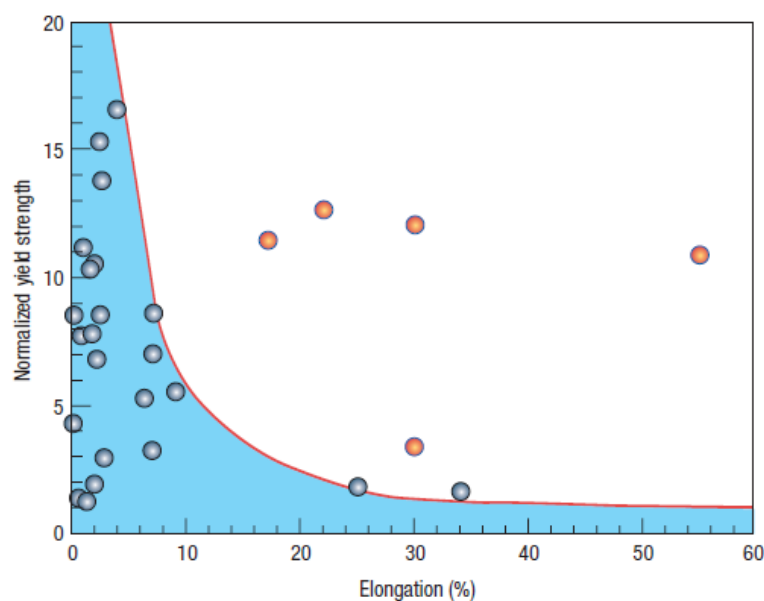
Figure 31. Normalized yield strength versus percentage elongation (ductility) for nanostructured metals [73].

Finding an optimum value of SFE can result in both high ductility and strength. These phenomena were examined for different type of alloys, i.e. Cu alloys [74] where lowering SFE leaded to the change of the mechanisms of plastic deformation from dislocation-dominated to twin-dominated. According to the authors, smaller SFE leads to grain refinement and creation of stacking faults and twins (Figure 32).
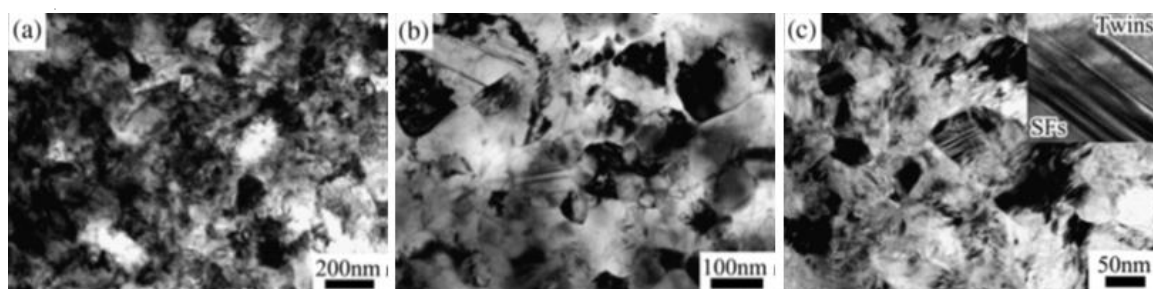
Figure 32. Typical microstructures of NS metals for (a) pure Cu, (b) Cu–5Al and (c) Cu–16Al; the microstructures of Cu–2.3Al and Cu–8Al were similar to Cu and Cu–16Al, respectively, and are not shown [74].

Regarding mechanical properties (Figure 33), addition of aluminium to copper results in increase of yield strength but only for UFG/NG materials obtained by severe plastic deformation techniques (ECAP - equal channel angular pressing; DPD – dynamic plastic deformation; HPT – high pressure torsion). For coarse-grained materials yield strength remains on the same level. Apparently this strengthening must be due to other factors than simple alloying; in this case it is grain refining related to lower SFE for materials with higher content of Al. Obviously the nature of processing is also an important factor (since curves for all three processes are not the same).

Figure 33. The relationship between the YS and Al content for Cu and Cu–Al alloys before (CG) and after processing by HPT, ECAP [12,22] (An et al., unpublished results) and DPD [74].

Attempts to find a relation between properties of alloys and their SFE

were done not only for binary alloys but also for steels, i.e. Fe-Mn-C austenitic alloys. Based on a variation of Gibbs free energy, Allain et al. [75] proposed a model for evaluation of SFE. The Gibbs energy is calculated here for each element during the austenite to martensite transformation. In these high manganese steels mechanisms of plastic deformation change with decreasing SFE, from perfect and partial dislocation gliding, through gliding and martensitic transformation to twinning. The results were confirmed by tensile tests with different parameters (yield strength, work hardening rate, elongation) at different temperatures. TEM analysis also showed different structures for samples deformed at different temperatures. Especially, after deformation at 293K (low SFE) twins were found.

Based on the same thermochemical model, Dumay et al. [76] investigated influence of addition elements (Cu, Cr, Al, Si) on SFE and mechanical properties of the same alloy (Fe-Mn-C). Selected elements change 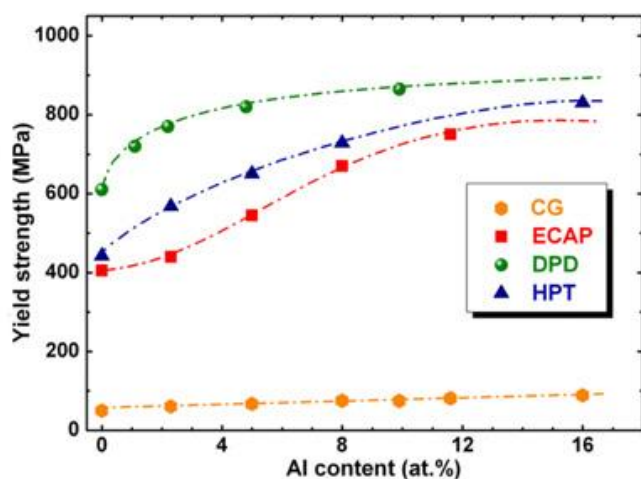SFE in different ways (Figure 34). Copper and aluminium increase SFE, while chromium decreases it. The effect of silicon is more complicated. These results were in agreement with experimental studies.
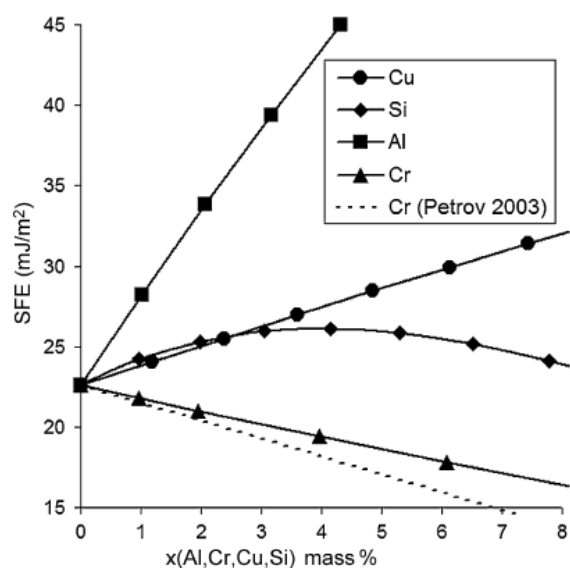
Figure 34. Predicted influence of alloying elements on the SFE of the Fe22Mn0.6C reference [76]**.**

The CoCrFeMnNi HEA is much more complex than conventional materials, though first publications on the stacking fault energy in this composition are available. Zaddach et al. [77] quantified SFE of alloys from Co-Cr-Fe-Mn-Ni family (with different proportions between elements) at room temperature by combination of an experimental approach and *ab initio* calculation methods (Table 3). SFE between different compositions varies strongly depending on the ratio of chromium and nickel. Decreasing nickel

concentration (known for its medium SFE [78]) results in reducing SFE, while the same effect is achieved with increasing chromium concentration. This leads to different mechanisms of plastic deformation and therefore changed mechanical properties. The authors suggest that in the case of equiatomic CoCrFeMnNi HEA, it should be relatively easy to improve its properties (strength, ductility) by simply changing ratios between elements.

Table 3. SFE of non-equiatomic HEAs [77]. **Green/red numbers correspond to a significant increase/decrease of the amount of the element.**

Alloy	SFE [mJ/m²]
Ni26Fe20-Cr14Co20Mn20	57.7
Ni23Fe20-Cr17Co20Mn20	19.7
Ni14Fe20-Cr26Co20Mn20	3.5
Ni14Fe21.5Cr21.5Co21.5Mn21.5	7.7

Huang et al. [79] proved that there is a close correlation between stacking fault energy and temperature (and thus modes of plastic deformation) in the equiatomic CoCrFeMnNi. SFE obtained at low temperature using *ab initio* calculations is ~3.4 mJ/m² (Figure 35 a) which is a very small value. With temperature this energy is increasing up to ~21 mJ/m² (room temperature) and then is growing with a lower slope. Presented results show that temperature has a strong influence on SFE, especially below room temperature. SFE can be divided into three parts: chemical, magnetic and strain part. Each part reacts differently to temperature. Chemical and magnetic parts strongly depend on temperature (Figure 35 b). The former depends on it almost linearly and the latter increases up to ~300K and then stays almost constant. A highest contribution to magnetic part comes mainly from Fe and Mn (these two elements have the highest average magnetic moments). With thermal lattice expansion this difference decreases. Strain part decreases slowly with temperature (also due to lattice expansion). These results are in agreement with work of Gludovatz et al. [80], where they show a transition from slip dislocation deformation to nanotwinning at low temperatures in

CoCrFeMnNi HEA. It means that for this alloy TWIP (twinning induced plasticity) effect occurs below a certain value of SFE and depends on temperature.
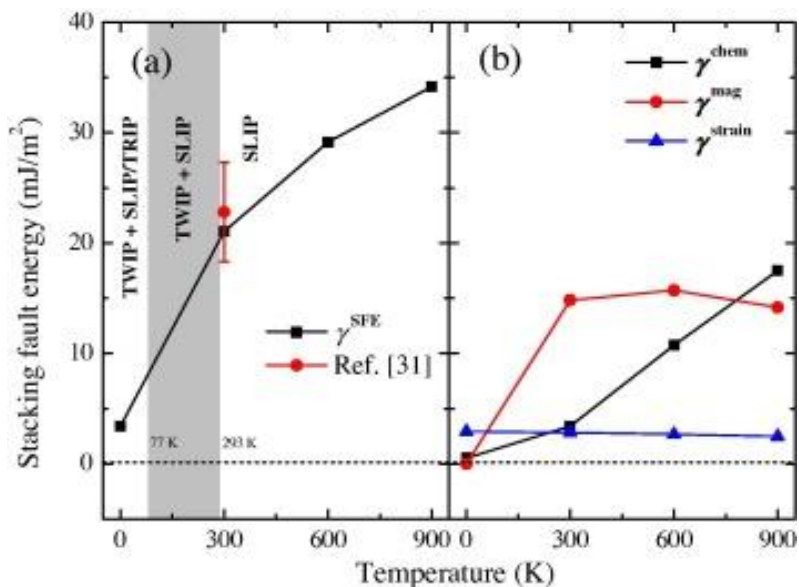
Figure 35. Theoretical stacking fault energy of FeCrCoNiMn high entropy alloy [79].

In summary, the properties of the CoCrFeMnNi HEA, which are already exceptional comparing to other conventional materials, can be modified by changing stacking fault energy value. This should be possible to obtain by composition modifications, since different elements influence SFE in various ways. Changing the SFE results in different mechanisms of plastic deformation and thus modifies such properties as strength and ductility [81]. Nevertheless appropriate ratios between elements must be preserved to avoid formation of new phases, especially brittle σ phase. For this reason, a series of thermodynamic calculations and simulations should be combined with composition changes to stay in a single phase regime. One of the tools that help in materials design is Thermo-Calc, already widely used in high entropy alloys optimization [82]–[85].

2. Dislocation structures

In materials with a face-centered cubic crystal structure, Burgers vector of the lowest energy dislocation is $\frac{1}{2}a[\bar{1}10]$. Another possible Burgers vector $a[100]$ is rarely observed due to much higher value of $\boldsymbol{b}^2$. The slip planes for $\frac{1}{2}a[\bar{1}10]$ Burgers vector are from {111} family of planes. In FCC metals, these perfect dislocations can dissociate into two Shockley partial dislocations:

$$\frac{1}{2}a[\bar{1}10] \rightarrow \frac{1}{6}a[\bar{2}11] + \frac{1}{6}a[\bar{1}2\bar{1}]$$

Two partial dislocations with Burgers vector of <112> type are glissile in the (111) plane. Dissociation into Frank partial dislocations is possible as well but less frequent. When Shockley dislocations repel each other, a stacking fault between them is created and its width depends on attractive force and thus stacking fault energy (larger the width, lower the SFE):

$$d = \frac{Gb^2 f(\theta_1,\theta_2)}{\pi(2\gamma_{SF}-\tau b|\sin\theta_2-\sin\theta_1|)}, f(\theta_1,\theta_2) = \cos\theta_1\cos\theta_2\frac{\sin\theta_1\sin\theta_2}{1-v}$$

where d is the equilibrium spacing between two straight parallel partial dislocations under zero stress, G is the shear modulus, , θ_1, θ_2 are the angles of the Burgers vector of partials with the line vector of the perfect dislocation, τ is the shear stress component, γ_{SF} is the stacking fault energy and v is Poisson's ratio [86]. Partials are then two separate dislocations connected by an intrinsic stacking fault. They can glide on the same planes as perfect dislocations, creating stacking faults (SFs) visible as "ribbons" in transmission electron microscope. These SFs are at the origin of deformation twinning, resulted from SF thickening. Since cross-slip of partials is more difficult in materials with low SFE (where recombining into a perfect screw dislocation to change the glide plane requires more energy), it may result in more brittle behavior. Here however, different factor contributing to ductility must be taken into account.

In the CoCrFeMnNi, considered as a single-phased FCC material, character of dislocations and mechanisms of plastic deformation have been studied in different conditions. After low strains (~2%) and at temperatures between 77K and 873K [66], deformation in this alloy occurs by planar glide of dislocations of <110> type in (111) planes, confirmed as well in other works [87]. This behavior is typical for FCC alloys [88]–[90]. Pile-ups of dislocations in (111) planes were stable after unloading, indicating high friction stress and no interaction with grain boundaries. Stacking-fault-coupled partial dislocations were present even after small plastic deformation, implying easy formation of Shockley partial dislocations at both low and elevated temperatures (Figure 36). For cryogenic temperatures, nanoscale twinning was observed as an additional deformation mode.
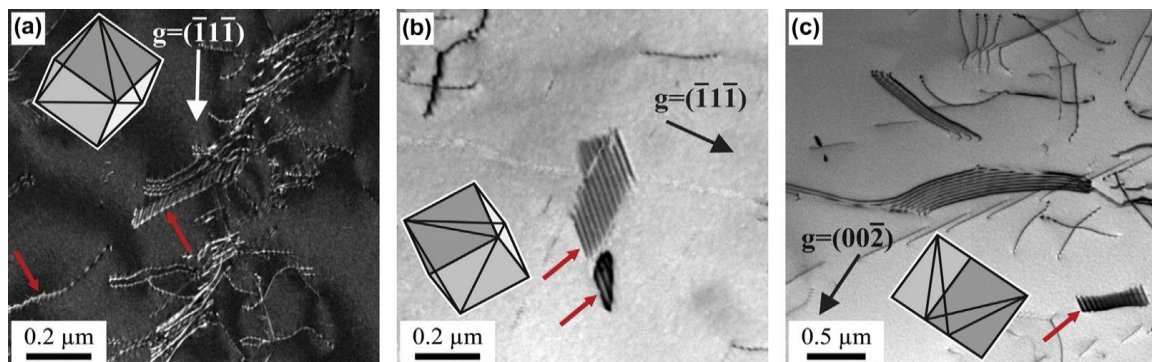
Figure 36. Stacking faults (marked by red arrows) in the coarse-grained CoCrFeMnNi alloy (grain size 155 lm) after plastic deformations of (a) 2.4% at 77 K (WBDF – Weak Beam Dark Field), (b) 2.1% at 293 K (BF – Bright Field) and (c) 1.7% at 873 K (BF) [66]**.**
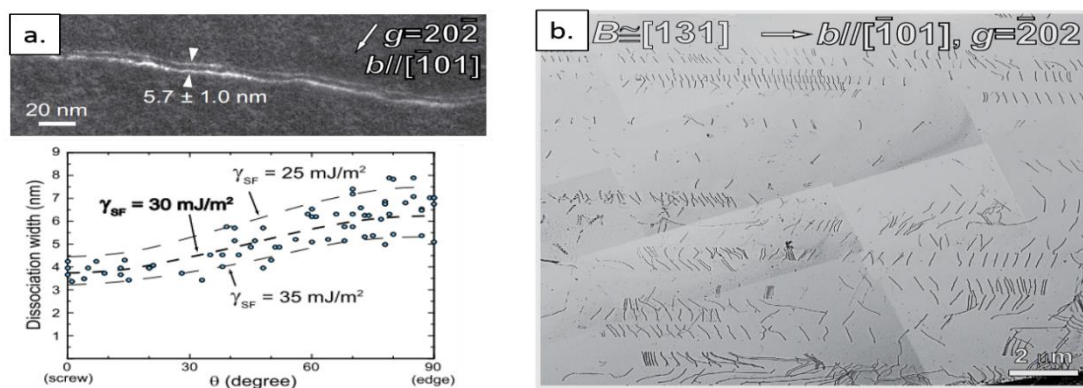
Figure 37. a) Weak-beam TEM image of a dislocation after deformation at 77K and calculated values of stacking fault energy; b) dislocations in the same sample [91]**.**
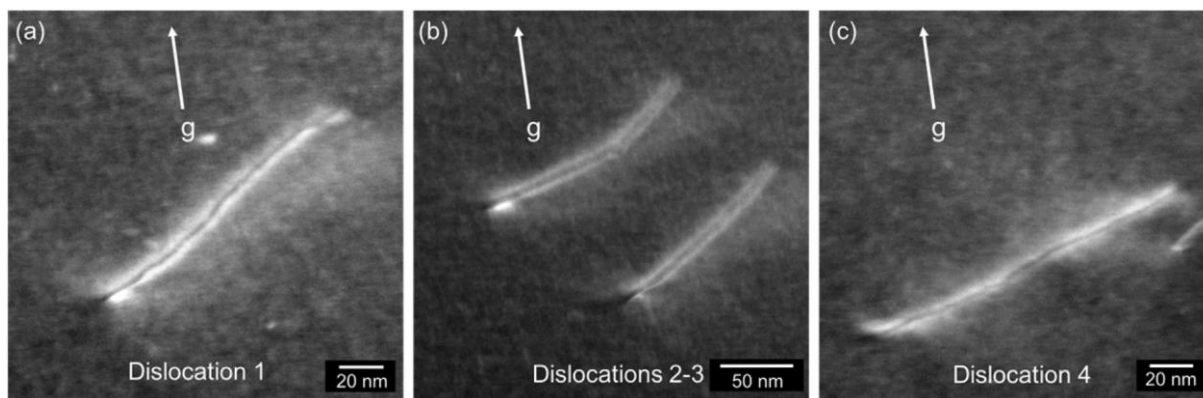
Figure 38. Weak beam g-3g $\overline{1}31$ dark field TEM images of dislocations in CoCrFeMnNi [87].

After deformation at liquid nitrogen temperature, the structures of dislocations are typical for FCC metals, with the Burgers vector parallel to <110> (Figure 37 b) [91]. The lack of preferred orientation of dislocations must be due to little anisotropy in mobility of edge and screw segments. Observed difficulties in cross-slip indicate low stacking fault energy. Dissociation of dislocations (Figure 37 a) was also confirmed, with a separation distance of few nanometers. Based on these distances, stacking fault energy was calculated, giving results of 30 ± 5 mJ/m^2, lower than in pure FCC metals (for example, for pure nickel it is 125 mJ/m^2). Moreover, high resolution EDX analysis at nanoscale does not provide any evidence of a significant segregation of any element around dislocations cores, confirming a solid solution character of the alloy. Since the solute configurations in the CoCrFeMnNi are very complex, the dislocation dissociation distances can vary [87] (Figure 38), and the stacking fault energy as well. Thus, in case of HEAs the SFE should not be considered as a global variable but rather as a local property. In pure FCC metals, very small variations of dissociation distances between dislocations were found, i.e. in pure nickel, copper and aluminium [92]–[94]. The average variation of this distance is about ±0.45 nm, an order of magnitude less than in the CoCrFeMnNi (±3.4 nm). The effect of solute concentration on dislocation dissociation was modeled in three different systems: pure Ni, Ni-2at.%Fe and concentrated Ni-20at.%Fe-26at.%Cr alloy. The latter was chosen as the closest to the CoCrFeMnNi since quinary interatomic potential for this system is not known. In two

former materials, the distance between partial dislocations remains constant along the dislocation line. This is not the case of the concentrated alloy, where this distance varies suggesting different SFE at the local scale. When the local SFE contribution was calculated, its variation becomes more significant with alloy's complexity (Figure 39). It can explain large dissociation distances observed in the CoCrFeMnNi. What is more, in the concentrated material SFE achieve negative values, signifying creation of more favorable local bounding environment.
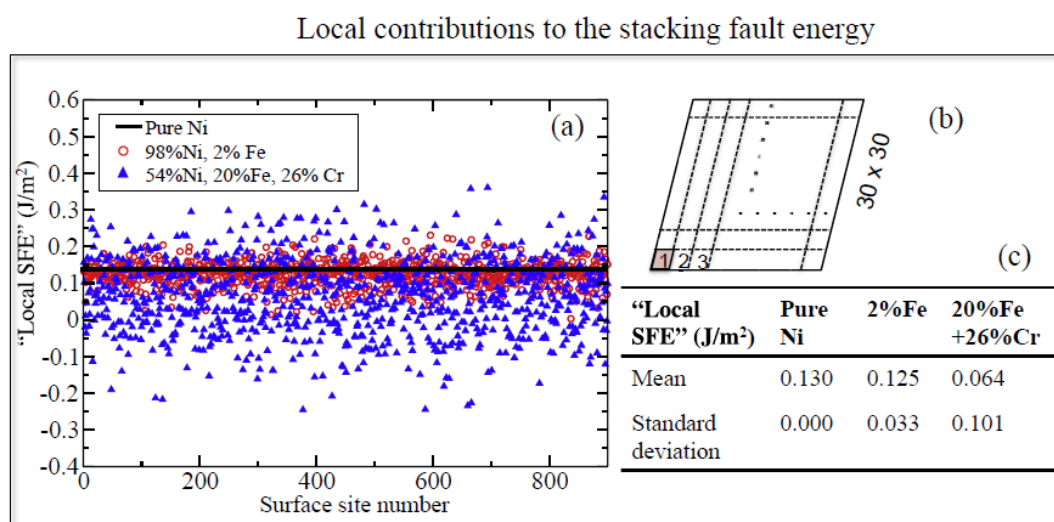
Figure 39. Variations in the "local stacking fault energy" values in the concentrated Ni-20 at%Fe-26 at%Cr alloy compared to pure Ni and the dilute Ni-2at%Fe alloy. The cross section of the 30x30x30 supercell used in the calculations is shown in (b) [87].

In situ TEM was used to study dislocation behavior in the CoCrFeMnNi in the vicinity of a crack [81]. Various mechanisms of deformation were identified. At the beginning of the deformation, only Shockley partial dislocations $\frac{1}{6}$<112> were active. Numerous stacking faults were observed as well, indicating low SFE. Partial dislocations can interact, forming additional obstacles to dislocation motion, such as stacking fault parallelepipeds (Figure 40). These are formed when slip on multiple {111} planes is activated and dislocations intersect, which can lead to important strain hardening. Yet, partial dislocations can easily move but at the same time they create barriers for other

dislocations. The authors suggest that this kind of defects could be at the origin of both ductility and strength, observed in equiatomic Cantor alloy.
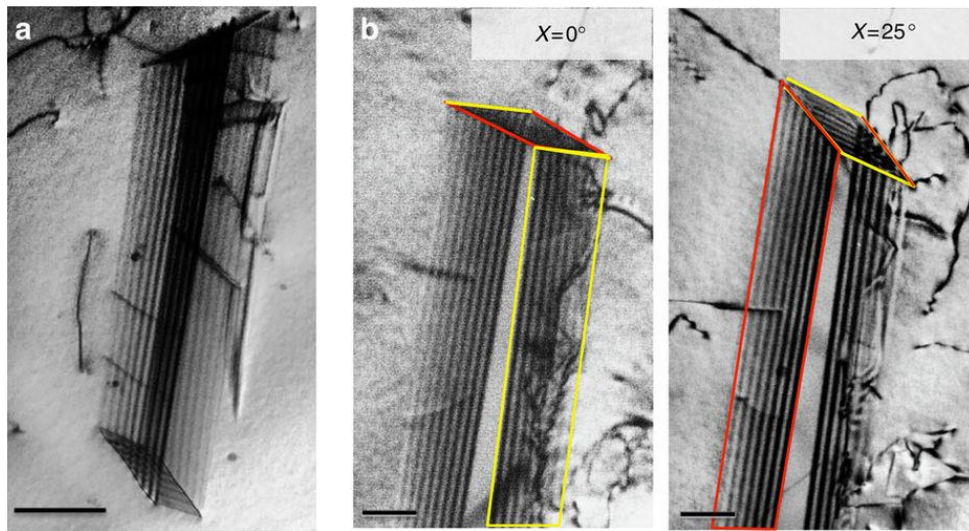
Figure 40. TEM image of the stacking-fault parallelepiped structure in CoCrFeMnNi [81]**.**

Surprisingly, while increasing applied stress, perfect dislocations become active. Their movement, however, was found difficult with a very low velocity, in contrary to partials (Figure 41 a). It leads to a planar slip of segments of pile-ups of dislocations, moving in localized bands. Partial dislocations are blocked on these bands (Figure 41 b), forming pile-ups and leading to an important increase of material's strength. These interactions seem to be a significant part of strengthening mechanisms in the CoCrFeMnNi.
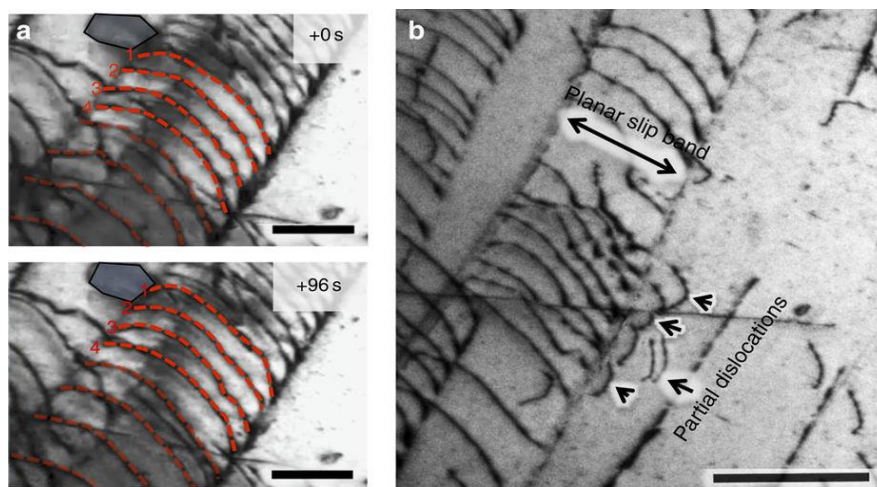
Figure 41. a) TEM images of the ½<110> dislocations; b) bright field images of blocking of partial dislocations [81]**.**

1.6. Motivations

Based on this bibliographic report, different problems will be under investigation in this work.

First, a new alloy will be developed, based on the equiatomic Cantor CoCrFeMnNi high entropy alloy. This alloy is one of the most promising among all known HEAs with a single-phased structure. The main aim is to further increase its phase stability (since decomposition is possible in certain conditions) and improve mechanical properties, especially yield strength and ductility. For this, CALPHAD and other thermodynamic calculations as well, based on bibliography and existing results, will be applied. The evaluation of microstructures and mechanical properties in different conditions will be proceeded. For example, a series of heat treatments will be conducted to verify if the higher stability of a solid stability is achieved in the new material. Later, different mechanical testing techniques will be applied in order to verify any improvements of properties, in high range from cryogenic to elevated temperatures.

A more detailed analysis of the mechanisms of deformation and phenomena such as recovery and recrystallization will be done. The possibilities of short range ordering, as well as the influence of Peierls energy and stacking fault energy will be taken into account. Dislocation behavior merits special attention since it strongly differs from classical face-centered cubic materials.

2. Methods and procedures

Thermo-Calc calculations – general aspects of the software

In this work, Thermo-Calc (TC) software (based on CALculation of PHAse Diagrams approach, CALPHAD) was used for high entropy alloys design and comparison with phases obtained experimentally. Thermo-Calc is a thermodynamic calculation software which allows predicting phase stability and transformations, phase fractions and their compositions, but also calculating the driving force of forming a phase. CALPHAD methodology works as follows: first experimental information, empirical rules and fundamental theories are gathered as a part of a critical evaluation leading to model description of each phase. Models for the thermodynamic properties of each phase are then calculated. In the next step, higher order systems are extrapolated and databases for model parameters are established [95]. The databases describe the Gibbs energy of individual phases of a system as a function of temperature, composition and pressure. The descriptions of the sub-systems can be combined to obtain multicomponent systems. The software uses thermodynamic databases to calculate i.e. stable and meta-stable heterogeneous phase equilibria, amounts of phases and their compositions, etc. Nowadays, several databases are available for different materials: steels and Fe-alloys, nickel-base superalloys, etc., as well as high entropy alloys [95]. In this work, TCFE5 (Fe base), TTNI8 (Ni base) and HEA1 (high entropy alloys database) were used.

At the beginning of this project, the optimization of new alloys was launched using TCFE5 and TTNI8 databases since no database for multicomponent alloys have existed at this time (September 2013). Recently, high entropy alloys database HEA1 was developed by TC company, within a 20-element framework. Thermo-Calc allows predicting multicomponent systems from binary and ternary subsystems. New database contains nearly all stable phases in assessed binaries and ternaries (163

solution and intermetallic phases are modelled). All the calculations for multicomponent systems are an extrapolation based on these binary and ternary alloys and may be visualized as pseudo-binary diagrams. For the systems with several elements it would be very difficult to create all phase diagrams to see the influence of each element. Because of a big number of phases in multicomponent systems, there may be no precise agreement between Thermo-Calc predictions and observations of a stable structure. Improving thermodynamic databases is needed for better results. Another challenge is to find descriptions of individual systems and phases valid over a wide range of composition. This database is still under development.

Investigated materials

In this work two compositions were chosen for investigation (Table 4): the X1 CoCrFeMnNi alloy with an equiatomic composition, taken from the literature as a reference alloy, and the novel A3S (for "Austenitic Super Stainless Steel"), with a composition optimized through thermodynamic calculations. This innovative material was patented by Anna Fraczkiewicz (France, 2014 [3]).

Table 4. Compositions of the X1 and A3S alloys (at. %).

	Co	Cr	Fe	Mn	Ni
X1	20	20	20	20	20
A3S	20	15	26	17	22

The alloys were prepared by Claude Varillon in the laboratory of the SMS Center by cold-crucible melting metals in a pod. The components are introduced one after the other. Only high purity elements were used as raw materials. Iron, chromium, nickel and cobalt have been purified in the laboratory (99.99% minimum). Manganese is purchased commercially with a purity of 99.9%.

Because as-cast metals have many defects (elemental segregation, metastable phases, non-uniform grain size, porosity), all the alloys were processed by hot forging (ingots

up to 3000 g forged at 1060°C to diameter of 12 mm with the total section reduction of about 40%) and partially by cold rolling (section reduction ~90%) to refine the microstructure and obtain balanced properties. Most of the studies were done on the forged materials.

Heat treatment

Heat treatments were performed to verify influence of the temperature on the microstructure and properties. All the heat treatments used during this thesis are listed in Table 5.

Long-time annealing (longer than 24 hours) were conducted in evacuated quartz capsules. Short-term annealing were conducted in argon atmosphere (only minor surface oxidation appeared).

Table 5. List of selected annealing temperatures and times.

Temperature [°C]	Time
500	1/2/3 weeks, 100/200/300 days
600	48h, 1 month
700	4h
800	8h
1000	2h
1100	10min, 5/14/48h, 2 weeks

Surface preparation

For microscopic investigations, all the samples were first manually grinded with SiC papers (grade P240 to P1200) and then polished up to 1μm. To reveal the microstructure for optical microscopy, specimens were etched either with oxalic acid, $C_2H_2O_4$ (in case of the X1), or a mixture of $HF+HNO_3+C_3H_8O_3$ in 1:1:1 proportions (in case of the A3S). For phase identification, specimens were electro-polished. The

electrolyte used here is a mixture of 10% perchloric acid ($HClO_4$) and ethanol (C_2H_5OH), applied at 25-35 V for 20-40 s.

Microscopy techniques

Chemical compositions were checked by two scanning electron microscopes (SEMs): JEOL 6500F and Zeiss Supra 55 VP, both equipped with energy dispersive spectrometer. Secondary electron images and backscattered electron images were taken for the surface and microstructural analysis. Electron backscatter diffraction (EBSD) measurements were made on selected metallographic cross-sections to measure grain size and grain boundary misorientations using the Zeiss SEM operated at 20 kV. The EBSD data were analyzed with the OIM Analysis software (EDAX, Mahwah, NJ, version 6.1.3). A grain was defined as an aggregate of data points that have relative misorientations higher than 2°. To reduce the number of data points (not all of the detected grains were real grains), a minimum grain size value was set (depending on specimen) and smaller results were deleted. Twins were included in these calculations.

Transmission electron microscopy (TEM) was applied to understand the mechanisms of deformation. Microstructures were observed with Philips CM200 TEM operated at 200 kV. Samples for TEM analysis were prepared by conventional twinjet electro-polishing of mechanically pre-thinned to 100 µm foils, in a 10% perchloric acid in ethanol ($10\%HClO_4 + C_2H_5OH$) at the 16 V potential and temperatures between 0 and -5^oC.

TEM *in situ* tensile tests and heating experiments were done at CEMES in Toulouse, France by courtesy of Dr. Marc Legros. All the tests were performed within the JEOL 2010 at 200 kV. The room temperature tensile loading was applied incrementally with a Gatan single tilt straining holder. For observation of dislocations behavior at higher temperatures, samples were heated up to 900^oC.

X-ray diffraction

Crystal structures of alloys in different states were analyzed for lattice parameter determination using an X-ray diffractometer (MRD PANALYTICAL) with Cu Kα radiation operated at 40 mA and 45 kV.

To determine dislocation density evolution, a line profile analysis was performed. The experiment was carried out in transmission at beamline ID31 ESRF (European Synchrotron Radiation Facility) using an X-ray energy of 70 keV ($\lambda = 1.771$ Å) and beam cross section of size 0.6×1.0 mm^2. Diffraction patterns were recorded with a 2048×2048 pixel CCD, mounted perpendicular to the incident X-ray beam. The sample was cut to a length of 10mm with the cross-sectional dimension of 1×1mm. It was mounted perpendicular to the incident of X-ray beam and rotated from 0° to 180° with 2° step size. During each of these steps diffraction patterns were recorded.

Atom Probe Tomography

Atom Probe Tomography (APT) was applied in Université de Rouen at the laboratory Groupe de Physique des Matériaux GPM by courtesy of Prof. Xavier Sauvage. These experiments were done to search for any fluctuations of composition at nanoscale. APT is highly accurate for structural analysis due to its almost atomic spatial resolution. This technique allows three-dimensional mapping (3D mapping) of the constituent elements with high detection sensitivity and near-atomic resolution and gives a chemical information on a nanometer scale [96]. Samples were cut with a low-speed precision saw to get very thin pieces - blanks of 20 x 0.3 x 0.3 mm^3. In the next step sharp needles are obtained. It can be done by electropolishing at room temperature in two steps: first using 30% perchloric acid $HClO_4$ in glacial acetic acid CH_3COOH and then 2% perchloric acid $HClO_4$ in monobutoethanol ($C_{15}H_{25}ClN_2O_2$) with voltage of 10-25 V DC.

Mechanical tests

Hardness measurements

Vickers microhardness measurements were conducted using Matsuzawa Microhardness Tester MX T70 under a load of 200 g. At least eight equally spaced indents were made and the average values were calculated.

Vickers hardness measurements were conducted under a load of 10 kg. At least five equally spaced indents were made and the average values were calculated.

Tensile and compression tests

For forged materials, tensile tests were performed on threated-headed specimens (L = 50 mm, $\varnothing$ = 4 mm, Figure 42 a) at room temperature in air with a strain rate of 10^{-3} s^{-1} and at low temperature on threated-headed specimens (L = 80 mm, $\varnothing$ = 5 mm, Figure 42 b) in liquid nitrogen (-130°C) with a strain rate of 10^{-3} s^{-1} in a screw-driven Schenck test rig. For rolled materials, tensile tests were performed on flat samples (L = 34 mm, a = 8mm, b = 1 mm, Figure 42 c). An extensometer was used to measure engineering strain.
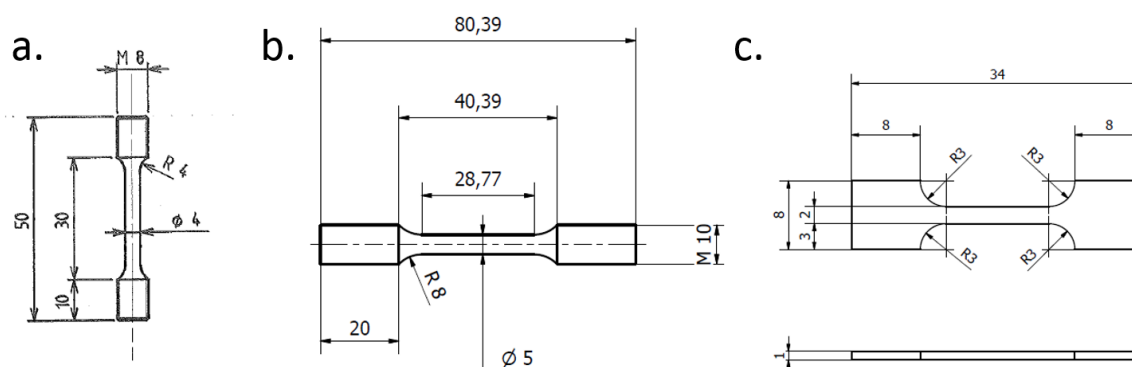

Figure 42. Schematic of tensile tests specimens: a) for room temperature, b) for cryogenic temperature, c) of rolled material.

Compression tests were performed on cylindrical samples (H= 9 mm, φ = 7 mm) at temperatures 20 - 500°C with a strain rate of 10^{-1} s^{-1} and 10^{-3} s^{-1} in the Schenck

compression machine. For dynamic recrystallization experiments, tests were done on the same machine at 750 - 900°C with a strain rate of 10^{-1} s^{-1}. Prior to deformation, specimens were held at temperature for 5 minutes and then deformed to 50% reduction in height (which corresponds to a true strain of approximately 0.7).

The yield strength was calculated as of the intersection of a line constructed parallel to the elastic part of the curve and offset by a strain of 0.2% to the right.

Charpy tests

Charpy tests were conducted on V-notch type specimens (L = 55 mm, a = b = 5 mm, Figure 43) hold in liquid nitrogen for five minutes. Samples were machined from the forged material.
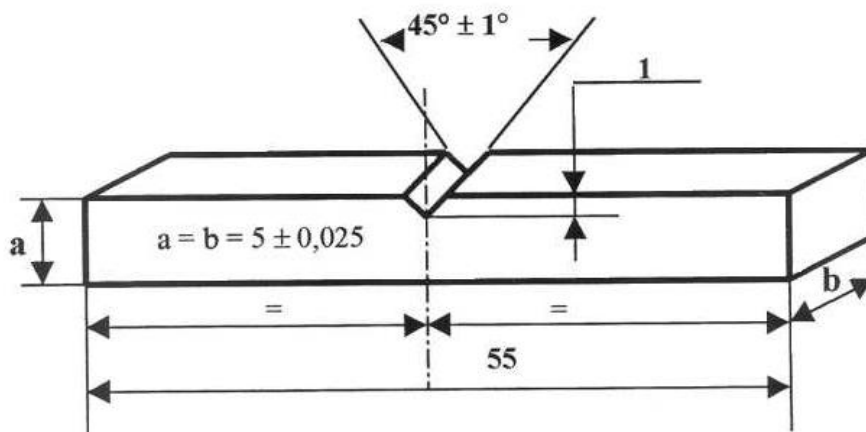

Figure 43. Schematic image of the sample for Charpy tests.

The Charpy impact toughness KCV is calculated from the formula:

$$KCV = \frac{KV}{S_0},$$

where KV is energy absorbed by rupture and S_0 is a surface of the sample in place of rupture.

3. Design of novel high entropy alloys

It was presented previously that in the large family of HEAs, equimolar CoCrFeMnNi remains among the most studied [58], [59], [63], [66], [67], [84], [97]–[102]. Even though this composition was proved to be single-phased [39], recent works [61]–[63] showed phase decomposition after different heat treatments. For this reason our approach of modification the reference material was to increase phase stability and, if possible, its mechanical properties. As was shown in Chapter 1.5.2, changing composition may influence i.e. stacking fault energy and thus should possibly effect strength and ductility of material. Additionally, other various compositions were studied as well.

In order to optimize the proportions between elements in our material, Thermo-Calc software was applied with different databases (iron, nickel and high entropy alloys databases). Fe and Ni databases were used at the beginning of this work (2013) since no database for multicomponent alloys was available. Results of both were successively studied in a critical manner and then compared with experimental outcome. Recently, a new database for high-entropy alloys was released. It allows us to compare previously obtained calculations and improve them, and then to compare with experiments as well.

3.1. Binary and ternary phase diagrams of CoCrFeMnNi

The diagrams for multi-component high entropy alloys are obtained on the basis of binary and ternary alloys by extrapolation. I.e. a five component system consists of ten binary and nine ternary diagrams (but for ten component alloy this number is much bigger - there would be 45 binaries and 120 ternaries [103]). Ten well-known binary alloys from Co-Cr-Fe-Mn-Ni system are presented here to explain obtained results (Figure 44 and Figure 45). According to the Gibbs phase rule there may be up to six phases in the equiatomic CoCrFeMnNi (X1) alloy. At room temperature the

constituent elements have different crystal structures (Table 6) and only nickel forms

an FCC structure. Still, the X1 is known as a single-phased material in most cases.
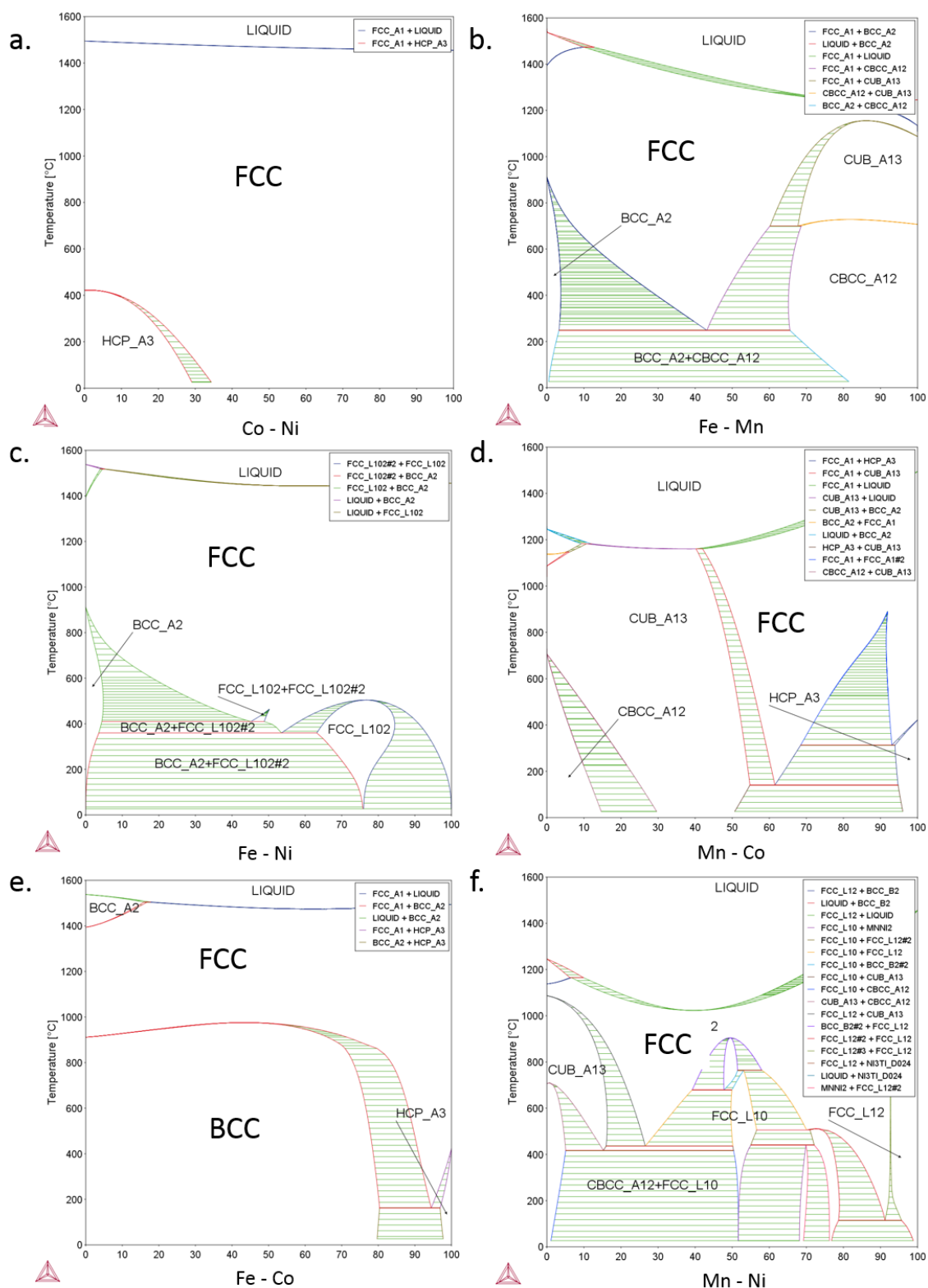
Figure 44. Binary systems of a) CoNi, b) FeMn, c) FeNi, d) MnCo, e) FeCo and f) MnNi in TCFE5 database.
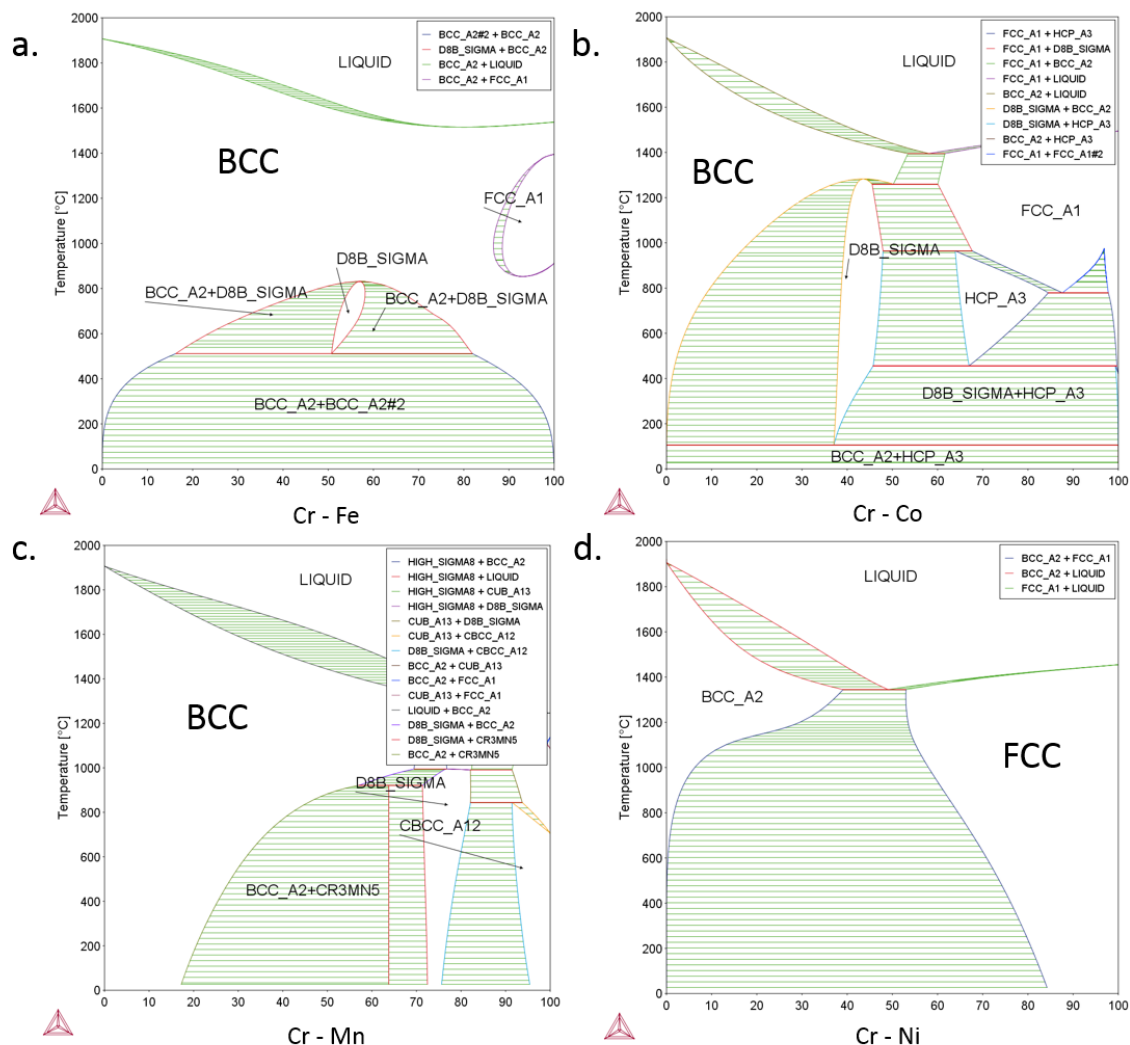
Figure 45. Binary systems of a) CrFe, b) CrCo, c) CrMn and d) CrNi, obtained with TCFE5 database.

Table 6. Crystal structures of Fe, Cr, Ni, Mn and Co at room temperature.

Element	Fe	Cr	Ni	Mn	Co
Structure	BCC	BCC	FCC	A12 (complex cubic)	HCP

In Figure 44 six binary system diagrams are presented: CoNi, FeMn, FeNi, MnCo, FeCo and MnNi. In all these systems FCC phase is either formed continuously or stable in large regions. Nickel indeed possesses an FCC structure from room temperature to the melting point (a). Cobalt has an FCC structure above 417°C to 1495°C (a). In iron, an FCC phase is stable in the range of 912-1394°C (b). In CoNi, FeNi and FeCo systems,

an FCC structure can be obtained in a wide range of temperatures and in an unrestricted atomic ratio (a, c, e). Manganese (A12 complex cubic phase up to 707°C) alloyed with other elements result in a stable FCC structure (b, d, f).

On the other hand, all diagrams involving the presence of chromium (CrFe, CrCo, CrMn and CrNi) look completely different (Figure 45). Chromium, which possesses BCC crystal structure at room temperature, stabilizes certainly BCC phase. Relatively big BCC areas are present in each case. FCC phase is either not present or not dominant and present only within a narrow temperature/composition range. Brittle σ phase is present as well in comparatively high temperature ranges in CrFe, CrCo and CrMn (Figure 45 a - c). Since chromium promotes forming a BCC and σ phase, then for a broadened FCC stability its amount probably should be decreased. Similarly in stainless steels, where chromium is known as an element decreasing the temperature range in which FCC phase exists. In conclusion, results from Figure 44 and Figure 45 confirm high possibility of obtaining FCC phase for Fe-Cr-Ni-Mn-Co composition, but the proportions between elements must be optimized.
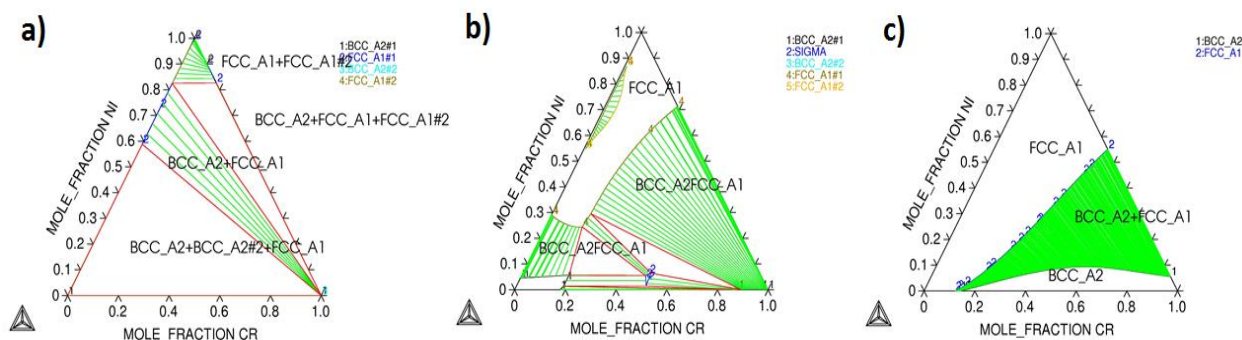
Figure 46. Isothermal ternary diagrams of Fe-Cr-Ni: a) 20°C, b) 500°C, c) 1000°C, obtained with TCFE5 database.

Further analysis of ternaries typical for austenitic stainless steels confirm these observations. In Figure 46, isothermal ternary diagrams of Fe-Cr-Ni at room temperature, 500°C and 1000°C are shown. Sigma phase appears only at 500°C for very limited area. FCC phase is present in almost each case depending on Ni amount, which is understandable because Ni is FCC phase stabilizer. The largest field of only FCC phase appears at 1000°C.

3.2. In search of a new HEA with high thermal stability

3.2.1. Thermo-Calc simulations

Optimization of a new HEA based on Cantor's equiatomic CoCrFeMnNi HEA was launched in 2013 with two databases available at this time: iron TCFE5 database and nickel TTNI8 database. Both were chosen due to high content of iron and nickel in the material and their high degree of development. Nevertheless, neither Fe nor Ni are dominant elements and thus these two different databases were compared carefully for the highest credibility. The principal aim was to increase FCC field and decrease temperatures of any possible phase transformations. The presence of σ phase, known as brittle, was eliminated. The objective was to increase, with such an approach, thermal stability of this new composition.

Figure 47. Quasi-binary Fe-Cr phase diagrams of the X1 alloy in a) iron TCFE5 and b) nickel TTNI8 database. Equiatomic composition is marked with a red dotted line.

In Figure 47, quasi-binary Fe-Cr (other elements fixed) phase diagrams of CoCrFeMnNi calculated in the TCFE5 and TTNI8 databases are presented. The highest stability of FCC single-phased region (in terms of extension of FCC domain to low temperatures) is reached for 15 at.% of chromium in both databases. Additionally

in Fe database, σ phase was predicted between 0-15 at.% Cr at room temperature. Thus, 15 at.% amount of chromium seemed reasonable for maximum FCC stability in the new composition. What is more, in stainless steels this phase is not observed when the amount of Cr is below 20 at.% [104]. Quasi-binary Fe-Ni phase diagrams (Figure 48) show a presence of σ phase between 0-18 at.% (Fe base) and 0-20 at.% (Ni base) at room temperature and above 21 and 29 at.% at higher temperatures, respectively. In case of Fe-Ni system, Ni database can be considered as more credible. Hence, in the new material 22 at.% of nickel was applied to avoid σ phase and remain in high entropy regime. Increasing amount of nickel maximize FCC stability as well. Lowering the decomposition temperature results also in slower diffusion in the multiphase area and thus higher chances of preserving a uniform structure even if it is not stable.
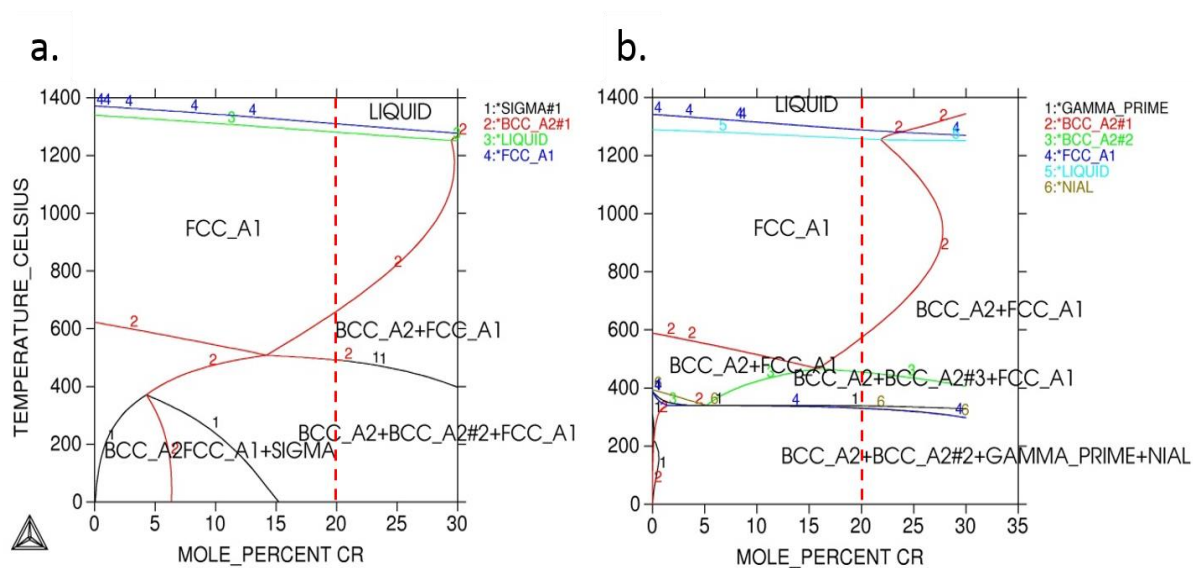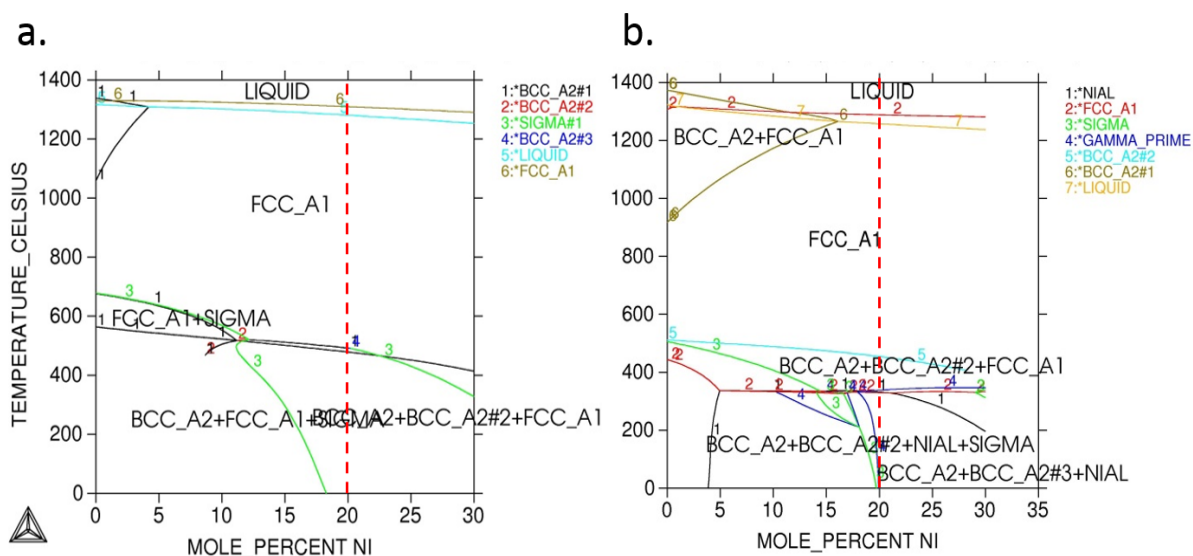

Figure 48. Quasi-binary Fe-Ni phase diagrams of the X1 alloy in a) iron TCFE5 and b) nickel TTNI8 database. Equiatomic composition is marked with a red dotted line.

Below around 600°C, the diagram becomes more complex with numerous phases. For instance, for 20% of nickel in TTNI8 base BCC_A2 rich in Fe-Co, BCC_A2#2 rich in Cr-Mn and FCC richer in Ni-Mn are predicted but no intermetallic compounds. Multiphase structures have often an effect of relatively worse physical properties. For this reason the X1 should be annealed at high temperature during processing to

stabilize FCC phase. For alloys annealed above 1000°C only single FCC phase should form, what was confirmed [102].

Since increasing the amount of Ni and decreasing that of Cr leads to larger (and thus more stable) FCC phase region without σ phase, it was decided to follow this idea to choose a new composition. Additionally, nickel is known as an FCC stabilizer. Amount of Mn was slightly increased, as it is known as an FCC stabilizer, too [105], and for improving mechanical properties. Finally, a new material, called A3S® (for Austenitic Super Stainless Steel), was designed.
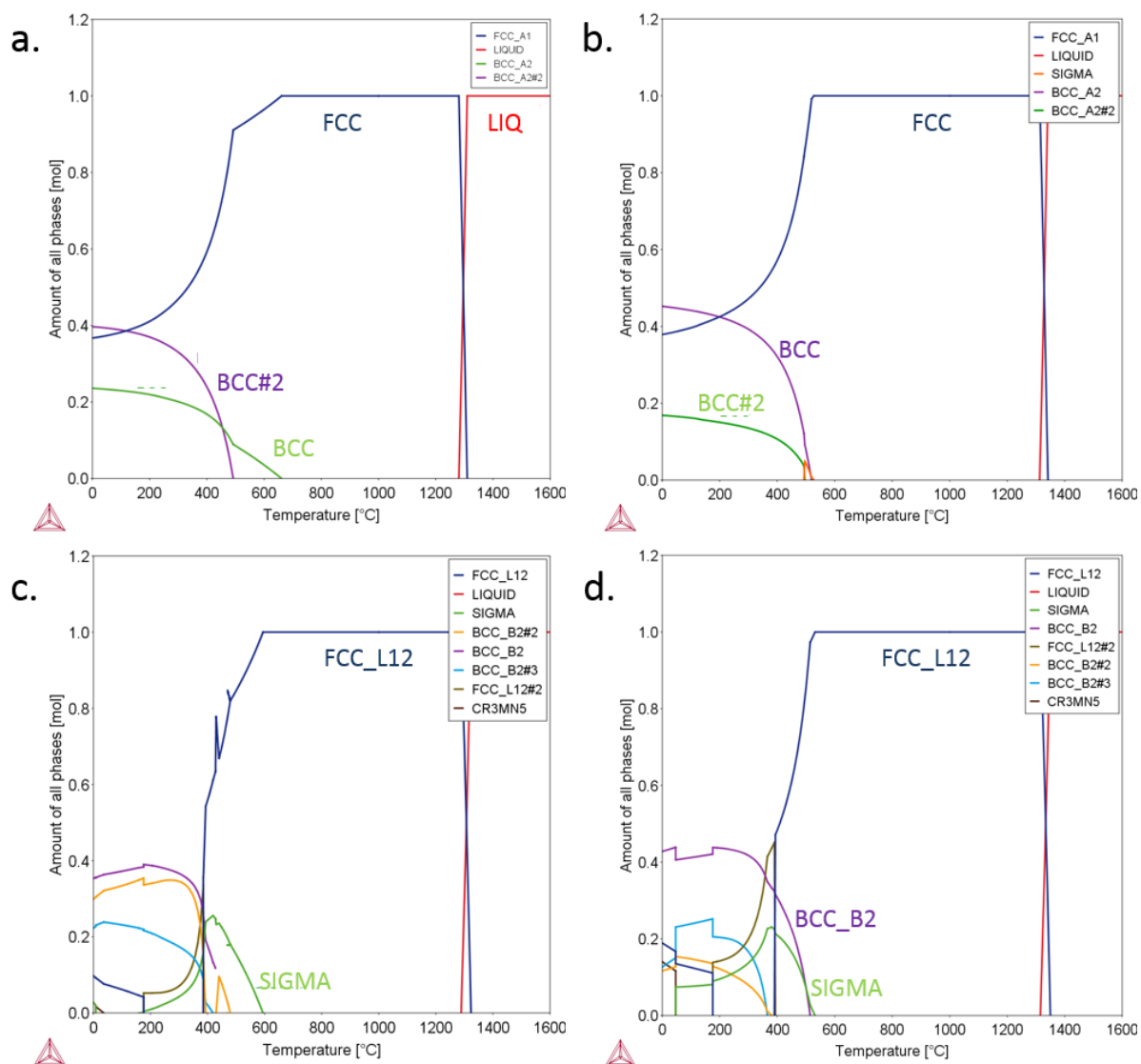

Figure 49. **Thermo-Calc diagrams of the a) X1 and b) A3S in TCFE5 database and c) X1 and d) A3S in TCHEA1 database.**

Once a new high entropy database (TCHEA1) was released by Thermo-Calc company in 2016, both new and reference materials could be compared. Calculated equilibrium phase diagrams of the X1 and A3S in two different databases (TCFE5 and TCHEA1 databases) are presented in Figure 49. In all cases, both materials solidify into one FCC phase. However, contrast between the TCFE5 (Figure 49 a, b) and the HEA1 database (Figure 49 c, d) is clearly visible. In the TCFE5 database, much less phases are predicted than in the TCHEA1 database. This is because the TCFE5 database was created principally for iron alloys with a content of iron above 50%. Nonetheless, the A3S presents higher stability of an FCC phase, even in the TCHEA1 database. Formation of a BCC phase in the A3S starts at 530°C, about 135°C lower than for the X1. In the TCHEA1 database the same tendency was observed, but here a σ phase starts forming at lower temperatures for the A3S and is stable in the multiphase region. The freezing range (difference between the liquidus and solidus) is smaller in the A3S comparing to the X1. It is desirable because for wide freezing range, voids can form in the casting and segregation of elements is stronger. Obtained stability of the FCC phase is higher since all the phase transformations occur at lower temperatures than for the X1.

On the other hand, the new database shows ordering in FCC and BCC structures by giving FCC L1$_2$ and BCC B2 phases as an outcome, which is entirely in disagreement with all previously recognized experimental results. However, in the TCHEA1 database both ordered and disordered FCC (and BCC) structures are modelled as one phase and labelled equivalently. For each specific composition, the site fractions of each elements in sublattices should be compared to distinguish between ordered and disordered phase. Still, the TCHEA1 database must undergo further development. It is established on nickel superalloys database but in HEAs none of the elements is a dominant one. Since there is no main component in the composition, choosing an appropriate database is essential for HEA's optimization and comparing different databases should be mandatory.

3.2.2. Application of basic thermodynamic parameters to predict formation of single solid solution in the A3S

As it was mentioned before, Thermo-Calc can be only a very first approach in finding compositions of high entropy alloys and, due to their high complexity, is not always fully credible. In Chapter 1.3 it was shown that there are few parameters which were successfully used to identify single-phased materials and that are helpful in prediction of the composition range of solid solution phase formation in HEAs. They should be applied as the next step to confirm the results obtained in Thermo-Calc. The values needed for calculation are presented in Table 7.

Table 7. Atomic radius, Pauling electronegativity, Vacancy Electron Concentration and melting temperature of the constituent elements of the examined alloys [106].

Element	Fe	Cr	Ni	Co	Mn
Atomic radius, Å	1.26	1.28	1.24	1.25	1.27
Allen electronegativity	1.80	1.65	1.88	1.84	1.75
VEC	8	6	10	9	7
Melting temperature, K	1808	2130	1726	1768	1517

In the calculation, following formulas were used:

$$\Delta r = \sqrt{\sum_{i=1}^{n} c_i (1 - r_i/\bar{r})^2}$$

$$\Delta S_{mix} = -R\sum_{i=1}^{n} c_i \ln c_i$$

$$\Delta H_{mix} = \sum_{i=1,i\neq j}^{n} c_i c_j \Gamma_{ij}$$

$$\Omega = \frac{T_m \Delta S_{mix}}{\Delta H_{mix}}$$

$$\triangle \chi = \sqrt{\sum_{i=1}^{n} c_i (1 - \frac{\chi_i}{\chi_a})^2}$$

$$\Delta VEC = \sqrt{\sum_{i=1}^{n} c_i (1 - \frac{VEC_i}{VEC_a})^2}$$

The melting temperature of alloys was calculated using the rule of mixtures:

$$T_M = \sum c_i \, (T_M)_i$$

Table 8. Mixing enthalpy for different systems [107]**.**

System	FeCr	FeNi	FeMn	FeCo	CrNi	CrMn	CrCo	NiMn	NiCo	MnCo
Γ_{ij}[kJ/mol]	-1.5	-1.6	0.2	-0.6	-6.7	2.1	-4.5	-8.2	-0.2	-5.2

Table 9. Calculated values of r, $\triangle$r, ΔS_{mix}, ΔH_{mix}, Ω, χ, $\triangle\chi$, VEC and T_M of the representative examined alloys.

Alloy	$\bar{r}$	Δr	ΔS_{mix} [J/K·mol]	ΔH_{mix} [kJ/mol]	Ω	χ_a	$\Delta\chi$	VEC	T_M [K]
X1	1.26	0.0112	13.38	-4.16	5.77	1.78	4.46	8	1790
A3S	1.258	0.0107	13.23	-3.87	6.09	1.79	4.13	8.17	1780

The results of calculations with used parameters are presented in Table 8 and

Table 9. The atomic size polydispersity, Δr, for both the X1 and the A3S-1 is smaller than 0.066, which indicates that a solid solution can form. The entropy of mixing is high (higher for the X1). The enthalpy of mixing is in the proper range of -11.6 – 3.2 kJ/mol. To form high entropy stabilized solid solution phases, Ω parameter should be bigger than 1.1. It is the case for both alloys but with a parameter of 6.09 in the A3S compared to 5.77 for the X1, thus the former should possess a solid solution phase with higher thermal stability. To avoid intermetallic compounds, the difference of electronegativity $\Delta\chi$ should be smaller than 6 and here it is indeed below this value. Yet, this parameter is larger for the X1. To promote FCC phase, VEC should be larger than 8 and for both alloys this condition is fulfilled. In conclusion, both alloys should form solid solutions (with a small chance of forming intermetallic compounds), based only on theoretical considerations.

3.3. In search of other promising HEA compositions

A series of different than "standard" (Fe-Cr-Mn-Ni-Co) elements were applied in Thermo-Calc: Al, Cu, Ti, Nb, W, V, Zr, Ta, etc. Mainly five-elements systems were investigated. In most of these cases, obtained systems were very complicated due to small solubility of elements, presence of many phases (including brittle σ phase), small areas of a single cubic phase and high temperatures of transition. For example, in case of CoCuFeNiV (Figure 50 a) there are no areas of a single solid solution. Other compositions seemed more promising (i.e. AlNbTaTiV, Figure 50 b, where a spinodal decomposition may be possible) but were not chosen due to the presence of σ phase, more complicated processing route or price of elements.

Many other simulations were also made which are not shown here to find the most promising compositions for other (new) alloys. Two equiatomic HEAs, CoCuFeMnNi and AlCrFeMnNi, have especially attracted our attention due to large areas with only simple solid solutions (BCC, FCC) and low temperatures of phase transformation (Figure 51).
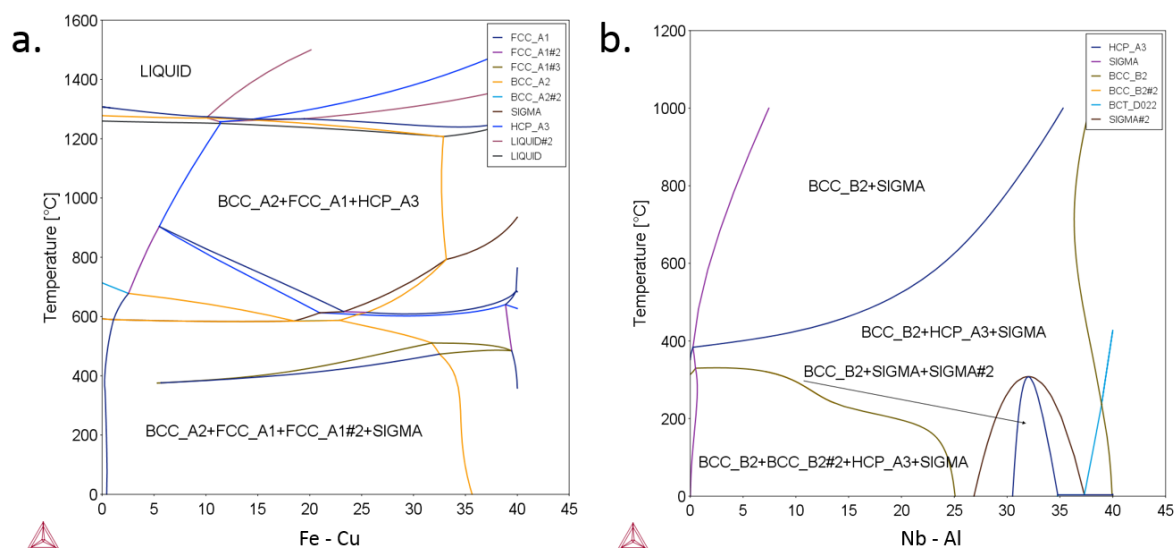

Figure 50. Quasi-binary phase diagrams of a) CoCuFeNiV (TCFE5 database) and b) AlNbTaTiV (TTNI8 database).

Both alloys were briefly examined in the frame of MINES intern projects. Microstructure and mechanical properties of the CoCuFeMnNi were investigated by Xiangyu Li supervised by Michał Mróz [108].
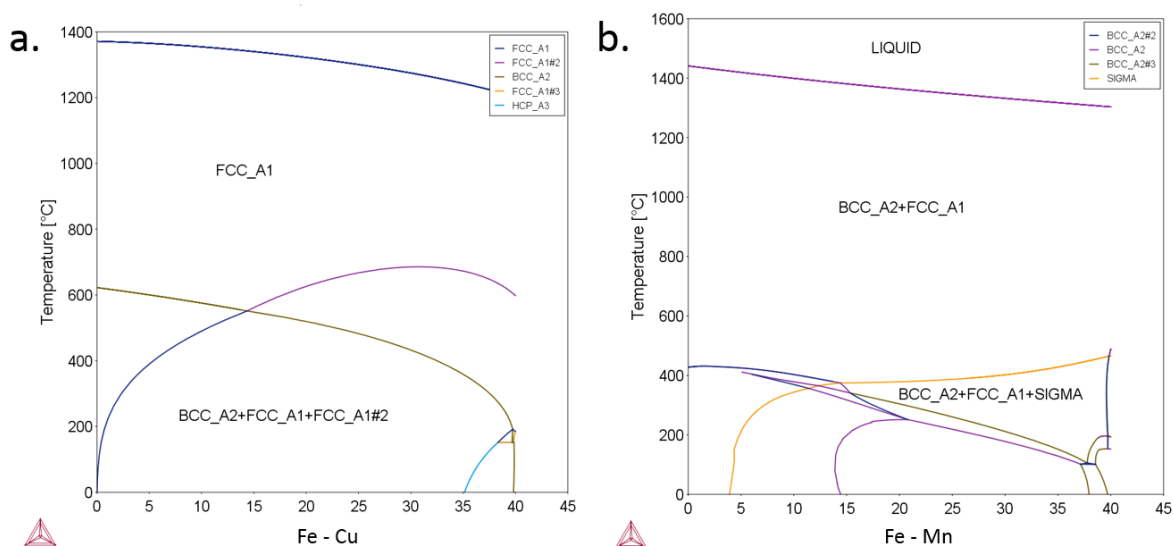

Figure 51. Quasi-binary phase diagrams of a) CoCuFeMnNi and b) AlCrFeMnNi (TCFE5 database).

The CoCuFeMnNi alloy was studied in as-cast and heat treated states. Its single-phased structure at 1000°C/24h confirms the TCFE5 predictions. At 600°C/24h, in accordance to TC calculation, the alloy decomposes (Figure 52) to a Fe-Co-rich BCC phase (a = 2.8 Å) and two FCC phases with nearby lattice parameters (a = 3.66 and a = 3.63 Å) (identified with XRD, not shown here). A large field of a solid solution exists above this temperature. Mechanical properties of the studied alloy (Figure 53 a) are interesting at low/intermediate temperatures, with a YS value of about 400 MPa between RT and 400°C and a satisfactory compressive behavior in these temperatures. Unfortunately, above 500°C the presence of eutectic mixture in grain boundaries leads to destruction of samples through intergranular liquefaction (Figure 54). Due to the presence of low-melting eutectic, no hot thermomechanical treatment was possible. This type of microstructure is in disagreement with the results obtained in Thermo-Calc. Yet, the alloy was successfully cold rolled (90% section reduction). Further optimization of the CoCuFeMnNi family of HEAs requires a modification of its

chemical composition to avoid the presence of low-melting eutectic. At this stage of work a continuation of the project was not confirmed.
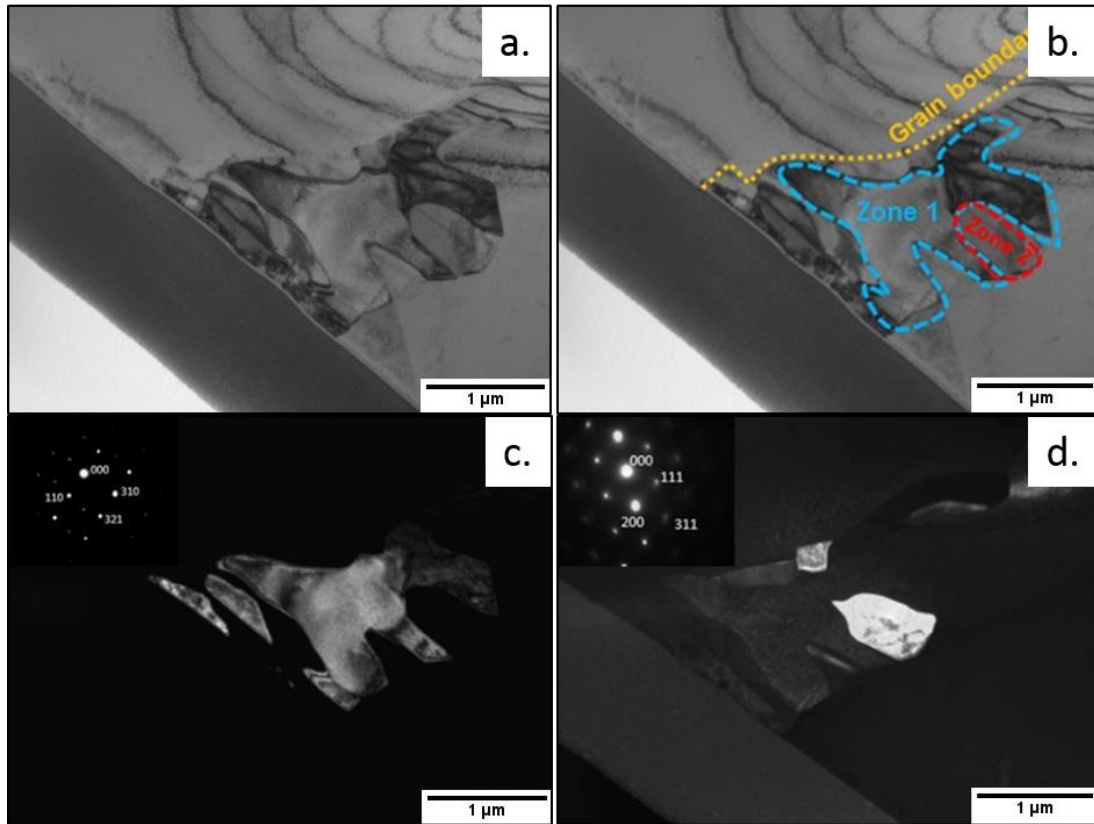

Figure 52. Intergranular region of CoCuFeMnNi annealed 500°C/24h; TEM observations. a) bright field (BF) image; b) identification of studied areas; c) dark field image; "zone 1", BCC phase, zone axis [001]; d) dark field image; "zone 2", FCC phase, zone axis [0-11] [108].
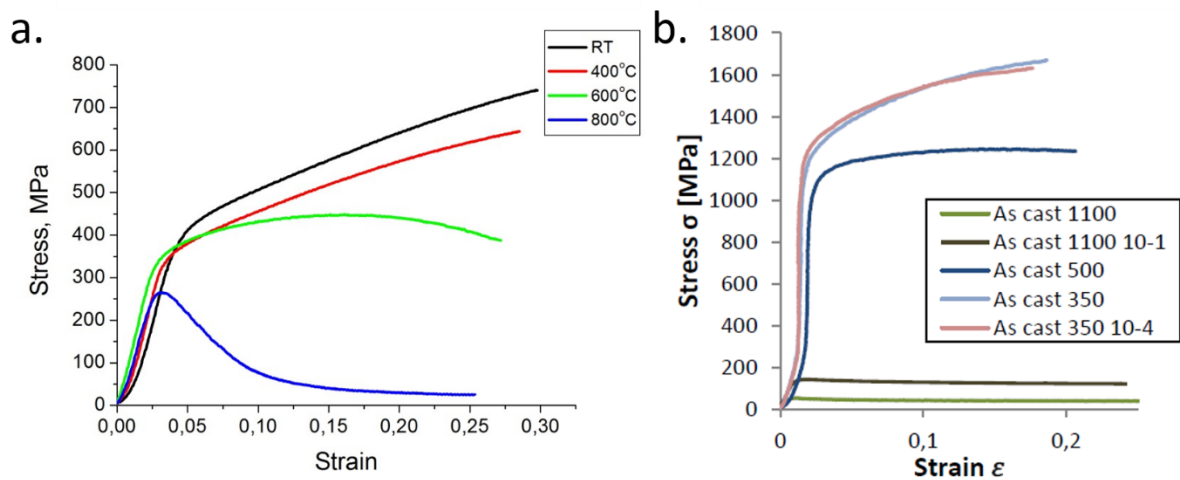

Figure 53. Stress-strain compression curves for equiatomic as-cast a) CoCuFeMnNi [108] **and b) AlCrFeMnNi** [109] **tested at different temperatures (1100, 500, 350°C) and strain rates (10^{-1} and 10^{-4} s^{-1}).**
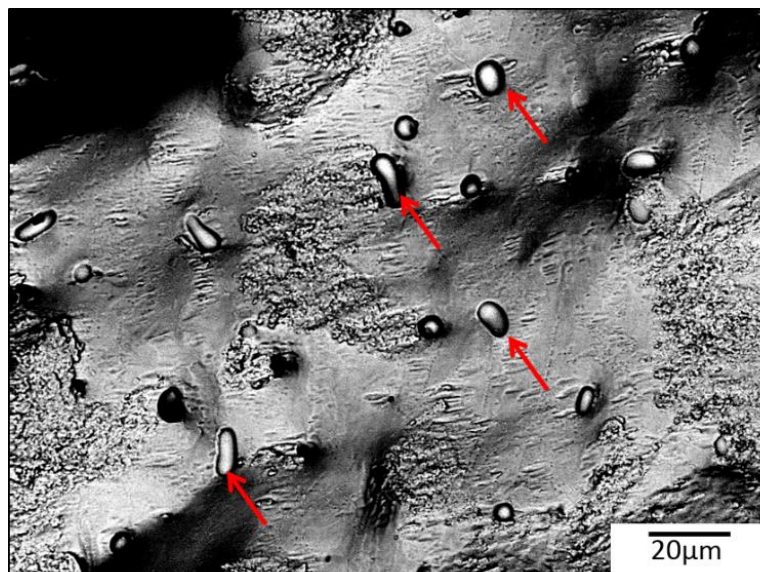
Figure 54. Liquefaction traces (marked with red arrows) in the CoCuFeMnNi compressed at 800°C.

Another HEA, studied by MINES student Guanzhong He and supervised by Julia Olszewska, was AlCrFeMnNi where Co was replaced by Al [109]. HEAs with aluminum are known for easy forming BCC phase since Al is a BCC stabilizing element [110], [111]. The composition was investigated in Thermo-Calc using TCFE5 and TCAL2 (aluminium) databases, showing important differences between both. Finally, obtained microstructures were in agreement with the aluminum database. Compression tests showed two different modes of deformation: at high temperatures (1100°C) the material was easily deformed with very low yield strength of about 100 MPa; at lower temperatures (<500°C) the

Figure 55. EDX chemical analysis of the AlCrFeMnNi [109]**.**

yield strength is above 1000 MPa (Figure 53 b).

Microstructural observations revealed strong decomposition of both dendritic and interdendritic areas in the as-cast state (Figure 55). Following, TEM was used t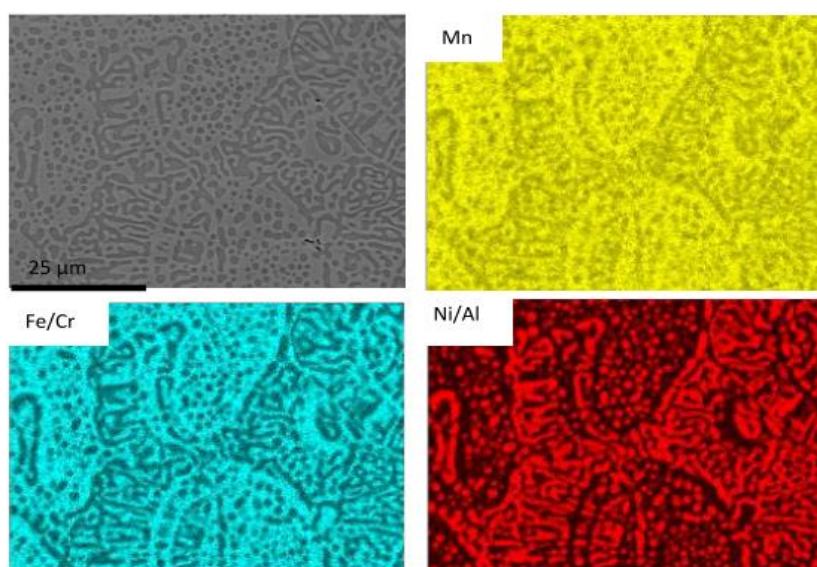o identify the exact composition and crystal structure of all phases (Figure 56). Dendrites are composed of B2 ordered NiAl rich

cubes embedded in a BCC FeCr rich solid solution and interdendrites have a lamellar structure of alternately ordered B2 NiAl rich phase and BCC FeCr rich solid solution. Even though this alloy was brittle at room temperature, it possesses interesting mechanical properties at higher temperatures, such as very high yield strength (over 1000 MPa up to 500°C).
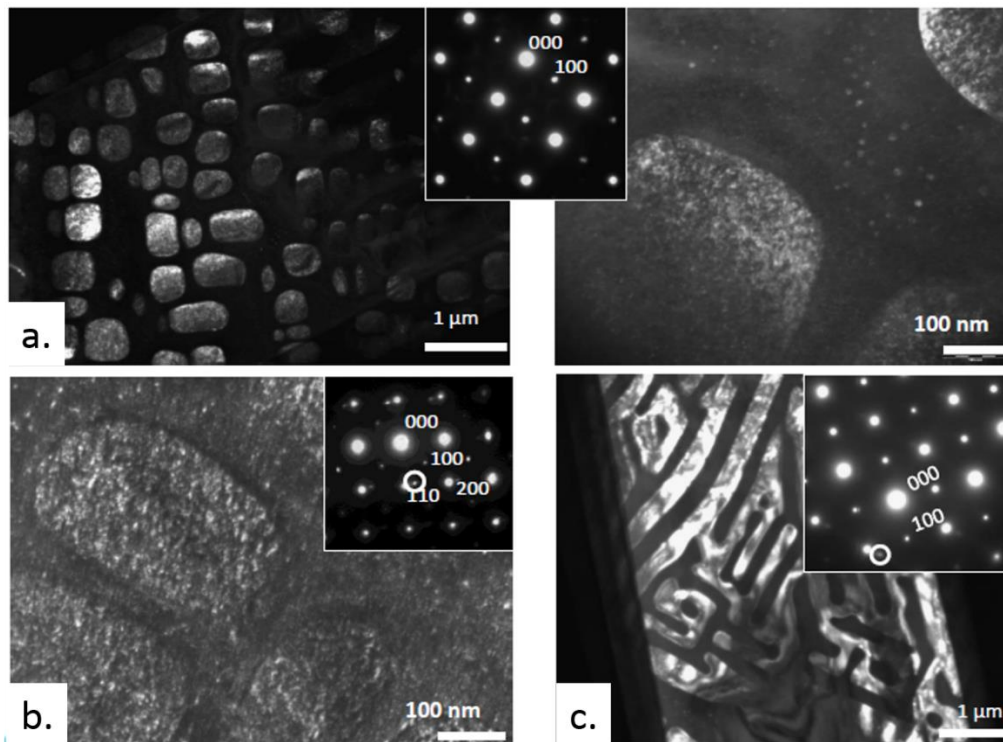
Figure 56. a) Dark Field (DF) TEM image of dendrite zone in <110> Zone Axis (ZA) and illuminated with (100) spot; b) DF in <100> and illuminated (110) spot; c) DF of interdendritic zone in <100> ZA and illuminated with (100) spot [109].

Still, these high entropy alloys will not be studied further in this work. The main focus is given to the novel composition A3S and its comparison with Cantor's equiatomic CoCrFeMnNi. Microstructures of the two materials as well as mechanical properties and influence of low and high temperature will be investigated.

4. Evaluation of the A3S in comparison with the X1: microstructures and mechanical properties

4.1.1. Microstructural characterization

Investigated equiatomic X1 and novel A3S were produced by cold crucible melting. Starting from the as-cast state, dendritic structure is visible in light microscope image in both alloys (Figure 57, here shown only for the A3S), which is a typical solidification morphology. Investigated samples consist of large grains up to 1 mm in length. EDX (Energy Dispersive X-Ray Analysis) mappings (not shown here) for the two as-cast materials reveal that the composition is not homogeneous; dendrite arms with different composition are present, with manganese segregating to interdendritic regions. For other elements this effect is weaker. Dendritic segregation in as-cast state is in line with previous studies [2], [57], [58]. For every element, especially for manganese, areas of segregation have been observed. These areas usually follow grain boundaries and dendrite arms. No traces of precipitations or secondary phases were found; small black point in the Figure 57 are a result of etching.

Figure 57. Optical image of the A3S in as-cast state. A dendritic structure can be seen. Dark spots are a result of etching.

Because the as-cast state can be only a very first indication of the characteristics of an alloy, subsequent experiments were carried out on the materials after forming (hot forged and cold rolled; conditions given in Chapter 2). The EDX mapping of the as-forged state for the

A3S confirms homogenized composition without any traces of dendrites or segregation of any of elements (Figure 58).
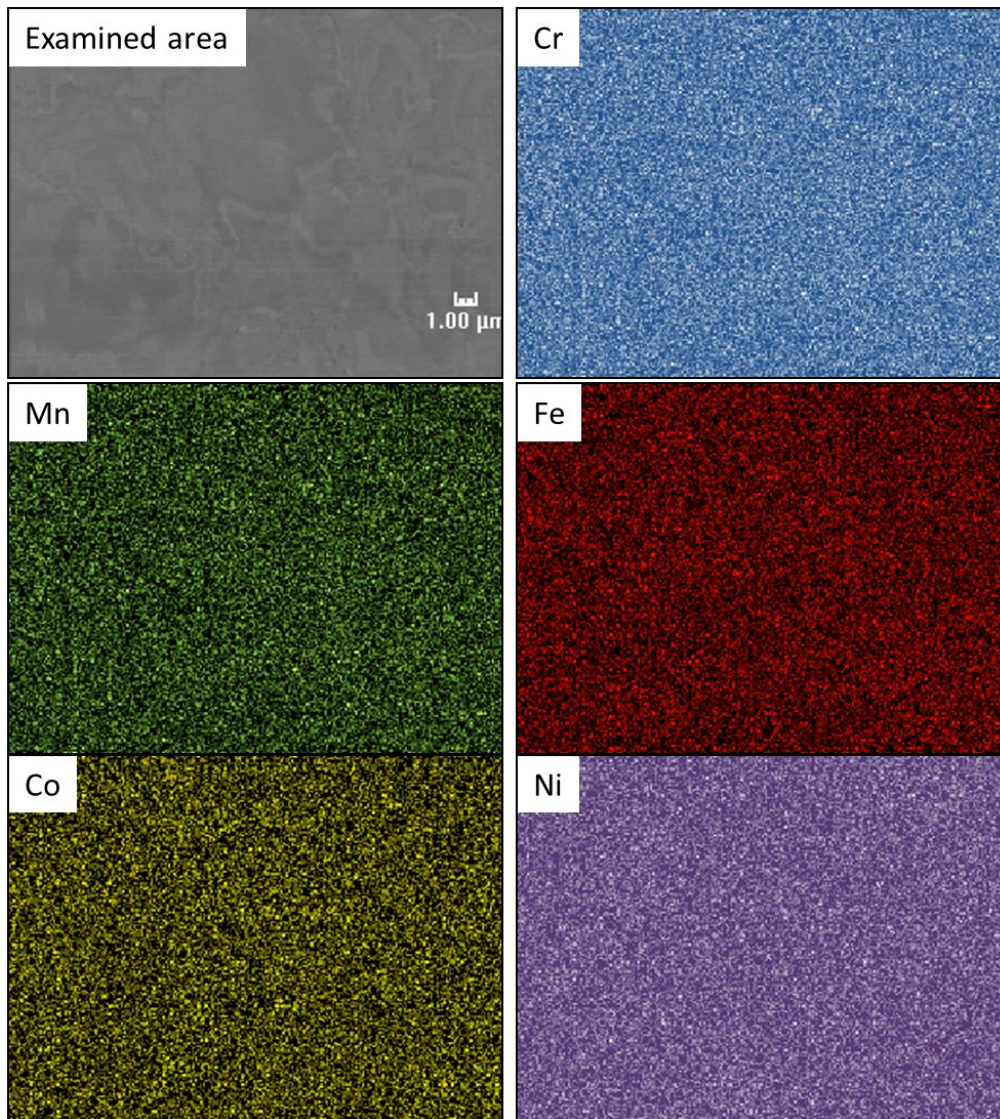
Figure 58. EDX mapping of the A3S in as-forged state. Lighter points indicate higher density of an element.

X-ray diffraction pattern of the as-forged A3S alloy is shown in Figure 59 a. Only one FCC phase was detected (likewise for the X1) with the lattice parameter of ~3.59 Å for both the as-forged and annealed state, in agreement with previous works [2]. Nevertheless, the lattice parameter is somewhat higher for the X1 (Table 10), which is in a good agreement with preceding calculations of atomic radii in two materials (see Chapter 3.2.2). Theoretically, after taking lattice parameter of all the elements, for the X1 this parameter should be of 3.563 Å and for the A3S of 3.569 Å.

Table 10. Values of lattice parameter measured in XRD for X1 and A3S after forging and annealing.

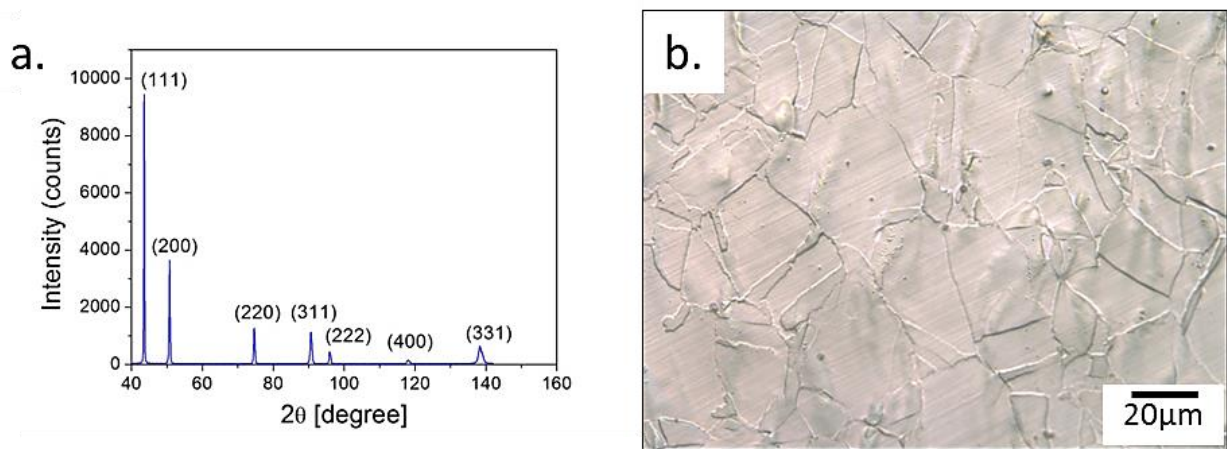| Alloy	State	Phase	Lattice parameter [Å]
X1	As-forged	FCC	3.5991±0.0006
	1000°C/2h annealed	FCC	3.5989±0.0005
A3S	As-forged	FCC	3.5903±0.0003
	1000°C/2h annealed	FCC	3.5954±0.0013

Figure 59. a) XRD pattern and b) optical image of the A3S in as-forged state.

When observed with an optical microscope, the microstructure of the as-forged A3S (Figure 59 b) consists of grains with wavy grain boundaries, as well as twins. This structure was observed more precisely with SEM + EBSD and TEM (Figure 60). It consists fully of FCC grains with high angle grain boundaries (HAGBs) and high density of low angle grain boundaries (LAGBs or subboundaries, Figure 60 a). This microstructure is typical for materials deformed at high temperature, where grains recrystallize dynamically with wavy boundaries and high density of dislocations (Figure 60 b) [112], [113]. No traces of phase separation were found. The average grain size, calculated with EBSD and excluding subboundaries, is of ~6 μm.
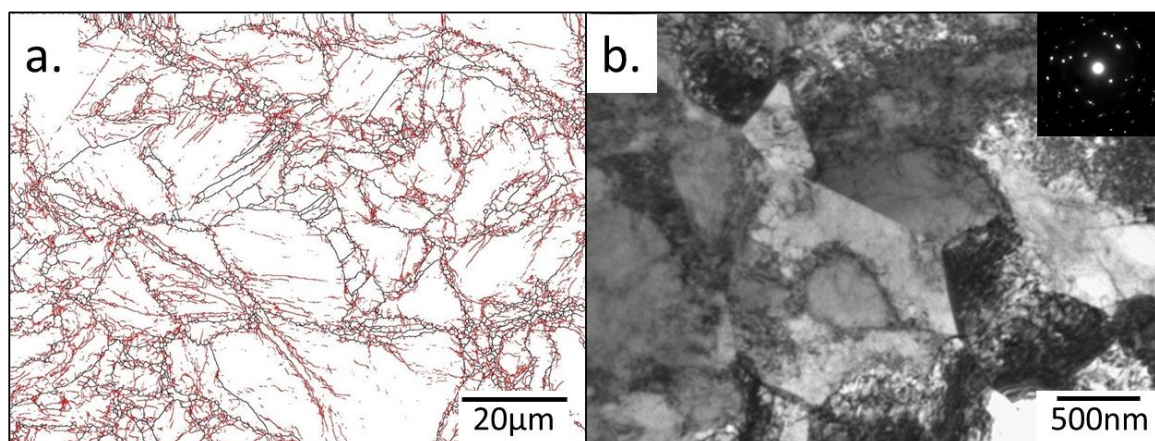
Figure 60. a) EBSD image and b) BF TEM image of the A3S in as-forged state. In a), black and red lines represent high (misorientation >15º) and low (2º-15º) angle grain boundaries, respectively.

In annealed state (1000ºC, 2 hours), microstructure observed at SEM-EBSD scale is free of subgrains, with homogeneous equiaxed grains of ~20 µm containing large number of annealing twins (Figure 61). XRD analysis confirmed single-phased character of both materials (Table 10).
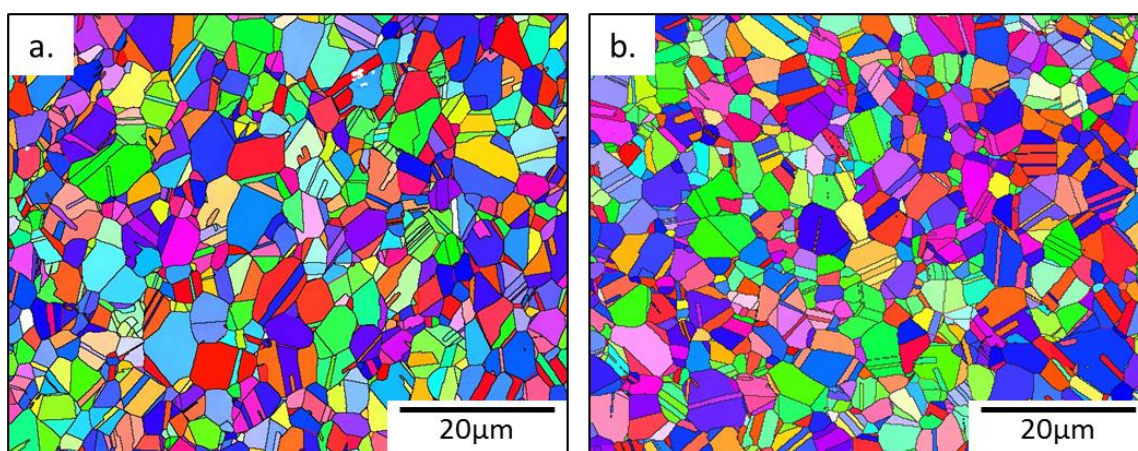
Figure 61. EBSD IPF (Inverse Pole Figure) image of the annealed (1000ºC/2h) microstructure of a) A3S and b) X1.

At these scales of observations, both the X1 and the A3S in the as-forged state can be characterized by similar type of grains. However, there are important differences between both materials seen on the nano/micrometric scale. Microstructure of the as-forged A3S (Figure 60 b) consists of deformed grains with cells created by high density of dislocations. These dislocations cells are of few hundred nanometers, with low-angle boundaries, which are clearly not sharp but rather with diffuse appearance. This

type of structure can be typically obtained after severe plastic deformation (i.e. ECAP) [114]. Yet, in case of both HEAs investigated in this work, the nanostructure was obtained after standard hot forging, indicating higher facility of obtaining very small grains compared to standard materials. Microstructure of the X1 in as-forged state, similarly to A3S, consists of cells with low angle boundaries and high density of dislocations (Figure 62 a). These cells are of hundreds of nanometers. Yet, main difference between the X1 and the A3S is that in the X1 nanotwins are present (Figure 62 b-d), hardly found in the A3S. Forming twins is probably easier in the X1 than A3S, which may be due to lower stacking fault energy of this material. Materials with low SFE (like copper alloys) are expected to form twins easily, especially at higher strains [115]. SFE is determined mainly by the chemical composition and apparently this effect is strong for the X1 and A3S, since the microstructures are not the same even though the proportions between the elements are not extraordinarily different. In the next step, phase stability and mechanical properties will be studied to confirm this significant distinction between the two materials.
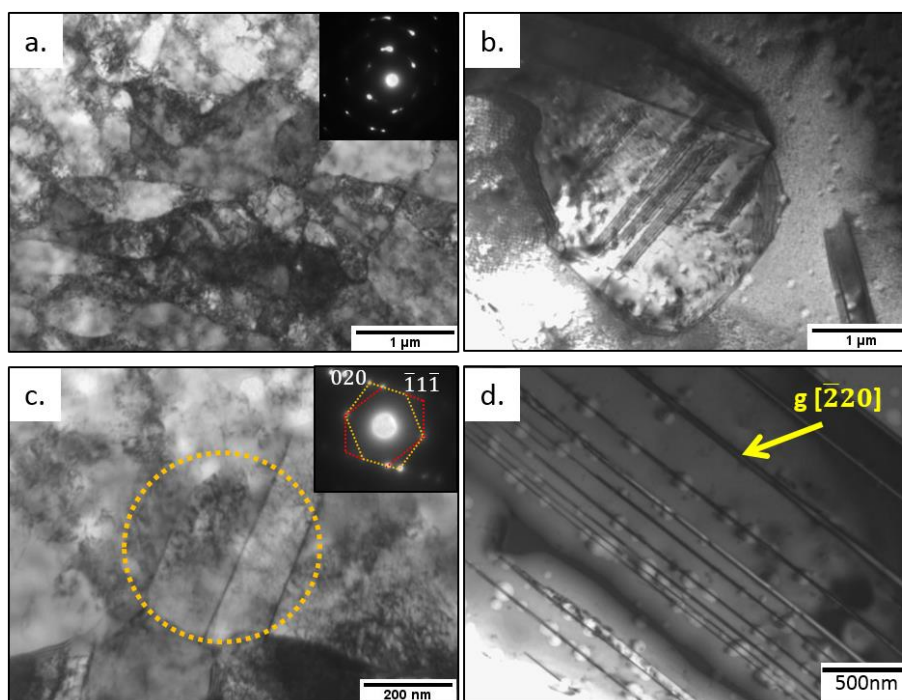

Figure 62. TEM bright field images of X1 in as-forged state: a) general structure, b) nanotwinned grain, c) twinned area with diffraction pattern, d) nanotwins in [110] ZA in (113) plane. Bubbles are due to sample preparation.

4.2. Solid solution stability

Recently few publications showed that the CoCrFeMnNi HEA is not as stable as it was expected at the beginning (see Chapter 1.5.1). Even though most of the first investigations proved a presence of only one FCC phase, in fact, its decomposition (into σ Cr-rich, Fe-Co-rich and Mn-Ni rich phases) takes place in a specific range of temperatures (between 450 and 800°C) [59]–[63]. The presence of new phases is also influenced by the processing: in case of severely deformed materials, this process (as a diffusion-dependent) is more rapid due to higher number of fast diffusion paths (grain boundaries, dislocations). On the other hand, kinetics of phase transformation in HEAs is known to be slow. These factors must be all taken into account in the heat treatment optimization.

At the beginning of this work, different heat treatments were applied between 500 and 1100°C, for various periods of time (from 2 hours to 21 days), and none of them showed any presence of secondary phases (only a single FCC phase has been found). Nevertheless, hypothesized TTT diagram for the X1 (based on the literature review, Figure 63) suggests that longer heat treatments are necessary to confirm solid solution stability. Thus, due to importance of thermal phase stability especially for industrial applications and following the bibliographic approaches, we have decided to verify possibility of decomposition after relatively long heat

Figure 63. Hypothesized TTT diagram for the X1.

treatments (21, 100, 200 and 300 days) at 500°C. At this temperature theoretically three different phases should be stable (Figure 64): one FCC solid solution phase (matrix), one BCC solid solution phase and σ phase (more detailed analysis of the composition of phases is given subsequently in Table 11).
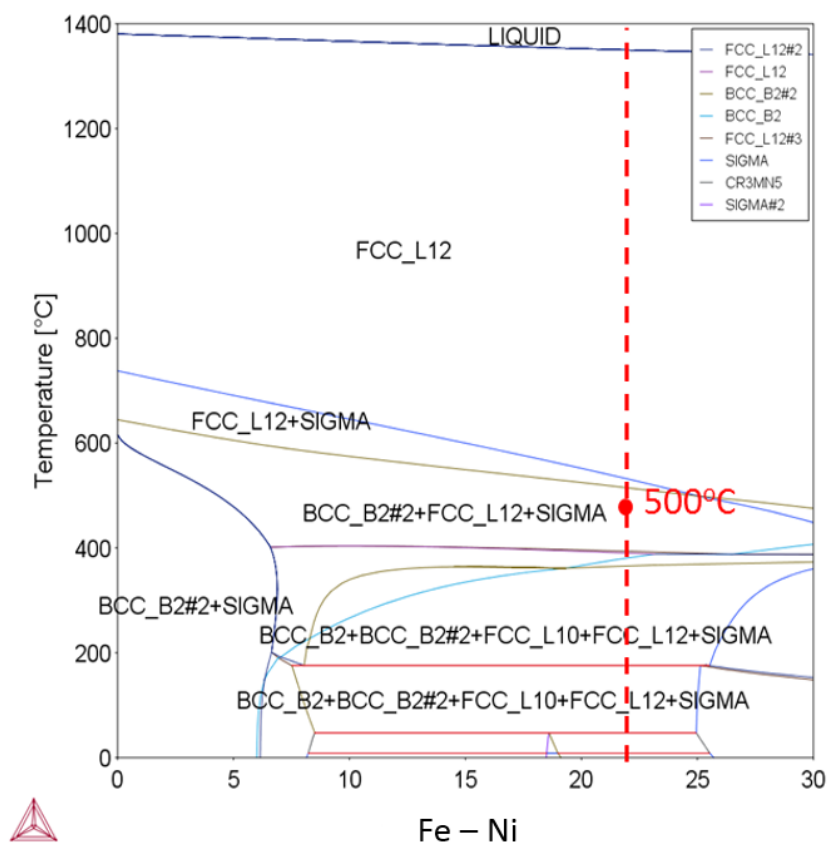
Figure 64. Quasi-binary Fe-Ni phase diagrams of the A3S alloy (HEA1 database).

Table 11. Chemical composition (at.%) of phases calculated in the X1 after 500°C/100 days annealing.

Method	Phase	Co	Cr	Fe	Mn	Ni
Thermo-Calc (HEA1 database)	BCC	38	3	49	1	8
	FCC	19	14	24	18	25
	σ	4	35	32	29	0.01
TEM-EDX	"1"	26	31	27	8	8
	"2"	15	16	15	26	27
	matrix	21	24	22	17	16

In case of the materials annealed for 100 and 200 days, the specimens were either in as-forged state (Figure 65) or recrystallized state (Figure 70) before annealing. In Figure 65 a one can see that the microstructure of the X1 after 100 days at 500°C is divided in two types of regions: one characteristic for the single-phased as-forged state and one with distinctive decomposition (more detailed in Figure 66). Obviously, the same type of decomposition was observed after 200 days at 500°C with higher volume fraction of new phases comparing to FCC matrix. In contrary, the A3S reveals only one homogeneous phase, indicating higher stability of this material (Figure 65 c, d).
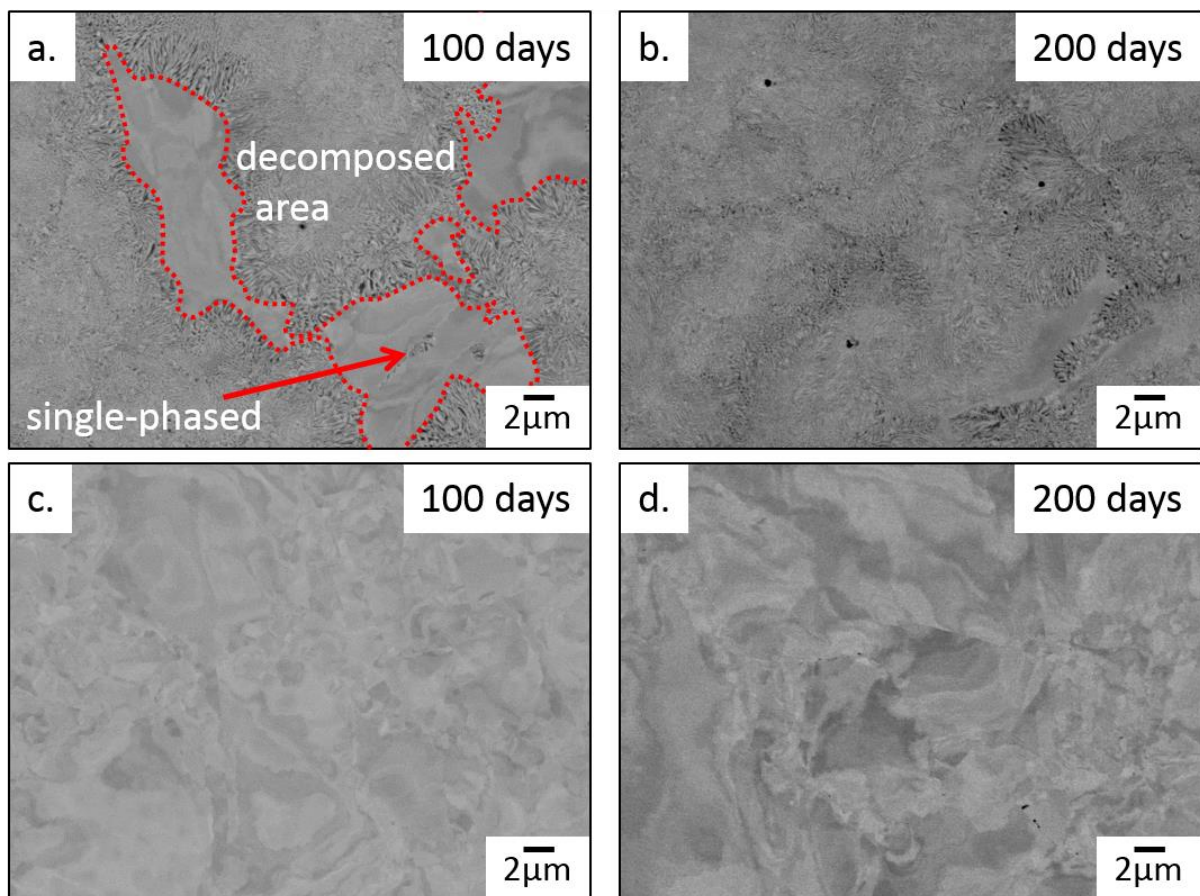

Figure 65. SEM images of a, b) X1 and c, d) A3S after annealing at 500°C for 100 and 200 days. Before the annealing all the samples were as-forged without additional heat treatments.

TEM observations of the decomposed area (Figure 66) allowed us to confirm differences in the chemical composition, with equiatomic matrix and areas much richer in Fe-Co-Cr and Mn-Ni (Table 11).
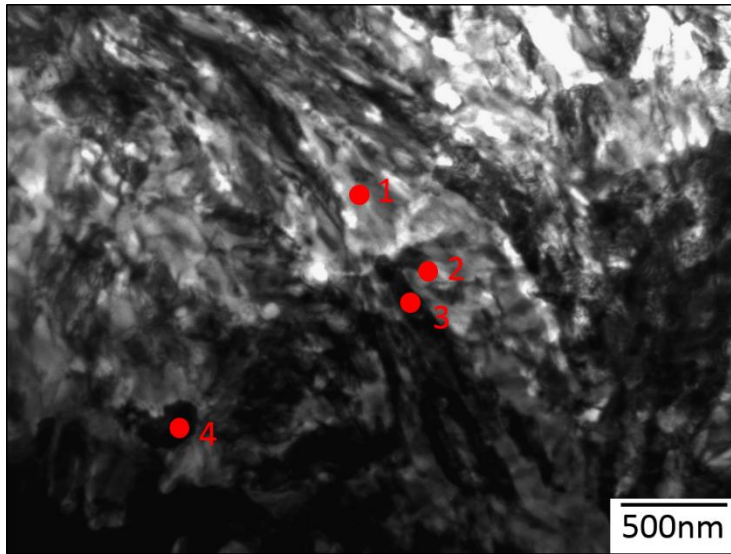
Figure 66. BF TEM image of the X1 after annealing at 500ºC for 100 days. Points 1-4 indicate areas of the EDX analysis of the chemical composition; values are given in Table 11.

Microstructure of the A3S in more details is shown in Figure 67. High density of dislocations and cells of few hundreds of nanometers, characteristic for the as-forged state, are still present. Nevertheless, the structure is more stabilized and dislocations are forming subboundaries (Figure 67 a, b). Still, dislocations density is very high (Figure 67 c). In some areas, rare recrystallized grains of about 200 nanometers were also found (Figure 67 d).

Figure 67. TEM images of the forged A3S after annealing at 500ºC for 100 days.

New phases after 100 days were identified using X-ray diffraction (Figure 68). In the A3S, only one FCC phase was detected with the lattice parameter of approximately 3.59 Å. In the X1, along with the FCC matrix phase, three new p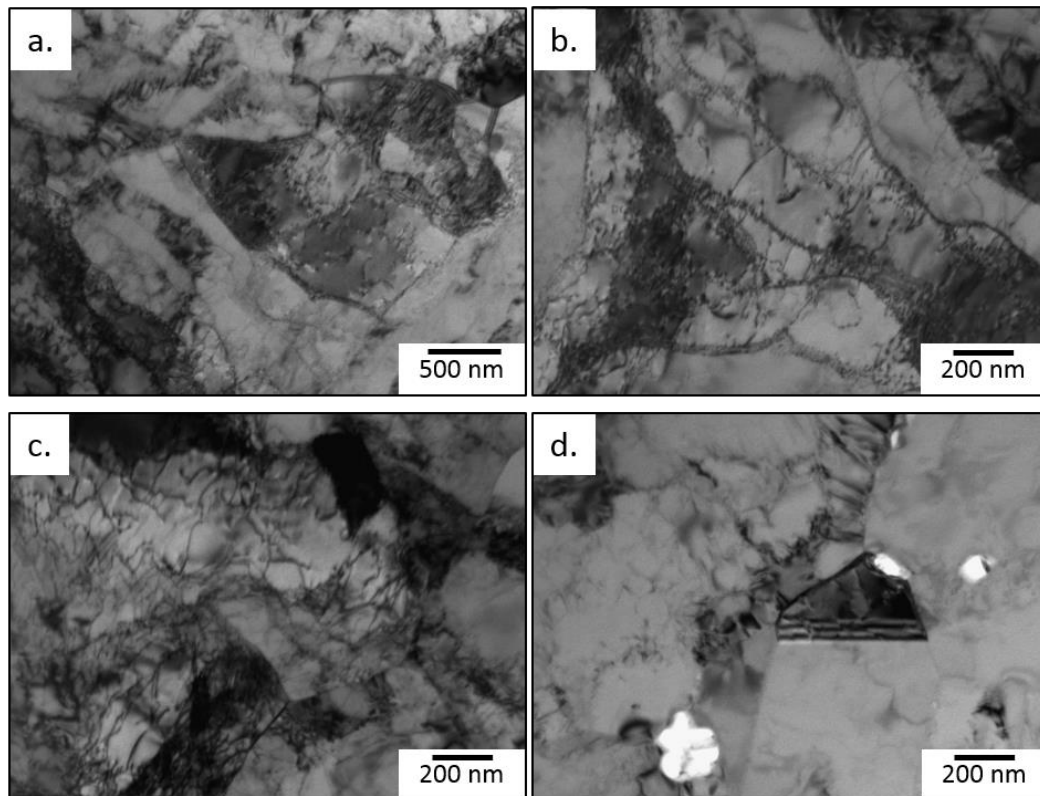hases were detected: BCC Cr phase (lattice parameter a = 2.88 Å), MnNi tetragonal phase (a = 2.64 Å, c = 3.52 Å) and FeCo cubic B2 phase (a = 2.86 Å). Similar peaks were found after 200 days
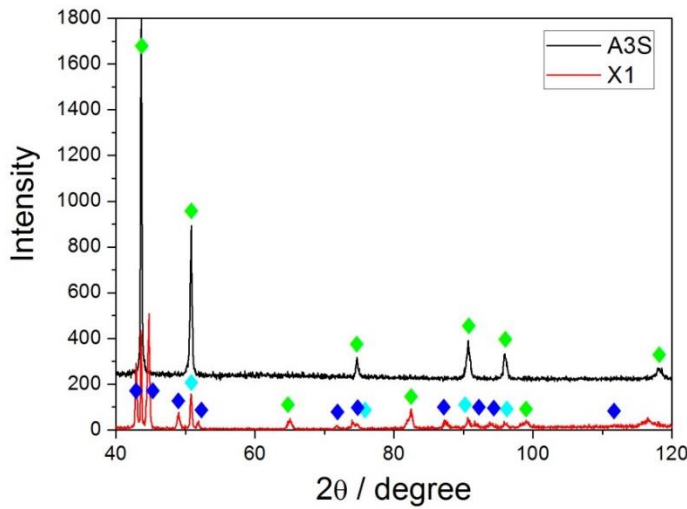
Figure 68. X-ray diffraction patterns of the X1 and A3S after annealing at 500°C for 100 days. Green points indicate FCC matrix phase; dark blue points: MnNi; cyan points: FeCo.

annealing (not shown here), but with increased intensity indicating increase in the volume fraction of these new phases. The identification of new phases is in a complete agreement with the literature after annealing in similar conditions (Figure 69). Comparing this results with Table 11, there are certain similarities. According to Thermo-Calc calculations, there are three phases present in the structure: one FCC matrix with closely homogeneous distribution of elements and two new phases: σ phase richer in Cr-Fe-Mn and BCC phase richer in Co-Fe. TC does not find any phase rich in Mn-Ni. In TEM-EDX, three phases were found as well, but only their composition was identified: one matrix phase, one phase richer in Mn-Ni and one richer in Co-Cr-Fe. Here, however, the resolution of measurement could be not precise enough to distinguish σ phase rich in Cr.
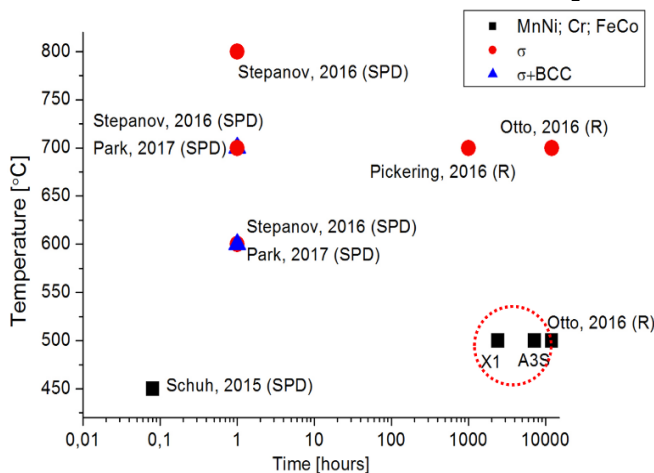
Figure 69. Summarized observations of the secondary phases in the X1 and A3S.

For the results of the specimens recrystallized before long time annealing, similar tendency was observed as for as-forged materials (Figure 70). Here again, in the X1 decomposition was found already after 100 days annealing. The single-phase microstructure of the A3S remains stable, without any traces of phase separation. Hence, only the X1 decomposes after prolonged heat treatment, but starting from as-forged state the fraction of secondary phases is much higher (more than 50% in previously forged material; in the annealed alloy, however, only some decomposition in grain boundaries). This is probably due to much higher dislocation density and number of (sub)boundaries in as-forged material, which can act as nucleation point for new phases [116], [117]. Additionally, diffusion in deformed state with a high number of grain boundaries is faster than in recrystallized one with larger grains [118]. After 200 days this difference is almost negligible.
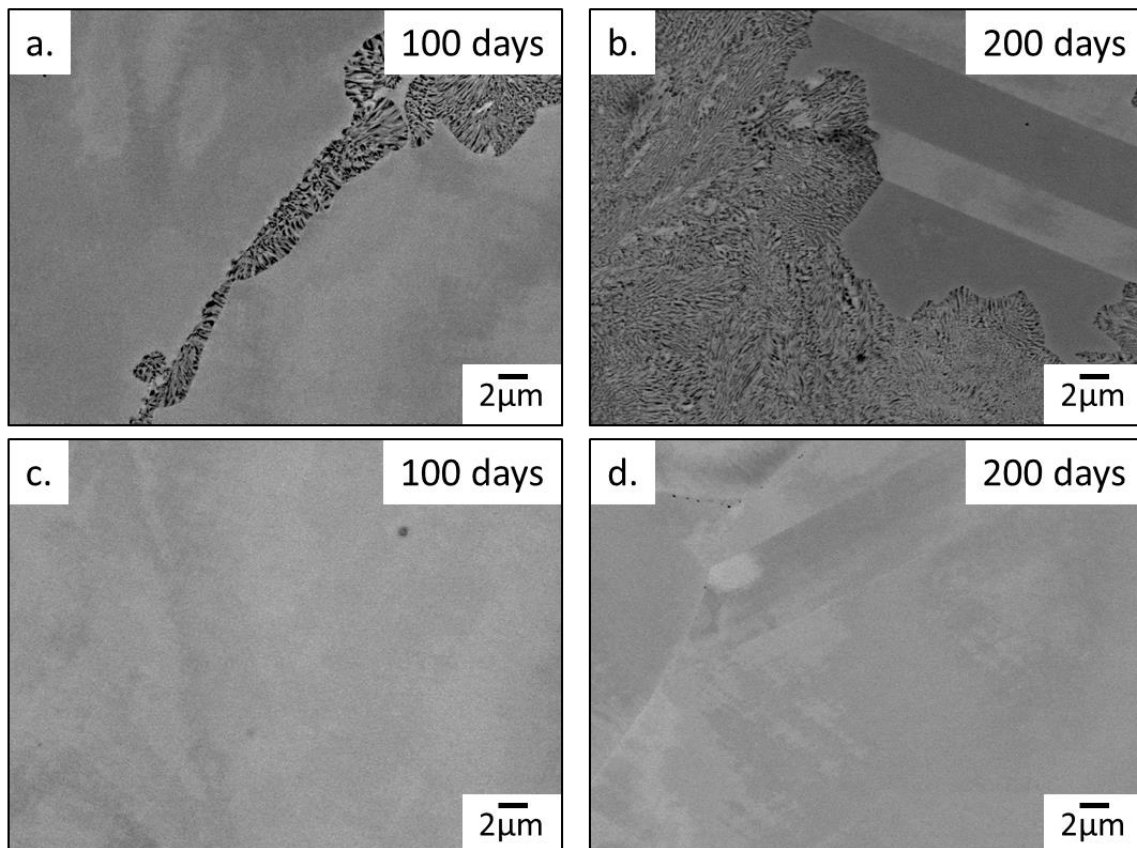

Figure 70. SEM images of a, b) X1 and c, d) A3S after annealing at 500ºC for 100 and 200 days. Before the annealing all the samples were annealed at 1000ºC for 2 hours.

After 300 days, the X1 is strongly decomposed, with higher ratio of new phases in the as-forged material (Figure 71 a, b). New phases begin to form for the first time in the A3S (Figure 71 c), but only in some regions of the as-forged material. The alloy recrystallized before annealing remains mostly single-phased (Figure 71 d), with only few small areas of decomposition. It is probably due to lower density of dislocations and thus fewer possible nucleation zones.
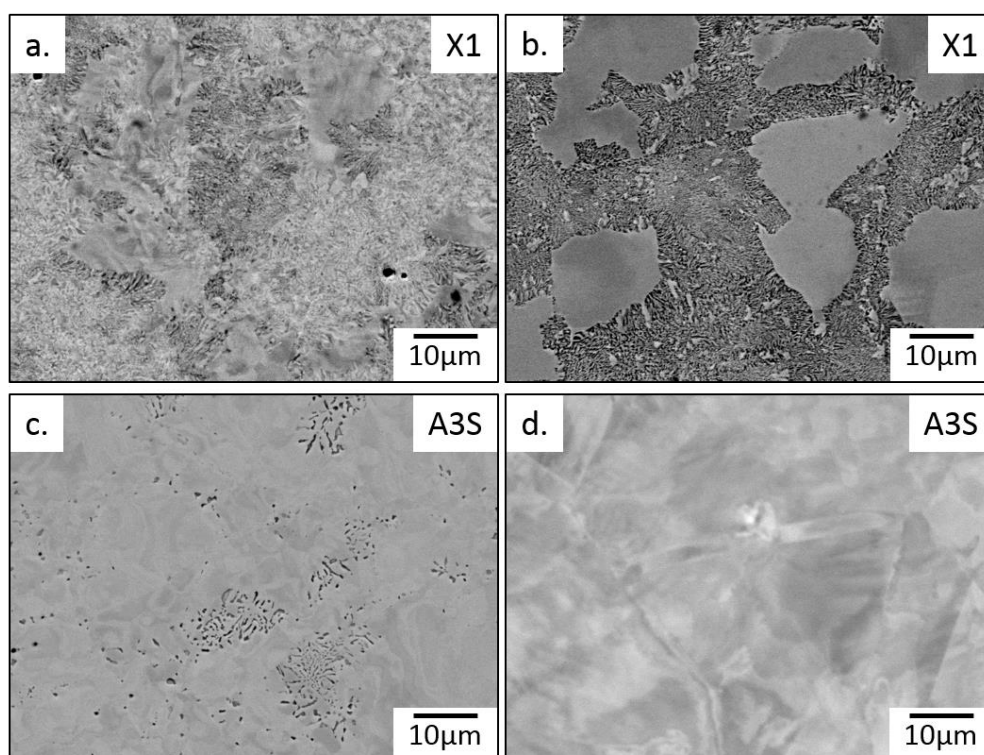
Figure 71. SEM images of a, b) X1 and c, d) A3S after annealing at 500°C for 300 days. Samples a) and c) were only forged and samples b) and d) were annealed at 1000°C/2h before long-term annealing.

These results confirm that the X1 is not stable even at relatively low temperature (500°C) when annealing is prolonged. Yet, the A3S remains almost single-phased even up to 300 days when it is initially annealed. Lack of phase separation is a first indication that the new modified non-equiatomic composition increases solid solution phase stability. This, together with discrepancies in the microstructure of two alloys shown in previous chapter, can presumably lead to more promising properties. Thermal stability is necessary in the conditions where properties must be conserved.

4.3. Influence of the microstructure on mechanical properties

The next part of this work deals with a comparison of mechanical properties of the two developed alloys. Vickers hardness tests were performed in the first step as the easiest way to analyze rapidly the resistance of material. Then, compression tests at different temperatures and strain rates were done. These tests are useful for an uncomplicated evaluation of mechanical properties (especially yield strength). For chosen cases, tensile tests were conducted at different temperatures to confirm yield strength values and to obtain a measurement of an elongation to fracture to evaluate ductility.

4.3.1. Hot-forged state
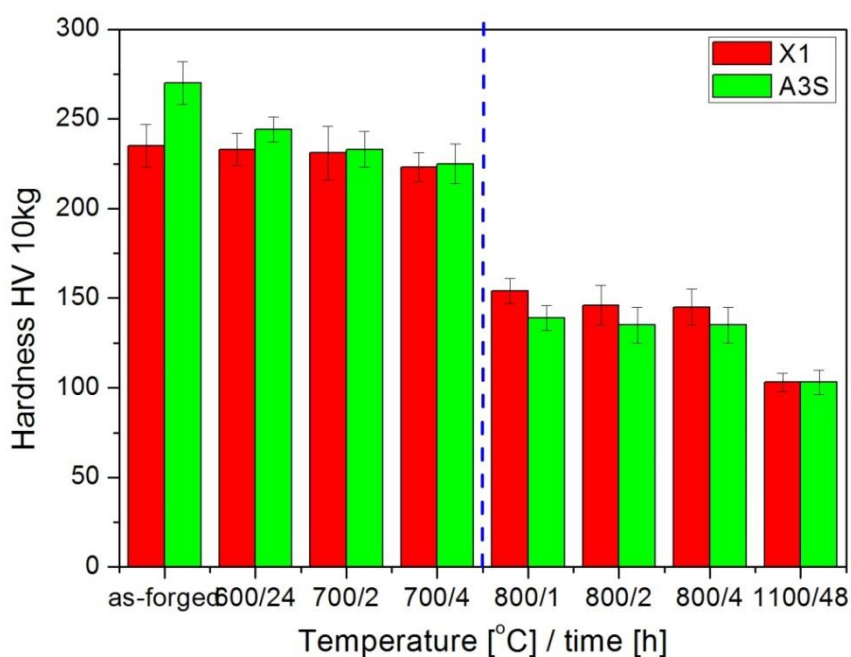
Figure 72. Effects of annealing on hardness of the hot forged X1 and A3S. Samples were air cooled after annealing.

Vickers hardness (Figure 72) reaches the highest values for as-forged specimens and is higher for the A3S (270 HV versus 235 HV for the X1). With subsequent isothermal annealing with increase of temperature and time, hardness values decrease slowly. Until 800°C, however, hardness remains relatively high (>220 HV) and almost constant

in both materials. At this temperature a strong drop of hardness is observed, to 154 HV for the X1 and 139 HV for the A3S. At higher temperatures hardness values are again stabilized.
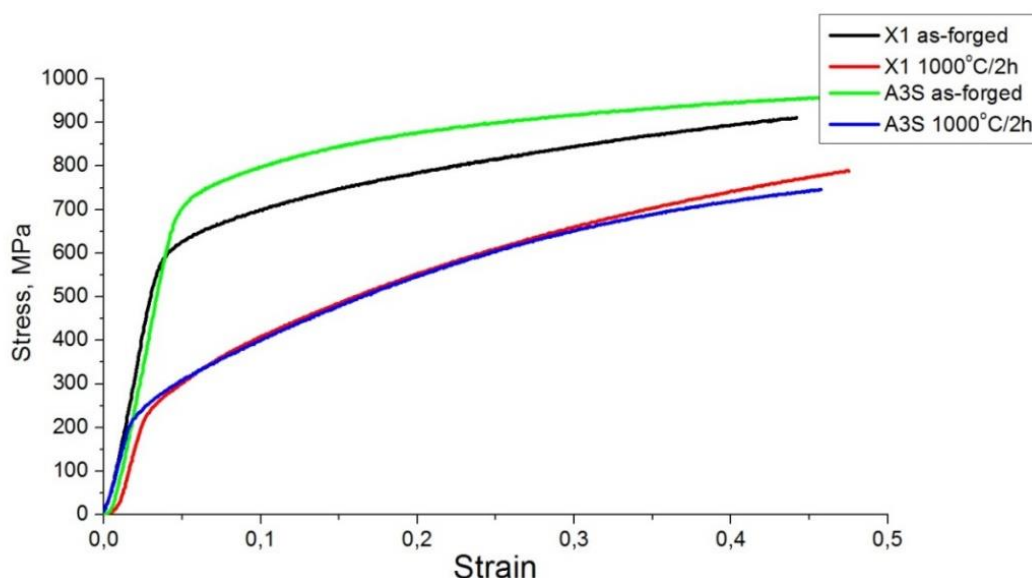
Figure 73. Compression stress-strain curves of the X1 and A3S in as-forged and annealed state (annealed at 1000°C/2h). Strain rate 10^{-3}s^{-1}, room temperature.

The results of compression tests with a strain rate of 10^{-3} s^{-1} performed on the samples in the as-forged and annealed state are shown in Figure 73. Numerical values are given in Table 12.

Table 12. Yield strength from compression tests of the X1 and A3S in different states.

State/Material	X1	A3S
As-forged	600 MPa	775 MPa
Annealed	240 MPa	240 MPa

In the as-forged state, the X1 exhibits a yield strength of 600 MPa, while the value for the A3S is much higher (775 MPa). Slope of the curve in plastic area for the two materials is low (it corresponds to work hardening which will be defined later). In the annealed state, however, both materials possess similar properties with a yield strength of 240 MPa and high slope in plastic area (in agreement with previous works on the equiatomic CoCrFeMnNi [66]). In both cases, no cracks were found on any of the samples after compression, indicating their high plasticity in any temperature conditions.
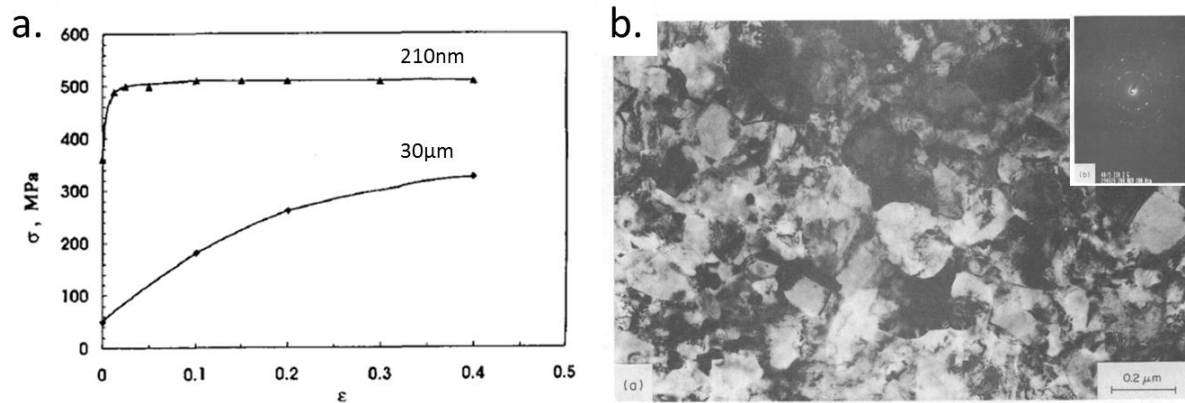
Figure 74. a) Compression stress-strain curves of coarse grained (CG) (30μm) and ultra-fine grained (UFG) (210nm) copper; b) microstructure of UFG copper [119].

These two characteristic types of stress-strain curves are simultaneously observed in different ultrafine-grained and coarse-grained materials, i.e. copper alloys (Figure 74). Here, higher yield strength and lower slope in plastic area for the UFG (in our case: as-forged) state is explained by high density of dislocations and grain boundaries. The deformation process is influenced by high level internal stresses [119].
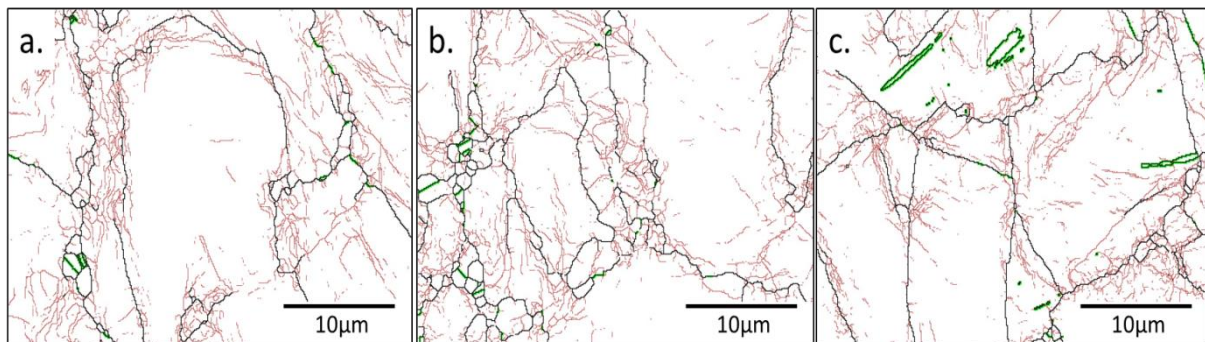
Figure 75. EBSD images of the A3S after deformation: a) 1.5%, b) 5%, c) 15%. Black, red and green lines are high, low and twin grain boundaries, respectively.

The parameter which strongly distinguishes the alloys in the as-forged and annealed state is a slope of the curves in plastic area: a work hardening coefficient (WHC). This coefficient (p) was calculated from the Hollomon equation:

$$\sigma = K\varepsilon^p$$

$$\log \sigma = \log K + p \cdot \log \varepsilon$$

where: σ is the stress, ε is the plastic strain and K is a material constant. The coefficient p was determined from the slope of a plot of log σ vs. log ε. Its typical values for metals are between 0.10 - 0.50; closer to 0 means that material is more "perfectly" plastic and closer to 1 – more elastic. Here, for the as-forged X1 and A3S this coefficient reaches 0.17 and 0.07, respectively. In recrystallized materials, the coefficient is similar for both and takes the value of 0.43.

Higher work hardening coefficient may be related to lower stacking fault energy [120], [121] and hence mechanical twinning [122] in FCC metals. This effect is seen in particular in TWIP steels [123]. For materials with high SFE twinning is more difficult and thus the WHC may be small. Low density of twins in the A3S even after deformation to 15% indicates high SFE (Figure 75). Another explanation of an important difference in work hardening between as-forged and annealed state comes from different behavior of dislocations. In as-forged state, considered here as nanostructured, density of (sub)grain boundaries is high and thus a high degree of strengthening is already achieved. These are obstacles to dislocation motion. As a consequence, additional strain-hardening is relatively small.

Strain rate is an important factor for designing of processes and tools in metal forming. Here, strain rate sensibility of the X1 and A3S has been investigated by a series of compression tests between room temperature and 400°C and with different strain rates (10^{-1} s^{-1} and 10^{-3} s^{-1}), see Figure 76. In both materials, rather low strain rate sensibility was observed, typical for FCC and UFG materials [119]. Small differences stay in the margin of error. Simultaneously, a high drop of the yield strength with temperature was observed. Similar phenomena has been already observed in the CoCrFeMnNi [64]. The strengthening of HEAs is more dependent on temperature than in classical FCC alloys in which barriers to dislocation motion can be easily overcome by thermal fluctuations.
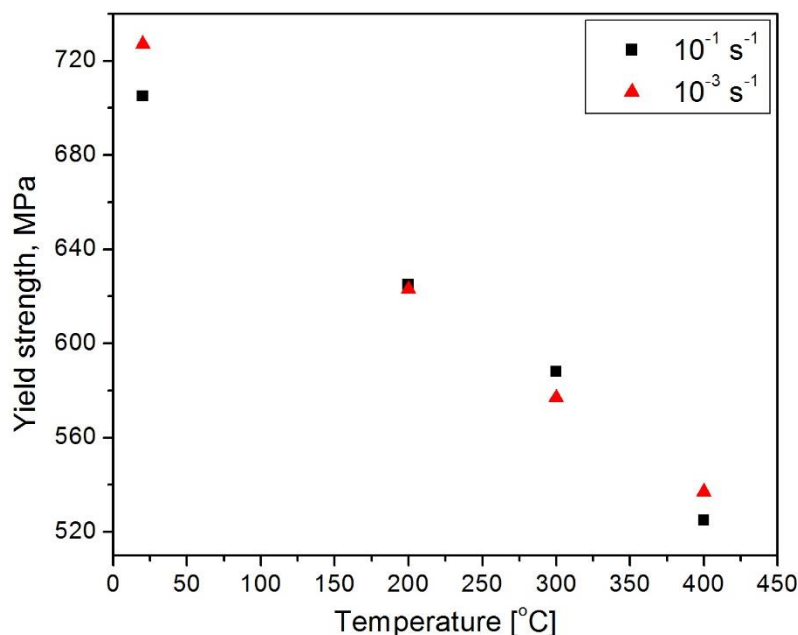
Figure 76. Yield strength vs. temperature after hot compression of the as-forged A3S with different strain rates (10^{-1} and 10^{-3} s^{-1}).

To evaluate the influence of heat treatment temperature on mechanical properties, the A3S was annealed at different temperatures (Figure 77; all the corresponding curves are shown in Annex 2). Until 600°C, the material remains in a "high strength" regime, with yield strength of above 600 MPa and low work hardening coefficient. However, at higher temperatures the curves become similar to the previously shown annealed state, with low yield strength and high work hardening coefficient. It must be related to a modification of the microstructure.

The results of tensile tests are comparable to compression results. The annealed X1 has a yield strength of 246 MPa and for the as-forged A3S it is 770 MPa (Figure 78). The elongation to failure for both as-forged materials is of 30% and for annealed of 50%. Ultimate tensile strength is of 600 MPa for both annealed alloys and of 805 MPa for as-forged alloys. Small differences between the results of compression and tensile tests were observed and they can be related to different applied stresses and additionally to various crystallographic textures of specimens. The properties of the A3S are conserved even after changing the content of chromium and nickel by ±2% (A3S-1, A3S-2 and A3S-3 curves in Figure 78), confirming originality of this material.
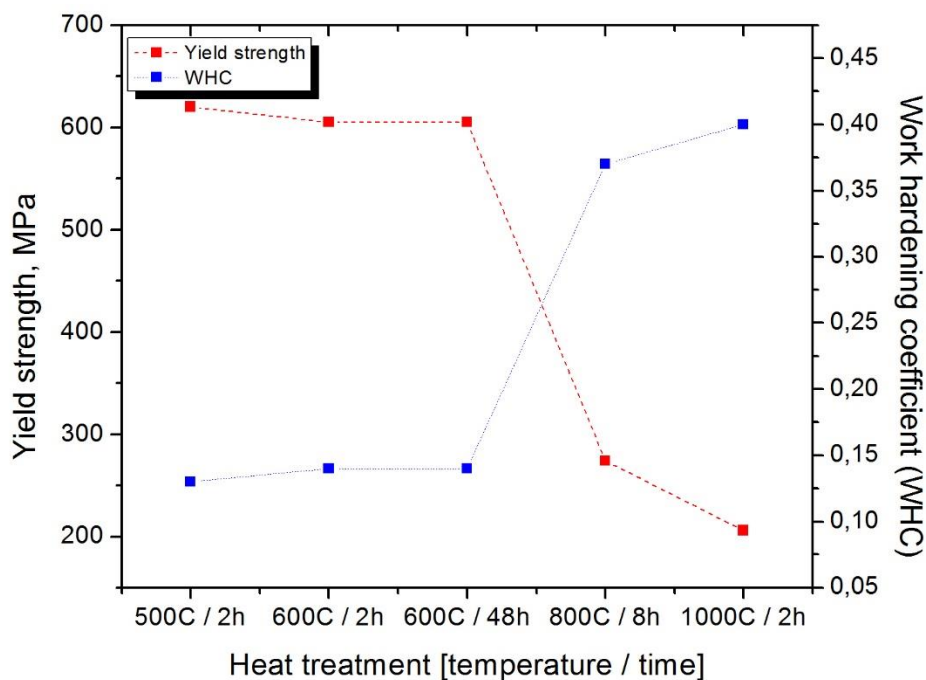
Figure 77. Yield strength and work hardening coefficient (WHC) vs. temperature obtained in stress-strain curves of the A3S forged and annealed at different temperatures and times. Strain rate 10^{-3} s^{-1}.
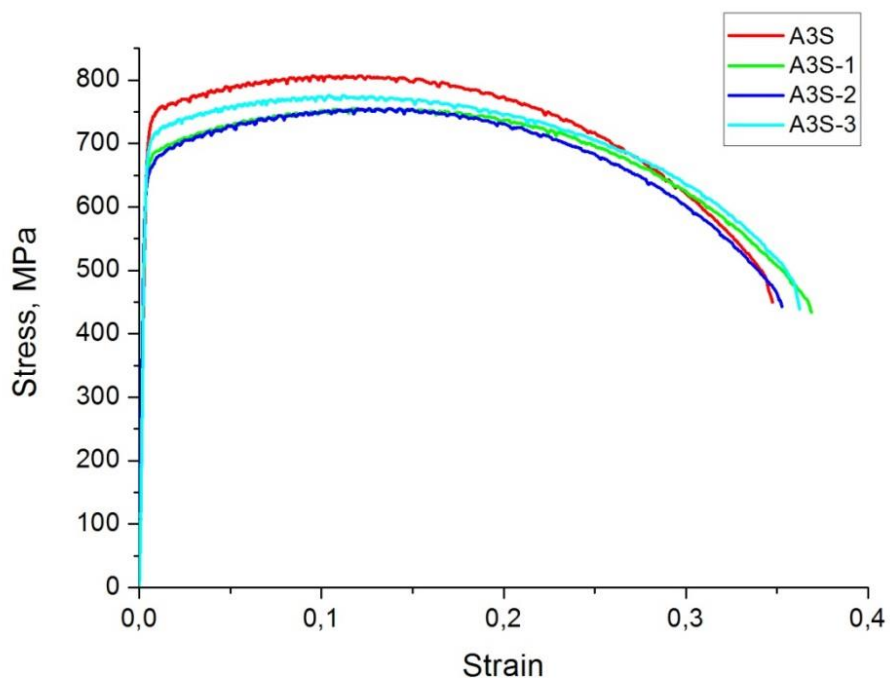

Figure 78. Tensile stress-strain curves of the as-forged A3S and its modifications (±2% of Cr and Ni). Room temperature, strain rate 10^{-3} s^{-1}.

In Figure 79 fracture surfaces for the annealed X1 and A3S are shown, with a dimple-like morphology typical for ductile deformation. For as-forged and different homogenized alloys pictures were similar and are not shown here.
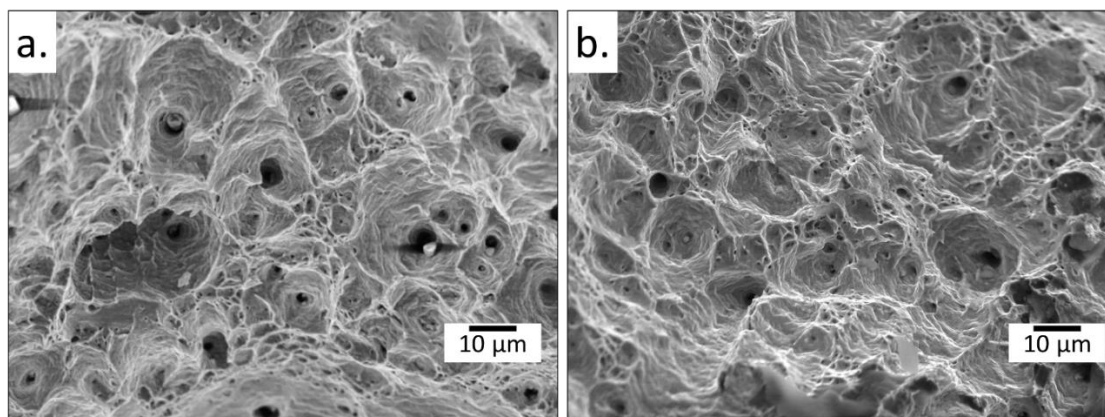
Figure 79. SEM secondary electron image of a fracture surface of the a) X1 and b) A3S in annealed state.

Comparing values from tensile tests with conventional stainless steels (Table 13), our high entropy alloy have much better mechanical properties. The yield strength of the A3S is about 2.5 times higher and the ultimate tensile strength increased by ~220MPa compared to 304 and 316 stainless steels, with somewhat smaller elongation. This is very promising for future industrial applications. The X1 also possess good mechanical properties, nevertheless the A3S remains stronger with similar ductility and other assets conserved. Even though the presented properties are of the A3S that was not annealed, in contrary to 304 and 316, for similar elongation both yield strength and ultimate tensile strength are significantly higher.

Table 13. Comparison of mechanical properties of the A3S and different steels.

Material	Yield strength [MPa]	Elongation %	Ultimate tensile strength [MPa]
A3S	770	30	805
304 [124]	210-230	40	500-750
316 [124]	220-240	40	520-730

4.3.2. Low temperature behavior

In recent publications [80], [125] the improvement of mechanical properties of the X1 was observed at cryogenic temperatures, around the liquid nitrogen temperature (-196°C / 77K). This was attributed to a difference in mechanisms of deformation at low temperatures due to lowered stacking fault energy and thus easier twinning. The X1 presents important temperature dependence of strength at these temperatures, in contrary to pure FCC metals [126]. More surprising is the simultaneous growth of both yield strength and elongation to fracture, while in classical materials a compromise between both is currently admitted. On the other hand, no martensitic transformation was observed. In regard to elevated mechanical properties at low temperatures of this HEA, it may be implemented in the future in different industrial functions. Hence, verifying the A3S in similar conditions was indispensable.

First, values of Charpy impact toughness of the as-forged A3S at room and liquid nitrogen temperature were determined through a Charpy impact test.

Table 14. Values of energy absorbed by rupture KV and Charpy impact toughness KCV obtained in Charpy tests.

Temperature	Material	KV [J]	KCV [J/cm^2]
Room temperature	A3S	25	126
	304 [127]	34	168
-130°C	A3S	25	125
	304 [127]	27	134

Obtained results are summarized in Table 14 and compared with 304L stainless steel (tests were made on exactly the same type of samples). There is no difference between room and low temperature for the A3S. Similarly to FCC materials, the A3S remains ductile at low temperatures. Values of 24-25 J for energy absorbed by rupture are relatively high. However, the energy of rupture and Charpy impact toughness decreases at low temperature for the 304, indicating more brittle character of rupture.
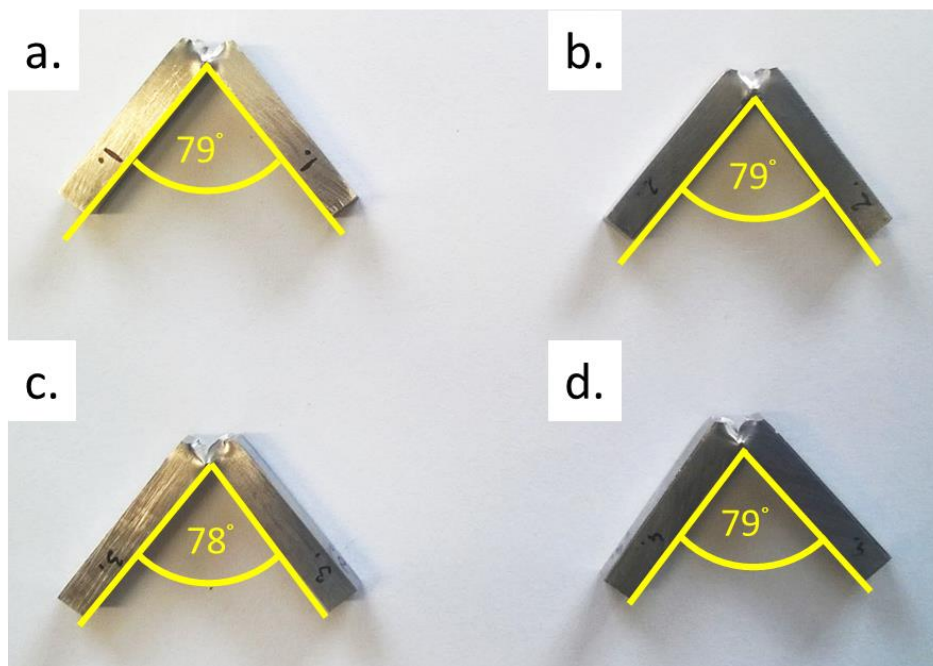
Figure 80. Samples after Charpy tests of the as-forged A3S: a, b) at room temperature; c, d) at liquid nitrogen temperature.

Samples of the A3S did not break during the test (Figure 80). In this case the value of the fracture toughness is underestimated. Based on these, fracture toughness is of 125-126 J/cm^2 and does not change with temperature. SEM images (Figure 81) at both temperatures show dimpled surface typical for a ductile fracture.

In the next step, high ductility at low temperatures was confirmed in tensile tests at -130°C. Figure 82 shows cryogenic-temperature engineering stress-strain curves for the A3S in as-forged and annealed state. In the as-forged state, yield strength and ultimate tensile strength obtain values of 807 MPa and 958 MPa, respectively, with an elongation to fracture of 54%. All these values are higher than obtained in as-forged state at room temperature (Table 15). The strength and elongation are also increased in annealed state compared to room temperature, with YS = 610 MPa, UTS = 835 MPa and elongation of 70%. Important rise of yield strength at low temperature in annealed state may be explained by creation of twins during deformation that work as strengthening mechanisms [80], [125]. This is not observed in as-forged state which is already nanostructured with high density of boundaries. On the other hand, in this

state an increase of elongation to fracture was considerable, on account of easier deformation compared to room temperature where twinning is much less significant.

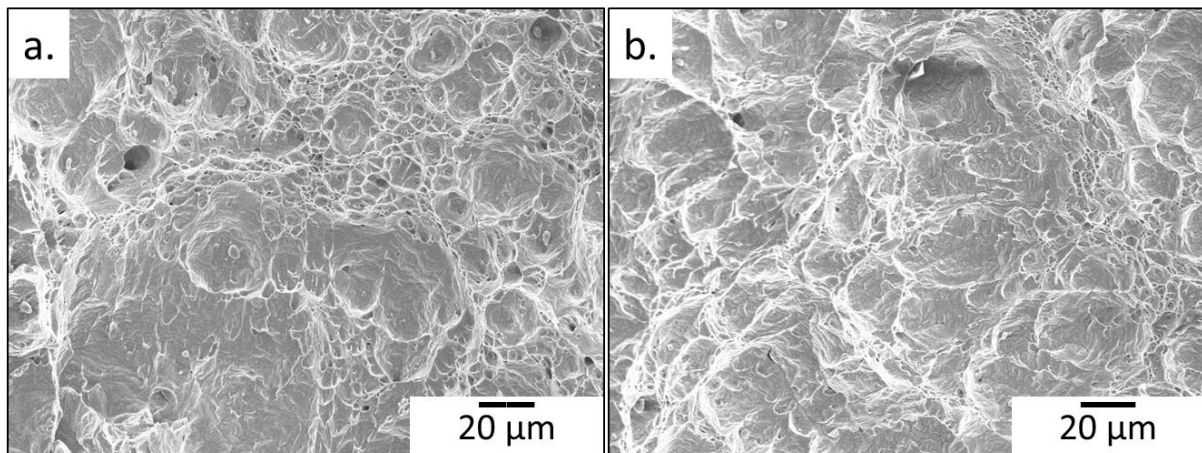**Figure 81. SEM secondary electron images of fracture surfaces of the A3S after Charpy test at: a) room temperature, b) liquid nitrogen temperature.**
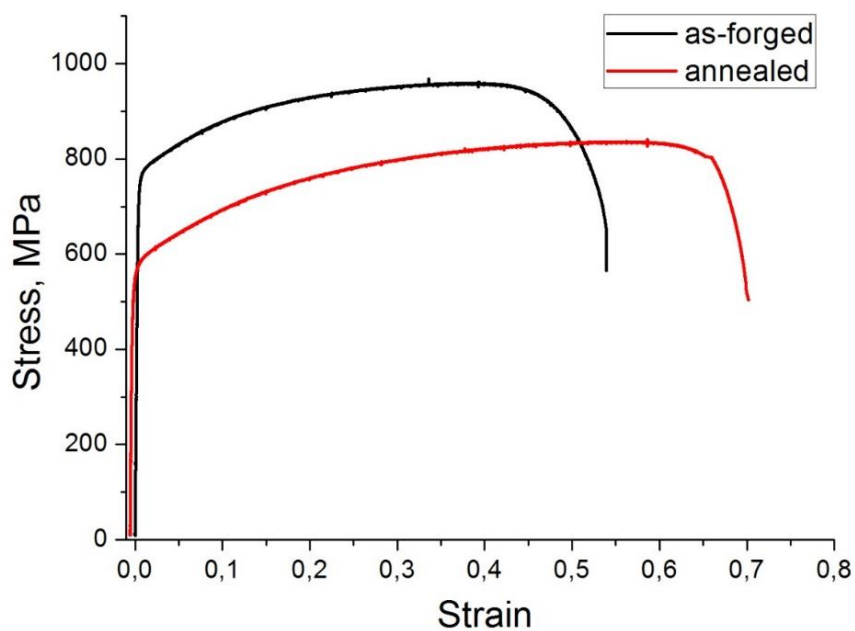

Figure 82. Cryogenic-temperature engineering stress-strain curves for the A3S in as-forged and annealed state. Strain rate 10^{-3} s^{-1}.

Here, similar to samples from Charpy test, SEM images (Figure 83) in both state show dimpled surface typical for a ductile fracture.

Table 15. Tensile mechanical properties of the A3S at low temperature (-130°C; LT) and room temperature (RT).

Material state	Yield strength [MPa]	Elongation %	Ultimate tensile strength [MPa]
As-forged (LT)	807	54	958
As-forged (RT)	770	30	805
Annealed (LT)	610	70	835
Annealed (RT)	255	63	618
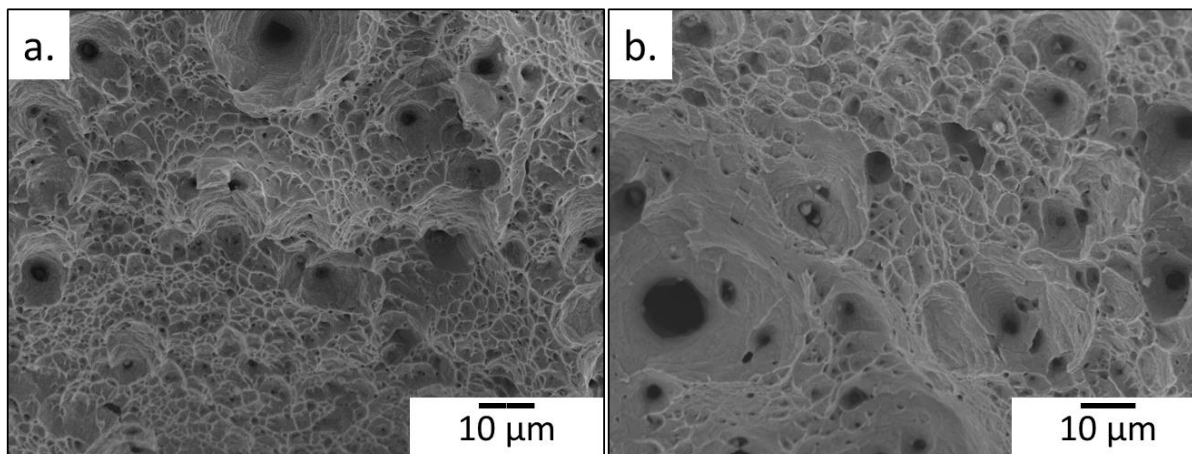
Figure 83. SEM secondary electron images of fracture surfaces of the A3S after tensile test at -130°C: a) as-forged, b) annealed.

Strength and ductility improvement can be justified by microstructure observations. Figure 84 shows EBSD inversed pole figure map of a region close to the fracture in the as-forged A3S. Here, in many grains high density of deformation twins were found with misorientation angle of 60°. More areas with deformation twins were found in annealed (and then deformed) material (not presented due to low quality of images). This can be explained by different initial states, since in the annealed samples grains were much bigger and subgrains-free. It was proven for different materials [128], as well for high entropy alloys [129], that twinning is easier in larger grains. Its effect

influences the critical stress for twinning which is more dependent on the grain size compared to the critical stress for slip.

This is in agreement with our results, where twinning is promoted in annealed state with large grains of few tens of micrometers. Here, the critical stress for twinning is small and thus deformation twins are presented in almost all the grains observed in EBSD. On the other hand, for the as-forged materials, only few regions contain deformation twins. This state is characterized, as it was shown before, by a large amount of ultra-fine grains in which twinning becomes more difficult.

The importance of twinning deformation mechanism at low temperature has been already found in the X1 [80]. At cryogenic temperatures, nanotwinning contributes to high ductility and fracture resistance of this material. Here, high density of twins was found as well in a zone next to the fracture tip.
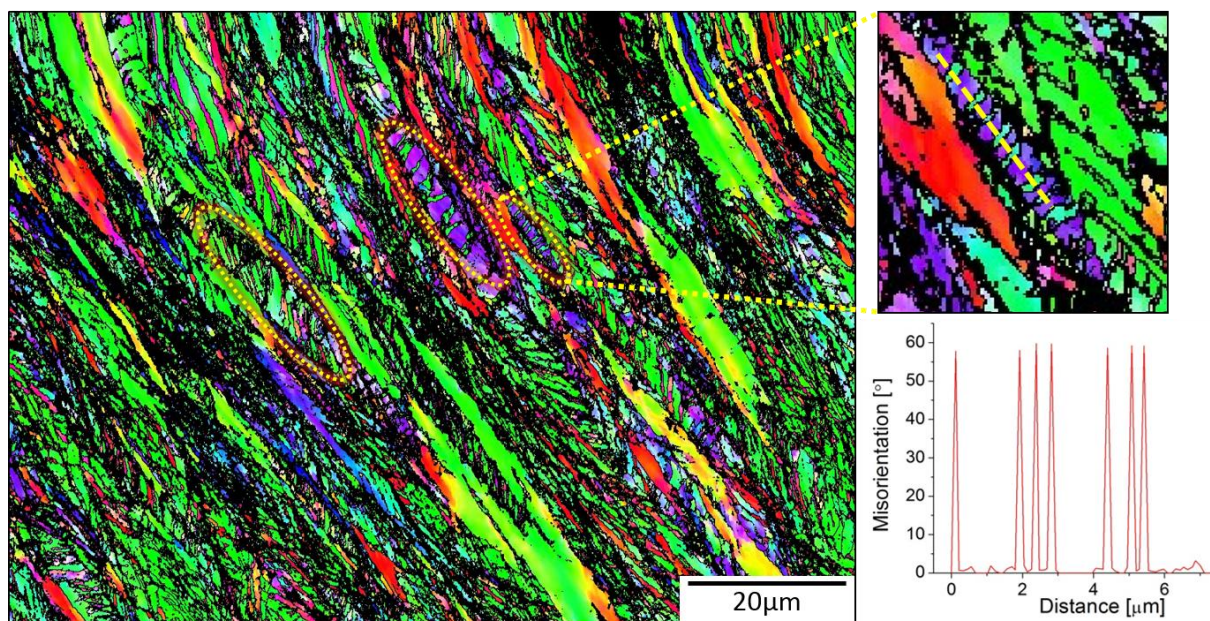

Figure 84. EBSD IPF image of the as-forged A3S after tensile test at -130ºC temperature. The analyzed zone was chosen close to the fracture. Twinned grains are marked in yellow circle; for one of them also misorientation profile is presented.

4.3.3. Cold-rolled state and the Hall-Petch law

Selected samples of the two materials were cold rolled (to 90% thickness reduction) after forging and hardness was measured as well (Figure 85). In the as-rolled state, hardness of both materials is high (408 HV for the X1 and 372 HV for the A3S) and higher for the X1. This latter preserves this level of hardness until 600°C while a decrease of hardness of the A3S starts at 550°C.
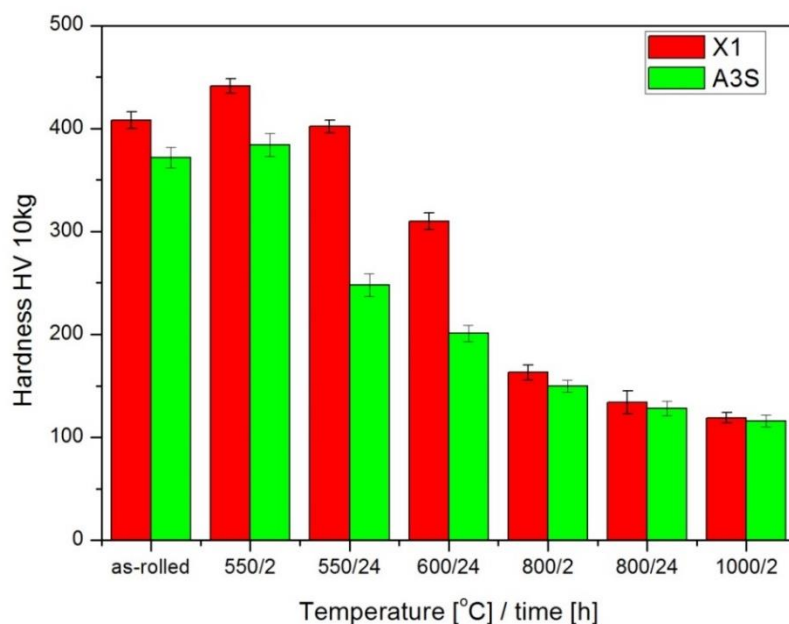
Figure 85. Effects of annealing temperature and time on hardness of the cold rolled X1 and A3S. Samples were air cooled after annealing.

In the as-rolled state the microstructure contains grains elongated in the direction of rolling (Figure 86 a). Again, alike in the as-forged state, the density of subgrains is very high, with subgrains of few hundreds of nanometers (Figure 86 b). Stability of this structure until 500°C was confirmed.

Proving hardness results, recrystallization of the X1 alloy is not finished after annealing at 550°C for 24h; only few recrystallized grains can be observed (Figure 87 a). Nonetheless, the recrystallization of the A3S is already completed after the same annealing (Figure 87 b). Recrystallization in HEAs is often slower than in conventional alloys because of the sluggish diffusion. Indeed the diffusion parameters are lower

than in conventional metals [13]. In fact, in HEAs there is no solvent because all the elements are mixed in the same proportions. As a result, the diffusion of an atom differs from one in conventional alloys. This provides different advantages for the properties, i.e. slower grain growth and higher recrystallization temperatures. Liu et al. [130] found that in equiatomic CoCrFeMnNi HEA the activation energy is high (~321 kJ/mol) and the coarsening kinetics is slow.
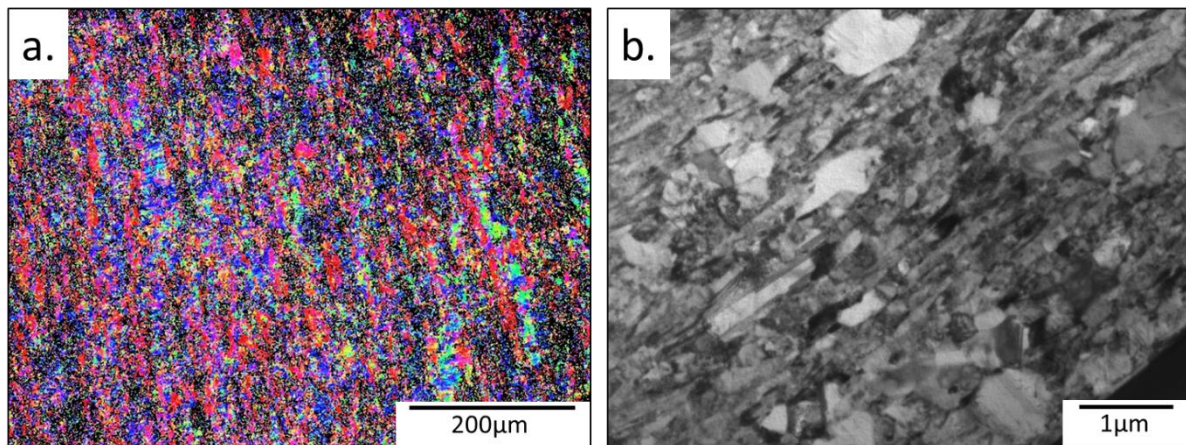
Figure 86. The rolled A3S: a) as-rolled IPF EBSD image (black points correspond to unindexed areas), b) BF TEM image after annealing (500°C/20h; M. Lenci, EMSE 2015).
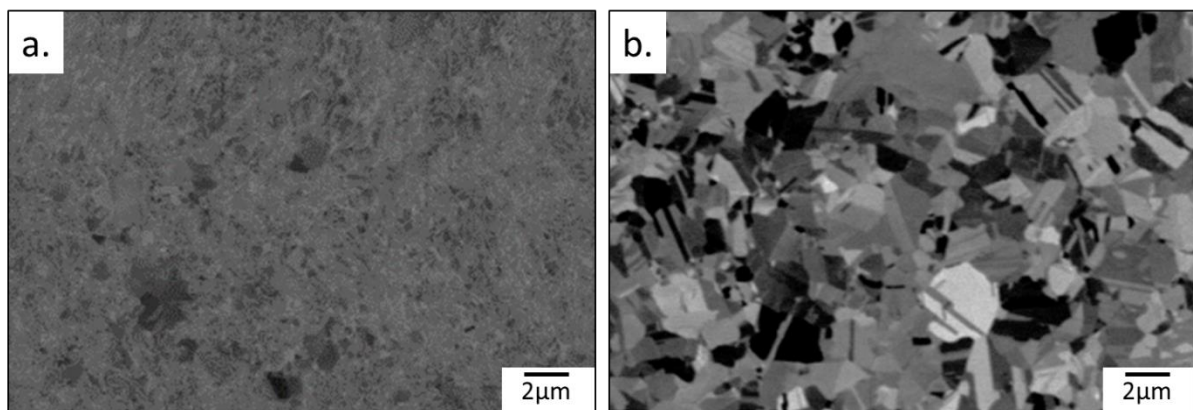
Figure 87. SEM images of the a) X1 and b) A3S after annealing at 550°C/24h.

After annealing at 1000°C for 2 hours, structure is fully recrystallized in both alloys, with similar grain size and high density of twins (Figure 88).
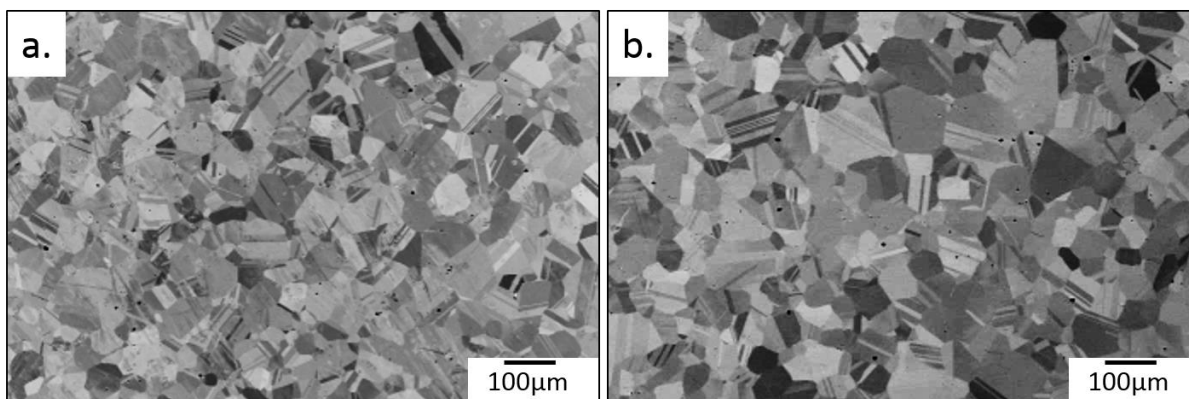
Figure 88. SEM images of the a) X1 and b) A3S after annealing at 1000ºC/2h.
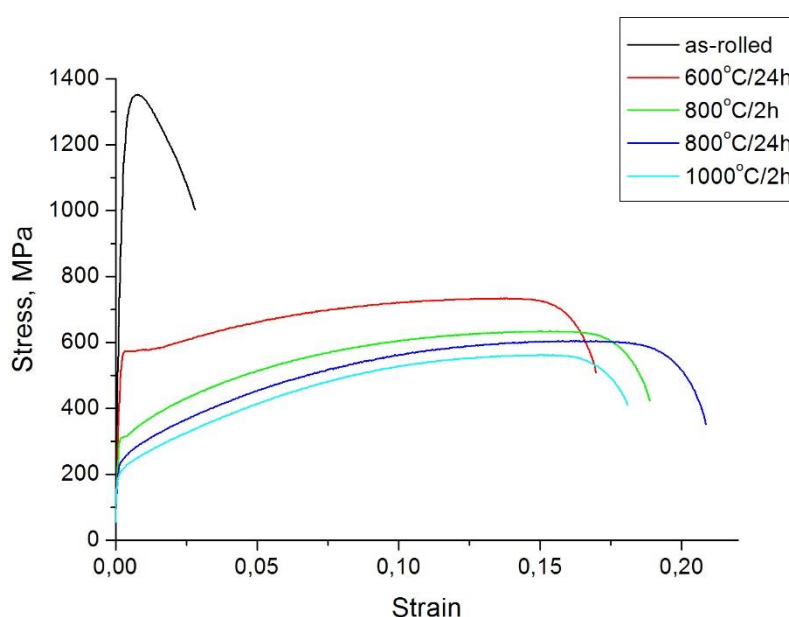
Figure 89. Tensile stress-strain curves of the A3S after different heat treatments.

Table 16. Values of YS and elongation obtained for the rolled A3S from tensile tests.

Heat treatment	Yield strength [MPa]	Elongation to fracture [%]
As-rolled	1333	2.6
600ºC/24h	560	16
800ºC/2h	325	18
800ºC/24h	261	20
1000ºC/2h	209	18

To evaluate the effect of grain growth on mechanical properties, tensile tests were conducted on samples annealed in various conditions (Figure 89). All the values are summarized in Table 16. In as-rolled state, yield strength of the A3S reaches a very high value (1333 MPa)

but its elongation to fracture is low (2.6%). For the samples annealed at 600°C/24 hours, yield strength is of 895 MPa for the X1 and 560 MPa for the A3S alloy. Regarding simple relationship between hardness and yield strength (YS = 3·HV, in MPa), obtained values are in agreement with hardness results. After heat treatments at higher temperatures, yield strength decreases and remains similar for all four alloys. Elongation is relatively high and in a range of 16-20%.
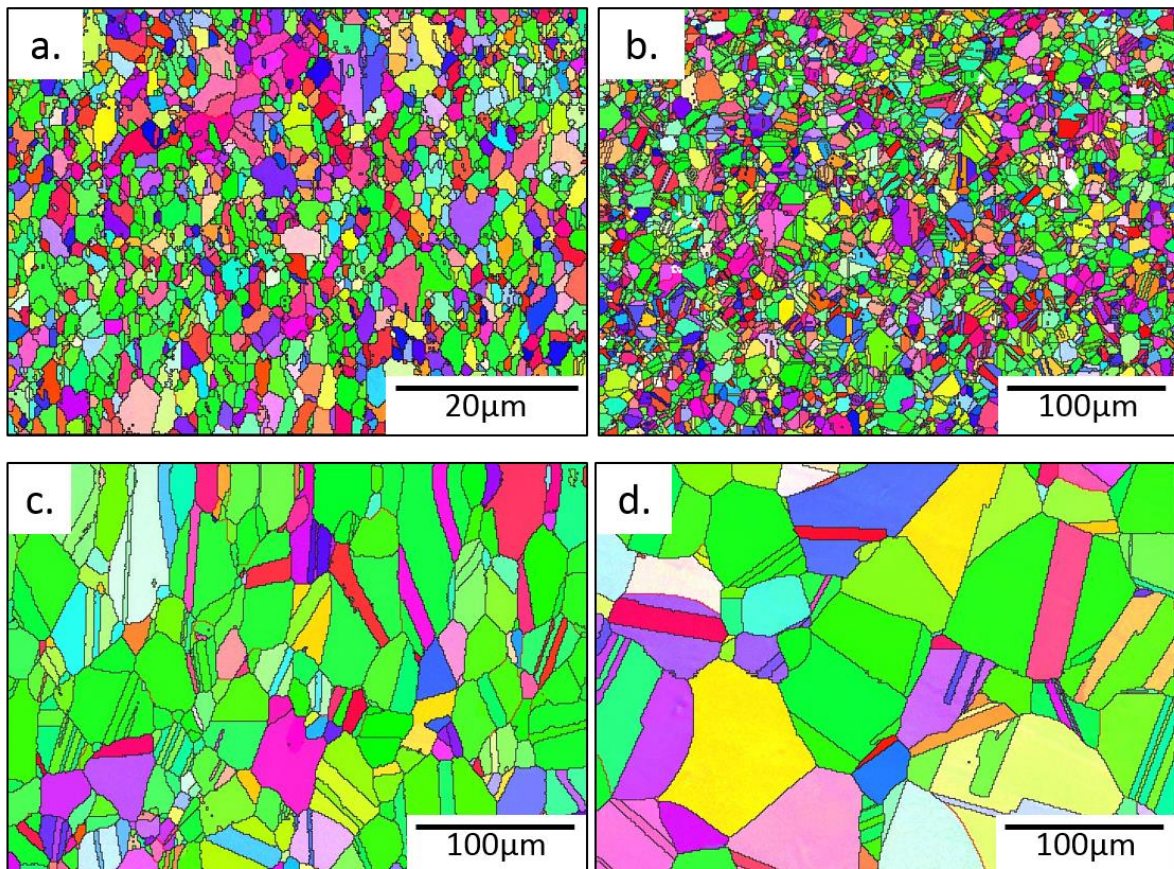
Figure 90. IPF EBSD images of the X1 after heat treatment: a) 600°C/24h, b) 800°C/2h, c) 800°C/24h, d) 1000°C/2h.

Then, the grain size obtained from the EBSD analysis (Figure 90) was calculated. Random distribution of grains was confirmed. All the images are not presented here.

The strength of alloys was studied as a function of grain size. Yield strength values follow the classical Hall–Petch relationship:

$$\sigma = \sigma_0 + \frac{k}{\sqrt{d}}$$

where σ_0 is the intrinsic strength of the alloy, d is the average grain size and k is the Hall–Petch coefficient. To make a direct comparison of the yield strength–grain size relationship, data are presented in a Hall–Petch plot in the form of yield strength versus $d^{-0.5}$ (Figure 91). If the Hall-Petch equation applies, the data can be presented as a straight line with a positive slope k. It can be observed in this graph that all the curves show a good linear relationship, indicating that the values of k and σ_0 obtained by the regression
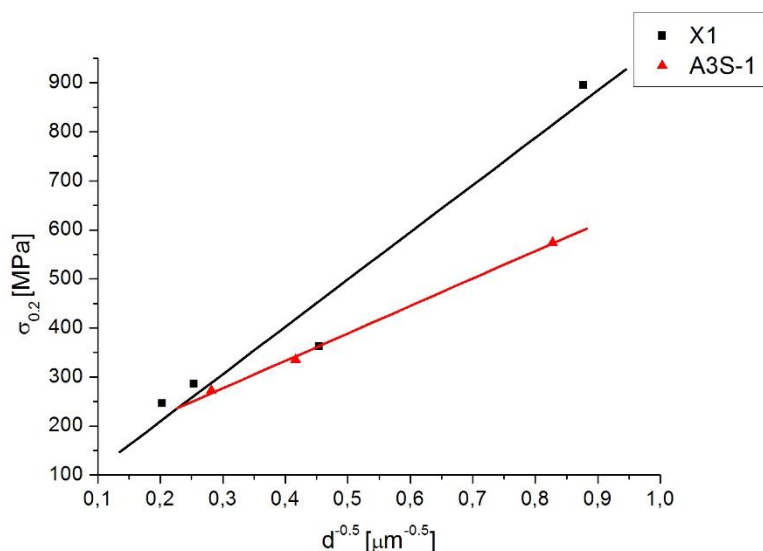
Figure 91. Hall-Petch plot.

analysis are reliable (Table 17). The results obtained by Otto et al. [66] for equiatomic CoCrFeMnNi are: 125 MPa for σ_0 and 494 MPa·$\mu m^{-0.5}$ for k. In other work [130] the coefficient k for equiatomic CoCrFeMnNi HEA takes a much higher value of 677 MPa·$\mu m^{-0.5}$. This is probably because of different initial state of the samples. From our experiments, obtained k value for the X1 (965 MPa·$\mu m^{-0.5}$) is twice higher than for the A3S, indicating more important strengthening in the X1. This difference can be however due to remaining strain hardening. Value obtained for the A3S is of 512 MPa·$\mu m^{-0.5}$, typical also for conventional low carbon steels [131]. Still, the error of this measurement is high due to low number of points on the graph.

Table 17. Parameters calculated from Hall-Petch law.

Alloy	σ_0 [MPa]	k [MPa $\mu m^{-0.5}$]
X1	16	965
A3S	117	512

To examine the kinetics of grain growth in investigated alloys, they were heat treated at chosen temperatures (800°C and 1000°C)

for different times. Initial grain size D_0 and kinetic constant K were obtained from the plot of grain size D as a function of annealing time t (Figure 92) using a formula [132]:

$$D^2 - D_0^2 = Kt$$
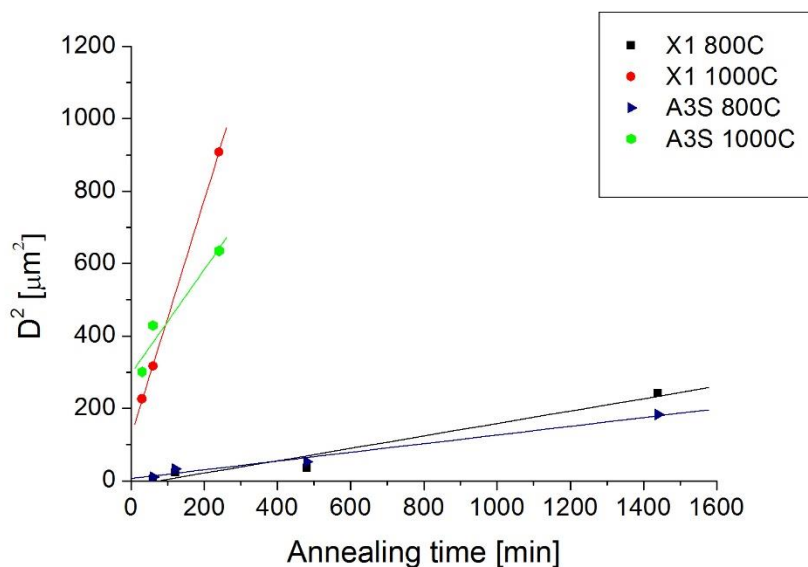
Figure 92. Grain size as a function of annealing time.

At lower temperature (800°C) grain growth is much slower than at 1000°C. From the graph two constants were calculated: K (from the slope) and D_0 (from the intercept). These values are specific for each material and temperature (Table 18).

The values of D_0 are experimentally uncertain considering that the offset state of the material was cold-rolled. Interestingly, for both materials D_0 parameter at 800°C is below 0 (X1) or close to 0 (A3S), resulting probably from recrystallization before grain growth. This is not the case of 1000°C, even though at higher temperature recrystallization should not be difficult. More detailed observations of the microstructure at elevated temperatures are needed and will be examined in the following chapter. Relatively low (twice lower in the A3S) value of K parameter, compared to classical alloys, in both materials can be strengthened by the fact that these alloys were prepared from high purity elements. Thus, all the possibility of grain growth inhibition by precipitations (carbides, oxides, etc.) is very limited and rather has its origins in sluggish diffusion. The K parameter is higher for the X1 at 800°C and especially at 1000°C, indicating slower grain growth in the A3S.

Table 18. D$_0$ and K parameters.

Alloy	Temperature [°C]	D$_0$ [μm]	K [μm²/min]	Q [kJ/mol]	K$_0$
X1	800°C	~0	0.171	167.3	16.99
	1000°C	11.12	3.258		
A3S	800°C	6.611	0.120	140.9	13.68
	1000°C	17.23	1.436		

From this data, also activation energy Q can be calculated, which is connected with grain growth:

$$K = K_0 e^{\frac{-Q}{RT}}$$

It is obtained from the plot of inversed absolute temperature vs kinetic constant (Figure 93).

Slope of this plot is:

$$a = \frac{-Q}{R}$$

where R is a gas constant; activation energy Q can be easily calculated which is a value specific for each material (Table 18). Values obtained for both alloys are similar to typical values for steels (304 stainless steel: 150 kJ/mol) but higher for the X1. This can explain easier start of recrystallization in the A3S, shown by previous values of hardness and SEM images. Still, here again the number of data points should be higher to reassure the credibility of obtained Q parameter.
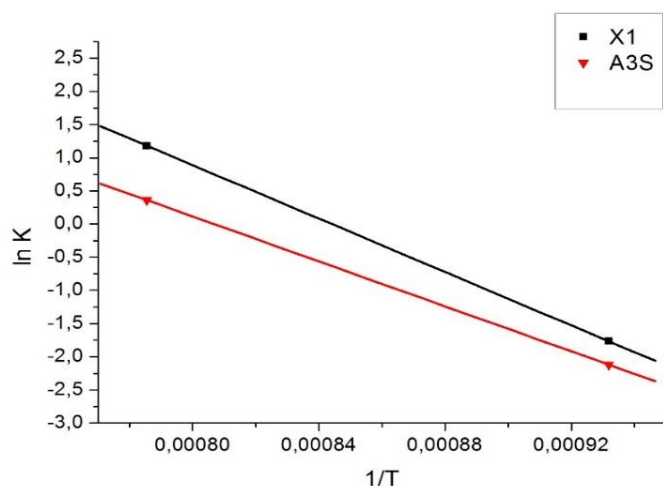
Figure 93. Plot of ln K vs 1/T.

All the results presented in this chapter confirm that investigated alloys are forgeable and ductile. Both materials obey the Hall-Petch law relationship and the hardening potency is higher in the X1 than in the A3S (higher Hall-Petch k coefficient for the X1). This part of work leads to the next chapter, focused on recovery and recrystallization behavior especially at higher temperatures and evolution of the microstructure during various heat treatments. Dislocations character will be studied as well since it contributes to hardening behavior of alloys.

5. Origins of the mechanical properties

Original properties of high entropy alloys come in all probability from specific phenomena occurring in their microstructure. Due to an important local lattice distortion, sluggish diffusion and possibility of short range ordering, phenomena such as recovery and recrystallization may differ from conventional alloys. Dislocation mobility is particularly strongly influenced.

5.1. Static recovery and recrystallization phenomena of the A3S

Classical processes occurring in a deformed material in the course of heating are static recovery and recrystallization, for which a driving force is the difference in internal energy between the strained and unstrained material. During recovery, at early stages of annealing, rearrangement of dislocations takes place into configurations with lower energy. Then, during recrystallization, new grains (recrystallization nuclei) are developed, and are free of dislocations. The growing areas replace strain-hardened grains (Figure 94). Recrystallization starts approximately at the temperature of about ~0.5 melting point (in Kelvin). After recrystallization, a growth of new regions begins for which the driving force is the energy of high angle grain boundaries.

Observations of hot forged samples annealed in temperatures up to 600°C confirm the classical recovery and recrystallization process. After annealing at 600°C during 48 hours, structure of the A3S is still of ultra-fine grained type (Figure 95 a), what is also seen in diffraction of this area (in the form similar to rings). However, appearance of grain boundaries is different (Figure 95 b) compared to as-forged material – part of them seems to be more equilibrated and sharp indicating high angle grain boundaries. Density of dislocations in grains is still high. It means that this temperature and time of annealing is not high enough to obtain recrystallized structure, but it enables

movement of dislocations and thus modification of grain boundaries character (recovery). No precipitations or traces of new phases were found.
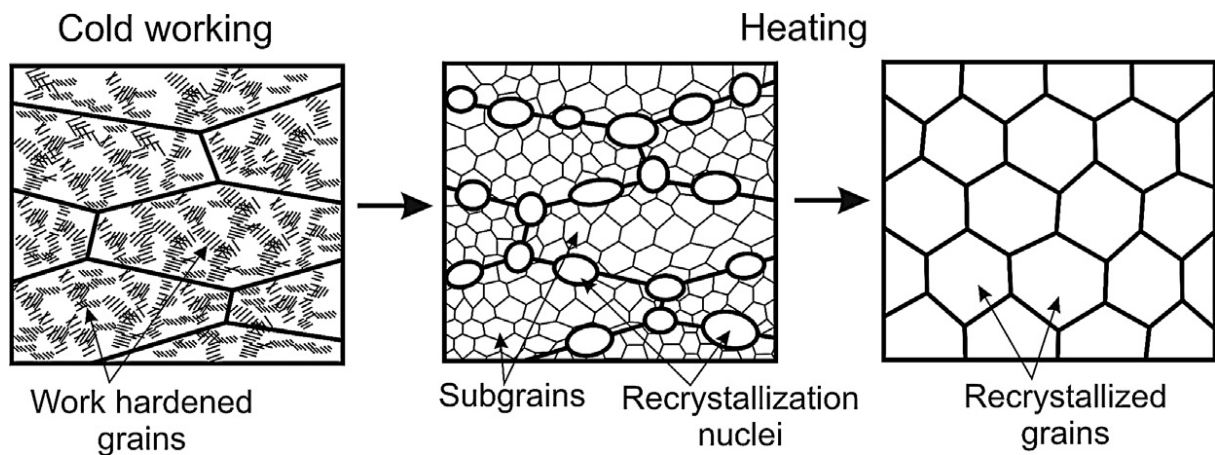
Figure 94. Schematic image of the discontinuous static recrystallization [69].
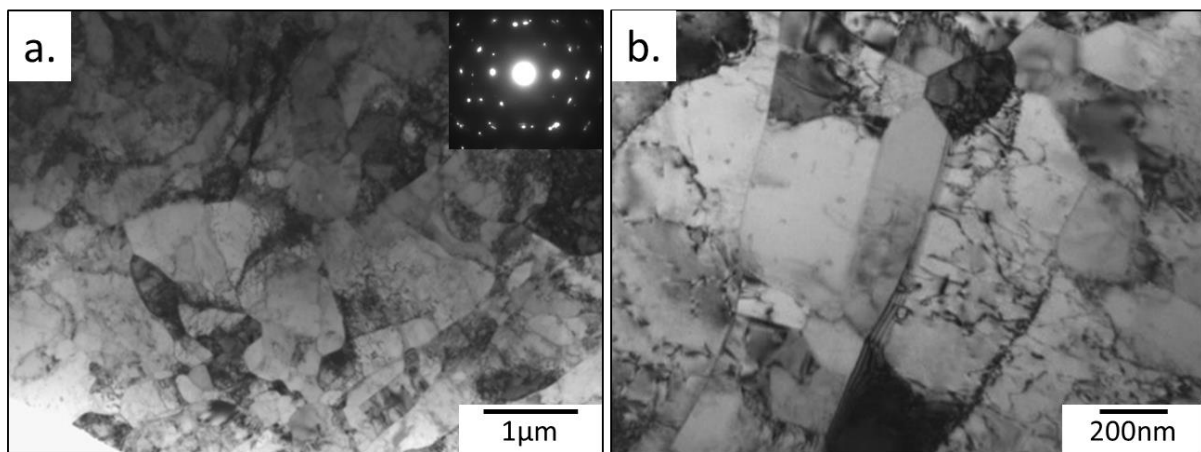
Figure 95. TEM bright field images of the A3S after annealing at 600ºC during 48 hours.

After longer heat treatment (1 month) at 600ºC, microstructure recrystallizes and consists of equiaxed grains of few micrometers and twins (Figure 96 a) with a very low dislocations density, typical for common recrystallized metallic alloys. Yet, still in some regions work hardened grains with high density of dislocations were present (Figure 96 b), which means that even annealing for a very long time (1 month) at 600ºC is not enough to fully recrystallize the microstructure. This annealing process,

allowing obtaining grains free of dislocations, will be applied later in our material to study the mechanisms of plastic deformation (and especially character of dislocations).
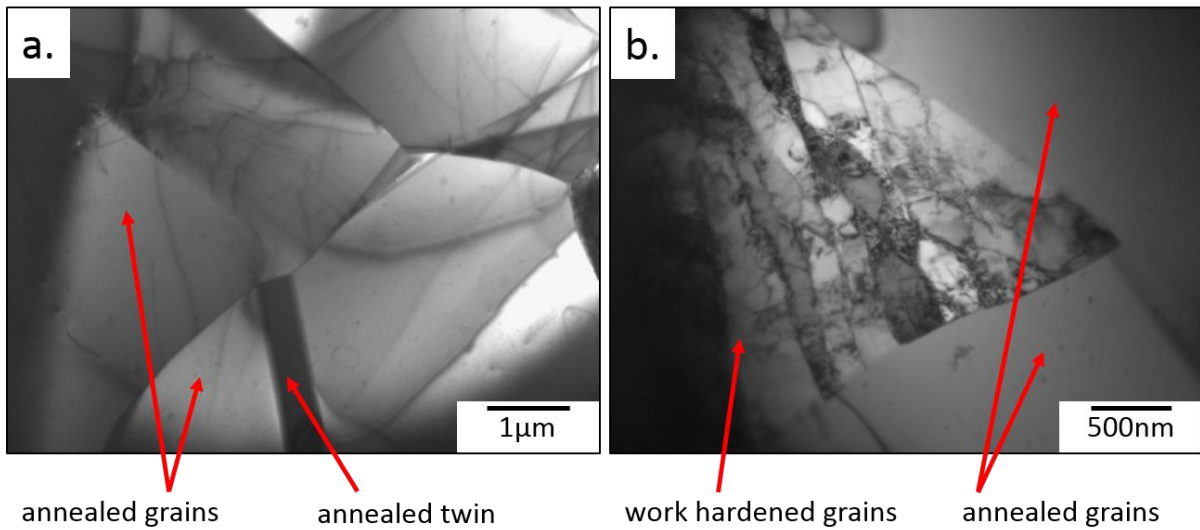
Figure 96. TEM bright field images of the A3S after annealing at 600ºC during 1 month (744 hours). Annealed and work hardened grains are marked with arrows.
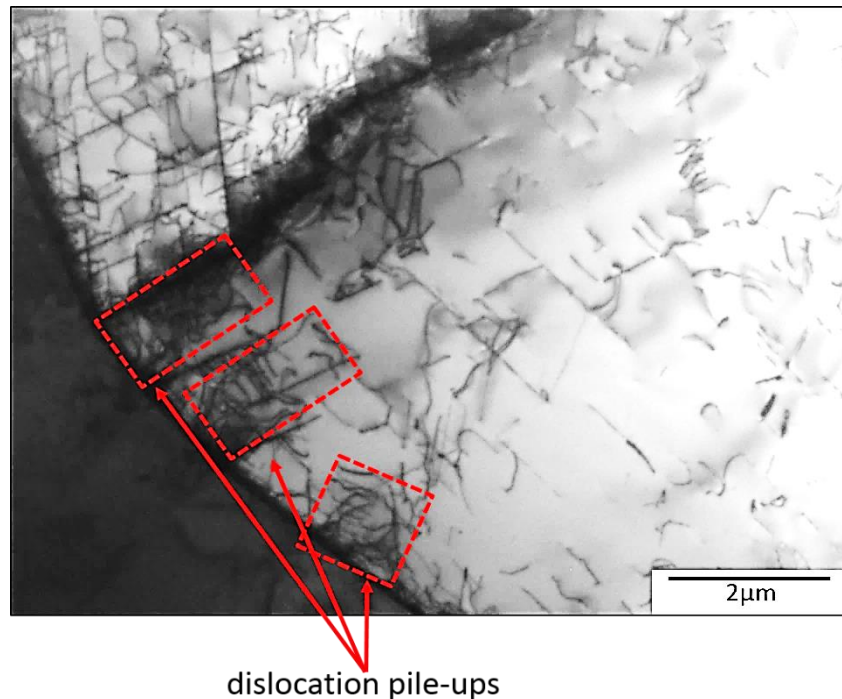
Figure 97. TEM bright field images of the A3S after annealing 800ºC during 8 hours. Dislocation pile-ups are marked with red dotted rectangles.
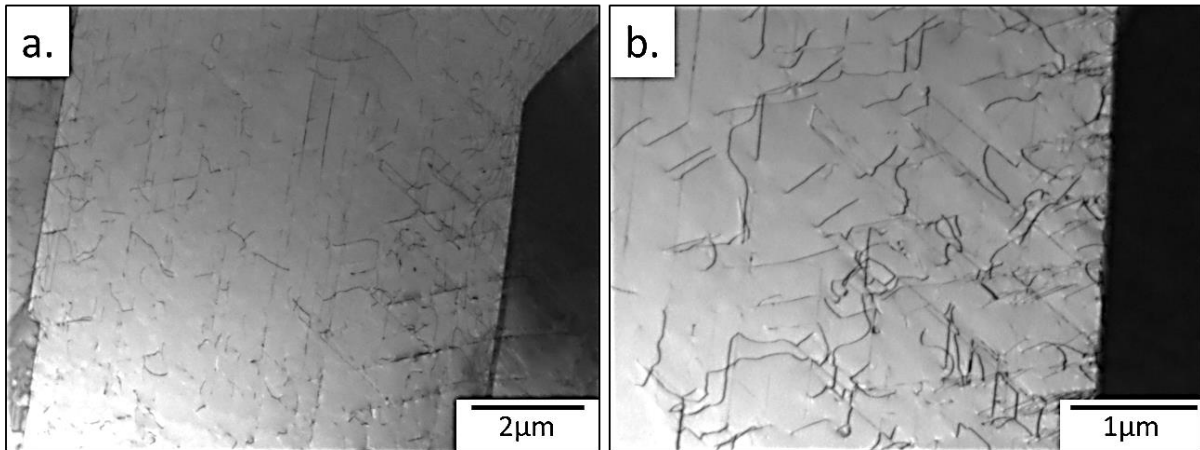
Figure 98. TEM bright field images of the A3S after annealing at 800°C during 8 hours.

Consequent annealing at higher temperatures were conducted, with the expectation that dislocation density will decrease and grain size will increase. Surprisingly, an unexpectedly high density of dislocations was found. Grains, however, were found to be of few tens of micrometers, without any traces of newly nucleated grains.

At 800°C large recrystallized grains of a few tens of micrometers with high angle grain boundaries were observed. A great number of dislocations is present near grain boundaries (pile-ups, Figure 97) and inside the grains (Figure 98 a, b), as well as annealing macrotwins. Dislocations are oriented in certain directions.

Dissociated dislocations with higher magnification and in dark field are shown in Figure 99.
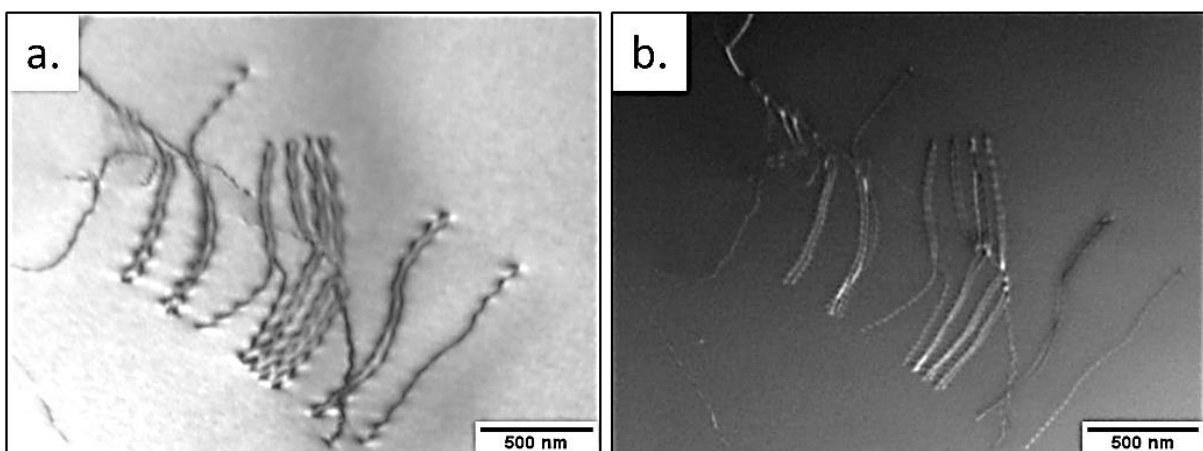
Figure 99. Dissociated dislocations in a) bright and b) dark field mode.

High density of dislocations was found as well after annealing at very elevated temperatures, at 1000°C and 1100°C (~0.8 T$_M$) for different times (Figure 100), in both alloys.
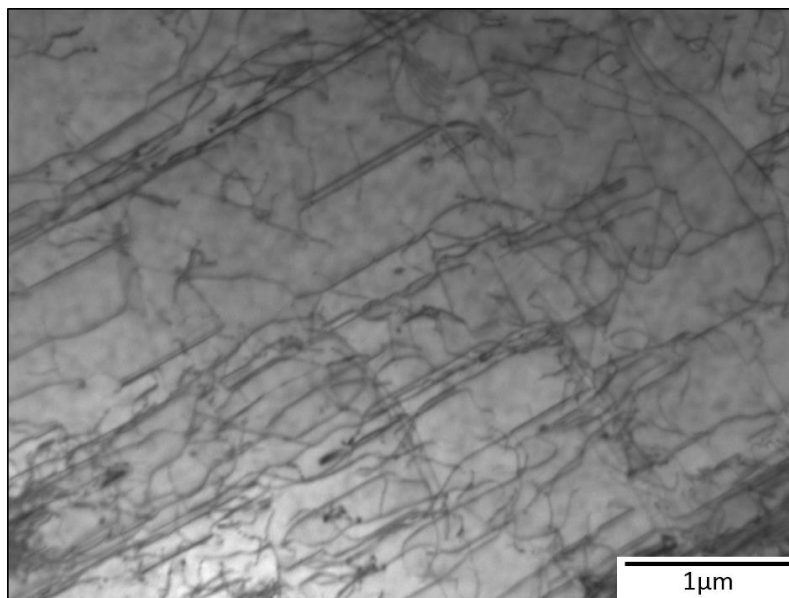
Figure 100. TEM bright field image of the A3S after annealing at 1100°C/48 hours.
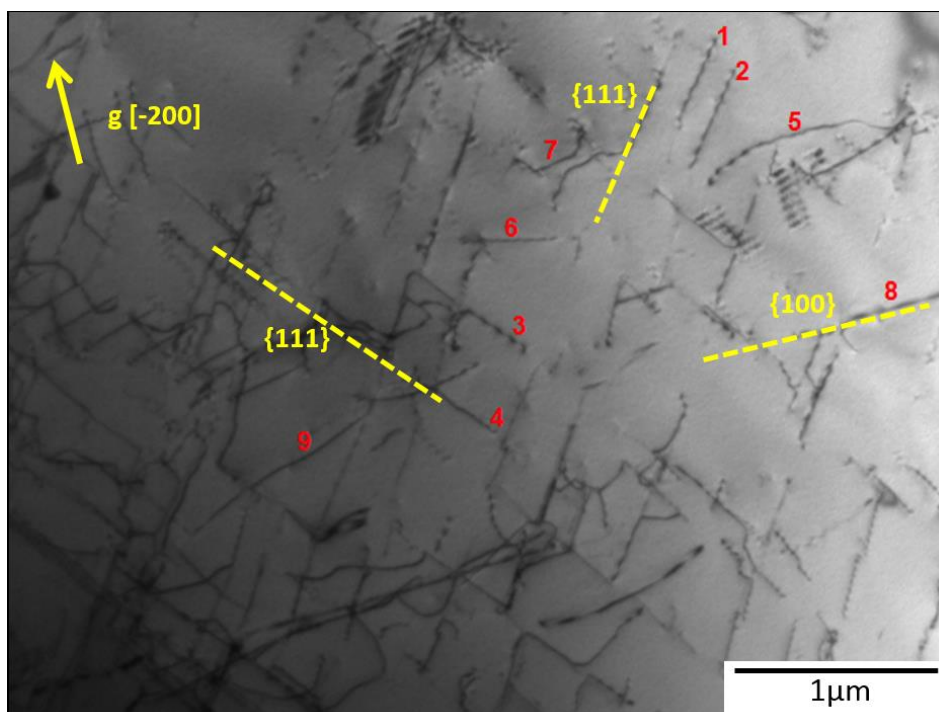
Figure 101. TEM bright field image of the analyzed area of the A3S after heat treatment at 1100°C during 10 minutes. Dislocations 1-9 were examined in different diffraction conditions (Figure 102).
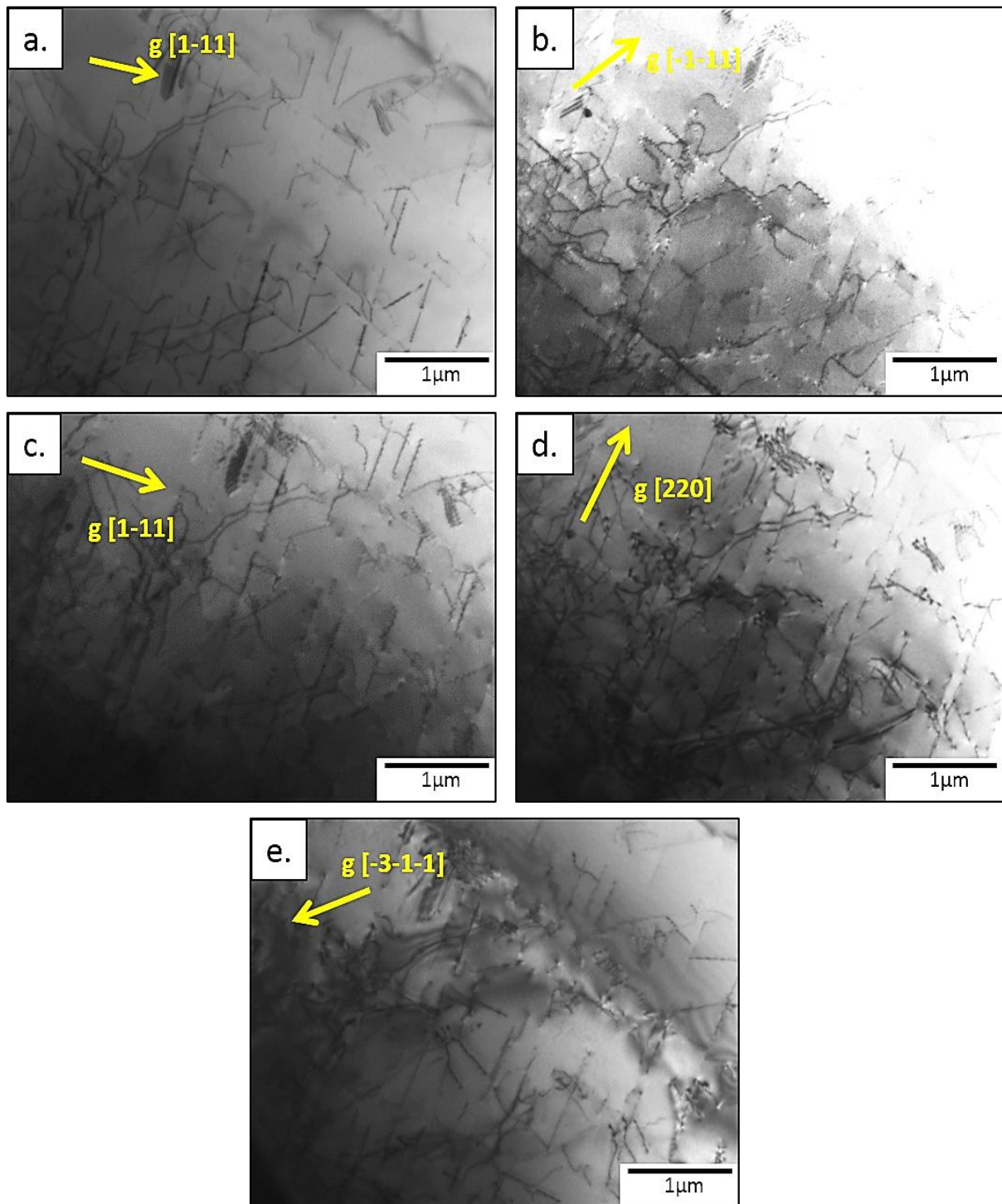
Figure 102. Series of bright field TEM images of the A3S after heat treatment at 1100ºC during 10 minutes in different diffraction conditions.

Character of these dislocations was studied in two beam conditions, using invisibility criterion $\mathbf{g} \cdot \mathbf{b} = 0$, where $\mathbf{g}$ is the diffraction vector and $\mathbf{b}$ is the Burgers vector. If the scalar product of the two vectors gives zero, dislocation will be invisible. Thus,

successive analysis of dislocations in different configurations allows identifying Burgers vector. Three noncoplanar **g** vectors which fulfill this criterion are sufficient to determine indices for **b**.

Selected zone (Figure 101) with different types of dislocations was observed in two different zone axis [011] and [1-1-2] with different two beams conditions. A systematic analysis is presented and Figure 102. Nine dislocations were chosen for calculations of Burgers vector. This choice was due to their straight shape and orientation in three different directions. Crystallographic orientation of this zone allowed calculating Burgers vectors for dislocations 1, 2, 5, 6 (it was [1-10]) and 3, 4, 7, 8 ([10-1]).

Table 19. Burgers vector of studied dislocations based on invisibility criterion.

Dislocation number	Burgers vector b	Line vector l
1, 2, 5, 6	1-10	110
3, 4, 7, 8	10-1	101

Thus, values of Burgers vectors **b** and line vector **l** (calculated from n = **b** x **l**, where n is a glide plane) are typical for FCC metals and the CoCrFeMnNi HEA.

All these results indicate that typical phenomena of recovery and recrystallization do not apply here. Instead of classical dislocation rearrangement at lower temperatures forming subgrains and recrystallized structure free of dislocations at high temperatures, here we observed the opposite. After heat treatment at 600°C during one month most of the grains are almost free of dislocations, in agreement with the classical theory. After annealing at high temperatures (800, 1000 and 1100°C, up to two weeks), however, dislocation density is very high and they are arranged in characteristic (111) and (100) planes.

Further experiments confirmed the results obtained in TEM. First, consequent EBSD experiments on samples heated at 1100°C from 6 minutes to 336 hours (Figure 103)

showed a grain growth without any signs of recrystallization, indicating rearrangement of nanocells of dislocations inside grains and growth of high angle grain boundaries from the as-forged state.
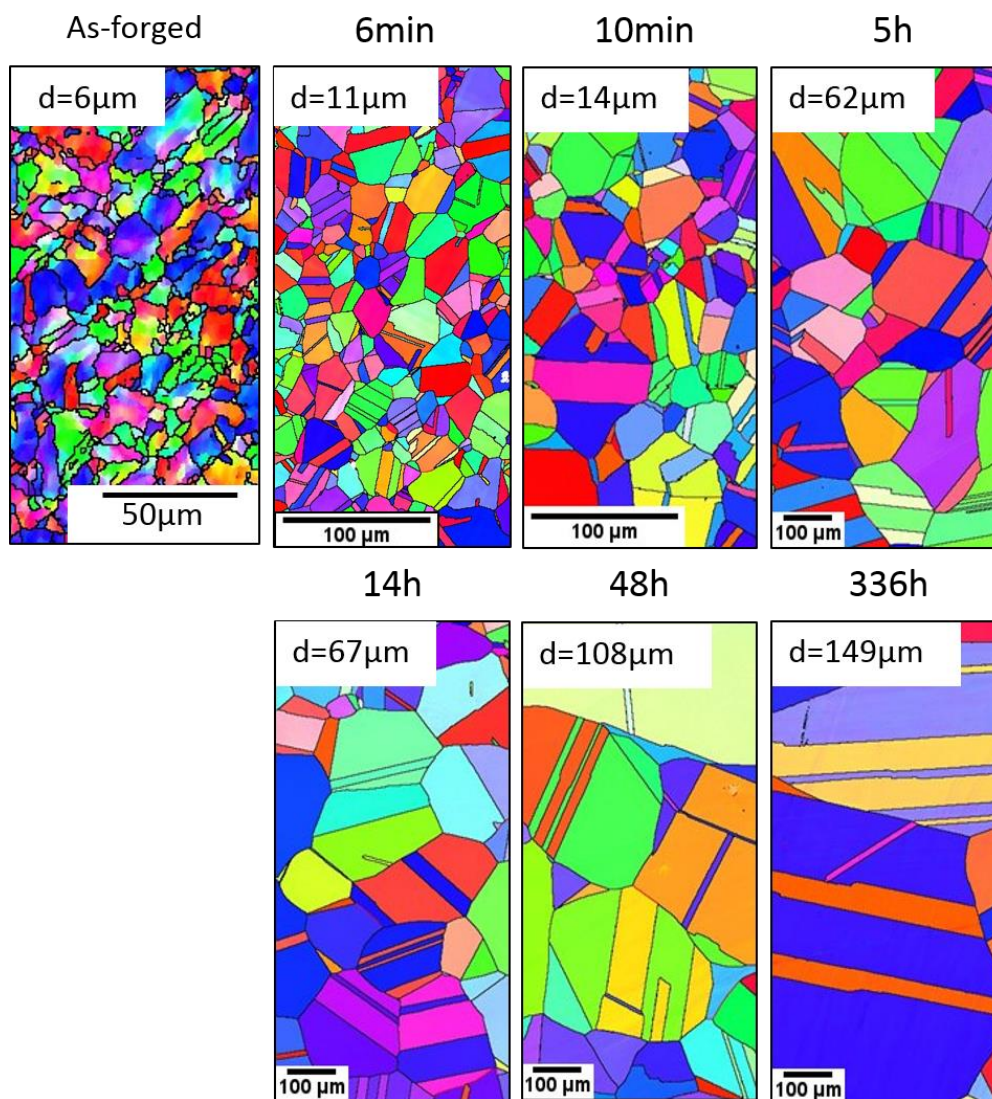
Figure 103. IPF EBSD images of the A3S in the as-forged state and after annealing at 1100°C for different times, with an average grain size.

Similar phenomena were observed in *in situ* TEM. The A3S (as-forged) was heated up to 900°C and different regions were observed, in focus on dislocation and grain boundaries movement. Until 800°C almost no mobility of dislocations was observed. Any nucleation or recrystallization did not occur, but rather grain growth (Figure 104), in agreement with previous EBSD analysis. This movement of grain boundaries was

observed at about 800°C. The density of dislocations, surprisingly, does not change with this boundary movement. This density of dislocations remained very high even at 900°C.
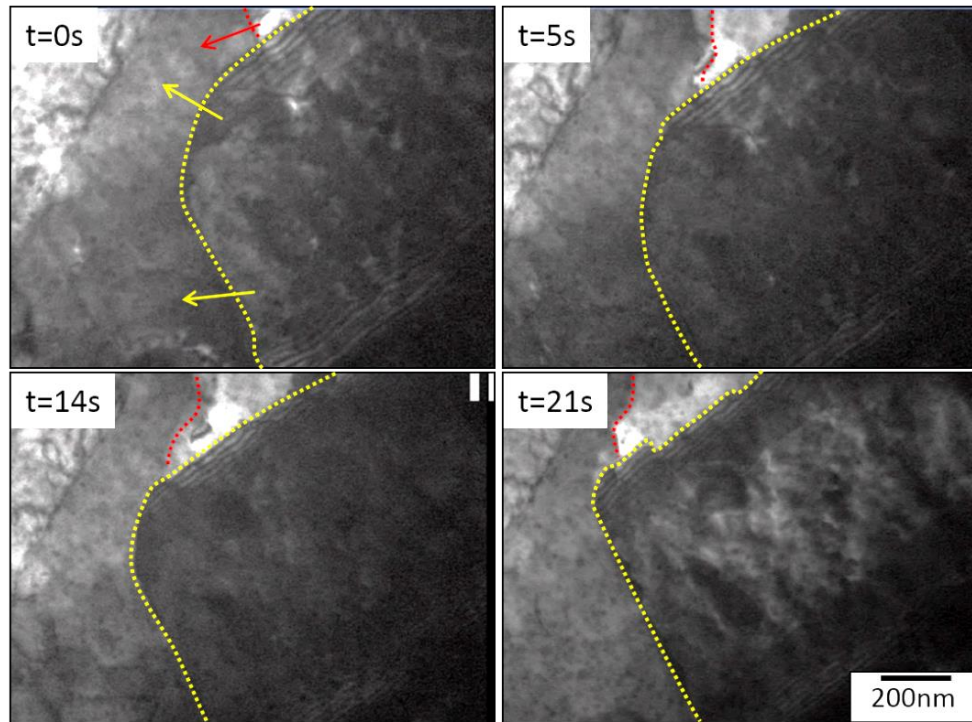
Figure 104. Grain growth during *in situ* heating experiments at about 800°C. Yellow dashed line indicate grain boundary position. Red dashed line is probably a subgrain boundary. No stress applied.
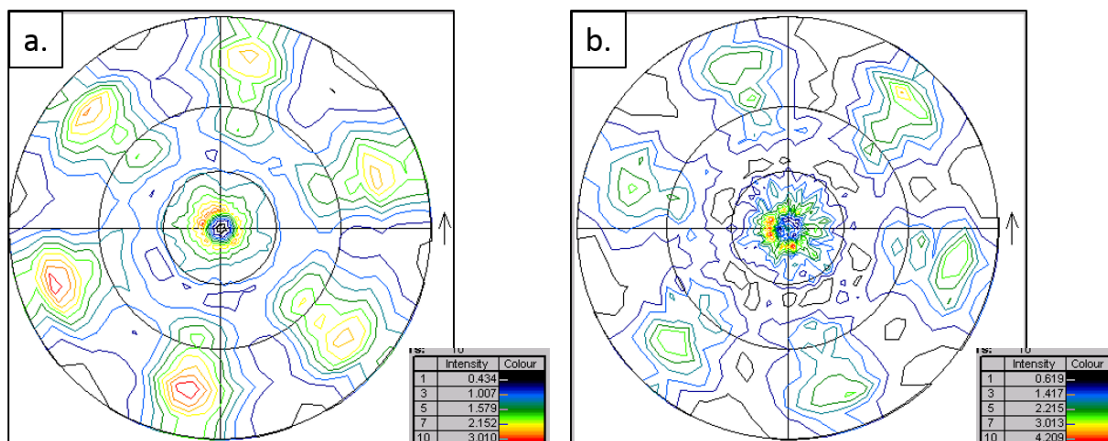
Figure 105. (111) pole figures of the a) as-forged and b) annealed (1100°C/10 min) A3S measured by XRD. The forging direction is normal to the paper.

The phenomena was further confirmed with XRD measurements of the texture. The as-forged A3S samples possesses a characteristic six-fold symmetry (Figure 105 a). In

the annealed state (1100°C/10 min), this symmetry is conserved and intensity of peaks increases in the same spots (Figure 105 b). It is probably an indication of lack of recrystallization and larger grain size, again in agreement with the hypothesis of grain growth rather than nucleation of new grains.

Finally, three types of microstructures can be distinguished (Figure 106), depending on the temperature of heat treatment:

- Low temperature structure (below 600°C): similar to the as-forged state, with cells/subgrains of few hundred of nanometers and high density of dislocations; stable FCC solid solution without decomposition or precipitation traces;

- Intermediate temperature structure (between 600°C and 700°C): with grains of few micrometers almost free of dislocations; some areas remain strongly deformed; considered as a recrystallized state;

- High temperature structure (above 700°C): with grains of few tens of micrometers and high density of dislocations which are arranged in characteristic planes of (111) and (100) type. Subgrains/cells of dislocations are not present anymore. A typical recrystallization was not observed here.
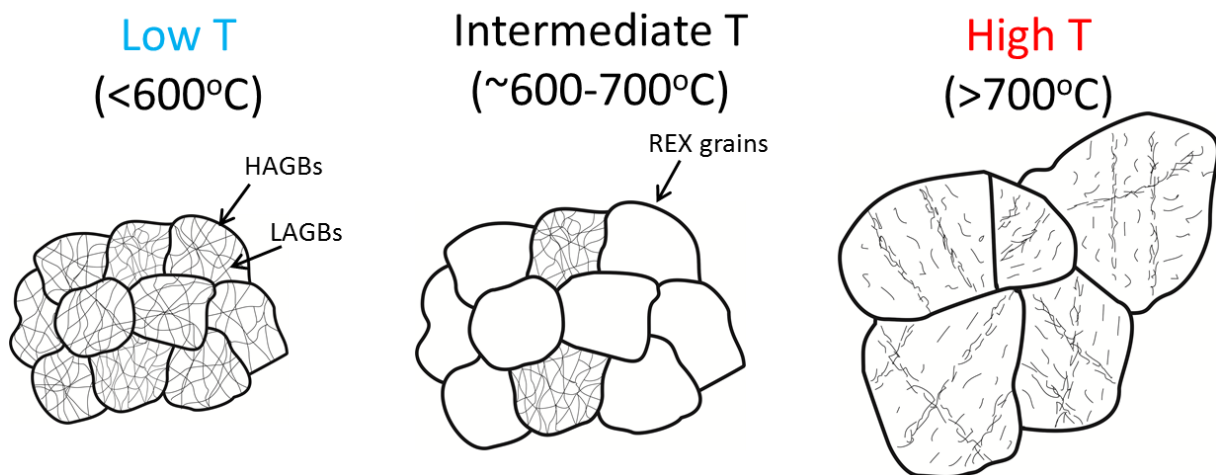
Figure 106. Three main types of microstructures obtained after different heat treatment processes.

This unusual phenomena of retaining high density of dislocations even after annealing at temperatures way much above 0.5 T$_M$ may be explained by lower driving force for recrystallization compared to pure metals (Figure 107). If the energy of a perfect crystal for HEAs is already elevated, an annihilation of dislocation will not be beneficial for the system and only some kind of rearrangement will take place.

Figure 107. Possible differences in energies of a perfect crystal for metals and high entropy alloys.
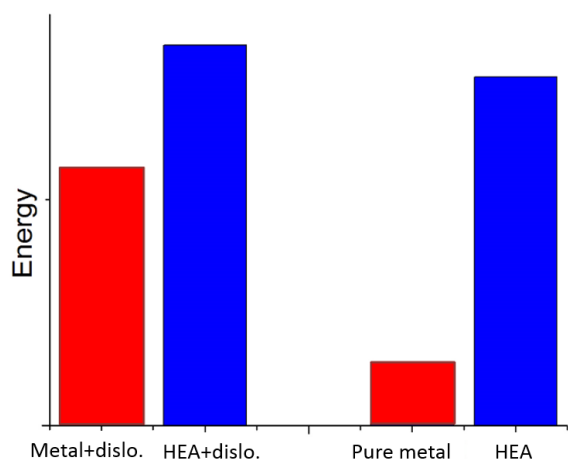
The subject of recovery and recrystallization in this new materials needs more examination due to its complexity. Other hypotheses will be further developed in Chapter 5.3.

5.2. Dislocation density measurements

The density of dislocations, even if seen as high with TEM, was evaluated in a more general manner. This density was calculated by X-ray diffraction peak profile analysis as a function of temperature. This approach is complementary to TEM, where only a very small area of the sample can be observed and thus it is not representative for a bulk material. The two techniques were compared.

The XRD profiles were analyzed with the variance method, based on the moments of the intensity profiles [133]. In this method, the particle size and strain induced broadening is related to the different asymptotic behavior of the k-th order restricted moments of the peak profile:

$$M(q') = \frac{\int_{-q'}^{q'} q^k I(q) dq}{\int_{-\infty}^{\infty} I(q) dq}$$

where $I(q)$ is the intensity distribution as a function of $q = \frac{2}{\lambda}[\sin(\theta) - \sin(\theta_0)]$, in which λ is the wavelength of the X-ray, θ is the diffraction angle and θ_0 is the Bragg angle. The second and the fourth order restricted moments can be defined as:

$$M_2(q) = \frac{1}{\pi^2 D_s} q - \frac{L}{4\pi^2 K^2 D_s{}^2} + \frac{\Lambda\langle\rho\rangle \ln(\frac{q}{q_0})}{2\pi^2}$$

$$\frac{M_4(q)}{q^2} = \frac{1}{3\pi^2 D_s} q + \frac{\Lambda\langle\rho\rangle}{4\pi^2} + \frac{3\Lambda^2\langle\rho^2\rangle}{4\pi^2 q^2} \ln^2(\frac{q}{q_1})$$

where L is the taper parameter, K is the Scherrer constant, D_s is the average column length of crystallites, ρ is the average dislocation density, q_0, q_1 are fitting parameters and $\Lambda = \frac{\pi}{2} g^2 b^2 C$, where g and b are the magnitudes of the diffraction and Burgers vectors, respectively. C is the dislocation contrast/orientation factor.

Here, two types of samples were investigated for both the X1 and A3S: first, nanostructured samples (in as-forged state and after heat treatment at 600°C/48 hours) and then, annealed samples (after heat treatment at 1100°C/48 hours and 1100°C/2

weeks). Figure 108 and Figure 110 show the (111), (200), (220) and (311) peaks for both the X1 and ASS in the as-forged state and after different heat treatments. The narrowing is observed for all peaks after annealing at 1100°C, where we already observed grain growth and lack of subgrains. After longer time of annealing at 1100°C the peaks become even narrower, indicating lower density of dislocations. Still, this density remains very high (Table 20), with magnitude of 10^{14} m$^{-2.}$ This density is typical for hot rolled steels [134] and in no case for recrystallized alloys.

Table 20. Dislocation density after different heat treatments.

Sample	X1 [x10^{14} m^{-2}]	A3S [x10^{14} m^{-2}]
As-forged	11	15
600°C/48h	10	13
1100°C/48h	2.7	2
1100°C/2 weeks	2.7	1.2
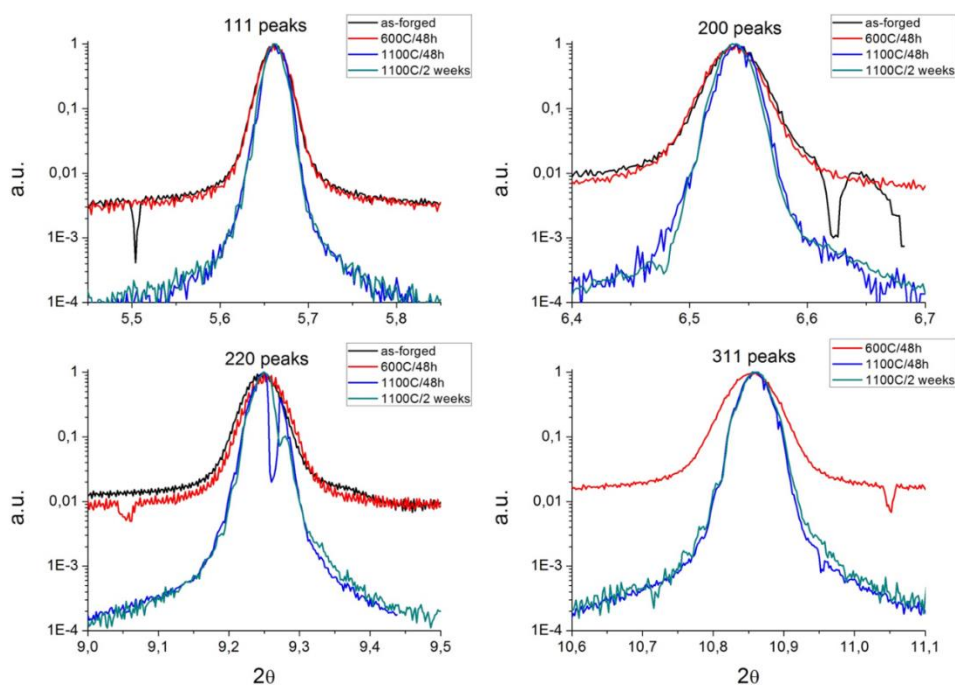
Figure 108. (111), (200), (220) and (311) peaks of the X1 after different heat treatments measured at ESRF (ID 31).
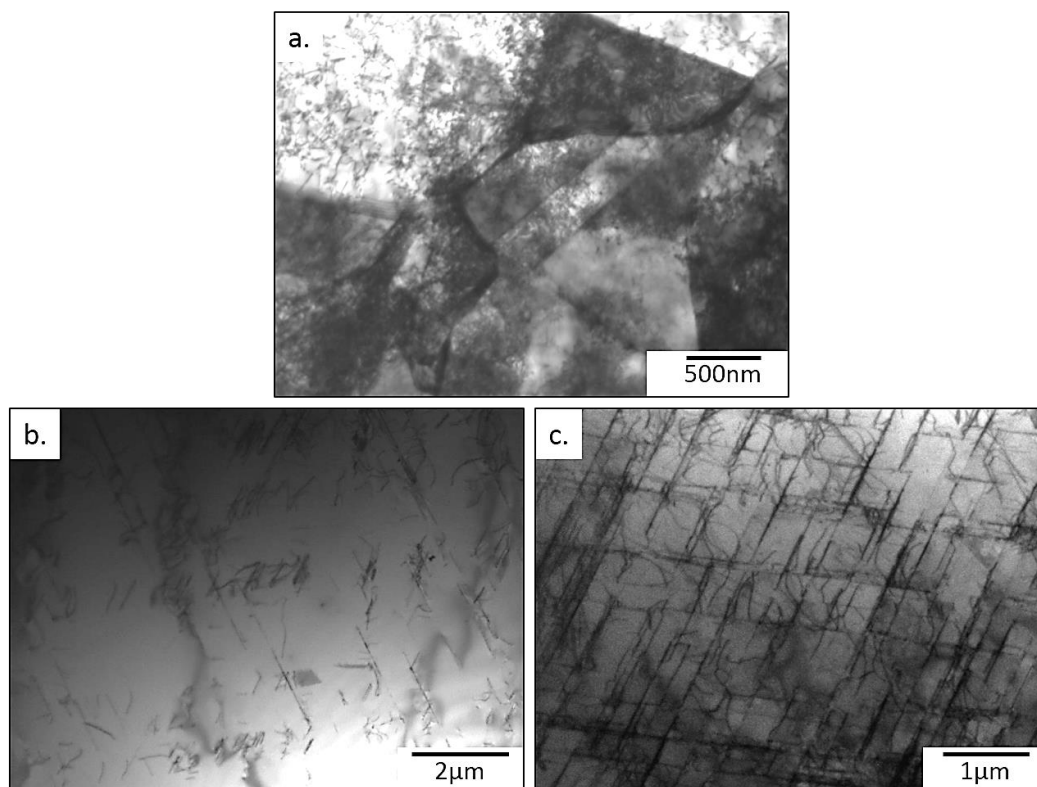
Figure 109. TEM bright field images of the X1 corresponding to Figure 108: a) as-forged, b) 1100ºC/48h, c) 1100ºC/2 weeks.
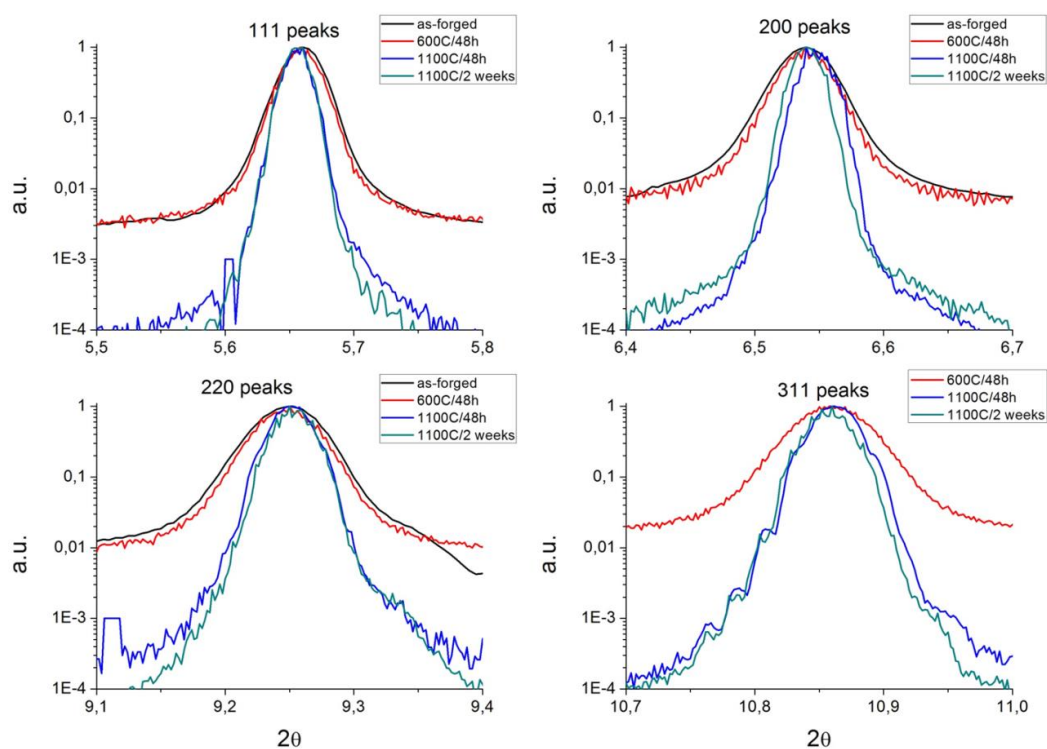
Figure 110. (111), (200), (220) and (311) peaks of the A3S after different heat treatments measured at ESRF (ID 31).
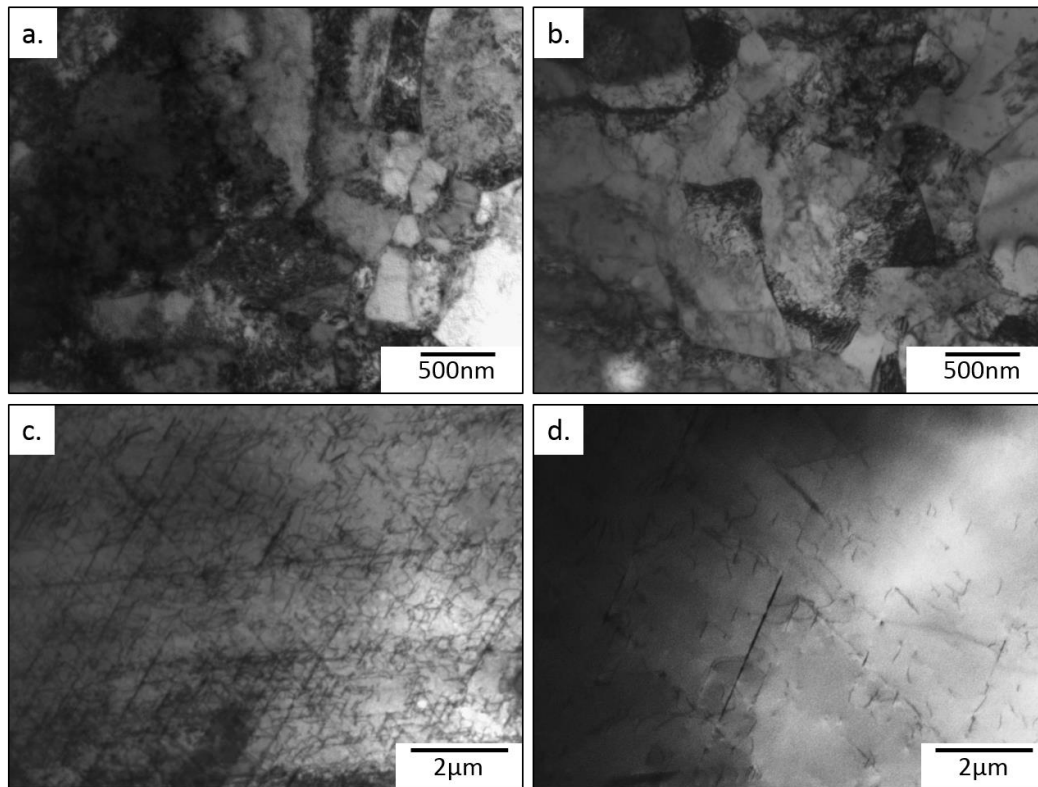
Figure 111. TEM bright field images of the A3S corresponding to Figure 110: a) as-forged, b) 600°C/48h, c) 1100°C/48h, d) 1100°C/2 weeks.

By comparing XRD measurements with corresponding TEM images (Figure 109, Figure 111), the obtained values of dislocation density are in a good qualitative agreement with microstructure observations. Comparing as-forged and medium-temperature annealed states with high-temperature annealed samples, in the latter this density decreases but remains elevated (typical values for recrystallized steel is of $10^{12} - 10^{13}\,\mathrm{m}^{-2}$ [135]). TEM, however, is not as representative as XRD, since there may be differences in the average density of dislocations in different regions or grains in the analysed sample. Higher observed density in a specific zone may be also due to larger thickness of the sample. Thus, both techniques should be applied and correlated.

5.3. Hypotheses on the origins of high dislocation density after annealing

5.3.1. Short range ordering and Peierls stress

First possible explanation of this phenomenon can be any kind of segregation or, at smaller scale, chemical fluctuations and short range ordering. Similar behavior, with high density of dislocations after high temperature heat treatment, was studied by Roy et al. [136] on aluminium alloy AA1235. This alloy was first cold-rolled (92%) and then annealed at different temperatures. Microstructures were observed in TEM. In deformed state (Figure 112 a), structure consists of cellules of dislocations of few hundred of nanometers. After annealing at 250°C/240 minutes (Figure 112 b), recrystallization grain growth is observed with almost no dislocations inside. Similar structure should be expected at higher temperature annealing, but (as authors explained) Al$_3$Fe particles precipitate and impede the motion of grain boundaries and dislocations (Figure 112 c, d). Thus, grains with a very high density of dislocations were found, similar to our microstructures annealed at 800°C and above.
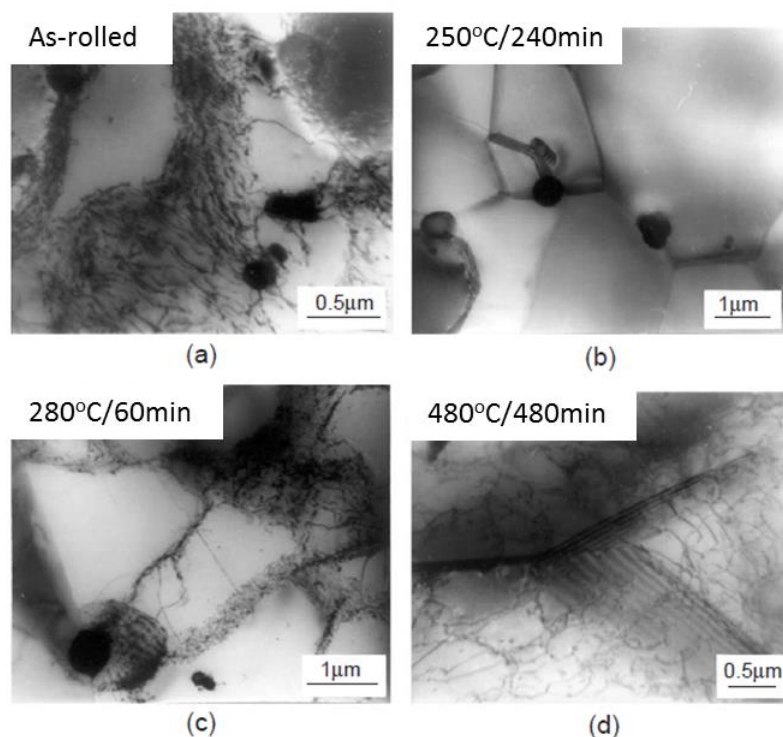
Figure 112. Microstructures of Al alloy AA1235 after different heat treatments [1].
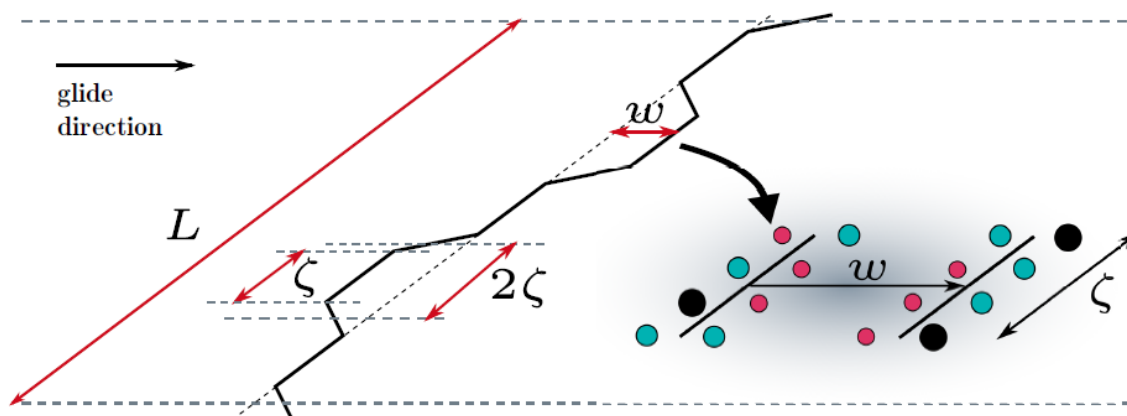
Figure 113. Schematic image of a low-energy wavy dislocation moving through a random field of atoms. Here 2ζ is a lateral length of a segment with ω amplitude [137].

In case of both the A3S and X1, however, only one FCC phase was found with a standard ~3.6 Å lattice parameter, confirmed in XRD analysis and TEM observations. Thus, fluctuations of the composition at atomic scale should be taken into consideration, namely short range order (SRO). This phenomenon is hard to measure and was found only in few HEAs [138], but can be an explanation of local barriers to dislocation movement. However, an indication of a SRO can be a wavy configuration of dislocations with segments lying in regions of favorable solute fluctuations [137]. Dislocations laying in specific planes minimize Peierls potential (Figure 113). This potential defines low-energy directions in which dislocations prefer to lie and can be overcome by a stress larger than an intrinsic critical shear stress. In FCC metals, dislocations glide at low Peierls stress of about 100 MPa or lower [139]. Here, however, distortion of the crystal lattice in high entropy alloys (Figure 114 a) leads to fluctuations (Figure 114 b) of Peierls potential and high friction stress [140].

Large friction stress was found in different multicomponent materials, like equi-atomic CoCrNi alloy [140]. Moreover, strength of an alloy is not simply connected with increasing number of elements but rather ratios between them and local chemical arrangement, since friction stress in CoCrFeMnNi was found to be smaller than in CoCrNi [141].
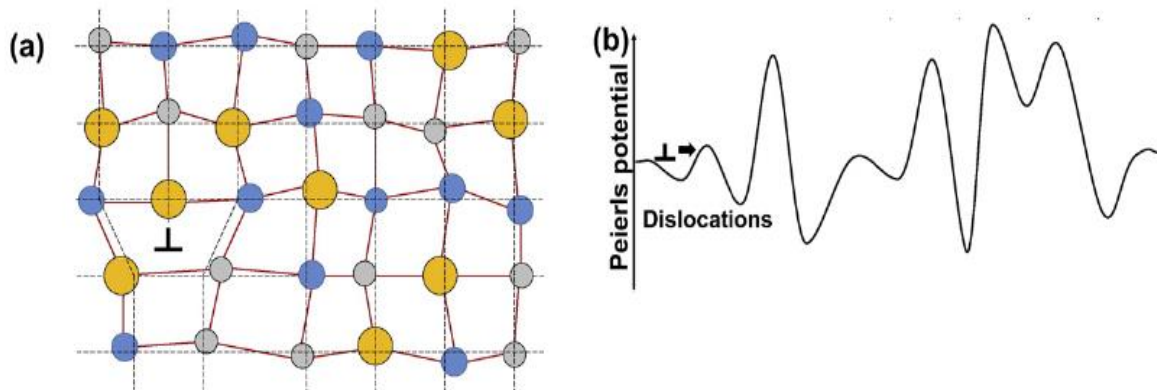
Figure 114. a) Locally-distorted lattice in high entropy alloys with a dislocation and b) resulting fluctuations of Peierls potential [140]**.**

In the samples annealed at high temperatures, wavy configurations of dislocations were found, i.e. in the A3S annealed at 1100°C during 14 hours (Figure 115). It may indicate local fluctuations of chemical composition leading to segments of dislocations laying in energetically favorable planes.
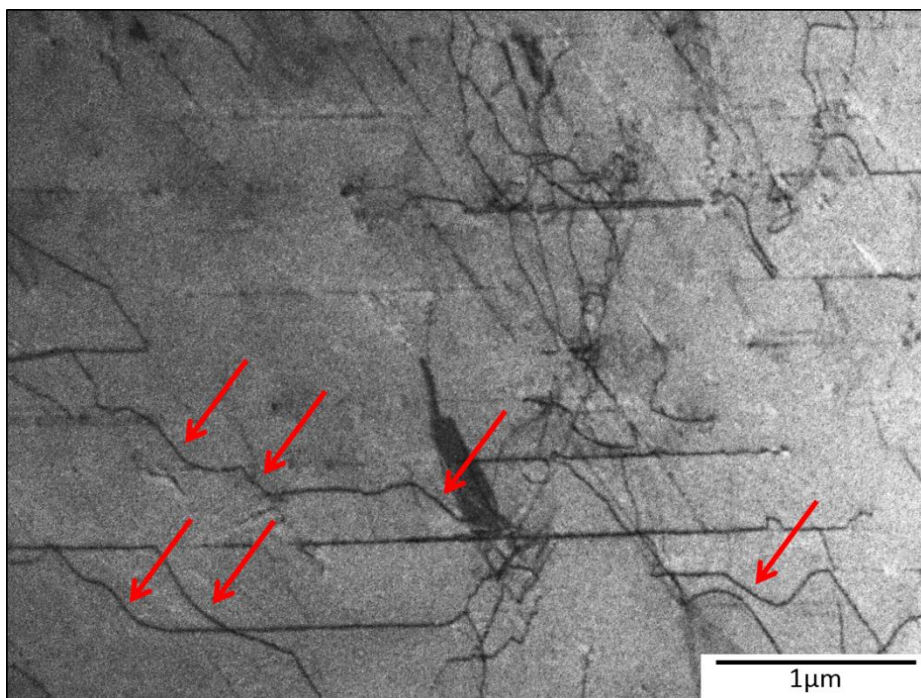
Figure 115. TEM bright field image of wavy dislocations in the A3S annealed at 1100°C/14h. Red arrows indicate low energy segments.

In some regions of the X1, dislocations pinning was observed (Figure 116). These may be due to presence of point defects or high concentration of elements, but also high Peierls energy barrier. If a segment of dislocation is located in a low energy position with elevated potential barrier, it will be difficult to change it position. This segment then becomes immobile and itself acts as a pinning point.
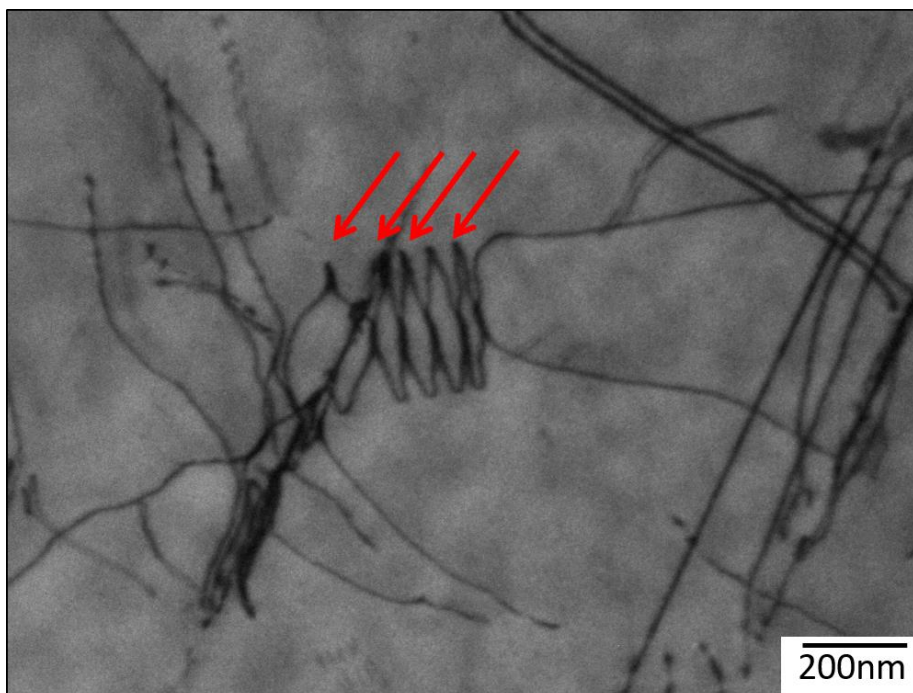
Figure 116. TEM bright field image of dislocation pinning in the X1 annealed at 1100°C/14h. Red arrows indicate pinning points.

This hypothesis is, so far, considered as the most credible explanation of high dislocation stability. In pure metals, dislocation parameters (width, Burgers vector) are constant and hence the Peierls stress is low. In HEAs, due to strong lattice distortion, Peierls barriers vary along the crystal structure and become inhibitors for dislocation movement.

Atom probe tomography measurements, however, did not reveal any important fluctuations of chemical composition in different states of both materials. This technique allows three-dimensional mapping (3D mapping) of the constituent elements with high detection sensitivity and near-atomic resolution. It gives a chemical

information on a nanometer scale. Both the X1 and A3S (Figure 117) in as-forged and annealed state were homogeneous. Annealing at 1000°C for 2 hours and subsequent annealing at 500°C for 21 days did not reveal any decomposition. No regions of segregation were found and the elements were uniformly distributed. Small fluctuations of chemical composition (±1%)
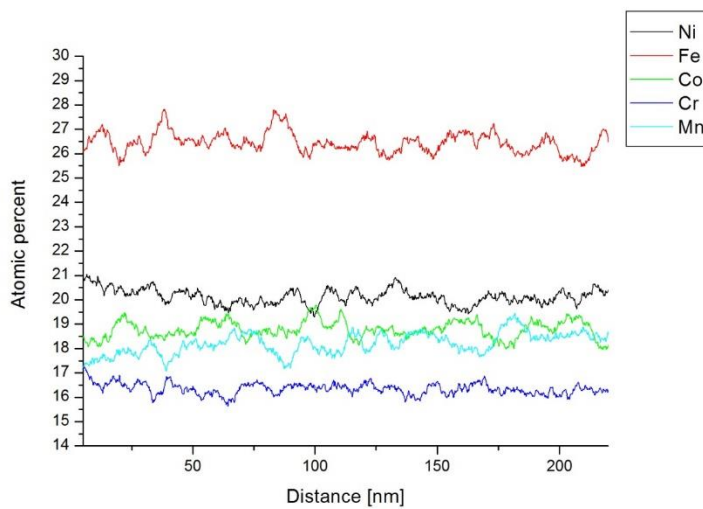
Figure 117. A3S annealed (homogenized+500°C/21 days) (2 149 000 atoms; dimensions: 76.9x76.9x365 nm3).

do not seem to be important, comparing to the literature results for other materials [142]. Because these experiments were conducted at the beginning of the project when the problem of unusual high density of dislocations was not revealed yet, certainly further analysis is necessary, especially after high temperature annealing and in specific regions of the samples.

5.3.2. Lomer-Cottrell junctions

In FCC materials, dislocations can interact with increasing strain creating junctions. Lomer-Cottrell (LC) junctions can be presented in a schema (Figure 118) [143]. Here, red and green dislocations on two different planes of type (111) attract each other and react in order to reduce their energy. Both incoming dislocation are dissociated and are forming a blue dislocation on the (100) plane. This is a Lomer-Cottrell dislocation, considered as highly stable and strong [144]. Since the (100) plane is not a close-packed plane in FCC metals, this dislocation will be immobile and act as a barrier to the motion of the others. Peierls stress of LC junctions is high, i.e. in nickel it is of 10 GPa [145].

$$\left(\frac{1}{2}[\bar{1}\,1\,0]\right)_{(111)} \quad + \quad \left(\frac{1}{2}[1\,0\,1]\right)_{(\bar{1}11)} \quad \Longrightarrow \quad \left(\frac{1}{2}[0\,1\,1]\right)_{(100)}$$
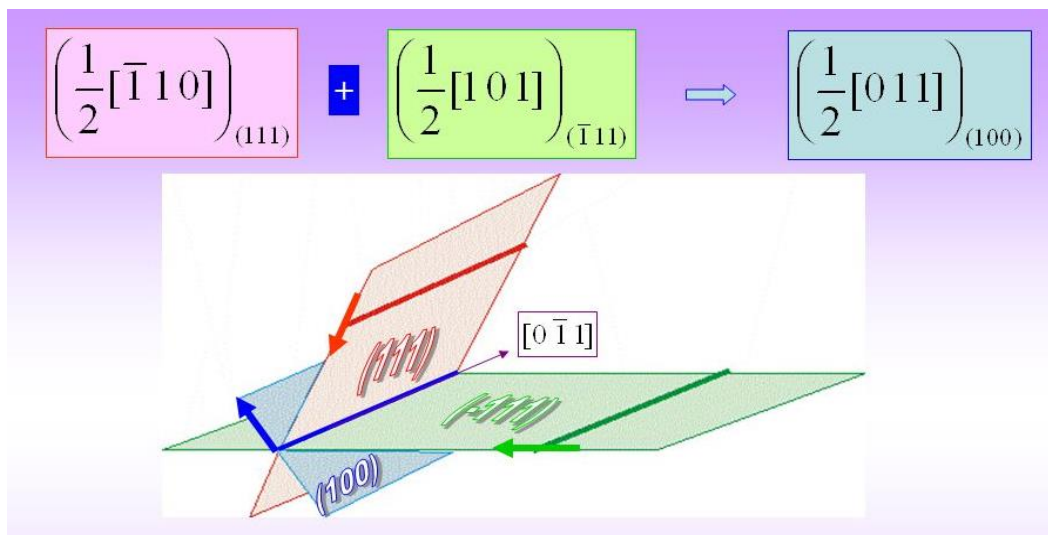
Figure 118. Lomer-Cottrell barriers [143]**.**

As it was mentioned in the beginning, this type of junctions are currently created under stress. However, one can imagine that during heating, when rearrangement of dislocations occurs, Lomer-Cottrell locks are formed. Thermal activation of dislocations leads to modification of their cores and equilibrium configuration as well. The dislocation core has an important effect on the lattice resistance to the LC junction mobility [146].
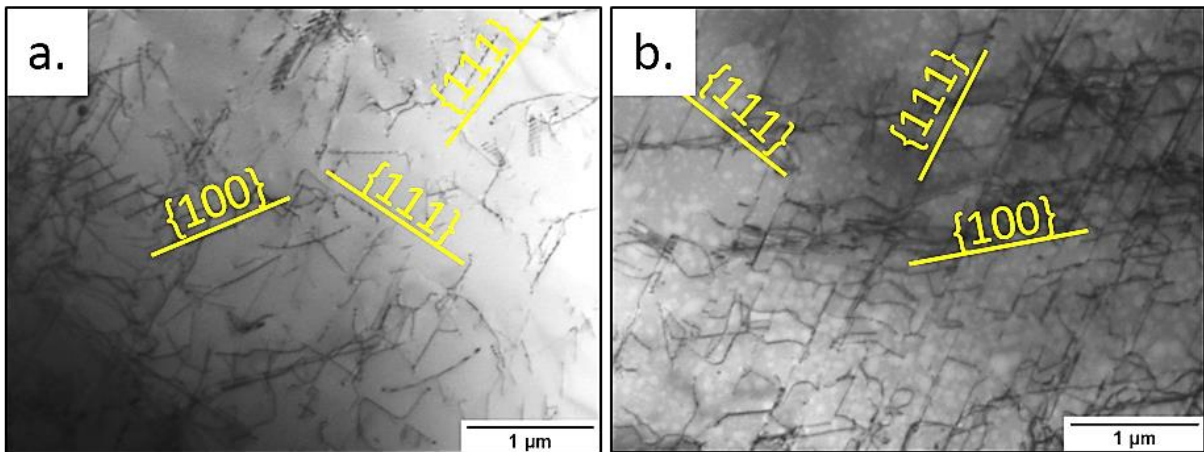
Figure 119. TEM bright field images of the A3S after annealing at: a) 1100ºC/10min (ZA=[011], g=[-200]), b) 1100ºC/48h (ZA=[011], g=[00-2]).

TEM analysis in different orientations (Figure 119) reveals that the dislocations lay in three characteristic planes (two of type {111} and one {100}), and this characteristic configuration reminds of the Lomer-Cottrell lock. This configuration was found in all samples annealed at high temperatures, in both the A3S and X1. Even after annealing at 1100ºC (which is about 0.8 T_M of the A3S) during 2 weeks, the same configuration of dislocations was found, still in high density (Figure 120).
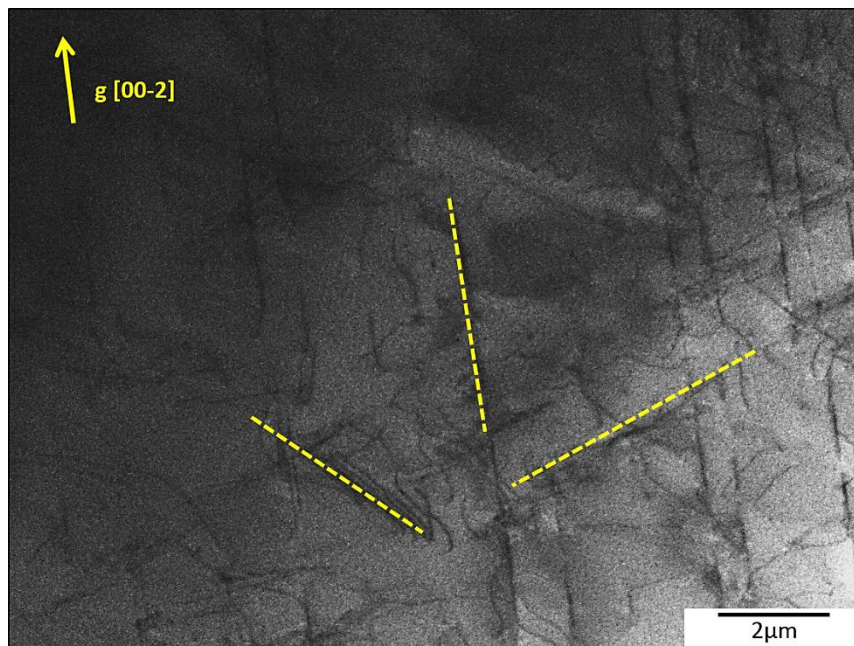
Figure 120. TEM bright field image of the A3S after annealing at 1100ºC/2 weeks in [110] ZA.

5.2. Experimental study of dislocation type and mobility

5.2.1. Room temperature deformation

To analyze differences in dislocation behavior after deformation at room and high temperatures, it was necessary to choose a state with a very low density of dislocations at the beginning. It is obviously not the as-forged material, where dislocation density is very elevated. The annealed A3S HEA, after heat treatment at 600°C during 1 month, has been chosen for studies of dislocation due to its recrystallized grains. This heat treatment was proved to provide grains almost free of defects, as it was shown before. Microstructures were examined in TEM after low (total strain of ~4.3%) and high (~30%) deformation in compression.
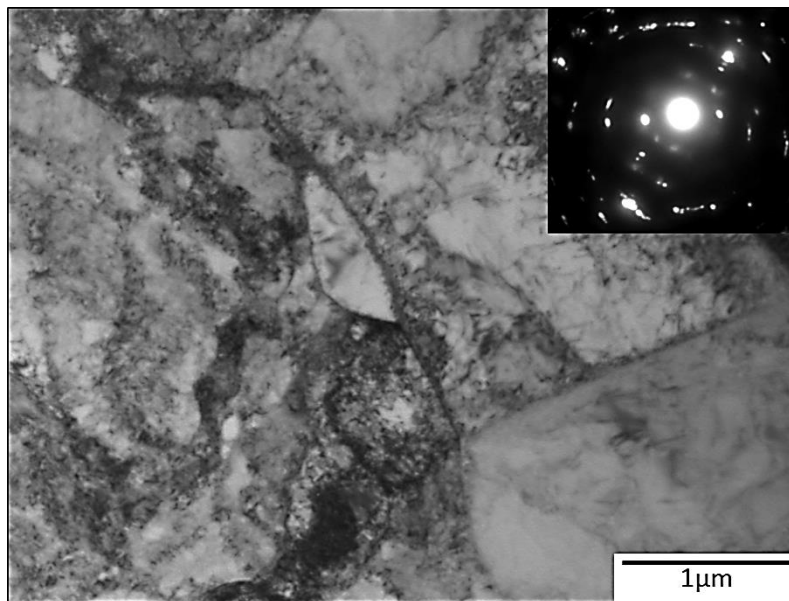
Figure 121. TEM bright field image of the A3S deformed (~4.3%) at room temperature.

The structure after low deformation consists already of high density of dislocations (Figure 121). Numerous pile-ups of dislocations in (111) planes (Figure 122) and slip bands (Figure 123) were found as well.
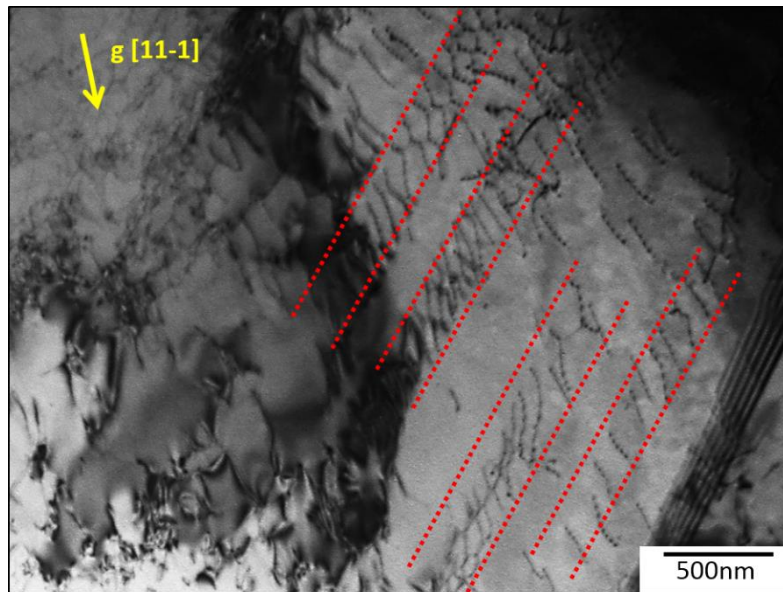
Figure 122. TEM bright field image of the A3S in [101] ZA deformed (~4.3%) at room temperature. Pile-ups of dislocations are marked with red dotted lines.
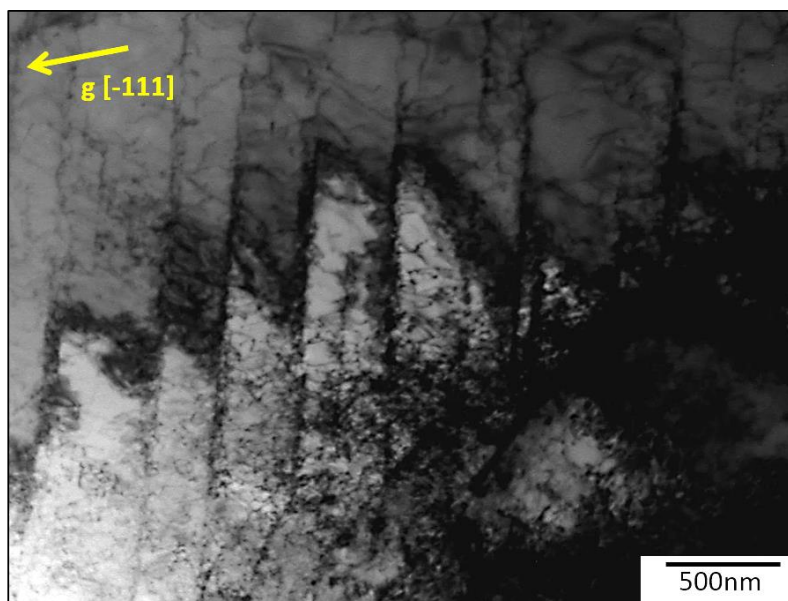
Figure 123. TEM bright field image of the A3S deformed (~4.3%) at room temperature. Slip bands are present.

In many regions, however, recrystallized grains with much lower density of dislocations were found (Figure 124).

A microstructure developed at larger strain (of ~30%) consists of very high density of dislocations, in which single dislocations cannot be distinguished, and deformation bands (Figure 125).
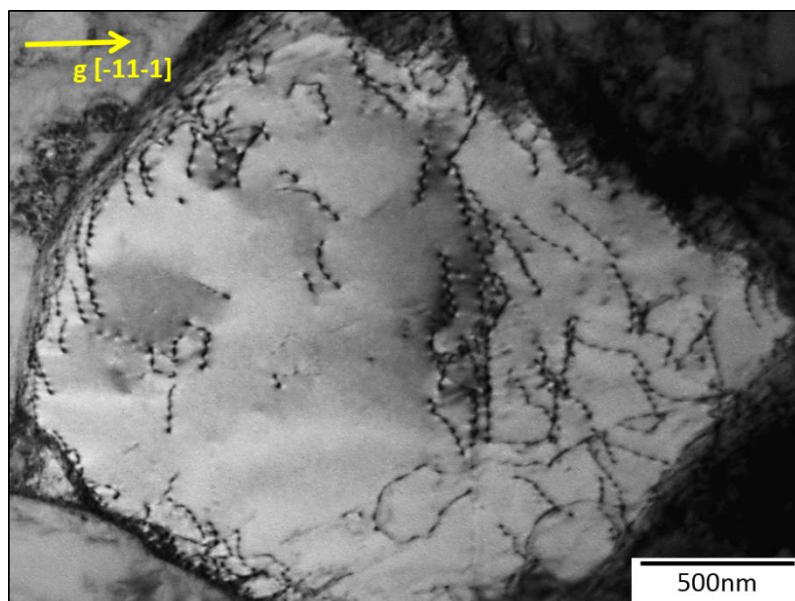
Figure 124. TEM bright field images of the A3S in [110] ZA deformed (~4.3%) at room temperature.
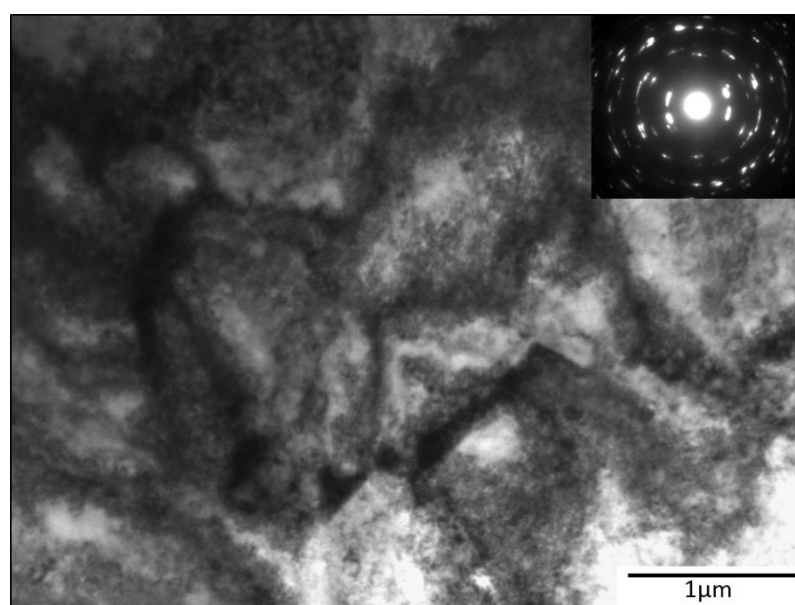
Figure 125. TEM bright field images of the A3S deformed (~30%) at room temperature.

The deformation mechanisms have been studied as well in *in situ* TEM in both the X1 and A3S at room temperature. The emission of a dislocation loop is shown in Figure 126. The dislocation glide in the (111) plane and has a [01-1] Burgers vector, determined from the invisibility criterion ($\mathbf{g} \cdot \mathbf{b} = 0$).

Figure 126. Dislocation loop propagation in the A3S recorded during *in situ* straining experiments.

Dislocations pile-ups formed during straining, typical for FCC metals, were observed as well (Figure 127).
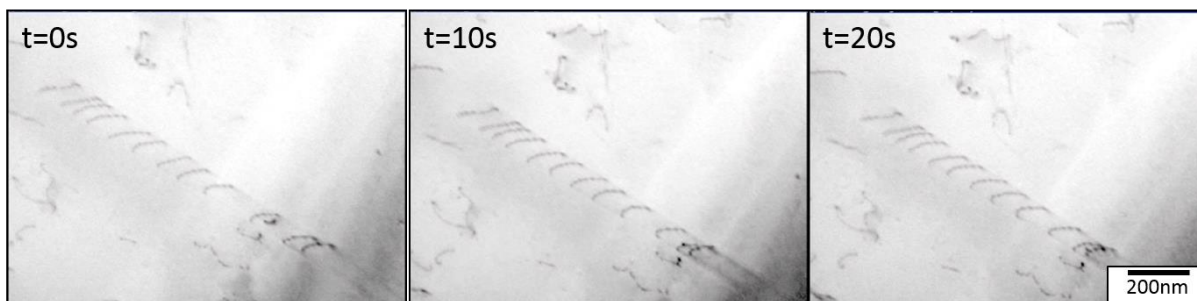
Figure 127. Pile up of dislocations in the A3S under stress.

In the X1, in contrary to the A3S and in agreement with earlier observations, nanotwins were found in two adjacent grains (Figure 128). This confirms again the hypothesis of higher stacking fault energy in the A3S and thus different mechanisms of plastic deformation.
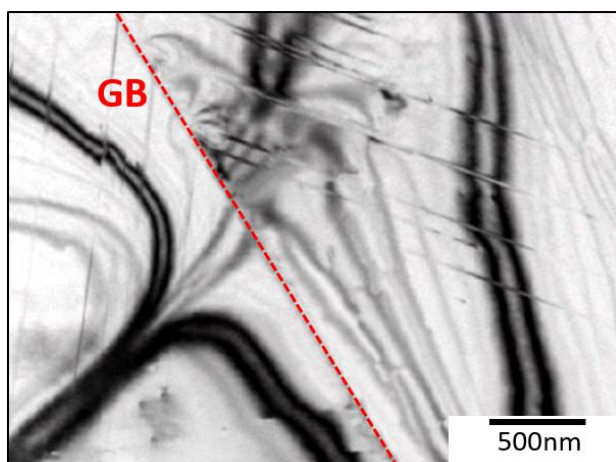
Figure 128. Nanotwins in the as-forged and deformed X1.

5.2.2. High temperature deformation

Elevated temperature (1100°C) has been chosen for two reasons. First, high density of dislocations and their ability to rearrange in characteristic planes was already shown in the previous chapter and is not clear. Thus, observing dislocation behavior in these conditions in grains free of dislocations (annealed at 600°C/1 month) at the beginning may be a reasonable starting point for further explanations. Second, at this temperature forging is processed, resulting in highly stable microstructure with stable nano-subgrains. However, their formation is still unclear.

Deformation (true strain 3.5% and strain rate of 10^{-3} s^{-1}) at 1100°C results in pile-ups of dislocations (Figure 129), typical for FCC alloys, and rearrangement of dislocations in subgrain boundaries due to dislocation climb and glide (Figure 130). At a similar temperature (~1050°C) the process of hot forging is conducted, after which a microstructure with subgrains of few hundred of nanometers with high density of dislocation is obtained. Grains with high angle grain boundaries were large (more than few micrometers) and any small, recrystallized grains were not found, indicating again the process of grain growth rather than recrystallization at elevated temperature.
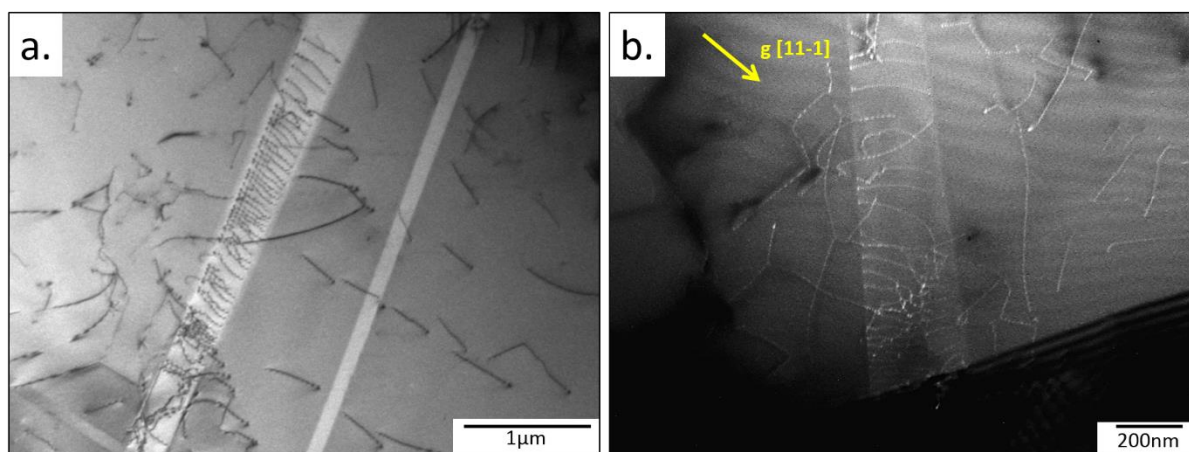
Figure 129. TEM images of the A3S deformed at 1100°C: a) bright field image of dislocation pile-ups, b) weak beam g-2g dark field image of dislocation pile-ups.

The formation of subboundaries is well presented in Figure 131, where a long line of dislocation pile-ups is formed in one grain. Two parts of the grain (marked as "1" and "2") have almost the same orientation. The subboundary is formed in between. These subboundaries are obstacles to dislocation movement (pile-ups of dislocations are created).

In many grains dislocation lines interact and create nodes (Figure 132).
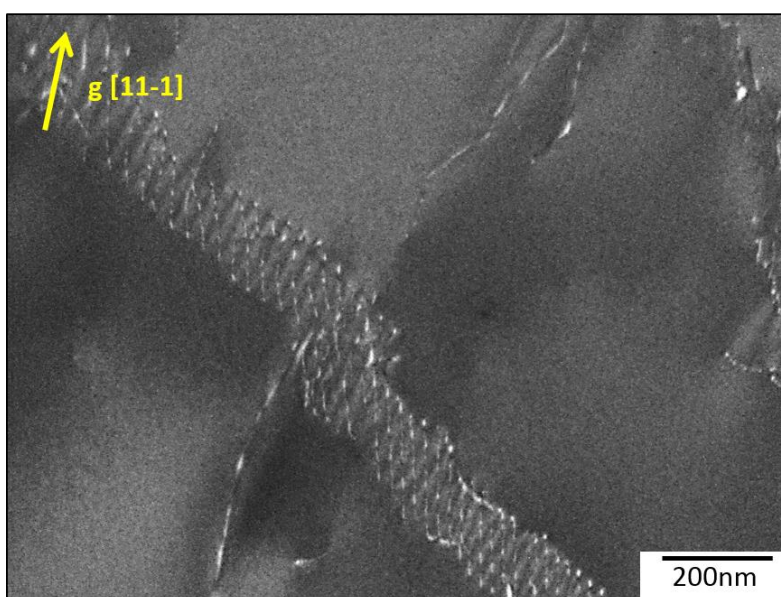
Figure 130. TEM weak beam g-2g dark field image of a subboundary. ZA = [21-1].
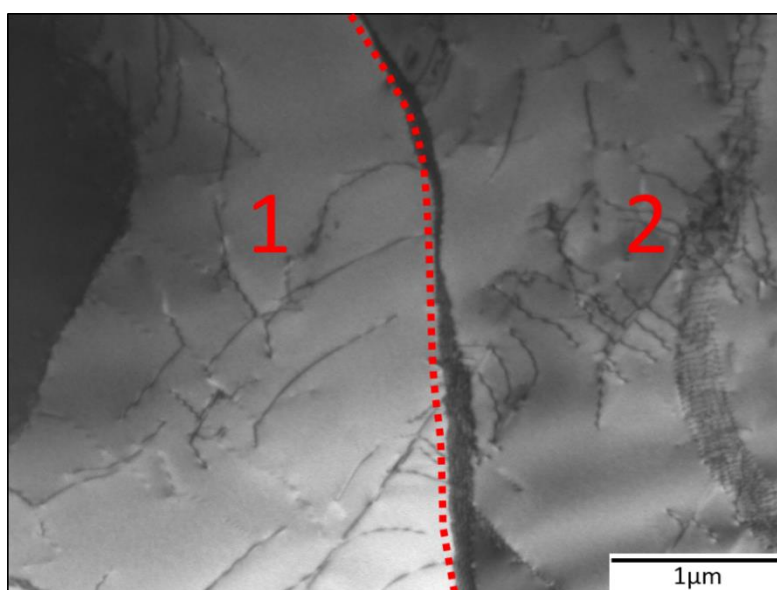
Figure 131. TEM bright field image of a grain with a subboundary formed and pile-ups of dislocations.
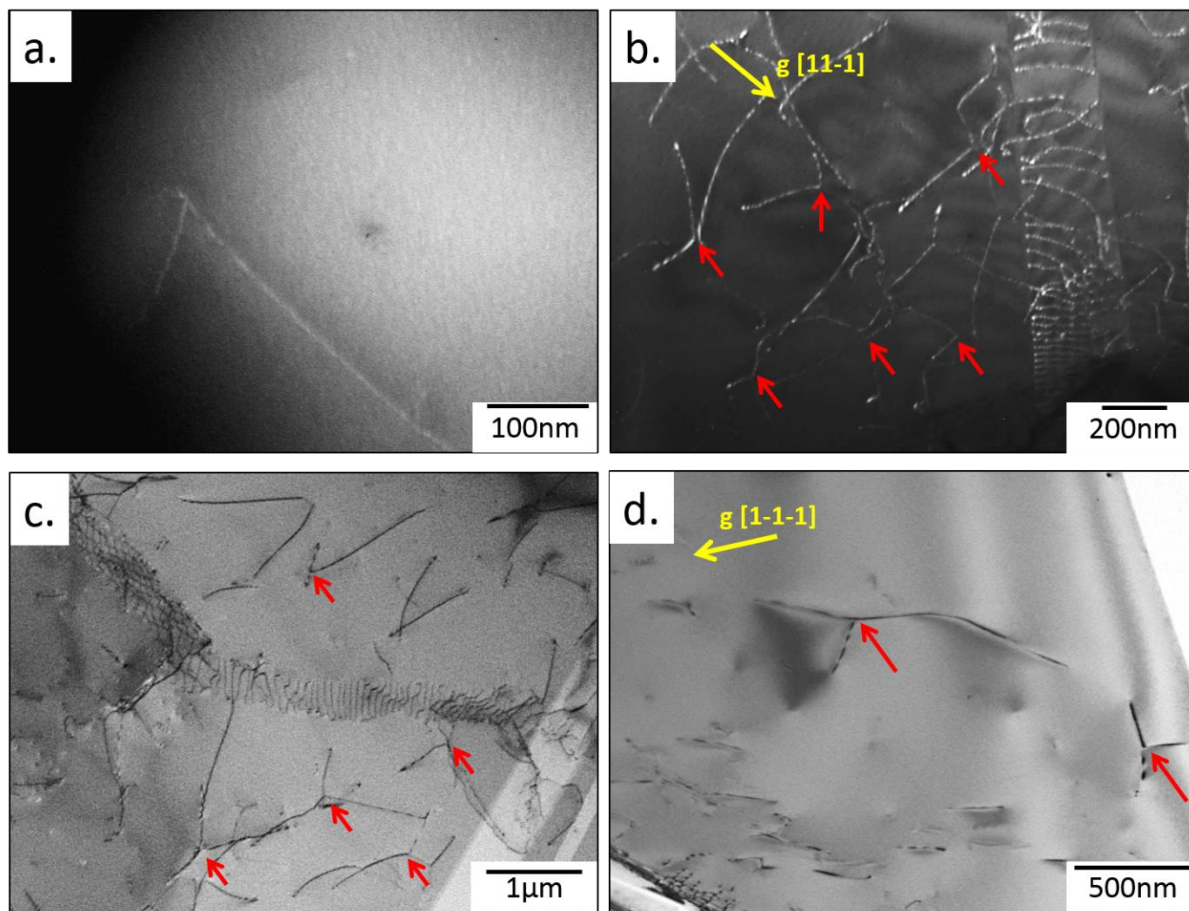
Figure 132. TEM a, b) weak beam g-2g dark field images and c, d) bright field images of dislocations.

In some regions, zig-zag instability of dislocations was observed (Figure 133 a), specific to elastic anisotropy and found i.e. in β-brass and Cu-Al alloys [147]. In others, long dislocations were found, possibly indicating their elevated energy (Figure 133 b).
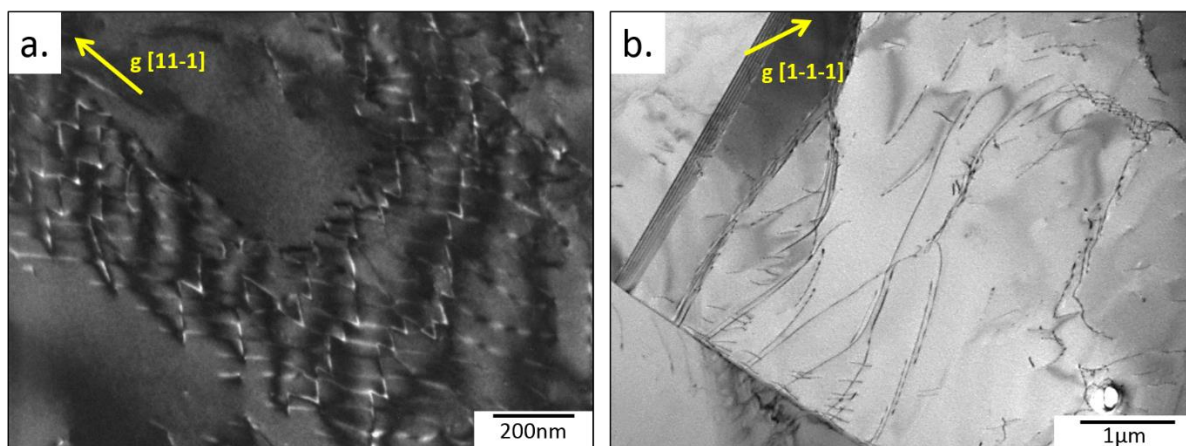
Figure 133. . TEM a) weak beam g-2g dark field image, ZA = [011]; b) bright field images, ZA = [110].

In this state, using weak beam g-2g dark field conditions, dissociated dislocations were found (Figure 134 and Figure 135). Based on the scale of measurement, the dissociation distance varies for different dislocations as a consequence of a complex configuration of the crystal structure.
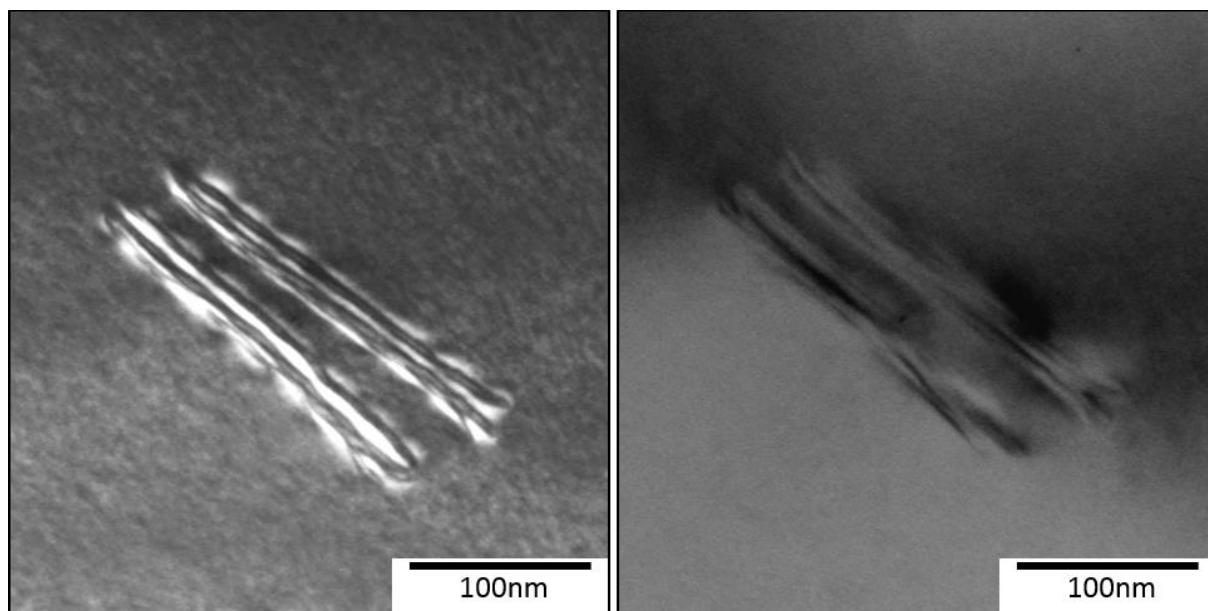
Figure 134. Weak beam g-2g dark field image of dislocations in the A3S deformed at 1100ºC. ZA = [111].
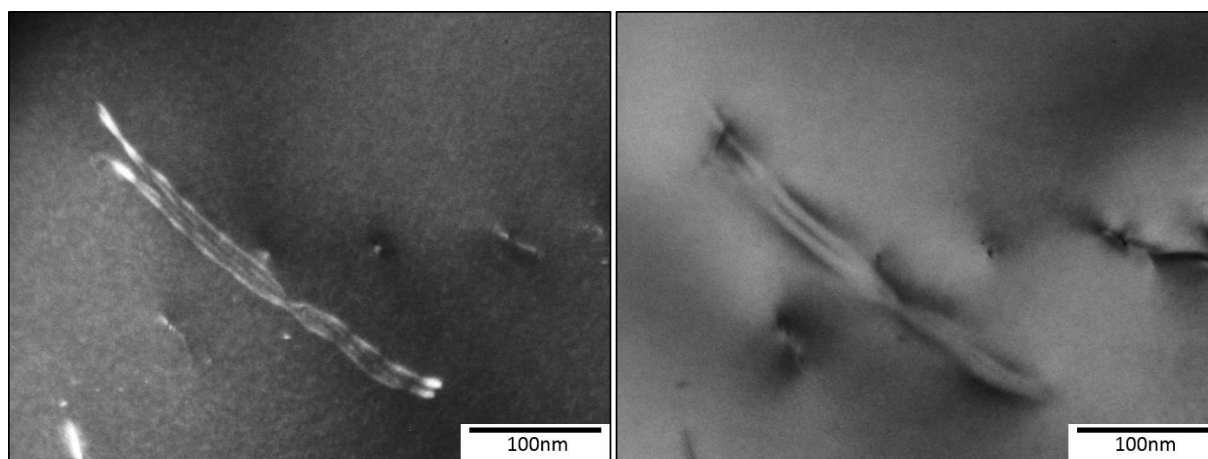
Figure 135. Weak beam g-2g dark field image of dislocations in the A3S deformed at 1100ºC. ZA = [111].

5.3. Dynamic recovery and recrystallization

The hot deformation can refine material microstructure and enhance its mechanical properties. Thus, its behavior in these conditions during thermo-mechanical processing must be understood.

Here, hot compression tests were used to simulate industrial forging processes and to determine the differences in behavior of the two alloys. In the unmodified CoCrFeMnNi alloy, discontinuous dynamic recrystallization is expected to take place [68]. The second derivative method [148] was implemented so as to detect the onset of DRX and of dynamic transformation in the two materials, the X1 and A3S. This led to a determination of the effect of stacking fault energy on the characteristics of dynamic recrystallization.
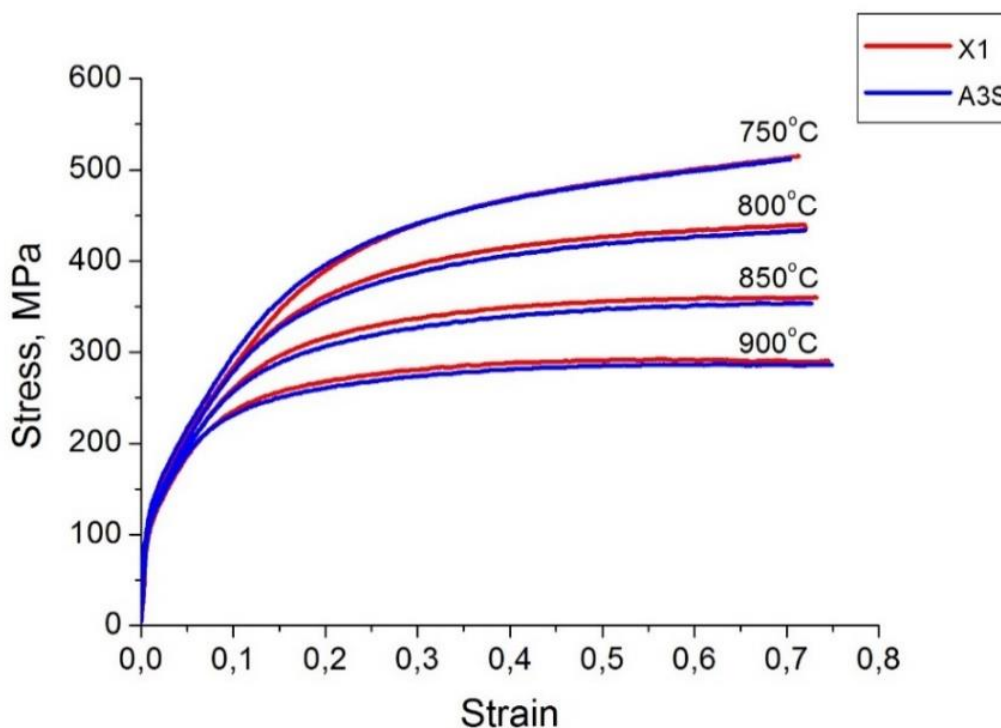
Figure 136. Comparison of the stress-strain curves for alloys X1 and A3S tested at a strain rate of 10^{-1} s^{-1}.

Stress-strain curves determined at a series of temperatures at a strain rate at 10^{-1} s^{-1} are presented in Figure 136. The samples were deformed to a height reduction of 50% without the appearance of any visible cracks. The flow stress increased gradually

without reaching a peak and the rate of work hardening decreased with strain. The yield stresses of the samples (Table 21) decreased with temperature and are slightly higher for alloy X1. The rate of strain hardening at 750°C is higher than at the higher temperatures. At 900°C, a steady state was achieved, with a plateau flow stress of about 285 MPa.
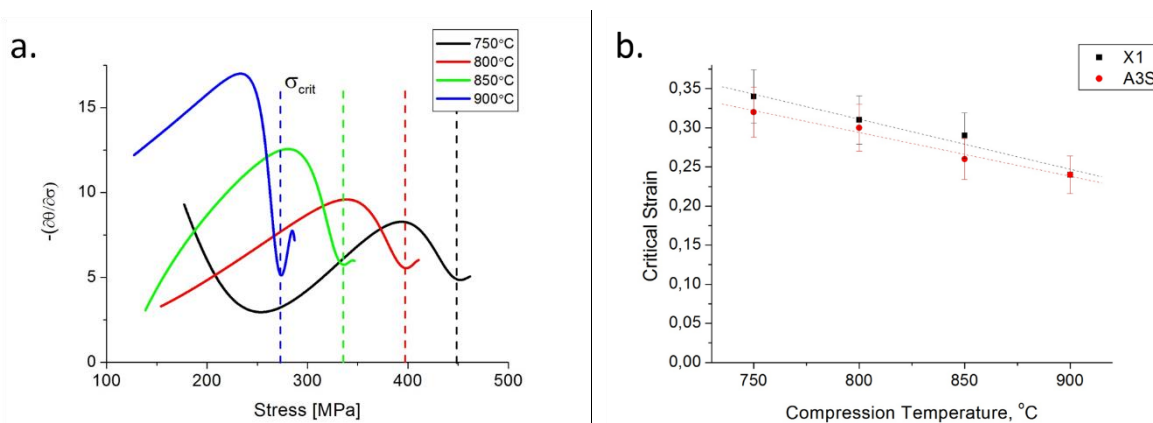
Figure 137. (a)$-(\partial\theta/\partial\sigma)$ vs. σ curves for the A3S alloy; θ is the conventional strain hardening rate; (b) Dependence of the critical strains on temperature in the two materials.

The curves from the hot compression tests were fitted with ninth-order polynomials using the MATLAB software after removing the initial parts of the curves below 2% strain (Figure 137 a). In all cases (except for 750°C) only one inflection point was found, which indicated the initiation of dynamic recrystallization.

Table 21. Yield stress values

at different temperatures.

Temperature	Yield Stress [MPa]	
	X1	A3S
750°C	124	116
800 °C	107	105
850 °C	104	104
900 °C	101	96

The dependences of the critical strains on temperature are illustrated in Figure 137 b. Here similar tendencies are observed for both materials in that the critical strains decrease with temperature.

The microstructure of the A3S after annealing at 1000°C for 2 hours consisted of recrystallized grains of diameter ~50μm containing a high density of twins. The microstructure of

the X1 after the same heat treatment was similar. The deformed microstructures (Figure 138) indicate that dynamic recrystallization was initiated at grain boundaries at 750°C, forming the characteristic necklace structures. At 900°C, these new grains are larger, due to faster diffusion, but the material is not fully recrystallized even at a strain of ε~0.7. There is a higher volume fraction of new grains in agreement with the lower critical strain at the latter temperature (Figure 137).
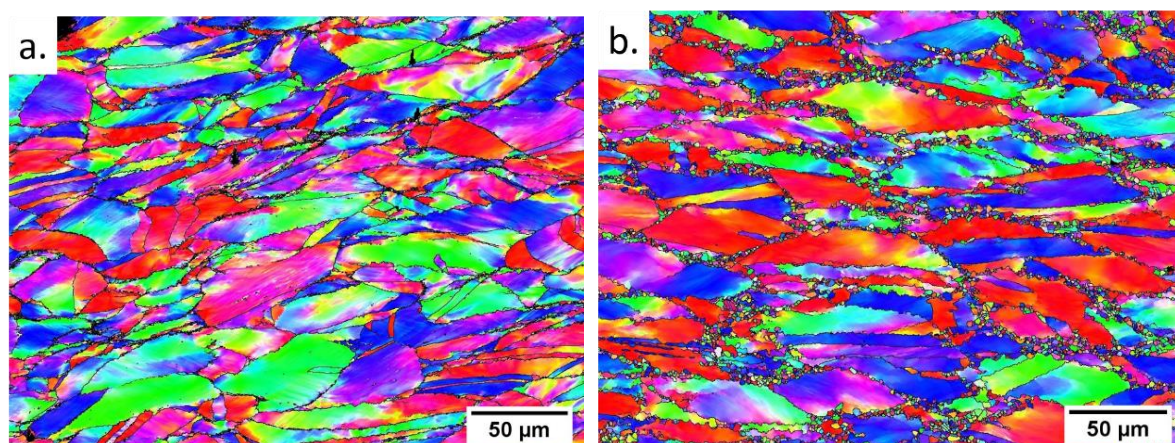
Figure 138. IPF images of the A3S after hot compression at a) 750°C and b) 900°C.

The microstructures were analyzed using EBSD so as to determine the type of recrystallization taking place (Figure 139). Here high angle grain boundaries (>10°) are outlined in black and low angle boundaries (>2°) in red. The microstructures of the two alloys were similar and consist mostly of elongated grains ~30 μm in diameter. New recrystallized grains can be seen along the boundaries of these grains, whose size increases with temperature.

Misorientation profiles were measured along lines 1 and 2 in Figure 139, see Figure 140. It can be seen from the point-to-origin profiles that misorientation gradients developed both along grain boundaries and within the grains. As can be seen, the magnitudes of these gradients decreased with temperature.
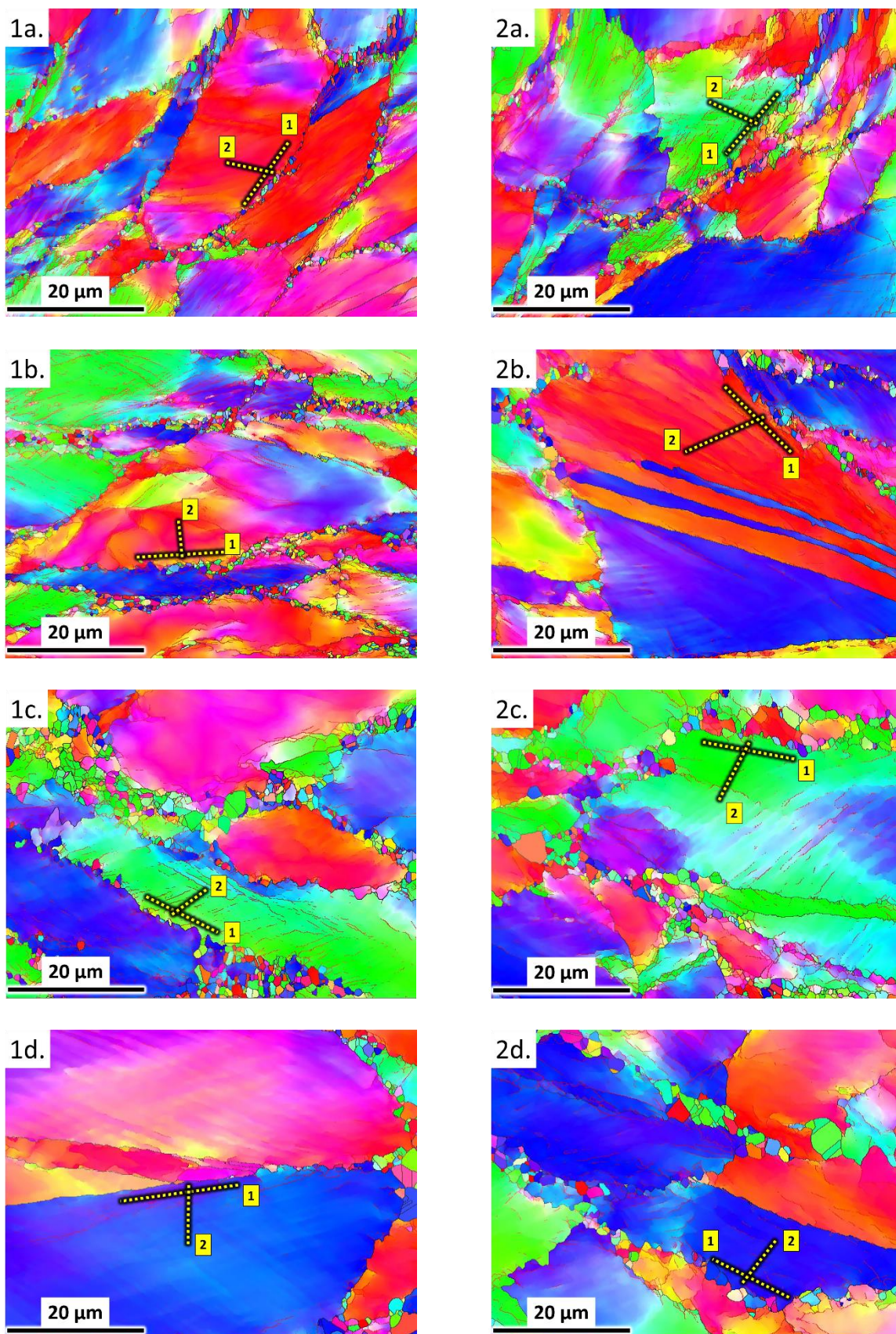
Figure 139. EBSD IPF images of X1 (1) and A3S (2) after hot compression at (a) 750, (b) 800, (c) 850 and (d) 900ºC.

Line 1   Line 2

750°C

800°C

850°C

900°C
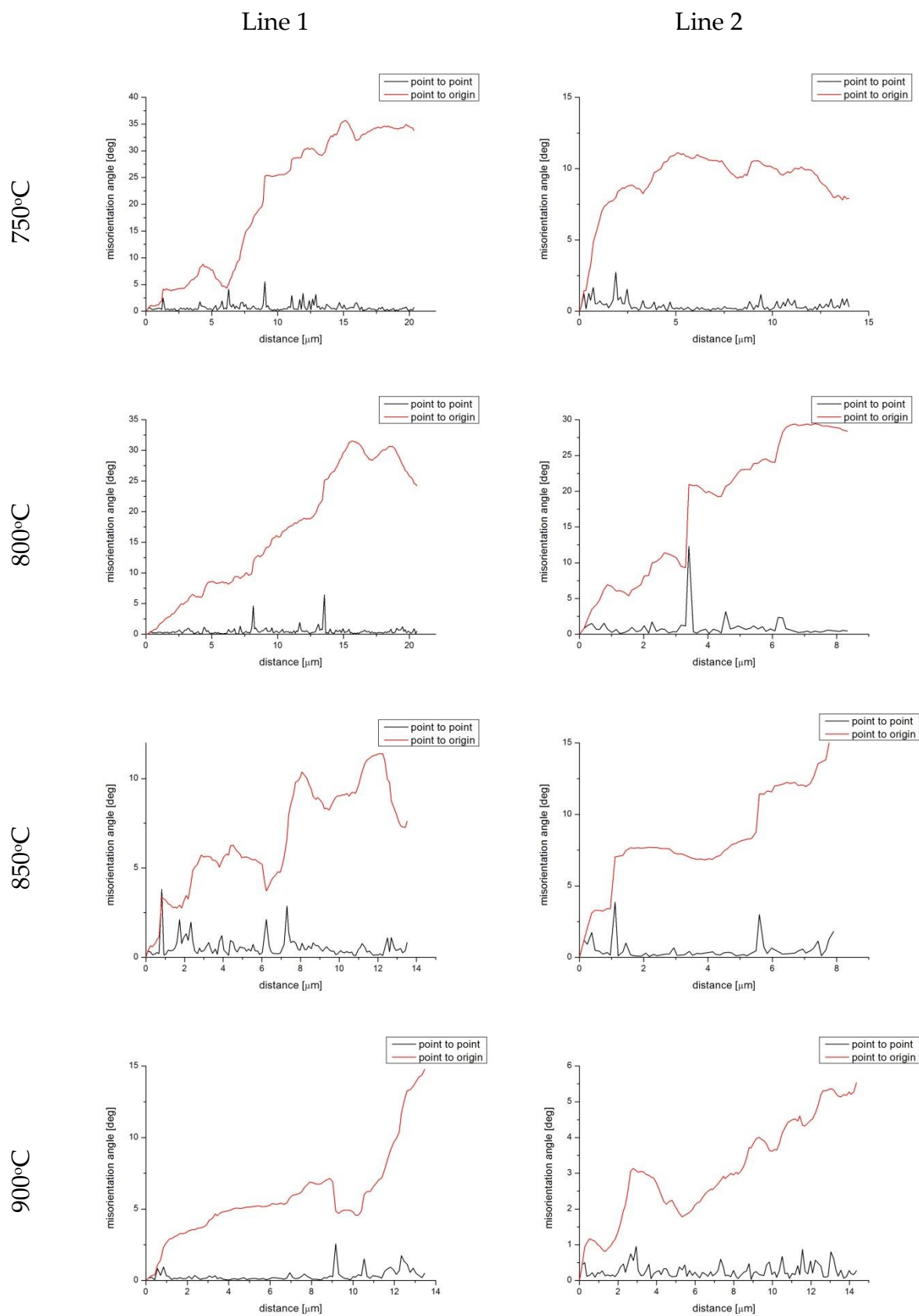
Figure 140. Misorientation profiles in samples of the X1 material measured along lines 1 and 2 in Figure 139.
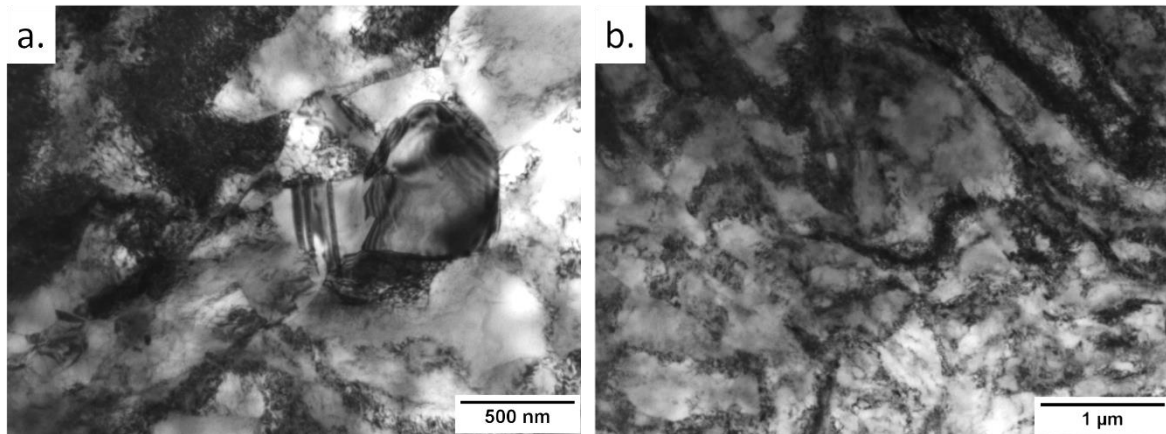
Figure 141. Microstructure of the X1 material deformed at 750ºC (bright field mode).

In order to determine the softening mechanisms operating in these alloys, selected samples were examined using transmission electron microscopy. Examples of the microstructure of the X1 after hot compression at 750ºC are presented in Figure 141. The microstructure consists of cells <500 nm in diameter as well as a high density of dislocations. Such structures are normally produced by severe plastic deformation, which indicates that such nanocells can readily form during the deformation of this family of high entropy alloys. Some twins also formed in the recrystallized grains (Figure 142 a, red arrow). The diffraction pattern of this area reveals that the subgrains have low-angle boundaries. The dislocation densities of the new grains are also lower than in the original grains.
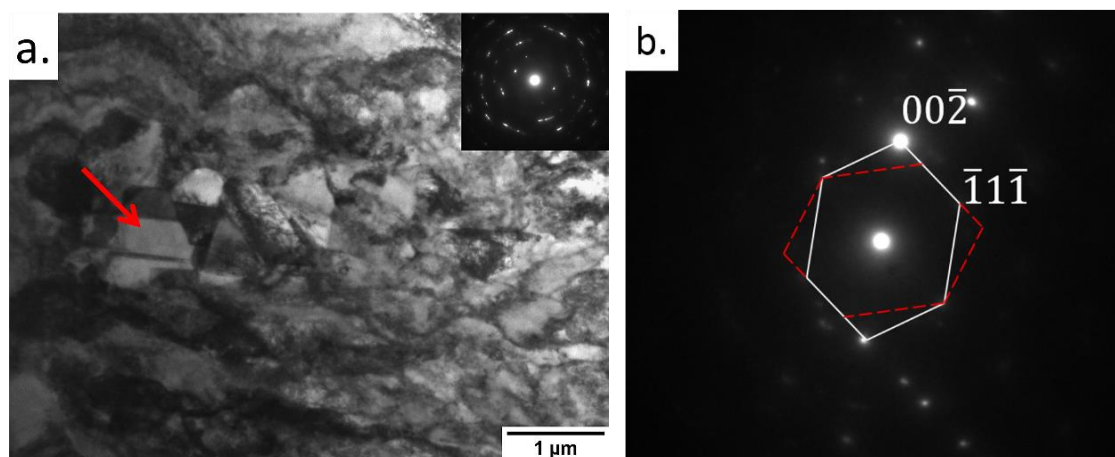
Figure 142. a) X1 microstructure after compression at 750ºC (bright field mode); b) diffraction pattern of twins.

Similar microstructures were observed in the A3S material, which was again characterized by nanocells of <500 nm and a high density of dislocations. However, there were fewer twins in keeping with the higher stacking fault energy of this composition. On increasing the temperature to 900°C, the microstructure was observed to contain more recrystallized grains, see Figure 143. These grains had well-formed boundaries and lower dislocation densities. Diffraction analysis confirmed the presence of twins, as in the previous example, but in greater number, both in the X1 and the A3S. The dislocation density was also lower and some of the recrystallized grains were nearly free of dislocations (Figure 143 a, c).
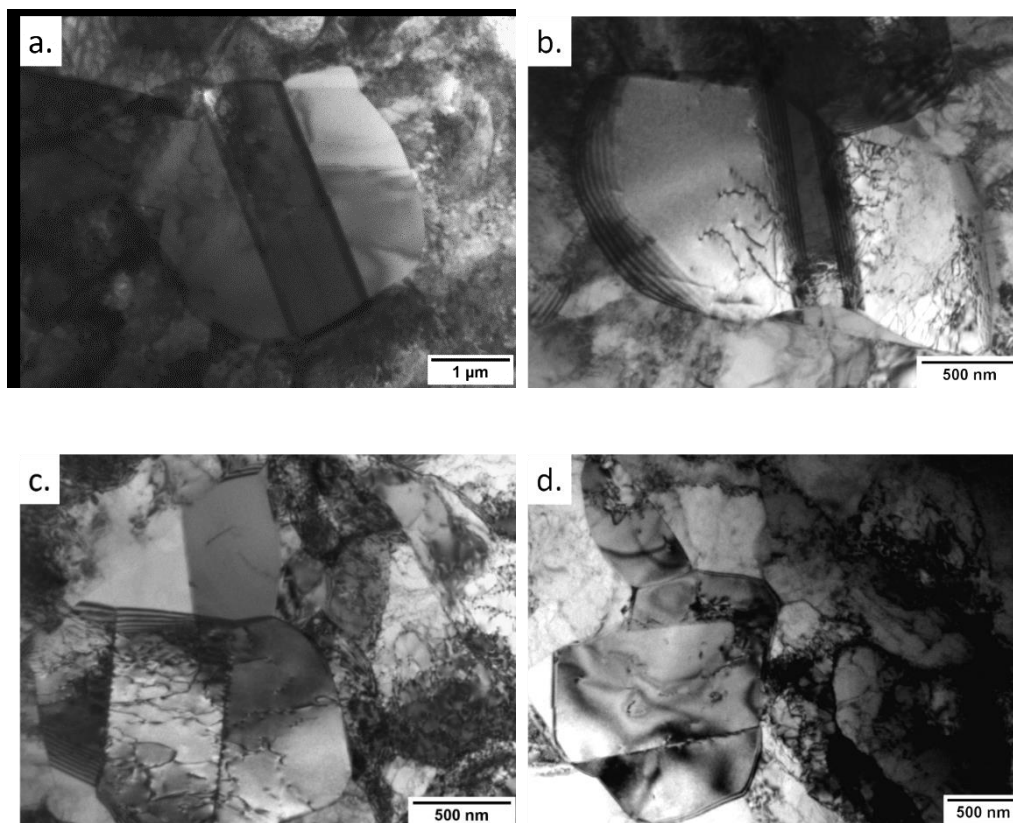
Figure 143. Microstructures of (a)-(b) the X1 and (c)-(d) the A3S materials after compression at 900°C (bright field mode).

It may be concluded that the main softening mechanism taking place during the hot compression of the present high entropy alloys is discontinuous dynamic recrystallization. Typical necklace structures were observed over the whole range of temperatures.

6. Conclusions and perspectives

Two different high entropy alloys from Cantor's family were examined from mechanical and microstructural point of view: the reference equiatomic CoCrFeMnNi (referred to as "X1") and the novel "A3S®" Co20Cr15Fe26Mn17Ni22. The latter composition was optimized with CALPHAD calculations in Thermo-Calc using following approach: face-centered cubic (FCC) solid solution region was augmented and brittle σ phase was rejected. These were reached, among others, by increasing amount of nickel and decreasing amount of chromium. The two alloys were cast from high purity elements and hot forged or/and cold rolled.

First evaluation of the A3S, in comparison with the X1, gave satisfying results. Both cast alloys possessed FCC crystal structure with standard lattice parameter and stable microstructure (no decomposition) after annealing at a wide range of temperatures (down to 500°C) and short times (up to 21 days). After long cycle anneal (100, 200 and 300 days), however, the X1 decomposed into three new phases: Cr-rich phase, MnNi tetragonal phase and FeCo cubic B2 phase, which is in agreement with the literature. The A3S, in contrary, presents stable FCC structure until 300 days when only first traces of new phases were found. Still, higher stability of its solid solution phase confirms a successful optimization procedure.

After hot forging, both alloys presented unexpected facility of creating nanostructures, with nanocells of few hundreds of nanometers. Even though these microstructures in the two materials were similar, much higher density of nanotwins was found in the X1. This may be related to lower stacking fault energy and thus facility of creating twins.

This microstructure is at the origin of the mechanical properties. In the as-forged state both alloys possess high yield strength at room temperature, higher for the A3S (775 MPa) than for the X1 (600 MPa), with similar elongation to fracture (~30%) and low

work hardening coefficient, typical for nanomaterials. Higher mechanical properties speak again, together with higher thermal stability, in favor of the novel A3S alloy. After annealing at 1000°C during two hours, the structure contained grains free of nanocells or subgrains, with high density of twins. Mechanical properties change as well, in a similar way for both alloys, with a yield strength of 240 MPa and elongation to fracture of ~60%. These properties (in both as-forged and annealed state) are enhanced at cryogenic temperature due to change of mechanisms of deformation: twinning becomes more favorable. No martensitic transformation was observed. The yield strength was improved after rolling to 1360 MPa but with a loss of ductility.

Classical theories of static recovery and recrystallization do not apply to these materials. Microstructural characterization with TEM after high temperature annealing (above 600°C up to 1100°C, which is about 0.8 of melting temperature) reveals high density of dislocations rearranged in two (111) and one (100) plane, of which in the latter dislocation movement is blocked. High stability of dislocations even at elevated temperatures is probably correlated with fluctuations of Peierls energy of dislocations. In hot compression, however, classical discontinuous dynamic recrystallization was observed, with new grains forming necklace structures.

Different phenomena occurring in the investigated high entropy alloys are still not explained and demand further research. The main difficulty comes from lack of theory since many of already established metallurgy rules simply do not apply here. Mobility and structure of dislocations at different temperatures and in different conditions of deformation are one of unknown elements necessary to better understand HEAs. Further calculations on various parameters, such as stacking fault energy, could help to explain strong influence of the chemical composition changes on the stability and properties, as increased amount of nickel and lowered amount of chromium in the A3S compared to the X1. Different techniques can be combines here, such as transmission electron microscopy and atomistic simulations.

Literature

[1] J. W. Yeh, S. K. Chen, S. J. Lin, J. Y. Gan, T. S. Chin, T. T. Shun, C. H. Tsau, and S. Y. Chang, "Nanostructured high-entropy alloys with multiple principal elements: Novel alloy design concepts and outcomes," *Adv. Eng. Mater.*, vol. 6, no. 5, p. 299–303+274, 2004.

[2] B. Cantor, I. T. H. Chang, P. Knight, and A. J. B. Vincent, "Microstructural development in equiatomic multicomponent alloys," *Mater. Sci. Eng. A*, vol. 375–377, no. 1–2 SPEC. ISS., pp. 213–218, 2004.

[3] "Patent Anna Fraczkiewicz FR-1459567, October 2014." .

[4] "https://en.wikipedia.org/wiki/Timeline_of_chemical_element_discoveries."

[5] S. Ranganathan, "Alloyed pleasures: Multimetallic cocktails," *Curr. Sci.*, vol. 85, no. 10, pp. 1404–1406, 2003.

[6] A. L. Mackay, "On complexity," *Crystallogr. Reports*, vol. 46, no. 4, pp. 524–526, 2001.

[7] G. Wolf, J. Lerchner, H. Schmidt, H. Gamsjäger, E. Königsberger, and P. Schmidt, "Thermodynamics of CaCO3 phase transitions," *J. Therm. Anal.*, vol. 46, no. 2, pp. 353–359, 1996.

[8] J. W. Yeh, "Recent progress in high-entropy alloys," *Ann. Chim. Sci. des Mater.*, vol. 31, no. 6, pp. 633–648, 2006.

[9] J. Yeh, "Alloy Design Strategies and Future Trends in High-Entropy Alloys," vol. 65, no. 12, pp. 1759–1771, 2013.

[10] D. B. Miracle and O. N. Senkov, "A critical review of high entropy alloys and related concepts," *Acta Mater.*, vol. 122, no. October, pp. 448–511, 2017.

[11] D. B. Miracle, J. D. Miller, O. N. Senkov, C. Woodward, M. D. Uchic, and J. Tiley, "Exploration and development of high entropy alloys for structural applications," *Entropy*, vol. 16, no. 1, pp. 494–525, 2014.

[12] S. Guo, Q. Hu, C. Ng, and C. T. Liu, "More than entropy in high-entropy alloys: Forming solid solutions or amorphous phase," *Intermetallics*, vol. 41, pp. 96–103, 2013.

[13] K. Y. Tsai, M. H. Tsai, and J. W. Yeh, "Sluggish diffusion in Co-Cr-Fe-Mn-Ni high-entropy alloys," *Acta Mater.*, vol. 61, no. 13, pp. 4887–4897, 2013.

[14] G. H. Vineyard, "Theory of order-disorder kinetics," *Phys. Rev.*, vol. 102, no. 4, pp. 981–992, 1956.

[15] M. Vaidya, S. Trubel, B. S. Murty, G. Wilde, and S. V. Divinski, "Ni tracer diffusion in CoCrFeNi and CoCrFeMnNi high entropy alloys," *J. Alloys Compd.*, vol. 688, pp. 994–1001, 2016.

[16] E. J. Pickering and N. G. Jones, "High-entropy alloys: a critical assessment of their founding principles and future prospects," *Int. Mater. Rev.*, vol. 61, no. 3, pp. 183–202, 2016.

[17] C. Y. Hsu, C. C. Juan, W. R. Wang, T. S. Sheu, J. W. Yeh, and S. K. Chen, "On the superior hot hardness and softening resistance of AlCoCrxFeMo0.5Ni high-entropy alloys," *Mater. Sci. Eng. A*, vol. 528, no. 10–11, pp. 3581–3588, 2011.

[18] O. N. Senkov, G. B. Wilks, J. M. Scott, and D. B. Miracle, "Mechanical properties of Nb25Mo25Ta25W25 and V20Nb20Mo20Ta20W20 refractory high entropy alloys," *Intermetallics*, vol. 19, no. 5, pp. 698–706, 2011.

[19] M.-H. Tsai, C.-W. Wang, C.-W. Tsai, W.-J. Shen, J.-W. Yeh, J.-Y. Gan, and W.-W. Wu, "Thermal Stability and Performance of NbSiTaTiZr High-Entropy Alloy Barrier for Copper Metallization," *J. Electrochem. Soc.*, vol. 158, no. 11, pp. H1161–H1165, 2011.

[20] T. T. Shun, C. H. Hung, and C. F. Lee, "Formation of ordered/disordered nanoparticles in FCC high entropy alloys," *J. Alloys Compd.*, vol. 493, no. 1–2, pp. 105–109, 2010.

[21] M.-H. Tsai, H. Yuan, G. Cheng, W. Xu, K.-Y. Tsai, C.-W. Tsai, W. W. Jian, C.-C. Juan, W.-J. Shen, M.-H. Chuang, J.-W. Yeh, and Y. T. Zhu, "Morphology, structure and composition of precipitates in Al 0.3 CoCrCu 0.5 FeNi high-entropy alloy," *Intermetallics*, vol. 32, pp. 329–336, 2013.

Literature

[22]   M.-H. Tsai, C.-W. Wang, C.-W. Tsai, W.-J. Shen, J.-W. Yeh, J.-Y. Gan, and W.-W. Wu, "Thermal Stability and Performance of NbSiTaTiZr High-Entropy Alloy Barrier for Copper Metallization," *J. Electrochem. Soc.*, vol. 158, no. 11, pp. H1161–H1165, 2011.

[23]   L. R. Owen, E. J. Pickering, H. Y. Playford, H. J. Stone, M. G. Tucker, and N. G. Jones, "Acta Materialia An assessment of the lattice strain in the CrMnFeCoNi high-entropy alloy," *Acta Mater.*, vol. 122, pp. 11–18, 2017.

[24]   J. W. Yeh, S. Y. Chang, Y. Der Hong, S. K. Chen, and S. J. Lin, "Anomalous decrease in X-ray diffraction intensities of Cu-Ni-Al-Co-Cr-Fe-Si alloy systems with multi-principal elements," *Mater. Chem. Phys.*, vol. 103, no. 1, pp. 41–46, 2007.

[25]   O. N. Senkov, G. B. Wilks, D. B. Miracle, C. P. Chuang, and P. K. Liaw, "Refractory high-entropy alloys," *Intermetallics*, vol. 18, no. 9, pp. 1758–1765, 2010.

[26]   S.-W. Kao, J. Yeh, and T.-S. Chin, "Rapidly solidified structure of alloys with up to eight equal-molar elements—a simulation by molecular dynamics," *J. Phys. Condens. Matter*, vol. 20, no. 14, p. 145214, 2008.

[27]   S.-W. Kao, J. Yeh, and T.-S. Chin, "Rapidly solidified structure of alloys with up to eight equal-molar elements—a simulation by molecular dynamics," *J. Phys. Condens. Matter*, vol. 20, no. 14, p. 145214, 2008.

[28]   C. L. Lu, S. Y. Lu, J. W. Yeh, and W. K. Hsu, "Thermal expansion and enhanced heat transfer in high-entropy alloys," *J. Appl. Crystallogr.*, vol. 46, no. 3, pp. 736–739, 2013.

[29]   H. P. Chou, Y. S. Chang, S. K. Chen, and J. W. Yeh, "Microstructure, thermophysical and electrical properties in AlxCoCrFeNi high-entropy alloys," *Mater. Sci. Eng. B Solid-State Mater. Adv. Technol.*, vol. 163, no. 3, pp. 184–189, 2009.

[30]   Y. F. Kao, S. K. Chen, T. J. Chen, P. C. Chu, J. W. Yeh, and S. J. Lin, "Electrical, magnetic, and Hall properties of AlxCoCrFeNi high-entropy alloys," *J. Alloys Compd.*, vol. 509, no. 5, pp. 1607–1614, 2011.

[31]   S. B. Newcomb and G. F. Vander Voort, "Smithells Metals Reference Book," *Smithells Met. Ref. B.*, pp. 1–87, 2004.

[32]   D. R. Lide, "CRC Handbook of Chemistry and Physics, 84th Edition, 2003-2004," *Handb. Chem. Phys.*, vol. 53, p. 2616, 2003.

[33]   J. F. Shackelford and W. Alexander, *CRC materials science and engineering handbook*, vol. 49. 2001.

[34]   M.-H. Tsai and J.-W. Yeh, "High-Entropy Alloys: A Critical Review," *Mater. Res. Lett.*, vol. 2, pp. 107–123, 2014.

[35]   J. H. Pi, Y. Pan, L. Zhang, and H. Zhang, "Microstructure and property of AlTiCrFeNiCu high-entropy alloy," *J. Alloys Compd.*, vol. 509, no. 18, pp. 5641–5645, 2011.

[36]   C. M. Lin and H. L. Tsai, "Evolution of microstructure, hardness, and corrosion properties of high-entropy Al0.5CoCrFeNi alloy," *Intermetallics*, vol. 19, no. 3, pp. 288–294, 2011.

[37]   U. Mizutani, "Hume-Rothery rules for structurally complex alloy phases," *MRS Bull.*, vol. 37, no. 2, p. 169, 2012.

[38]   F. R. De Boer, R. Boom, W. C. M. Mattens, A. R. Miedema, and A. K. Niessen, *Cohesion in Metals*, vol. 1, no. 758. 1988.

[39]   M. X. Ren, B. S. Li, and H. Z. Fu, "Formation condition of solid solution type high-entropy alloy," *Trans. Nonferrous Met. Soc. China (English Ed.)*, vol. 23, no. 4, pp. 991–995, 2013.

[40]   X. Yang and Y. Zhang, "Prediction of high-entropy stabilized solid-solution in multi-component alloys," *Mater. Chem. Phys.*, vol. 132, no. 2–3, pp. 233–238, 2012.

[41]   S. Guo, C. Ng, J. Lu, and C. T. Liu, "Effect of valence electron concentration on stability of fcc or bcc phase in high entropy alloys," *J. Appl. Phys.*, vol. 109, no. 10, 2011.

[42]   M. G. Poletti and L. Battezzati, "Electronic and thermodynamic criteria for the occurrence of high entropy alloys in metallic systems," *Acta Mater.*, vol. 75, pp. 297–306, 2014.

Literature

[43]   D. Ma, B. Grabowski, F. Körmann, J. Neugebauer, and D. Raabe, "Acta Materialia Ab initio thermodynamics of the CoCrFeMnNi high entropy alloy : Importance of entropy contributions beyond the configurational one," *Acta Mater.*, vol. 100, pp. 90–97, 2015.

[44]   F. Tancret, I. Toda-Caraballo, E. Menou, and P. E. J. Rivera Díaz-Del-Castillo, "Designing high entropy alloys employing thermodynamics and Gaussian process statistical analysis," *Mater. Des.*, vol. 115, pp. 486–497, 2017.

[45]   O. N. Senkov, D. Isheim, D. N. Seidman, and A. L. Pilchak, "Development of a refractory high entropy superalloy," *Entropy*, vol. 18, no. 3, pp. 1–13, 2016.

[46]   Z. G. Yang, D. M. Paxton, K. S. Weil, J. W. Stevenson, and P. Singh, "Materials Properties Database for Selection of High-Temperature Alloys and Concepts of Alloy Design for SOFC Applications," no. November, p. 74, 2002.

[47]   D. Raabe, C. C. Tasan, H. Springer, and M. Bausch, "From high-entropy alloys to high-entropy steels," *Steel Res. Int.*, vol. 86, no. 10, pp. 1127–1138, 2015.

[48]   "https://www.nei.org/Knowledge-Center/Nuclear-Statistics/World-Statistics." .

[49]   F. Granberg, K. Nordlund, M. W. Ullah, K. Jin, C. Lu, H. Bei, L. M. Wang, F. Djurabekova, W. J. Weber, and Y. Zhang, "Mechanism of Radiation Damage Reduction in Equiatomic Multicomponent Single Phase Alloys," *Phys. Rev. Lett.*, vol. 116, no. 13, 2016.

[50]   L. Koch, F. Granberg, T. Brink, K. Albe, F. Djurabekova, and K. Nordlund, "Ordering versus irradiation effects in high-entropy alloys: Steady-state conditions in a driven system," pp. 1–11, 2017.

[51]   Z. Li, K. G. Pradeep, Y. Deng, D. Raabe, and C. C. Tasan, "Metastable high-entropy dual-phase alloys overcome the strength–ductility trade-off," *Nature*, pp. 4–11, 2016.

[52]   B. Gludovatz, A. Hohenwarter, D. Catoor, E. H. Chang, E. P. George, and R. O. Ritchie, "A fracture-resistant high-entropy alloy for cryogenic applications.," *Science*, vol. 345, no. 6201, pp. 1153–8, 2014.

[53]   X. Ye, M. Ma, Y. Cao, W. Liu, X. Ye, and Y. Gu, "The property research on high-entropy alloy AlxFeCoNiCuCr coating by laser cladding," *Phys. Procedia*, vol. 12, no. PART 1, pp. 303–312, 2011.

[54]   S. J. Mary, R. Nagalakshmi, and R. Epshiba, "High Entropy Alloys Properties and Its Applications – an Overview," vol. 4, no. 6, pp. 279–284, 2015.

[55]   W. H. Wu, C. C. Yang, and J. W. Yeh, "Industrial development of high-entropy alloys," *Ann. Chim. Sci. des Mater.*, vol. 31, no. 6, pp. 737–747, 2006.

[56]   B. S. Murty, J. W. Yeh, and S. Ranganathan, "High Entropy Alloys," *High Entropy Alloy.*, no. January, pp. 159–169, 2014.

[57]   M. Laurent-Brocq, A. Akhatova, L. Perriere, S. Chebini, X. Sauvage, E. Leroy, and Y. Champion, "Insights into the phase diagram of the CrMnFeCoNi high entropy alloy," *Acta Mater.*, vol. 88, pp. 355–365, 2015.

[58]   C. C. Tasan, Y. Deng, K. G. Pradeep, M. J. Yao, H. Springer, and D. Raabe, "Composition Dependence of Phase Stability, Deformation Mechanisms, and Mechanical Properties of the CoCrFeMnNi High-Entropy Alloy System," *Jom*, vol. 66, no. 10, pp. 1993–2001, 2014.

[59]   B. Schuh, F. Mendez-Martin, B. Völker, E. P. George, H. Clemens, R. Pippan, and A. Hohenwarter, "Mechanical properties, microstructure and thermal stability of a nanocrystalline CoCrFeMnNi high-entropy alloy after severe plastic deformation," *Acta Mater.*, vol. 96, pp. 258–268, 2015.

[60]   E. J. Pickering, R. Muñoz-Moreno, H. J. Stone, and N. G. Jones, "Precipitation in the equiatomic high-entropy alloy CrMnFeCoNi," *Scr. Mater.*, vol. 113, pp. 106–109, 2016.

[61]   F. Otto, A. Dlouhý, K. G. Pradeep, M. Kuběnová, D. Raabe, G. Eggeler, and E. P. George, "Decomposition of the single-phase high-entropy alloy CrMnFeCoNi after prolonged anneals at intermediate temperatures," *Acta Mater.*, vol. 112, pp. 40–52, 2016.

[62]   N. D. Stepanov, D. G. Shaysultanov, M. S. Ozerov, S. V. Zherebtsov, and G. A. Salishchev, "Second phase formation in the CoCrFeNiMn high entropy alloy after recrystallization annealing," *Mater. Lett.*, vol. 185,

pp. 1–4, 2016.

[63] N. Park, B.-J. Lee, and N. Tsuji, "The phase stability of equiatomic CoCrFeMnNi high-entropy alloy: Comparison between experiment and calculation results," *J. Alloys Compd.*, vol. 719, pp. 189–193, 2017.

[64] A. Gali and E. P. George, "Tensile properties of high- and medium-entropy alloys," *Intermetallics*, vol. 39, pp. 74–78, 2013.

[65] Y. Zhang, T. T. Zuo, Z. Tang, M. C. Gao, K. A. Dahmen, P. K. Liaw, and Z. P. Lu, "Microstructures and properties of high-entropy alloys," *Prog. Mater. Sci.*, vol. 61, no. October 2013, pp. 1–93, 2014.

[66] F. Otto, A. Dlouhy, C. Somsen, H. Bei, G. Eggeler, and E. P. George, "The influences of temperature and microstructure on the tensile properties of a CoCrFeMnNi high-entropy alloy," *Acta Mater.*, vol. 61, no. 15, pp. 5743–5755, 2013.

[67] F. Otto, N. L. Hanold, and E. P. George, "Microstructural evolution after thermomechanical processing in an equiatomic, single-phase CoCrFeMnNi high-entropy alloy with special focus on twin boundaries," *Intermetallics*, vol. 54, pp. 39–48, 2014.

[68] N. D. Stepanov, D. G. Shaysultanov, N. Y. Yurchenko, S. V. Zherebtsov, A. N. Ladygin, G. A. Salishchev, and M. A. Tikhonovsky, "High temperature deformation behavior and dynamic recrystallization in CoCrFeNiMn high entropy alloy," *Mater. Sci. Eng. A*, vol. 636, pp. 188–195, 2015.

[69] T. Sakai, A. Belyakov, R. Kaibyshev, H. Miura, and J. J. Jonas, "Dynamic and post-dynamic recrystallization under hot, cold and severe plastic deformation conditions," *Prog. Mater. Sci.*, vol. 60, no. 1, pp. 130–207, 2014.

[70] N. N. Guo, L. Wang, L. S. Luo, X. Z. Li, R. R. Chen, Y. Q. Su, J. J. Guo, and H. Z. Fu, "Hot deformation characteristics and dynamic recrystallization of the MoNbHfZrTi refractory high-entropy alloy," *Mater. Sci. Eng. A*, vol. 651, pp. 698–707, 2016.

[71] H. Zhang, K. Zhang, S. Jiang, H. Zhou, C. Zhao, and X. Yang, "Dynamic recrystallization behavior of a γ'-hardened nickel-based superalloy during hot deformation," *J. Alloys Compd.*, vol. 623, pp. 374–385, 2015.

[72] A. Rollett, F. Humphreys, G. S. Rohrer, and M. Hatherly, *Recrystallization and Related Annealing Phenomena: Second Edition*. 2004.

[73] Y. T. Zhu and X. Liao, "Nanostructured metals: retaining ductility.," *Nat. Mater.*, vol. 3, no. 6, pp. 351–352, 2004.

[74] X. H. An, Q. Y. Lin, S. D. Wu, Z. F. Zhang, R. B. Figueiredo, N. Gao, and T. G. Langdon, "The influence of stacking fault energy on the mechanical properties of nanostructured Cu and Cu-Al alloys processed by high-pressure torsion," *Scr. Mater.*, vol. 64, no. 10, pp. 954–957, 2011.

[75] S. Allain, J. P. Chateau, O. Bouaziz, S. Migot, and N. Guelton, "Correlations between the calculated stacking fault energy and the plasticity mechanisms in Fe-Mn-C alloys," *Mater. Sci. Eng. A*, vol. 387–389, no. 1–2 SPEC. ISS., pp. 158–162, 2004.

[76] A. Dumay, J. P. Chateau, S. Allain, S. Migot, and O. Bouaziz, "Influence of addition elements on the stacking-fault energy and mechanical properties of an austenitic Fe-Mn-C steel," *Mater. Sci. Eng. A*, vol. 483–484, no. 1–2 C, pp. 184–187, 2008.

[77] A. J. Zaddach, C. Niu, C. C. Koch, and D. L. Irving, "Mechanical properties and stacking fault energies of NiFeCrCoMn high-entropy alloy," *JOM*, vol. 65, no. 12, pp. 1780–1789, 2013.

[78] C. B. Carter and S. M. Holmes, "The stacking-fault energy of nickel," *Philos. Mag.*, vol. 35, no. 5, pp. 1161–1172, 1977.

[79] S. Huang, W. Li, S. Lu, F. Tian, J. Shen, E. Holmström, and L. Vitos, "Temperature dependent stacking fault energy of FeCrCoNiMn high entropy alloy," *Scr. Mater.*, vol. 108, pp. 44–47, 2015.

[80] B. Gludovatz, A. Hohenwarter, D. Catoor, E. H. Chang, E. P. George, and R. O. Ritchie, "A fracture-resistant high-entropy alloy for cryogenic applications," *Science (80-.).*, vol. 345, no. 6201, pp. 1153–1158, 2014.

[81] Z. Zhang, M. M. Mao, J. Wang, B. Gludovatz, Z. Zhang, S. X. Mao, E. P. George, Q. Yu, and R. O. Ritchie,

"Nanoscale origins of the damage tolerance of the high-entropy alloy CrMnFeCoNi," *Nat. Commun.*, vol. 6, pp. 1–6, 2015.

[82]   F. He, Z. Wang, P. Cheng, Q. Wang, J. Li, Y. Dang, J. Wang, and C. T. Liu, "Designing eutectic high entropy alloys of CoCrFeNiNbx," *J. Alloys Compd.*, vol. 656, pp. 284–289, 2016.

[83]   A. Manzoni, H. Daoud, S. Mondal, S. Van Smaalen, R. Volkl, U. Glatzel, and N. Wanderka, "Investigation of phases in Al23Co15Cr 23Cu8Fe15Ni16 and Al 8Co17Cr17Cu8Fe17Ni 33 high entropy alloys and comparison with equilibrium phases predicted by Thermo-Calc," *J. Alloys Compd.*, vol. 552, pp. 430–436, 2013.

[84]   M. Gao and D. Alman, "Searching for Next Single-Phase High-Entropy Alloy Compositions," *Entropy*, vol. 15, no. 10, pp. 4504–4519, 2013.

[85]   A. M. Manzoni, S. Singh, H. M. Daoud, R. Popp, R. Volkl, U. Glatzel, and N. Wanderka, "On the path to optimizing the Al-Co-Cr-Cu-Fe-Ni-Ti high entropy alloy family for high temperature applications," *Entropy*, vol. 18, no. 4, 2016.

[86]   T. S. Byun, "On the stress dependence of partial dislocation separation and deformation microstructure in austenitic stainless steels," *Acta Mater.*, vol. 51, no. 11, pp. 3063–3071, 2003.

[87]   T. M. Smith, M. S. Hooshmand, B. D. Esser, F. Otto, D. W. Mccomb, E. P. George, M. Ghazisaeidi, and M. J. Mills, "Acta Materialia Atomic-scale characterization and modeling of 60 dislocations in a high-entropy alloy," vol. 110, pp. 352–363, 2016.

[88]   V. Gerold and H. P. Karnthaler, "On the origin of planar slip in f.c.c. alloys," *Acta Metall.*, vol. 37, no. 8, pp. 2177–2183, 1989.

[89]   M. J. Whelan, P. B. Hirsch, R. W. Horne, and W. Bollmann, "Dislocations and Stacking Faults in Stainless Steel," *Proc. R. Soc. A Math. Phys. Eng. Sci.*, vol. 240, no. 1223, pp. 524–538, 1957.

[90]   A. Korner and H. P. Karnthaler, "Analysis of the stacking faults of dissociated glide dislocation sin fcc metals," *Phys. Status Solidi*, vol. 68, pp. 19–28, 1981.

[91]   N. L. Okamoto, S. Fujimoto, Y. Kambara, M. Kawamura, Z. M. T. Chen, H. Matsunoshita, K. Tanaka, H. Inui, and E. P. George, "Size effect, critical resolved shear stress, stacking fault energy, and solid solution strengthening in the CrMnFeCoNi high-entropy alloy," *Sci. Rep.*, vol. 6, no. 1, p. 35863, 2016.

[92]   C. B. Carter and I. L. F. Ray, "Observations of constrictions on dissociated dislocation lines in copper alloys," *Philos. Mag.*, vol. 29, no. 5, pp. 1231–1235, 1974.

[93]   M. J. Mills, N. L. Baluc, and P. M. Sarosi, "HRTEM of dislocation cores and thin-foil effects in metals and intermetallic compounds," *Microsc. Res. Tech.*, vol. 69, no. 5, pp. 317–329, 2006.

[94]   C. B. Carter and S. M. Holmes, "The stacking-fault energy of nickel," *Philos. Mag.*, vol. 35, no. 5, pp. 1161–1172, 1977.

[95]   T. Software, "THERMO-CALC & DICTRA, Computational Tools For Materials Science J-O Andersson, Thomas Helander,Lars Hdghmd, Pingfang Shi, Bo Sundman," *Calphad Comput. Coupling Phase Diagrams Thermochem.*, vol. 26, no. 2, pp. 273–312, 2002.

[96]   K. G. Pradeep, N. Wanderka, P. Choi, J. Banhart, B. S. Murty, and D. Raabe, "Atomic-scale compositional characterization of a nanocrystalline AlCrCuFeNiZn high-entropy alloy using atom probe tomography," *Acta Mater.*, vol. 61, no. 12, pp. 4696–4706, 2013.

[97]   D. Ma, M. Yao, K. G. Pradeep, C. C. Tasan, H. Springer, and D. Raabe, "Phase stability of non-equiatomic CoCrFeMnNi high entropy alloys," *Acta Mater.*, vol. 98, no. 1, pp. 288–296, 2015.

[98]   G. D. Sathiaraj and P. P. Bhattacharjee, "Effect of starting grain size on the evolution of microstructure and texture during thermo-mechanical processing of CoCrFeMnNi high entropy alloy," *J. Alloys Compd.*, vol. 647, pp. 82–96, 2015.

[99]   N. D. Stepanov, D. G. Shaysultanov, G. A. Salishchev, M. A. Tikhonovsky, E. E. Oleynik, A. S. Tortika, and O. N. Senkov, "Effect of v content on microstructure and mechanical properties of the CoCrFeMnNiVx high entropy alloys," *J. Alloys Compd.*, vol. 628, pp. 170–185, 2015.

Literature

[100]	G. Laplanche, O. Horst, F. Otto, G. Eggeler, and E. P. George, "Microstructural evolution of a CoCrFeMnNi high-entropy alloy after swaging and annealing," *J. Alloys Compd.*, vol. 647, pp. 548–557, 2015.

[101]	P. P. Bhattacharjee, G. D. Sathiaraj, M. Zaid, J. R. Gatti, C. Lee, C. W. Tsai, and J. W. Yeh, "Microstructure and texture evolution during annealing of equiatomic CoCrFeMnNi high-entropy alloy," *J. Alloys Compd.*, vol. 587, pp. 544–552, 2014.

[102]	F. Otto, Y. Yang, H. Bei, and E. P. George, "Relative effects of enthalpy and entropy on the phase stability of equiatomic high-entropy alloys," *Acta Mater.*, vol. 61, no. 7, pp. 2628–2638, 2013.

[103]	F. Zhang, C. Zhang, S. L. Chen, J. Zhu, W. S. Cao, and U. R. Kattner, "An understanding of high entropy alloys from phase diagram calculations," *Calphad Comput. Coupling Phase Diagrams Thermochem.*, vol. 45, pp. 1–10, 2014.

[104]	J. Kelly, *Stainless Steels*, vol. 734, no. 1993. 2007.

[105]	I. Shuro, S. Kobayashi, T. Nakamura, and K. Tsuzaki, "Determination of α/γ phase boundaries in the Fe-Cr-Ni-Mn quaternary system with a diffusion-multiple method," *J. Alloys Compd.*, vol. 588, pp. 284–289, 2014.

[106]	G. Samsonov, "Handbook of the Physicochemical Properties of the Elements," in *Handbook of the Physicochemical Properties of the Elements*, 1968, pp. 387–446.

[107]	A. Takeuchi and A. Inoue, "Mixing enthalpy of liquid phase calculated by miedema's scheme and approximated with sub-regular solution model for assessing forming ability of amorphous and glassy alloys," *Intermetallics*, vol. 18, no. 9, pp. 1779–1789, 2010.

[108]	To be published: M. Mroz and A. Fraczkiewicz, "Microstructure and compression behavior of equiatomic CoCuFeMnNi high-entropy alloy," 2016.

[109]	To be published: J. Olszewska, M. Mroz, M. Mondon, G. He, and A. Fraczkiewicz, "Evaluation of an original grade of HEA alloys from AlCrFeMnNi family."

[110]	J. Y. He, W. H. Liu, H. Wang, Y. Wu, X. J. Liu, T. G. Nieh, and Z. P. Lu, "Effects of Al addition on structural evolution and tensile properties of the FeCoNiCrMn high-entropy alloy system," *Acta Mater.*, vol. 62, no. 1, pp. 105–113, 2014.

[111]	K. Zhang and Z. Fu, "Effects of annealing treatment on phase composition and microstructure of CoCrFeNiTiAlx high-entropy alloys," *Intermetallics*, vol. 22, pp. 24–32, 2012.

[112]	T. Sakai, "Dynamic recrystallization microstructures under hot working conditions," *J. Mater. Process. Technol.*, vol. 53, no. 1–2, pp. 349–361, 1995.

[113]	C. M. Sellars, "Recrystallization of Metals during Hot Deformation," *Philos. Trans. R. Soc. A Math. Phys. Eng. Sci.*, vol. 288, no. 1350, pp. 147–158, 1978.

[114]	P. K. Jayakumar, K. Balasubramanian, and G. Rabindranath Tagore, "Recrystallisation and bonding behaviour of ultra fine grained copper and Cu-Cr-Zr alloy using ECAP," *Mater. Sci. Eng. A*, vol. 538, pp. 7–13, 2012.

[115]	K. R. Williams, "Deformation twinning in alloys of low stacking-fault energy," *J. Mater. Sci.*, vol. 8, no. 1, pp. 109–115, 1973.

[116]	C. C. Dollins, "Nucleation on dislocations," *Acta Metall.*, vol. 18, no. 11, pp. 1209–1215, 1970.

[117]	U. Zugrundelegung, "On dislocations*," vol. 1, no. 1, pp. 1–4, 1957.

[118]	S. V Divinski, J. Ribbe, G. Reglitz, Y. Estrin, and G. Wilde, "Ultra-Fast Diffusion in Severely Deformed Materials," vol. 11, pp. 1–2, 2009.

[119]	B. B. R.Z. Valiev, E.V. Kozlov, Yu. F. Ivanov, J. Lian, A. A. Nazarov, "DEFORMATION BEHAVIOUR OF ULTRA-FINE-GRAINED," vol. 42, no. 7, pp. 2467–2475, 1994.

[120]	R. Xiong, H. Peng, S. Wang, H. Si, and Y. Wen, "Effect of stacking fault energy on work hardening behaviors in Fe-Mn-Si-C high manganese steels by varying silicon and carbon contents," *Mater. Des.*, vol. 85, pp. 707–714, 2015.

Literature

[121] Y. Z. Tian, L. J. Zhao, S. Chen, A. Shibata, Z. F. Zhang, and N. Tsuji, "Significant contribution of stacking faults to the strain hardening behavior of Cu-15%Al alloy with different grain sizes," *Sci. Rep.*, vol. 5, no. October, p. 16707, 2015.

[122] P. H. Adler, G. B. Olson, and W. S. Owen, "Strain Hardening of Hadfield Manganese Steel," *Metall. Mater. Trans. A*, vol. 17, no. 10, pp. 1725–1737, 1986.

[123] S. Curtze and V. T. Kuokkala, "Dependence of tensile deformation behavior of TWIP steels on stacking fault energy, temperature and strain rate," *Acta Mater.*, vol. 58, no. 15, pp. 5129–5141, 2010.

[124] Eurinox, "Stainless Steel: Tables of Technical Properties." [Online]. Available: www.worldstainless.org/Files/issf/non-image-files/PDF/Euro_Inox/Tables_TechnicalProperties_EN.pdf.

[125] N. Stepanov, M. Tikhonovsky, N. Yurchenko, D. Zyabkin, M. Klimova, S. Zherebtsov, A. Efimov, and G. Salishchev, "Effect of cryo-deformation on structure and properties of CoCrFeNiMn high-entropy alloy," *Intermetallics*, vol. 59, pp. 8–17, 2015.

[126] A. Haglund, M. Koehler, D. Catoor, E. P. George, and V. Keppens, "Polycrystalline elastic moduli of a high-entropy alloy at cryogenic temperatures," *Intermetallics*, vol. 58, pp. 62–64, 2015.

[127] J. Olszewska, "Thesis in preparation."

[128] E. El-Danaf, S. R. Kalidindi, and R. D. Doherty, "Influence of grain size and stacking-fault energy on deformation twinning in fcc metals," *Metall. Mater. Trans. A*, vol. 30, no. May, pp. 1223–1233, 1999.

[129] Y. H. Jo, S. Jung, W. M. Choi, S. S. Sohn, H. S. Kim, B. J. Lee, N. J. Kim, and S. Lee, "Cryogenic strength improvement by utilizing room-temperature deformation twinning in a partially recrystallized VCrMnFeCoNi high-entropy alloy," *Nat. Commun.*, vol. 8, p. 15719, 2017.

[130] W. H. Liu, Y. Wu, J. Y. He, T. G. Nieh, and Z. P. Lu, "Grain growth and the Hall-Petch relationship in a high-entropy FeCrNiCoMn alloy," *Scr. Mater.*, vol. 68, no. 7, pp. 526–529, 2013.

[131] K. Takeda, N. Nakada, T. Tsuchiyama, and S. Takaki, "Effect of Interstitial Elements on Hall–Petch Coefficient of Ferritic Iron," *ISIJ Int.*, vol. 48, no. 8, pp. 1122–1125, 2008.

[132] J. MORAVEC, "DETERMINATION OF THE GRAIN GROWTH KINETICS AS A BASE PARAMETER FOR NUMERICAL SIMULATION DEMAND," *MM Sci. J.*, no. 2, pp. 665–669, 2015.

[133] A. Borbely and J. H. Driver, "Disloaction Density Measurement by X-ray Profile Analysis in Texture Components of Deformed Metals," *Archives of Metallurgy and Materials*, vol. 50. pp. 65–76, 2005.

[134] Z. Yanushkevich, A. Mogucheva, M. Tikhonova, A. Belyakov, and R. Kaibyshev, "Structural strengthening of an austenitic stainless steel subjected to warm-to-hot working," *Mater. Charact.*, vol. 62, no. 4, pp. 432–437, 2011.

[135] A. Kalinenko, P. Kusakin, A. Belyakov, R. Kaibyshev, and D. A. Molodov, "Microstructure and mechanical properties of a high-MN twip steel subjected to cold rolling and annealing," *Metals (Basel).*, vol. 7, no. 12, 2017.

[136] R. K. Roy, S. Kar, K. Das, and S. Das, "A study of precipitation and recrystallization behaviour of aluminium alloy AA1235," *J. Mater. Sci.*, vol. 41, no. 4, pp. 1039–1045, 2006.

[137] C. Varvenne, A. Luque, and W. A. Curtin, "Theory of strengthening in fcc high entropy alloys," *Acta Mater.*, vol. 118, pp. 164–176, 2016.

[138] Y. Ma, Q. Wang, C. Li, L. J. Santodonato, M. Feygenson, C. Dong, and P. K. Liaw, "Chemical short-range orders and the induced structural transition in high-entropy alloys," *Scr. Mater.*, vol. 144, pp. 64–68, 2018.

[139] C. Varvenne, A. Luque, W. G. Nöhring, and W. A. Curtin, "Average-atom interatomic potential for random alloys," *Phys. Rev. B*, vol. 93, no. 10, 2016.

[140] S. Yoshida, T. Bhattacharjee, Y. Bai, and N. Tsuji, "Scripta Materialia Friction stress and Hall-Petch relationship in CoCrNi equi-atomic medium entropy alloy processed by severe plastic deformation and subsequent annealing," *Scr. Mater.*, vol. 134, pp. 33–36, 2017.

[141] Z. Wu, H. Bei, G. M. Pharr, and E. P. George, "Temperature dependence of the mechanical properties of

equiatomic solid solution alloys with face-centered cubic crystal structures," *Acta Mater.*, vol. 81, pp. 428–441, 2014.

[142]   S. Singh, N. Wanderka, B. S. Murty, U. Glatzel, and J. Banhart, "Decomposition in multi-component AlCoCrCuFeNi high-entropy alloy," *Acta Mater.*, vol. 59, no. 1, pp. 182–190, 2011.

[143]   G. Dieter, "http://slideplayer.com/slide/5956651/." .

[144]   W. D. Nix, "Partial Dislocation Tutorial for FCC Metals." .

[145]   V. Bulatov, F. F. Abraham, L. Kubin, B. Devincre, and S. Yip, "Connecting atomistic and mesoscale simulations of crystal plasticity," *Nature*, vol. 391, no. 6668, pp. 669–672, 1998.

[146]   W. Cai, V. V. Bulatov, J. Chang, J. Li, and S. Yip, *Chapter 64 Dislocation core effects on mobility*, vol. 12, no. C. 2005.

[147]   A. K. Head, "Unstable Dislocations in Anisotropic Crystals," *Phys. status solidi*, vol. 19, no. 1, pp. 185–192, 1967.

[148]   E. I. Poliak and J. J. Jonas, "A one-parameter approach to determining the critical conditions for the initiation of dynamic recrystallization," *Acta Mater.*, vol. 44, no. 1, pp. 127–136, 1996.

Annexes

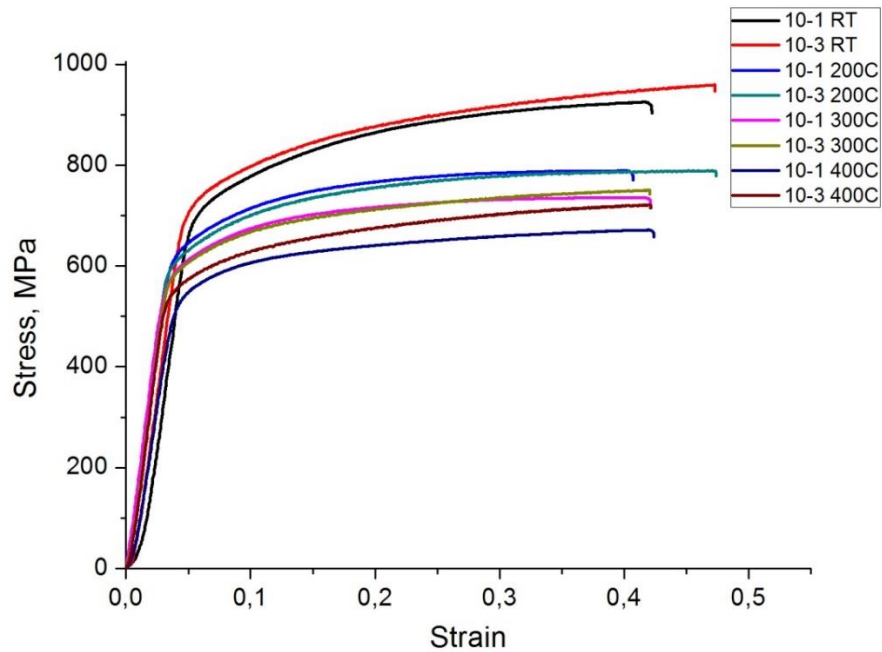## Annex 1. The results of compression tests

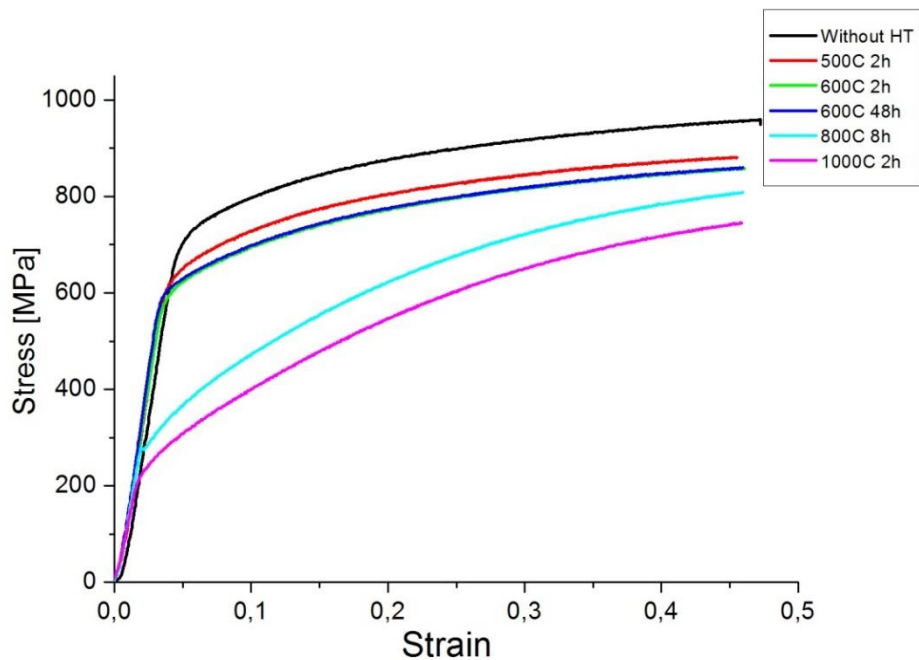**Figure A.1. Hot compression stress-strain curves of the as-forged A3S with different strain rates (10^{-1} and 10^{-3} s^{-1}).**

Figure A.2. Compression stress-strain curves of the A3S forged and annealed at different temperatures and times. Strain rate 10^{-3} s^{-1}.

Annex 2. Summary of all the chapters in French / Résumé de tous les chapitres en français

<u>Chapitre 1: L'état de l'art des alliages à haute entropie</u>

Introduction: Dans ce chapitre, la définition d'un alliage à haute entropie (HEA, *high entropy alloy* en anglais) est donnée, décrite par les principes thermodynamiques. Plus tard, les quatre effets principaux dans les HEAs sont expliqués. Ensuite, des critères fondamentaux pour la formation de HEA sont listés qui serviront pour d'autres investigations. Des exemples d'applications de HEA sont également donnés. La composition étudiée, CoCrFeMnNi, est décrite en ce qui concerne sa structure, sa stabilité et ses propriétés mécaniques. A la fin, les motivations pour un travail ultérieur sont données.

Résumé: Les alliages à haute entropie sont constitués de cinq éléments ou plus dans des rapports similaires avec une structure de solution solide. L'importance du sujet se reflète dans le nombre croissant de publications chaque année. L'une des principales motivations du travail sur les alliages à haute entropie était d'explorer la région centrale des diagrammes de phase dans les alliages à plusieurs composants. Par conséquent, le contenu des différents éléments dans les HEAs est approximativement égal et devrait être compris entre 5% et 35%. En outre, le nombre d'éléments doit être supérieur à cinq pour faciliter la formation d'une solution solide. On peut distinguer quatre effets fondamentaux influençant les propriétés, la microstructure, la thermodynamique et la cinétique des HEA: entropie élevée, distorsion sévère du réseau, diffusion ralentis et effet cocktail. Puisque les HEA ne sont pas des matériaux classiques avec un élément principal mais contiennent de nombreux éléments dans des proportions similaires, ces effets diffèrent des alliages conventionnels.

Les règles standard de formation d'une solution entre deux éléments ne sont pas suffisantes pour des systèmes beaucoup plus complexes comme les alliages à haute entropie. Quelques paramètres importants doivent être considérés lors de la recherche

de nouveaux alliages à haute entropie: rayon atomique, entropie et enthalpie de mélange, concentration d'électrons de valence et électronégativité. Ceux-ci devraient être un premier indicateur dans le choix des compositions HEA, mais pas les seuls. Normalement, ces paramètres doivent être combinés avec des simulations thermodynamiques plus avancées telles que CALPHAD (CALculation de PHAse Diagrams) ou des méthodes *ab initio*.

Depuis 2004, l'alliage équiatomique CoCrFeMnNi est devenu l'un des HEAs les plus étudiés, avec un nombre croissant de publications chaque année. L'intérêt des universités et des centres de recherche les plus connus est remarquable. Cet alliage ne contient qu'une seule phase FCC et se solidifie dendritiquement. Cependant, un nombre important d'articles récents ont montré que sa microstructure est instable après différents traitements thermiques, lorsque la formation d'une phase BCC et / ou σ devient possible. Ses propriétés mécaniques sont élevées, notamment aux basses températures où les mécanismes de déformation plastique changent.

Conclusions: Les HEAs sont un nouveau groupe de matériaux aux propriétés prometteuses. Leur conception doit être basée sur des calculs thermodynamiques, en ce qui concerne la stabilité de phase. Parmi eux, avec ses propriétés mécaniques remarquables, CoCrFeMnNi HEA semble être l'une des compositions les plus intéressantes. Ces propriétés doivent être étudiées en particulier à des températures basses et élevées, où l'énergie de défaut d'empilement et donc les mécanismes de déformation changent. Les phénomènes de déformation plastique et de renforcement des solutions solides n'ont pas encore été entièrement compris et doivent être caractérisés plus précisément.

Chapitre 2: Méthodes et procédures

Résumé: Dans ce chapitre, les techniques appliquées pendant la thèse sont décrites.

Chapitre 3: Conception de nouveaux alliages à haute entropie

Introduction: Il a été présenté précédemment que dans la grande famille des HEA, CoCrFeMnNi reste parmi les plus étudiés. Même si cette composition s'est révélée avoir une phase solide, des études récentes ont montré une décomposition en plusieurs phases après différents traitements thermiques. Pour cette raison notre approche de modification du matériau de référence était d'augmenter la stabilité de phase et, si possible, ses propriétés mécaniques.

Résumé: Dans ce chapitre, une procédure d'optimisation d'un nouvel alliage est présentée. Il est développé sur la base de l'alliage équiatomique à haute entropie CoCrFeMnNi. Cet alliage est l'un des plus prometteurs parmi tous les HEA connus avec une structure monophasée. L'objectif principal est d'augmenter encore sa stabilité de phase (puisque la décomposition est possible dans certaines conditions) et d'améliorer les propriétés mécaniques, en particulier la limite d'élasticité et la ductilité. Pour cela, CALPHAD et d'autres calculs thermodynamiques, basés sur la bibliographie et les résultats existants, sont appliqués. Des séries de diagrammes de phase binaires et quasi-binaires sont présentées, ainsi que d'autres calculs de paramètres thermodynamiques nécessaires à la formation de HEA. A la fin, une nouvelle composition est donnée.

Conclusion: Avec une approche appropriée, une nouvelle composition est donnée, basée sur un alliage de référence, avec une stabilité en solution solide théoriquement plus élevée. La stabilité obtenue de la phase FCC est plus élevée puisque toutes les transformations de phase se produisent à des températures plus basses que pour le matériau de référence. Ce nouvel alliage s'appelle A3S (comme pour Austenitic Super Stainless Steel).

Chapitre 4: Évaluation de l'A3S par rapport aux X1: microstructures et propriétés mécaniques

Introduction: L'évaluation des microstructures et des propriétés mécaniques dans différentes conditions est effectuée. Par exemple, une série de traitements thermiques est effectuée pour vérifier si la plus grande stabilité d'une stabilité solide est atteinte dans le nouveau matériau. Plus tard, différentes techniques d'essais mécaniques sont appliquées afin de vérifier toute amélioration des propriétés, dans une gamme de températures cryogéniques à élevées.

Résumé: Les alliages ont été coulés et forgés à chaud, certains d'entre eux ont été laminés à froid. La microstructure de l'A3S forgé est composée de grains avec des joints de grains ondulés, ainsi que des macles. Cette structure a été observée plus précisément avec SEM + EBSD et MET. Il se compose entièrement de grains FCC avec des joints de grains à angle élevé et une densité élevée de joints de grains à faible angle. Cette microstructure est typique pour les matériaux déformés à haute température, où les grains recristallisent dynamiquement avec des limites ondulées et une forte densité de dislocations. Aucune trace de séparation de phases n'a été trouvée. La taille moyenne des grains est de ~6 μm. A l'état recuit (1000°C, 2 heures), la microstructure observée à l'échelle SEM-EBSD est exempte de sous-grains, avec des grains équiaxes homogènes de ~20 μm contenant un grand nombre de jumeaux de recuit. L'analyse DRX a confirmé le caractère monophasé des deux matériaux. Dans le cas des deux HEAs étudiés dans ce travail, la nanostructure a été obtenue après forgeage à chaud standard, ce qui indique une plus grande facilité d'obtention de très petits grains par rapport aux matériaux classiques. La microstructure du X1 à l'état forgé, similaire à A3S, se compose de cellules avec des limites d'angle faibles et une forte densité de dislocations. Ces cellules sont de centaines de nanomètres. Pourtant, la principale différence entre le X1 et l'A3S est que dans le X1 nanomacles sont présents, à peine trouvé dans l'A3S. La formation de macles est probablement plus facile dans le X1 que

dans le A3S, ce qui peut être dû à une énergie d'erreur d'empilement plus faible de ce matériau. Les matériaux à faible énergie de faute d'empilement (SFE) devraient former facilement des macles, en particulier à des contraintes plus élevées. Le SFE est principalement déterminé par la composition chimique et apparemment cet effet est fort pour les X1 et A3S, car les microstructures ne sont pas les mêmes bien que les proportions entre les éléments ne soient pas extraordinairement différentes.

Après recuit à 500°C pendant 100 jours, une décomposition du X1 a été observée. Ces résultats confirment que le X1 n'est pas stable même à une température relativement basse (500°C) lorsque le recuit est prolongé. Pourtant, l'A3S reste monophasé même jusqu'à 300 jours lorsqu'il est recuit. Le manque de séparation de phase est une première indication que la nouvelle composition non-équiatomique modifiée augmente la stabilité de la phase solide en solution. Ca, ainsi que les anomalies dans la microstructure de deux alliages présentés dans le chapitre précédent, peut vraisemblablement conduire à des propriétés plus prometteuses.

A l'état forgé, le X1 présente une limite d'élasticité de 600 MPa, tandis que la valeur de l'A3S est beaucoup plus élevée (775 MPa). La pente de la courbe dans la zone plastique pour les deux matériaux est faible (elle correspond à un écrouissage). Cependant à l'état recuit les deux matériaux possèdent des propriétés similaires avec une limite d'élasticité de 240 MPa et une pente élevée dans la zone plastique. Dans les deux cas, aucune fissure n'a été trouvée sur aucun des échantillons après la compression, indiquant leur haute plasticité dans toutes les conditions de température.

Dans l'étape suivante, une ductilité élevée à basse température a été confirmée dans des essais de traction à -130°C. A l'état brut, la limite d'élasticité et la résistance à la traction finale atteignent respectivement 807 MPa et 958 MPa, avec un allongement à la rupture de 54%. Toutes ces valeurs sont supérieures à celles obtenues à l'état brut à température ambiante. La résistance et l'allongement sont également augmentés à l'état recuit par rapport à la température ambiante, avec YS = 610 MPa, UTS = 835 MPa

et un allongement de 70%. Une augmentation importante de la limite d'élasticité à basse température à l'état recuit peut être expliquée par la création de macles pendant la déformation qui fonctionnent comme mécanismes de renforcement.

Conclusions: Le nouveau matériau, A3S, possède une stabilité thermique supérieure et des propriétés mécaniques supérieures à celles de l'alliage de référence X1. Les origines de ces propriétés seront étudiées dans le chapitre suivant.

Chapitre 5: Origines des propriétés mécaniques

Introduction: Les propriétés d'origine des alliages à haute entropie proviennent vraisemblablement de phénomènes spécifiques se produisant dans leur microstructure. En raison d'une distorsion importante du réseau local, d'une diffusion ralentis et l'existence possible d'un ordre à courte distance, des phénomènes tels que la restauration et la recristallisation diffèrent des alliages conventionnels. La mobilité des dislocations est particulièrement fortement influencée. Dans ce travail, un comportement inhabituel de dislocations a été observé à des températures élevées, où leur densité reste stable indépendamment de la croissance des grains. La résistance à la restauration classique et à la recristallisation est hypothétiquement expliquée par les fluctuations de la friction du réseau (friction de Peierls) et une contrainte de frottement plus élevée dans les HEAs ainsi que par la création de jonctions Lomer-Cottrell.

Résumé: Après une série de traitements thermiques, trois types de microstructures peuvent être distingués, en fonction de la température du traitement thermique. Premièrement, une structure à basse température (inférieure à 600°C): similaire à l'état de forgeage, avec des cellules/sous-grains de quelques centaines de nanomètres et une forte densité de dislocations; solution solide FCC stable sans traces de décomposition ou de précipitation. Ensuite, une structure de température intermédiaire (entre 600°C et 700°C): avec des grains de quelques micromètres presque sans dislocations; certaines zones restent fortement déformées; considéré comme un état recristallisé. Enfin, une

structure à haute température (supérieure à 700°C): avec des grains de quelques dizaines de micromètres et une forte densité de dislocations qui sont disposées dans des plans caractéristiques de type {111} et {100}. Une recristallisation typique n'a pas été observée ici.

Cela signifie que dans les HEAs étudiés, la restauration classique et la recristallisation n'ont pas lieu à des températures élevées. Au lieu de cela, seule une croissance de grain a été observée, confirmée dans XRD et EBSD, ainsi que dans MET *in situ*. En même temps, une très forte densité de dislocations a été trouvée, inhabituelle pour ces conditions. Cette densité peut s'expliquer par les fluctuations du potentiel de Peierls et la formation de jonctions Lomer-Cottrell. Le comportement des dislocations lors de la déformation a été trouvé comme dans les alliages FCC classiques mais avec des traces de pinning, indiquant des fluctuations de la composition chimique. Dans des conditions dynamiques, une recristallisation dynamique classique a été révélée.

Conclusion: Des phénomènes inhabituels pour les matériaux FCC classiques, tels que le fort stress de Peierls et ses fluctuations, sont à l'origine d'une densité inhabituelle de dislocations observées à haute température. Cela influence aussi les mécanismes de restauration et de recristallisation.

École Nationale Supérieure des Mines

de Saint-Étienne

Michal MROZ

DISSERTATION TITLE: Design and structural optimization of a high entropy alloy (HEA) of the CoCrFeMnNi family with high mechanical resistance.

Speciality : Sciences et Génie des Matériaux

Abstract :

High entropy alloys (HEAs) are a new class of materials obtained with a novel approach. They are made of at least 5 elements in similar proportions, which results in increased configurational entropy of the system and in some cases in higher stability of single solid solutions. Promising mechanical and other properties are coming from specific phenomena such as highly distorted crystal structure.

In this work, a novel HEA based on equiatomic CoCrFeMnNi was optimized, characterized and patented. This alloy, referred to as A3S® (austenitic super stainless steel), consists of 5 elements in non-equiatomic proportions ($Co_{20}Cr_{15}Fe_{26}Mn_{17}Ni_{22}$). This composition was optimized with CALPHAD (Computer Coupling of Phase Diagrams and Thermochemistry) in Thermo-Calc software. The material possesses stable face-cubic centered solid solution structure and, unlike the equiatomic one, remains stable after annealing at 500°C up to 300 days. The facility of forming a nanostructure after hot forging is remarkable, and results in high resistance as well as ductility compared to stainless steels. These properties are improved at cryogenic temperatures where an additional mechanism of deformation by twinning is being activated. This compilation of properties is very promising for industry where new materials are required.

A comparative study between the novel A3S and the equiatomic reference material has been conducted. First, the procedure of the alloy optimization by thermodynamic calculations has been presented. Then, microstructures and mechanical properties in different conditions (various annealing temperatures and times as well as types of deformation) have been examined. Finally, the last part reviews the mechanisms of recovery and recrystallization which differ significantly from classical material. Here, standard recrystallization occurs at lower temperatures (600°C), however at high temperatures (above 800°C) only grain growth was observed without any traces of nucleation and very high density of dislocations rearranged in specific planes. Possible origins of this phenomena are discussed.

École Nationale Supérieure des Mines

de Saint-Étienne

NNT : 2018 LYSE M003

Michal MROZ

TITRE DE LA THÈSE : Design et optimisation structurale d'un alliage à forte entropie (HEA) de la famille CoCrFeMnNi a haute résistance mécanique.

Spécialité: Sciences et Génie des Matériaux

Mots clés: alliages à haute entropie, CoCrFeMnNi, nanomatériaux

Résumé :

Les alliages à haute entropie (high entropy alloys ou HEAs en anglais) sont une nouvelle classe de matériaux obtenus avec nouvelle approche originale. Ils sont constitués d'au moins 5 éléments dans des proportions similaires, ce qui entraîne une entropie de configuration accrue et dans certains cas une plus grande stabilité des solutions solides. Des propriétés mécaniques (et autres) prometteuses proviennent de phénomènes spécifiques tels qu'une structure cristalline fortement déformée.

Dans ce travail, un nouveau HEA basé sur CoCrFeMnNi a été optimisé, caractérisé et breveté. Cet alliage, appelé A3S®, est constitué de 5 éléments en proportions non équiatomiques. Cette composition a été optimisée avec CALPHAD (Computer Coupling of Phase Diagrams and Thermochemistry) dans le logiciel Thermo-Calc. Le matériau possède une structure de solution solide cubique à face centrées et qui, contrairement à la structure équiatomique, reste stable après un recuit à 500°C jusqu'à 300 jours. La facilité de formation d'une nanostructure après forgeage à chaud est remarquable et résulte en une résistance élevée ainsi qu'une bonne ductilité. Ces propriétés sont améliorées aux températures cryogéniques où un mécanisme supplémentaire de déformation par le maclage est activé.

Une étude comparative entre le nouvel A3S et le matériau de référence équiatomique a été réalisée. Tout d'abord, la procédure d'optimisation de l'alliage par des calculs thermodynamiques a été présentée. Ensuite, les microstructures et les propriétés mécaniques dans différentes conditions (différentes températures et durées de recuit ainsi que les types de déformation) ont été examinées. Enfin, la dernière partie passe en revue les mécanismes de restauration et de recristallisation qui diffèrent significativement des matériaux classiques. Ici, la recristallisation standard se produit à des températures plus basses (600°C), mais, à des températures élevées (supérieures à 800°C), seule la croissance des grains est observée sans aucune trace de nucléation et une très forte densité de dislocations réarrangées dans des plans spécifiques. Les origines possibles de ce phénomène sont discutées.